Optimal Control of Quantum Information Tasks in Open Quantum Systems

Dissertation

zur Erlangung des akademischen Grades
Doktor der Naturwissenschaften
(Dr. rer. nat.)
im Fach Physik

vorgelegt am
Fachbereich Naturwissenschaften und Mathematik
der Universität Kassel
von

Daniel Basilewitsch

Betreuerin: Prof. Dr. Christiane P. Koch
Zweitgutachter: Prof. Dr. Frank Wilhelm-Mauch

Eingereicht am 30.07.2020
Disputation am 16.12.2020

Was sind denn zuletzt die Wahrheiten des Menschen?
— Es sind die unwiderlegbaren Irrtümer des Menschen.
Friedrich Nietzsche

Contents

Abstract

Every quantum system inevitably interacts with its environment. This is a fundamental requirement that allows us to control, measure and, in general, interact with quantum systems. In that respect, a quantum system's openness can be interpreted as prerequisite that enables quantum technologies in the first place. The latter are built to harness the intrinsic quantum mechanical behavior of quantum devices in order to build new, powerful technologies. However, a quantum system's openness also causes it to interact uncontrollably with all kinds of other environmental modes. This leads to dissipation whose impact is mostly detrimental. The ability to steer an open quantum system in a desired way and to protect it against dissipation is therefore of crucial importance.

This thesis explores how optimal control techniques can be used to improve the control of open quantum systems. The first part focuses on the development of new methods for the study of such systems. To this end, a new, reliable distance measure that allows optimization towards mixed target states has been constructed. This measure provides more information about existing state mismatches than comparable measures and is by construction compatible with gradient-based optimization algorithms. Mixed target states occur, for example, in the preparation of squeezed states in cavity optomechanics. Their preparation can be substantially accelerate when the control fields are optimized using the new distance measure. Moreover, a new method that allows to identify decoherence-free subspaces via optimal control techniques has been introduced. The method's general functionality and performance has been demonstrated by identifying decoherence-free subspaces in a network of qubits. However, the method's general abilities are not restricted to the search for decoherence-free subspaces.

The remainder of the thesis then focuses on how optimal control allows for deriving new control strategies that cope best with the environment's presence. To this end, three tasks have been considered that are fundamental for quantum technologies. First, qubit

reset has been considered, where the presence of the environment is even a necessity for the task's feasibility. Optimal control has been used to identify the fundamental limits of qubit reset in time and fidelity and has derived time-optimal reset strategies. These results have been obtained for qubit reset employing a tunable environment as well as when utilizing a single, strongly coupling ancilla mode from the environment. The other two examples focus on how optimized control fields can assist in diminishing the environment's detrimental impact. To this end, a state discrimination task has been investigated, which is a typical problem in quantum metrology. It has been shown that, in the presence of dissipation, optimized control fields improve the distinguishability between states and thus improve the metrological performance of the discrimination task. Lastly, the implementation of an entangling quantum gate between qubits has been considered, which is pivotal for quantum computers. By means of optimal control, an analytical control strategy has been derived that readily accelerates the implementation of an entangling quantum gate between bosonic modes. Due to the reduction in the gate duration, this leads to an improved robustness of the gate with respect to dissipation.

Zusammenfassung

Jedes Quantensystem wechselwirkt unweigerlich mit seiner Umgebung. Dies ist eine grundlegende Notwendigkeit, die es uns erlaubt, Quantensysteme zu kontrollieren, zu messen und im Allgemeinen mit ihnen zu interagieren. Im Hinblick darauf kann die Offenheit eines Quantensystems als Voraussetzung interpretiert werden, welche Quantentechnologien überhaupt ermöglicht. Letztere sind konstruiert, um intrinsisch quantenmechanisches Verhalten gezielt auszunutzen und damit neue, leistungsfähige Technologien zu entwickeln. Die Offenheit eines Quantensystems führt jedoch auch zu unkontrollierter Wechselwirkung mit diversen Moden innerhalb seiner Umgebung. Dies führt zu Dissipation, deren Auswirkung in den meisten Fällen negativ ist. Die Möglichkeit offene Quantensysteme in einer gewünschten Weise zu steuern und sie gegen Dissipation zu schützen ist daher von entscheidener Bedeutung.

Diese Arbeit untersucht, wie Methoden der optimalen Kontrolltheorie genutzt werden können, um die Kontrolle offener Quantensysteme zu verbessern. Der erste Teil fokussiert sich dabei auf die Entwicklung neuer Methoden für die Untersuchung solcher Systeme. Zu diesem Zweck wurde ein neues, zuverlässiges Abstandsmaß konstruiert, welches Optimierung auf gemischte Zielzustände ermöglicht. Dieses Maß liefert dabei mehr Informationen über existierende Zustandsdiskrepanzen als vergleichbare Maße und ist per Konstruktion kompatibel mit gradientenbasierten Optimierungsalgorithmen. Gemischte Zielzustände kommen zum Beispiel bei der Präparation gequetschter Zustände in der *Cavity Optomechanics* vor. Ihre Präparation kann entscheidend beschleunigt werden, wenn die Kontrollfelder mithilfe des neuen Abstandsmaßes optimiert werden. Des Weiteren wurde eine neue Methode eingeführt, welche die Identifikation von dekohärenzfreien Unterräumen durch Techniken der optimalen Kontrolle ermöglicht. Die Fuktionalität der Methode wurde durch das Identifizieren eines dekohärenzfreien Unterraums in einem Netzwerk von Qubits gezeigt. Die Möglichkeiten der Methode bleiben dabei allerdings

nicht auf die Suche nach dekohärenzfreien Unterräumen beschränkt.

Der Rest der Arbeit fokussiert sich anschließend darauf, wie optimale Kontrolle verwendet werden kann, um neue Kontrollstrategien zu finden, welche die Präsenz der Umgebung bestmöglich berücksichtigen. Zu diesem Zweck wurden drei Aufgaben betrachtet, welche fundamental für Quantentechnologien sind. Zuerst wurde dazu Qubit-Reset betrachtet, für welches die Präsenz der Umgebung sogar eine Notwendigkeit für die Durchführbarkeit der Aufgabe ist. Optimale Kontrolle wurde dabei verwendet, um die fundamentalen Grenzen in Fidelität und Zeit für Qubit-Reset zu identifizieren und zeit-optimale Kontrollstrategien herzuleiten. Die Ergebnisse wurden für Qubit-Reset mithilfe einer steuerbaren Umgebung erzielt sowie durch Nutzung einer einzelnen, stark koppelnden Umgebungsmode. Die beiden weiteren Aufgaben fokussieren sich hingegen darauf, wie optimierte Kontrollfelder verwendet werden können, um die negativen Effekte der Umgebung zu vermindern. Dazu wurde die Aufgabe der Zustandsunterscheidung untersucht, welche eine typische Aufgabe in den Quantenmetrologie ist. Es wurde gezeigt, dass, unter Berücksichtigung von Dissipation, optimierte Kontrollfelder die Unterscheidbarkeit von Zuständen verbessern und somit die metrologische Leistung der Aufgabe erhöhen. Zuletzt wurde die Implementierung von verschränkenden Quantengattern zwischen Qubits betrachtet, welche von zentraler Wichtigkeit für Quantencompuer ist. Eine analytische Kontrollstrategie, welche die Implementierung von verschränkenden Quantengattern zwischen bosonischen Moden beschleunigt, wurde mithilfe optimaler Kontrolle hergeleitet. Aufgrund der Reduzierung der Implementierungsdauer führt dies zu einer Verbesserung der Robustheit des Quantengatters im Hinblick auf Dissipation.

Acknowledgments

Above all, I want to thank my supervisor Christiane Koch for supporting me throughout my entire academic career. She has been an outstanding source of knowledge, inspiration and encouragement during all this time and has therefore enabled me to obtain the results presented in this thesis in the first place.

Furthermore, I would like to thank Steven Girvin with whom I had the opportunity and pleasure to work with and who hosted me at the Yale Quantum Institute. It has been a truly fantastic time and one that has sparked my passion for quantum information even more.

I am also deeply grateful to Daniel Reich for many enlightening discussions. His incredible didactic talent allows even complex topics to appear simple. In addition, I would like to thank Michael Goerz who taught me almost everything I know about programming and that it can be fun.

Last but not least, my thanks goes to all former and present members of the group in Kassel for a very pleasant working atmosphere. In particular, I want to thank Sabrina Patsch and Fernando Gago with whom I had countless conversations about almost everything and who sometimes reminded me that life is not only about research.

A special thanks goes to my parents for their endless support.

List of Publications

1. **Daniel Basilewitsch**, Rebecca Schmidt, Dominique Sugny, Sabrina Maniscalco, Christiane P. Koch.
   Beating the limits with initial correlations.
   New J. Phys. **19**, 113042 (2017).

2. **Daniel Basilewitsch**, Lutz Marder, Christiane P. Koch.
   Dissipative Quantum Dynamics and Optimal Control using Iterative Time Ordering: An Application to Superconducting Qubits.
   Eur. Phys. J. B **91**, 161 (2018).

3. **Daniel Basilewitsch**, Christiane P. Koch, Daniel M. Reich.
   Quantum Optimal Control for Mixed State Squeezing in Cavity Optomechanics.
   Adv. Quantum Technol. **2**, 1800110 (2019).

4. Jonas Fischer, **Daniel Basilewitsch**, Christiane P. Koch, Dominique Sugny.
   Time-optimal purification of a qubit in contact with a structured environment.
   Phys. Rev. A **99**, 033410 (2019)

5. **Daniel Basilewitsch**, Francesco Cosco, Nicola Lo Gullo, Mikko Möttönen, Tapio Ala-Nissilä, Christiane P. Koch, Sabrina Maniscalco.
   Reservoir Engineering via Quantum Optimal Control for Qubit Reset.
   New J. Phys. **21**, 093054 (2019).

6. Michael H. Goerz, **Daniel Basilewitsch**, Fernando Gago-Encinas, Matthias G. Krauß, Karl P. Horn, Daniel M. Reich, Christiane P. Koch.
   Krotov: A Python implementation of Krotov's method for quantum optimal control.
   SciPost Phys. **7**, 080 (2019).

7. **Daniel Basilewitsch**, Jonas Fischer, Daniel M. Reich, Dominique Sugny, Christiane P. Koch.
   Fundamental bounds for qubit reset.
   arXiv:2001.09107 (2020).

8. **Daniel Basilewitsch**, Haidong Yuan, Christiane P. Koch.
   Optimally controlled quantum discrimination and estimation.
   Phys. Rev. Research **2**, 033396 (2020)

1 Introduction

The advent of information processing technologies in the second half of the 20th century marks the birth of today's *Information Age*. In the history of humankind, it also marks the starting point for a period of remarkable and incredibly fast-paced technological progress, which — judging by innovations from recent years — is by far not over yet. While information technologies come nowadays in various forms and affect almost every part of everyday life, the invention and subsequent public availability of computers can be regarded as the spark that ignited this technological revolution. Back in these days, computers did not only constitute a novel way of quantifying and thinking about information — namely in terms of binary numbers — but also introduced themselves as the machines to process these information reliably and automatically. Their computational power has increased ever since and, by now, any computer is routinely capable of solving incredibly challenging computational tasks that were not deemed solvable decades ago.

While a computer or, to be more precise, a classical computer follows strictly deterministic rules and obeys the laws of classical physics, Richard Feynman was the first to think about the possibility of a computer that follows the strange laws of quantum physics [1]. Although this idea might have appeared odd due to the probabilistic nature of quantum mechanics, it has now become the foundation for an entire field of research. This field focuses on how to actively harness the potential of quantum effects in order to create new powerful technologies that outperform their classical counterparts. Nowadays,

major pillars of these so-called quantum technologies involve quantum computing and simulation, quantum metrology as well as quantum cryptography and communication [2].

Presently, we are in what is termed the "second quantum revolution". This term refers to quantum technologies that are designed to actively exploit quantum effects. This is at the heart of any quantum technologies [3]. For instance, in view of quantum computers, this implies the exploitation of entanglement — one of quantum theory's most peculiar properties that has no classical analogue — as a key resource. By carefully designing quantum algorithms that make use of this property, a quantum computer is in general capable of tasks a classical computer can not perform in reasonable time [4, 5]. Similar examples can be found for other quantum technologies.

Unfortunately, it is rather unlikely that a quantum system will perform the task a user wants it to do all by itself, i.e., just by waiting. Thus, the possibility to control a quantum system's underlying dynamics is required and crucial in order to exploit quantum effects for quantum technologies in practice. Time-dependent control fields that interact with the quantum system are what is commonly used as control handles and allow to shape a quantum system's dynamics to fulfill the user's demand.

Besides the plain necessity to steer a quantum system's dynamics, another crucial requirement for quantum control is that it needs to diminish all detrimental influences that might potentially impair the device's performance. On the one hand, quantum control needs to ensure that only those parts of a large-scale, multipartite quantum system interact that are supposed to interact at that specific point of time. In detail, quantum control is required to control the interactions between internal modes, since an uncontrolled interaction will most likely lead to a loss of performance. On the other hand, quantum control also needs to minimize the detrimental interaction of any quantum system with its environment, i.e., its interaction with external modes. Especially the latter poses a major challenge, as the environment's impact is what predominantly limits quantum technologies to fully unfold their inherent power in practice. For quantum computing, after decades of research and improvements in device properties, we have now reached the regime recently termed "noisy intermediate-scale quantum" (NISQ) technology [6]. It describes the current era of quantum computing devices, where environmental noise can already be kept at bay sufficiently much such as to allow interesting first applications of quantum technologies, despite their error-prone hardware, that are no longer possible with classical devices. One particular example is Google's recent demonstration of quantum supremacy [7].

The technological progress that has led to the current NISQ era has been largely fueled — besides the obvious enhancement of device properties — by establishing new,

advanced control strategies. In addition to quantum control's critical role as the tool that enables operation of any quantum device in the first place, a clever choice for the underlying control strategy can easily improve the device's performance beyond the point that is reachable by plain hardware engineering. For instance, such an improvement can originate from finding strategies that simply realize certain tasks faster and/or are naturally more resistant to dissipation. Many of these advanced control strategies have not been identified by trial and error but by quantum optimal control [8]. The latter can be viewed as a collection of sophisticated mathematical and numerical techniques that allow to derive optimized control fields that are shaped to perform a particular task in an optimal fashion. It does not matter whether ideal conditions are assumed or if the control solutions are derived in the presence of dissipation [9]. The latter scenario even allows for finding control strategies that best cope with the environment.

In this thesis, we will derive new control strategies to realize fundamental tasks for quantum technologies. The presence of the environment will thereby not always be a mere nuisance but will sometimes play an important role for the task's success. We will use a combination of analytical and numerical tools from optimal control to find these control strategies. To this end, Chap. 2 starts by briefly reviewing the basic notations of quantum mechanics before it continues to introduce open quantum systems and their dynamics as well as quantum optimal control theory, both of which are central concepts for this thesis. Chapter 3 finalizes the discussion of optimal control theory by formulating basic mathematical conditions that any reliable optimization functional needs to fulfill. In view of these conditions, a new functional is derived and subsequently applied to a control problem from cavity optomechanics, where the goal is to accelerate the preparation of a squeezed quantum state.

The next chapter continues to introduce new concepts for optimal control. While traditional optimal control methods primarily focus on optimizing time-dependent control fields in order to steer a quantum system's dynamics in a desired way, Chap. 4 explores how optimal control can assist in the identification of decoherence-free subspaces in open quantum systems. This requires conceptually new optimization functionals as well as parametrization methods for arbitrary subspaces, both of which are introduced and their operation demonstrated.

Chapter 5 constitutes a central chapter in this thesis. We will explore how optimized control fields can help to minimize the required time and to improve the achievable fidelity of qubit reset — a task that is vital for almost all quantum technologies. It is even a particularly interesting control task as it fundamentally requires the presence of an environment. Any control strategy therefore needs to incorporate the on-demand nature

of the environmental interaction, which should be large when resetting the qubit and at best vanish otherwise. We will examine qubit reset that utilizes a tunable environment as well as a controlled interaction with an ancilla mode. We will explore the impact of initial correlations between qubit and environment and how the form of their interaction affects the reset time and its general feasibility. Time-optimal control strategies are identified in all cases by a mixture of analytical and numerical tools from optimal control.

In Chap. 6, we turn towards a control task from quantum metrology. While the general idea of quantum metrology is to exploit quantum effects in order to create measurement devices of unprecedented sensitivity, we will here focus on one of its elementary tasks — namely to improve the distinguishability between quantum states. Although the Ramsey scheme provides a simple and reliable protocol to this end, we will show that it can be significantly improved in the presence of environmental noise by using optimized control fields.

Finally, Chap. 7 will be devoted to one of quantum computing's most fundamental tasks: the implementation of an entangling gate between qubits. To this end, we consider an architecture for encoding and coupling qubits that has been established within the last years. We will demonstrate how optimized control fields can be used to accelerate the implementation of an entangling gate, which thus minimizes the detrimental influence of the environment. Chapter 8 concludes and points out possible future directions.

2

Dynamics and Control of Open Quantum Systems

This thesis focuses in large parts on how to optimally control the dynamics of open quantum systems in order to realize quantum information tasks with highest fidelity or in shortest time. This chapter is therefore devoted to introduce the necessary mathematical framework and terminology used in quantum dynamics and optimal control theory. We start in Sec. 2.1 by briefly reviewing the basic concepts for states, operators, dynamical maps and Hilbert and Liouville space. The latter one is especially important for the description of open quantum systems, i.e., quantum systems that interact with their environment, which are introduced in more detail in Sec. 2.2. We discuss the difference of Markovian and non-Markovian dynamics of open quantum system and briefly review common environmental noise forms and the types of dynamics which they give rise to. The case of Markovian dynamics, albeit being usually an approximation of the true dynamics, yields a specific class of dynamical maps, which describe most of the open quantum systems discussed throughout this thesis. We will furthermore explore the time-dependent properties of dynamical maps, which arise when time-dependent control fields interact with the open quantum system. The prevalent question will be how such control fields have to be shaped such that they generate a desired dynamical map that carries out a predefined task in the best possible way. To this end, Sec. 2.3 introduces quantum optimal control theory (OCT) thoroughly, as it plays a central role in this thesis

and provides the means to derive the required field shapes.

The intention of this chapter is to serve as sufficiently detailed, albeit not exhaustive, summary of important concepts from open quantum systems and optimal control theory and builds the theoretical foundation for all later chapters. Its content is taken from the textbooks of Breuer and Petruccione [10] and D'Alessandro [11] about open quantum systems and quantum control, respectively.

2.1 States, Operators, Spaces and Maps

This section briefly reviews the basic concepts and notations of quantum mechanics and dynamics.

The Hilbert space $\mathcal{H}$ constitutes the fundamental space for pure quantum states. It provides the vector space structure for expressing arbitrary superpositions of quantum states — a key feature of quantum mechanics and one of its striking differences to classical physics. For $|\psi\rangle, |\phi\rangle \in \mathcal{H}$ we have $\alpha|\psi\rangle + \beta|\phi\rangle \in \mathcal{H}$ for all $\alpha, \beta \in \mathbb{C}$. Moreover, $\mathcal{H}$ provides a scalar product denoted $\langle\cdot|\cdot\rangle$ such that $\langle\psi|\phi\rangle \in \mathbb{C}$. From a merely physical perspective, we also require that $\|\psi\|^2 = \langle\psi|\psi\rangle = 1$ for all $|\psi\rangle \in \mathcal{H}$ that correspond to *physical* quantum states. This normalization condition ensures that the probability of measuring the state $|\psi\rangle$ "somewhere" amounts to 100%, which is at the heart of the Copenhagen interpretation of quantum mechanics.

After having established the Hilbert space $\mathcal{H}$ as the appropriate space for pure quantum states, we introduce the Liouville space $\mathfrak{L}_\mathcal{H}$ as the space of bounded operators on $\mathcal{H}$. The Liouville space is a vector space in itself and one can show the isomorphism $\mathfrak{L}_\mathcal{H} \cong \mathcal{H} \otimes \mathcal{H}$, which highlights its vector space character and connection to $\mathcal{H}$. Thus, with $\dim\{\mathcal{H}\} = N$ we have $\dim\{\mathfrak{L}_\mathcal{H}\} = N^2$. For all operators $\mathsf{O} \in \mathfrak{L}_\mathcal{H}$ we have $\mathsf{O} : \mathcal{H} \to \mathcal{H}; |\psi\rangle \mapsto |\phi\rangle = \mathsf{O}|\psi\rangle$, where it should be noted that if the input $|\psi\rangle$ is a *physical* state, the output $|\phi\rangle$ is usually not due to the potential change in norm.

Unfortunately, the Hilbert space $\mathcal{H}$ is not sufficient to express the variety of states that are relevant for describing fully general quantum states in practice. To be more precise, every $|\psi\rangle \in \mathcal{H}$ is technically a coherent or pure state. However, nature gives also rise to statistical mixtures of coherent states. Such mixtures can not be expressed by a single coherent state and, hence, not expressed by a single element of $\mathcal{H}$ anymore. These incoherent or mixed states ρ are described by the density matrix formalism. Let $\mathrm{span}\{|\psi_i\rangle\} = \mathcal{H}$, then

$$\rho = \sum_i p_i |\psi_i\rangle\langle\psi_i|, \qquad \sum_i p_i = 1, \qquad p_i \geq 0 \ \forall i, \tag{2.1}$$

where $|\psi_i\rangle\langle\psi_i|$ denotes the dyadic product which makes the operator $|\psi_i\rangle\langle\psi_i|$ a rank one projector in $\mathfrak{L}_\mathcal{H}$. ρ is therefore sometimes also referred to as density operator or density matrix. Physically, the weights p_i in Eq. (2.1) indicate the probability with which the coherent state $|\psi_i\rangle$ enters the mixture ρ. Conversely, in the notation of density matrices, any coherent, i.e, pure, state can always be written as $\rho = |\psi\rangle\langle\psi|$. In consequence, an arbitrary density matrix ρ corresponds to a pure state iff there exists an orthonormal basis $\text{span}\{|\psi_i\rangle\} = \mathcal{H}$ such that $p_j = 1$ and $p_k = 0$ for all $k \neq j$, cf. Eq. (2.1). This is equivalent to ρ being a rank one projector in $\mathfrak{L}_\mathcal{H}$. In order to express this property independent on the basis $\{|\psi_i\rangle\}$, we can first introduce the Hilbert-Schmidt overlap, i.e., the general scalar product in Liouville space $\mathfrak{L}_\mathcal{H}$, which we will denote by

$$\langle\langle \mathsf{A}|\mathsf{B}\rangle\rangle \equiv \text{tr}\left\{\mathsf{A}^\dagger\mathsf{B}\right\}, \qquad \mathsf{A},\mathsf{B} \in \mathfrak{L}_\mathcal{H}, \tag{2.2}$$

and then write the purity of a density matrix ρ as

$$\mathcal{P}(\rho) \equiv \langle\langle\rho|\rho\rangle\rangle = \text{tr}\left\{\rho^\dagger\rho\right\} = \text{tr}\left\{\rho^2\right\} \tag{2.3}$$

such that $\mathcal{P}(\rho) = 1$ iff ρ corresponds to a pure state and $\mathcal{P}(\rho) < 1$ iff ρ represents a mixed state. In the last step of Eq. (2.3) we have already used the Hermiticity of ρ. The properties of density matrices can be summarized as follows.

Definition 2.1. *Let $\mathfrak{L}_\mathcal{H}$ be the Liouville space over Hilbert space $\mathcal{H}$ with $\dim\{\mathcal{H}\} = N$. $\rho \in \mathfrak{L}_\mathcal{H}$ is a density matrix if*

1. $\rho = \rho^\dagger$ *(Hermiticity)*
2. $\rho \geq 0$ *(positive semi-definiteness)*
3. $\text{tr}\{\rho\} = 1$ *(population norm.)*
4. $\frac{1}{N} \leq \mathcal{P}(\rho) \leq 1$ *(purity)*

Note that the density matrices form a subset $\mathcal{S}_\mathcal{H} \subset \mathfrak{L}_\mathcal{H}$ of Liouville space that does not form a vector space in itself. Similar to a state $|\psi\rangle \in \mathcal{H}$ with $\langle\psi|\psi\rangle = 1$ that represents a *physical* state in $\mathcal{H}$, a density matrix describes a *physical* state in $\mathfrak{L}_\mathcal{H}$.

Until now, we have briefly reviewed the basic concepts to represent pure and mixed quantum states. However, in order to describe the dynamics of any quantum system, we need an operation that maps states to states, e.g. from initial time t_0 to time t. Note that since we will primarily use the density matrix formalism, and not Hilbert space vectors, to represent states within this thesis, we only discuss a map between density matrices. In its most general from, such a map is given by the dynamical map $\mathcal{D}_{t,t_0} : \mathfrak{L}_\mathcal{H} \to \mathfrak{L}_\mathcal{H}$ — a completely-positive and trace-preserving (CPTP) operation on $\mathfrak{L}_\mathcal{H}$. The latter two properties ensure that any dynamical map $\mathcal{D}_{t,t_0}$ fulfills $\mathcal{D}_{t,t_0}[\mathcal{S}_\mathcal{H}] \subseteq \mathcal{S}_\mathcal{H}$ and thus maps

density matrices to density matrices or, in other words, physical states to physical states. $\mathcal{D}_{t,t_0} \in \mathcal{B}(\mathfrak{L}_\mathcal{H})$, i.e., the dynamical map is itself an element of $\mathcal{B}(\mathfrak{L}_\mathcal{H})$, the set of bounded linear operators on $\mathfrak{L}_\mathcal{H}$. It can always be written in its Kraus representation,

$$\mathcal{D}_{t,t_0}[\rho] = \sum_k \mathsf{E}_k(t)\rho\mathsf{E}_k^\dagger(t), \qquad \sum_k \mathsf{E}_k^\dagger(t)\mathsf{E}_k(t) = \mathbb{1}, \qquad \mathsf{E}_k(t) \in \mathfrak{L}_\mathcal{H}, \tag{2.4}$$

where $\mathsf{E}_k(t)$ are time-dependent operators, called Kraus operators. Unfortunately, they are in most cases neither unique nor known and it is usually difficult to find an expression beyond Eq. (2.4) without already imposing severe constraints on the dynamics. In the next section we will discuss some mathematical conditions that will allow us to find a more practical form of $\mathcal{D}_{t,t_0}$.

Before proceeding, however, we take a look at quantum control and emphasize its intimate connection to designing specific dynamical maps at an experimenter's will. Physically, quantum control assumes that there exist static and dynamic control knobs, accessible by an experimenter, which influence the dynamics and can thus be used to steer the dynamics in a desired way. Typical control knobs available in experiments are time-dependent control fields, e.g. laser or microwave fields, or static parameters that can be chosen in advance. Without such control knobs, the dynamical map $\mathcal{D}_{t,t_0}$ would be entirely predetermined at each time t. In contrast, time-dependent control fields $\{\mathcal{E}_k(t)\}$ interacting with a quantum system ultimately allow the experimenter to alter $\mathcal{D}_{t,t_0}$ such that it becomes a mere element of a larger set of dynamical maps $\{\mathcal{D}_{t,t_0}\}$ that are available by appropriately choosing $\{\mathcal{E}_k(t)\}$. The exact details of this set usually depend on the type of available controls and their experimental constraints. The natural question for quantum control is then how the control fields need to be chosen such that it gives rise to a desired map $\mathcal{D}_{t,t_0}^{\text{trgt}} \in \{\mathcal{D}_{t,t_0}\}$. Quantum optimal control takes this task one step further and even demands to achieve this goal with highest fidelity or in shortest time, cf. Sec. 2.3.

2.2 Open Quantum Systems

A quantum system that interacts with its environment is called open. Theoretically, this immediately implies that every quantum system is open, since every quantum system interacts to some extent with its environment. Nevertheless, this interaction is sometimes sufficiently weak and we can faithfully treat the system as being closed. In all remaining cases, where the environmental interaction can not be neglected, the influence of the environment must be correctly accounted for when describing the dynamics of the open

quantum system. While one might theoretically argue that the environment is always given by the entire universe, it is usually sufficient to restrict it to those systems that interact with the open system up to some noticeable and relevant degree. To identify, let alone accurately model, all these environmental modes is usually not straightforward. Besides, even the relevant part of the environment has in many cases infinite many degrees of freedom, which makes this endeavor analytically and numerically intractable. In consequence, the description of open quantum systems resorts to methods that do not involve solutions for the environmental part of the dynamics — in which we are anyway not interested in — but which merely model the environment's impact in an approximate fashion on the level of the open system.

Before delving deeper into the subject it should be noted that this environmentally induced disturbance of the open system is typically called dissipation or decoherence but sometimes also referred to as quantum noise due to its typical detrimental impact on the dynamics. Moreover, such noise does not exclusively originate from an uncontrollable but unavoidable environment but might as well originate from some required experimental apparatus needed to control, manipulate or measure the quantum system [12].

Let $\mathcal{H}_\mathrm{S}$ and $\mathcal{H}_\mathrm{E}$ be the Hilbert spaces of the open system and its environment, respectively. The Hamiltonian for the total system, composed of open system and environment, with its Hilbert space being $\mathcal{H} = \mathcal{H}_\mathrm{S} \otimes \mathcal{H}_\mathrm{E}$, is given by

$$\mathsf{H}(t) = \mathsf{H}_\mathrm{S}(t) \otimes \mathbb{1}_\mathrm{E} + \mathbb{1}_\mathrm{S} \otimes \mathsf{H}_\mathrm{E} + \mathsf{H}_\mathrm{I}(t) \tag{2.5}$$

with $\mathsf{H}_\mathrm{S}(t)$, H_E and $\mathsf{H}_\mathrm{I}(t)$ the individual Hamiltonians for system, environment and their interaction, respectively. The total system has no further relevant environment and we can assume it to be closed and its dynamics to be unitary. Thus, it fulfills the von Neumann equation ($\hbar = 1$)

$$\frac{\mathrm{d}}{\mathrm{d}t}\rho(t) = -\mathrm{i}\left[\mathsf{H}(t), \rho(t)\right], \tag{2.6}$$

which can straightforwardly be derived from the Schrödinger equation. $\rho(t) \in \mathfrak{L}_\mathcal{H}$ is the density matrix describing the state of the total system, which evolves unitarily. The solution, i.e., the dynamical map $\mathcal{D}_{t,t_0}$, for any system fulfilling Eq. (2.6) reads

$$\rho(t) = \mathcal{D}_{t,t_0}\left[\rho(t_0)\right] = \mathsf{U}_{t,t_0}\rho(t_0)\mathsf{U}_{t,t_0}^\dagger, \qquad \mathsf{U}_{t_2,t_1} = \mathcal{T}\exp\left\{-\mathrm{i}\int_{t_1}^{t_2}\mathsf{H}(\tau)\mathrm{d}\tau\right\}, \tag{2.7}$$

with U_{t_2,t_1} the time-evolution and $\mathcal{T}$ the time-ordering operator. We are not interested in the dynamics of the total system with Hilbert space $\mathcal{H}$ but only in the dynamics of

the open system with Hilbert space $\mathcal{H}_\mathrm{S}$. We can obtain the reduced state $\rho_\mathrm{S}(t) \in \mathfrak{L}_{\mathcal{H}_\mathrm{S}}$ by virtue of the partial trace $\rho_\mathrm{S}(t) = \mathrm{tr}_\mathrm{E}\{\rho(t)\}$ over the environmental degrees of freedom. Its corresponding exact dynamical map $\mathcal{D}^{\mathrm{S,ex}}_{t,t_0}$ reads

$$\rho_\mathrm{S}(t) = \mathcal{D}^{\mathrm{S,ex}}_{t,t_0}\left[\rho_\mathrm{S}(t_0)\right] = \mathrm{tr}_\mathrm{E}\left\{\mathcal{D}_{t,t_0}\left[\rho(t_0)\right]\right\} = \mathrm{tr}_\mathrm{E}\left\{\mathsf{U}_{t,t_0}\rho(t_0)\mathsf{U}^\dagger_{t,t_0}\right\}. \tag{2.8}$$

Unfortunately, evaluating $\mathcal{D}^{\mathrm{S,ex}}_{t,t_0} \in \mathcal{B}(\mathfrak{L}_{\mathcal{H}_\mathrm{S}})$ requires knowledge of $\mathcal{D}_{t,t_0} \in \mathcal{B}(\mathfrak{L}_{\mathcal{H}})$ in order to obtain $\rho(t) = \mathcal{D}_{t,t_0}[\rho(t_0)]$. This is usually not available due to the size and complexity of the environment, which makes it — despite some exceptions — impossible to calculate $\mathsf{U}_{t,t_0} \in \mathfrak{L}_{\mathcal{H}}$, neither analytically nor numerically. However, for practical purposes, it is be sufficient to find an approximate expression $\mathcal{D}^{\mathrm{S}}_{t,t_0}$ such that $\mathcal{D}^{\mathrm{S}}_{t,t_0} \approx \mathcal{D}^{\mathrm{S,ex}}_{t,t_0}$ for all t. At best, such a map $\mathcal{D}^{\mathrm{S}}_{t,t_0}$ would only depend on operators in $\mathfrak{L}_{\mathcal{H}_\mathrm{S}}$, respectively $\mathcal{B}(\mathfrak{L}_{\mathcal{H}_\mathrm{S}})$. This would be very favorable from a numerical perspective, since $\mathcal{H}_\mathrm{S}$ is usually sufficiently small (compared to $\mathcal{H}_\mathrm{E}$) to allow for a numerical treatment.

2.2.1 Markovian Dynamics

A first step towards an analytical expression for the dynamical map $\mathcal{D}^{\mathrm{S}}_{t,t_0}$ is to consider a time-independent Hamiltonian $\mathsf{H}(t) = \mathsf{H}$ — an assumption that we will lift later — and to assume

$$\mathcal{D}^{\mathrm{S}}_{t_1+t_2,t_0} = \mathcal{D}^{\mathrm{S}}_{t_1+t_2-t_0} = \mathcal{D}^{\mathrm{S}}_{t_1-t_0}\mathcal{D}^{\mathrm{S}}_{t_2-t_1} = \mathcal{D}^{\mathrm{S}}_{t_2-t_1}\mathcal{D}^{\mathrm{S}}_{t_1-t_0} \qquad \forall t_1, t_2 \geq t_0. \tag{2.9}$$

This is a very strong mathematical assumption. It implies two things, namely that (i) the dynamical map $\mathcal{D}^{\mathrm{S}}_{t_1+t_2,t_0}$ is only characterized by the length $t_1+t_2-t_0$ of the time interval and not by both the initial and final time, t_0 and t_1+t_2, and that (ii) the map $\mathcal{D}^{\mathrm{S}}_{t_1+t_2-t_0}$ is divisible, i.e., the dynamics in an fictitious second time interval t_2-t_1 does not depend on the dynamics in the first interval t_1-t_0. In fact, both intervals can even be interchanged as only their lengths matter. This corresponds to a Markovian or memoryless process, where the future evolution of $\rho_\mathrm{S}(t_1)$, given by $\mathcal{D}^{\mathrm{S}}_{t_2-t_1}$, never depends explicitly on the past evolution, given by $\mathcal{D}^{\mathrm{S}}_{t_1-t_0}$, but only on the current state of the system $\rho_\mathrm{S}(t_1)$ — the way how $\rho_\mathrm{S}(t_1)$ got there in the first place is irrelevant.

Equation (2.9) can also be motivated from physical properties and assumptions concerning the dynamics that are in some practical cases well justified. These assumptions comprise (i) weak coupling between open system and environment, i.e., small $\mathsf{H}_\mathrm{I}(t)$ in Eq. (2.5), (ii) an initially separable state of open system and environment, i.e., $\rho(t_0) = \rho_\mathrm{S}(t_0) \otimes \rho_\mathrm{E}(t_0)$, (iii) that the environment is much larger than the open system

and (iv) its dynamics happens on a much faster timescale. Especially the latter two points imply that any change in the state $\rho_{\mathrm{S}}(t)$ has an almost negligible impact on the environment. This can be justified as follows. On the one hand, any change of the environmental state $\rho_{\mathrm{E}}(t)$, induced by a change of $\rho_{\mathrm{S}}(t)$, is anyway small in the first place due to the interaction being weak and due to the fact the environment is much larger than the open system. On the other hand, $\rho_{\mathrm{E}}(t)$ also equilibrates much faster due to the faster timescale of its evolution. In consequence, $\rho_{\mathrm{E}}(t) \approx \rho_{\mathrm{E}}$ appears approximately constant on the timescale of the open system. Hence, the environment immediately "forgets" all the information it receives from the open system and the latter one always "sees" the environment in the same state. This describes a memoryless environment for the open system and physically motivates the divisibility assumption in Eq. (2.9). The afore-mentioned assumptions are typically summarized under the term Born-Markov approximations. It should be stressed out that although these approximations hold for many open systems they are not universally valid. These exceptions, where the dynamics becomes non-Markovian, will be briefly addressed in Subsec. 2.2.2.

The divisibility property of Eq. (2.9) has one important mathematical implication. It causes the continuous, one-parameter family of maps $\{\mathcal{D}_t^{\mathrm{S}}\}$ to form a semigroup. In the context of quantum dynamics it is sometimes also called a quantum dynamical semigroup. Note that in accordance with Eq. (2.9), t simply denotes the length of the time interval independent on its initial and final time. Such a semigroup can be expressed as [13]

$$\mathcal{D}_t^{\mathrm{S}} = \exp\{\boldsymbol{\mathcal{L}} t\}\,, \tag{2.10}$$

where $\boldsymbol{\mathcal{L}} \in \mathcal{B}(\mathfrak{L}_{\mathcal{H}_{\mathrm{S}}})$ defines its generator. It satisfies the general mathematical form [14]

$$\boldsymbol{\mathcal{L}}[\rho_{\mathrm{S}}(t)] = -\mathrm{i}\,[\mathsf{H}_{\mathrm{S}}, \rho_{\mathrm{S}}(t)] + \sum_{i,j=1}^{N_{\mathrm{S}}^2-1} a_{ij}\left(\mathsf{F}_i \rho_{\mathrm{S}}(t) \mathsf{F}_j^\dagger - \frac{1}{2}\left\{\mathsf{F}_j^\dagger \mathsf{F}_i, \rho_{\mathrm{S}}(t)\right\}\right), \tag{2.11}$$

where $\{\cdot,\cdot\}$ denotes the anticommutator, $N_{\mathrm{S}} = \dim\{\mathcal{H}_{\mathrm{S}}\}$ and $\mathsf{F}_i \in \mathfrak{L}_{\mathcal{H}_{\mathrm{S}}}$, $i = 1, \ldots, N_{\mathrm{S}}^2 - 1$. The positive and Hermitian matrix a_{ij} can be diagonalized and yields

$$\boldsymbol{\mathcal{L}}[\rho_{\mathrm{S}}(t)] = -\mathrm{i}\,[\mathsf{H}_{\mathrm{S}}, \rho_{\mathrm{S}}(t)] + \underbrace{\sum_{k=1}^{N_{\mathrm{S}}^2-1} \gamma_k \left(\mathsf{L}_k \rho_{\mathrm{S}}(t) \mathsf{L}_k^\dagger - \frac{1}{2}\left\{\mathsf{L}_k^\dagger \mathsf{L}_k, \rho_{\mathrm{S}}(t)\right\}\right)}_{\boldsymbol{\mathcal{L}}_{\mathrm{diss}}[\rho_{\mathrm{S}}(t)]} \tag{2.12}$$

with coefficients $\gamma_k \geq 0$ and Lindblad operators $\mathsf{L}_k \in \mathfrak{L}_{\mathcal{H}_{\mathrm{S}}}$. The generator $\boldsymbol{\mathcal{L}}$ is sometimes referred to as Liouvillian. In combination with Eq. (2.10) it yields the Liouville-von

Neumann equation

$$\frac{\mathrm{d}}{\mathrm{d}t}\rho_{\mathrm{S}}(t) = \boldsymbol{\mathcal{L}}\left[\rho_{\mathrm{S}}(t)\right], \tag{2.13}$$

which is the most general equation of motion for Markovian open quantum systems. It is sometimes also called Lindblad or Markovian master equation. It resembles the von Neumann Eq. (2.6), which describes purely unitary dynamics, but is extended by the dissipator $\boldsymbol{\mathcal{L}}_{\mathrm{diss}} \in \mathcal{B}(\mathfrak{L}_{\mathcal{H}_{\mathrm{S}}})$, cf. Eq. (2.12). While the commutator $-\mathrm{i}[\mathsf{H}_{\mathrm{S}}, \rho_{\mathrm{S}}(t)]$ describes the unitary or coherent part of the open system dynamics, determined by Hamiltonian H_{S}, the dissipator $\boldsymbol{\mathcal{L}}_{\mathrm{diss}}$ describes the influence of the environment and renders the dynamics non-unitary or incoherent.

At this point we can conclude that Eqs. (2.10) and (2.12) indeed represent the desired description of the open system dynamics via the dynamical map $\mathcal{D}_t^{\mathrm{S}}$ such that it purely relies on operators in $\mathfrak{L}_{\mathcal{H}_{\mathrm{S}}}$ and $\mathcal{B}(\mathfrak{L}_{\mathcal{H}_{\mathrm{S}}})$. However, the divisibility argument (2.9) with its implicit semigroup property for $\mathcal{D}_t^{\mathrm{S}}$, only tells us that a generator $\boldsymbol{\mathcal{L}}$, which satisfies Eq. (2.12), exists and that we can write any dynamical map $\mathcal{D}_t^{\mathrm{S}} : \mathfrak{L}_{\mathcal{H}_{\mathrm{S}}} \to \mathfrak{L}_{\mathcal{H}_{\mathrm{S}}}$ as $\mathcal{D}_t^{\mathrm{S}} = \exp\{\boldsymbol{\mathcal{L}}t\}$. In fact, it does not provide any information about the actual form of the Lindblad operators L_k and their corresponding coefficients γ_k. Expressions for L_k and γ_k can be derived by treating the total system of open system and environment from a microscopical perspective. The general idea is to start from the total Hamiltonian (2.5) and obtain (without approximations) the integro-differential equation [10]

$$\frac{\mathrm{d}}{\mathrm{d}t}\rho_{\mathrm{S}}(t) = \int_{t_0}^{t} \mathrm{tr}_{\mathrm{E}}\left\{[\mathsf{H}_{\mathrm{I}}, [\mathsf{H}_{\mathrm{I}}, \rho(s)]]\right\} \mathrm{d}s. \tag{2.14}$$

Employing the Born-Markov approximations together with further algebraic transformations allows to bring the equation of motion (2.14) to the Lindblad form (2.13). While the general formulas for L_k and γ_k can even then be quite difficult, they sometimes become sufficiently simple when the open system or environment is simple.

As an example, we consider a two-level system exposed to an environment consisting of bosonic modes. Their individual Hamiltonians read [15]

$$\mathsf{H}_{\mathrm{S}} = \frac{\omega_0}{2}\sigma_{\mathrm{z}}, \qquad \mathsf{H}_{\mathrm{E}} = \sum_k \omega_k \mathsf{b}_k^\dagger \mathsf{b}_k, \qquad \mathsf{H}_{\mathrm{I}} = \sum_k g_k \left(\sigma_+ \mathsf{b}_k + \sigma_- \mathsf{b}_k^\dagger\right) \tag{2.15}$$

with ω_0 the energy difference between ground state $|0\rangle$ and excited state $|1\rangle$ of the two-level system, $\sigma_{\mathrm{z}} = |1\rangle\langle 1| - |0\rangle\langle 0|$ and b_k the bosonic annihilation operator that destroys one photon of energy ω_k in the environment. g_k determines the coupling strength between bosonic mode k and the two-level system and $\sigma_- = |0\rangle\langle 1|$ and $\sigma_+ = |1\rangle\langle 0|$. After following

the steps according to the microscopic derivation, we arrive at the Lindblad form (2.13) with exactly two Lindblad operators [15],

$$\mathsf{L}_1 = \sigma_-, \qquad \mathsf{L}_2 = \sigma_+, \qquad \gamma_1 = \gamma_0 \left[N\left(\omega_0\right) + 1\right], \qquad \gamma_2 = \gamma_0 N\left(\omega_0\right), \tag{2.16}$$

with the Planck distribution $N(\omega) = [\exp\{\beta\omega\} - 1]^{-1}$ and $\beta^{-1} = k_\mathrm{B} T_\mathrm{env}$ the inverse thermal energy with Boltzmann constant k_B and temperature T_env. The Lindblad operators in Eq. (2.16) describe two simple physical processes. L_1 describes environmentally induced cooling, i.e., spontaneous hopping from $|1\rangle$ to $|0\rangle$ that occurs with rate γ_1, while L_2 describes the reverse process, i.e., environmentally induced heating, occurring with rate γ_2. Note that $\gamma_1 > \gamma_2$ for all temperatures $T_\mathrm{env} < \infty$. In the limiting case of $T_\mathrm{env} \to 0\,\mathrm{K}$ no thermal heating, i.e., spontaneous hopping from $|0\rangle$ to $|1\rangle$ can be induced as is reflected in a vanishing γ_2.

This derivation can also be performed for an interaction of the form [16]

$$\mathsf{H}_\mathrm{I} = \sum_k g_k \left(\sigma_+ \mathsf{b}_k^\dagger \mathsf{b}_k + \sigma_- \mathsf{b}_k^\dagger \mathsf{b}_k\right) \tag{2.17}$$

in which case it yields the single Lindblad operator

$$\mathsf{L}_3 = \sigma_+ \sigma_- \tag{2.18}$$

with decay rate γ_3. In contrast to the Lindblad operators in Eq. (2.18), L_3 does not change the population in states $|0\rangle$ or $|1\rangle$ but does cause the coherence between those states to decay with a rate determined by γ_3. In terms of a density matrix expressed in the basis $\{|0\rangle, |1\rangle\}$, this implies that the process leaves the diagonal elements invariant while the off-diagonal elements decay exponentially. Note that the action of $\mathsf{L}_3 = \sigma_+\sigma_-$ within the Lindblad master equation is equivalent to σ_z, which is why $\mathsf{L}_3 = \sigma_\mathrm{z}$ is sometimes used to describe the same physical process.

An even more general form of these Lindblad operators can be obtained if we consider an harmonic oscillator instead of a two-level system as open system. In this case the Lindblad operators and decay rates become [16]

$$\begin{aligned} &\mathsf{L}_{T_1,\downarrow} = \mathsf{a}, && \mathsf{L}_{T_1,\uparrow} = \mathsf{a}^\dagger, && \mathsf{L}_{T_2} = \mathsf{a}^\dagger \mathsf{a}, \\ &\gamma_{T_1,\downarrow} = \frac{1}{T_1}\left[N\left(\omega_0\right) + 1\right], && \gamma_{T_1,\uparrow} = \frac{1}{T_1} N\left(\omega_0\right), && \gamma_{T_2} = \frac{1}{T_2}, \end{aligned} \tag{2.19}$$

where ω_0 is the harmonic oscillator's frequency and a is the standard annihilation operator, i.e., $\mathsf{a}\,|i\rangle = \sqrt{i}\,|i-1\rangle$ with $|i\rangle$ the ith excited state. $\mathsf{L}_{T_1,\downarrow}$ and $\mathsf{L}_{T_1,\uparrow}$ are thereby

the generalizations of L_1 and L_2 from Eq. (2.16) and L_{T_2} the generalization of L_3 from Eq. (2.18). Note that in Eq. (2.19) we have already employed the notation indicating the connection of these operators to the commonly used T_1 and T_2 times, which determine the time scale on which these processes occur. The T_1 and T_2 times can be measured experimentally and are an excellent indicator for how well a quantum system is shielded from its environment. Since we will primarily consider two-level system as well as harmonic and weakly anharmonic oscillators, the Lindblad operators of Eq. (2.19) will be the main model to describe dissipation within this thesis.

At last, one important subtlety regarding the description of Markovian dynamics via semigroups needs to be stressed out. In order for $\{\mathcal{D}_t^{\mathrm{S}}\}$ to form a one-parameter semigroup, its generator $\boldsymbol{\mathcal{L}}$ needs to be time-independent. In fact, this requires H to be time-independent as well. Thus, $\mathcal{D}_t^{\mathrm{S}} = \exp\{\boldsymbol{\mathcal{L}}t\}$ is strictly speaking only valid for a time-independent total Hamiltonian H, cf. Eq. (2.5). Unfortunately, the derivation when starting from a given time-dependent Hamiltonian $\mathsf{H}(t)$ does mathematically not yield a semigroup structure. Nevertheless, the general argument for Markovian dynamics remains unchanged and the formal solution, that allows time-dependent Hamiltonians, is to alter the divisibility condition (2.9) to read [15, 17]

$$\mathcal{D}_{t_3,t_1}^{\mathrm{S}} = \mathcal{D}_{t_3,t_2}^{\mathrm{S}}\mathcal{D}_{t_2,t_1}^{\mathrm{S}}, \qquad \forall\ 0 \le t_1 \le t_2 \le t_3, \tag{2.20}$$

which makes $\{\mathcal{D}_{t,t_0}^{\mathrm{S}}\}$ a two-parameter family of dynamical maps. Equation (2.20) again corresponds to a memoryless (Markovian) process and is well fulfilled as long as the Born-Markov approximations are valid. Although the Markov approximation often does not hold in combination with time-dependent Hamiltonians, in those cases where it does, the derivation proceeds as outlined before and we arrive at the time-local Lindblad master equation [18]

$$\frac{\mathrm{d}}{\mathrm{d}t}\rho_{\mathrm{S}}(t) = \boldsymbol{\mathcal{L}}(t)\left[\rho_{\mathrm{S}}(t)\right], \tag{2.21}$$

with

$$\boldsymbol{\mathcal{L}}(t)\left[\rho_{\mathrm{S}}(t)\right] = -\mathrm{i}\left[\mathsf{H}_{\mathrm{S}}(t), \rho_{\mathrm{S}}(t)\right] + \underbrace{\sum_{k=1}^{N_{\mathrm{S}}^2-1} \gamma_k(t)\left(\mathsf{L}_k(t)\rho_{\mathrm{S}}(t)\mathsf{L}_k^\dagger(t) - \frac{1}{2}\left\{\mathsf{L}_k^\dagger(t)\mathsf{L}_k(t), \rho_{\mathrm{S}}(t)\right\}\right)}_{\boldsymbol{\mathcal{L}}_{\mathrm{diss}}(t)[\rho_{\mathrm{S}}(t)]} \tag{2.22}$$

and the dynamical map given by [17]

$$\mathcal{D}^{\mathrm{S}}_{t,t'} = \mathcal{T} \exp\left\{ \int_t^{t'} \boldsymbol{\mathcal{L}}(\tau) \mathrm{d}\tau \right\}, \tag{2.23}$$

which emphasize its similarity to the time-evolution operator U_{t,t_0} in Eq. (2.7). Note that since we will primarily work with time-dependent Hamiltonians $\mathsf{H}_{\mathrm{S}}(t)$, we will use the time-local Lindblad master equation (2.21) to describe an open system's dynamics instead of its semigroup version, cf. Eq. (2.13).

The Lindblad master equation has found widespread application in quantum information [19–24] and many other fields [25]. Unfortunately, it is not always possible to derive Lindblad operators formally, in which case it can be used phenomenologically to describe the environment's impact. In many of these phenomenological cases, the description based on T_1 and T_2 describes the environment's impact on the open system's dynamics sufficiently well. The equation's relevance is especially remarkable, since many quantum information platforms, e.g. superconducting qubits [21] or color center in diamond [22–24], are known to exhibit memory effects that technically violate the Markovian assumptions.

2.2.2 Non-Markovian Dynamics

Non-Markovian dynamics, i.e., dynamics that memorizes and partially depends on its past, has become a focus of research over the past decade [26–28]. On the one hand, due to memory effects, which are absent in any Markovian evolution, non-Markovianity intrinsically allows for a larger variety of dynamical maps beyond semigroups. Hence, it increases the set of conceivable maps. On the other hand, it also causes the environment to partially lose its detrimental character, since information flowing into the environment are not immediately lost and might be recoverable. Moreover, with sufficient knowledge about the interaction mechanism and the right control scheme, non-Markovianity even holds the promise to exploit the environment for good. Interestingly, many physical qubit platforms behave non-Markovian as the Markovian assumptions, e.g. weak coupling or different timescales of open system and environment, do not hold in practice. This is for instance the case for many condensed matter systems such as superconducting qubits, exposed to $1/f$ noise [29, 30], quantum dots [31–33] or photonic systems [34]. However, non-Markovianity occurs also in other fields of physics and even in systems as large as in biophysics [35].

Unfortunately, non-Markovianity is difficult to study from a theoretical perspective as the theory lacks a general analytical expression or generator for $\mathcal{D}^{\mathrm{S}}_{t,t_0}$. While in the Markovian case every conceivable map $\mathcal{D}^{\mathrm{S}}_{t,t_0}$ is generated by the Liouvillian (2.22), it can

be shown that a time-local Lindblad master equation (2.21) with partially negative decay rates $\gamma_k(t)$ provides one possible description for a non-Markovian process [18]. Hence, the appearance of negative decay rates, which is prohibited for Markovian dynamics, can be regarded as a witness for non-Markovianity. In the same spirit, Ref. [36] suggests a different approach for a non-Markovianity witness based on the distance between a given dynamical map $\mathcal{D}^{\mathrm{S}}_{t,t_0}$ and its closest semigroup-generated form.

Interestingly, albeit the technical difficulties to model non-Markovian dynamics, a lot of measures that quantify the non-Markovianity of a dynamics have been developed. Such measures are based on the deviation from the divisibility criteria [37, 38], various measures of information flow [39–42], entanglement [43], quantum discord [44], accessible state space volume [45], entropy production rate [46], local quantum uncertainty [47] and abstract information invariants [48] to name a few. On the one hand, this vast amount of measures and the fact that yet no unified measure exists that captures all non-Markovian evolutions [18] highlights the general need for a better understanding of non-Markovianity. On the other hand, especially in combination with control techniques, non-Markovianity has already been utilized [49–53]. Although we will partially consider environments giving rise to non-Markovian dynamics in this thesis, the focus will not be on assessing or quantifying the non-Markovianity but on how such structured environments can be exploited for typical quantum information tasks.

In the following, we present a simple way to describe non-Markovian dynamics while still making use of the Lindblad master equation. The key idea is to separate the environment into two parts — one for the strongly coupled modes, represented by Hilbert space $\mathcal{H}^{(1)}_{\mathrm{E}}$, called the primary environment, and one for the rest, represented by Hilbert space $\mathcal{H}^{(2)}_{\mathrm{E}}$, called the secondary environment [52]. Thus, the total Hilbert space of open system and environment becomes $\mathcal{H} = \mathcal{H}_{\mathrm{S}} \otimes \mathcal{H}^{(1)}_{\mathrm{E}} \otimes \mathcal{H}^{(2)}_{\mathrm{E}}$. Due to the strong coupling of the primary environment to the open system, its impact will be significant and we can not treat it in an approximate fashion without severely altering the open system's true dynamics. On the other hand, the secondary environment with Hilbert space $\mathcal{H}^{(2)}_{\mathrm{E}}$ couples weakly to both the open system and the primary environment. The total Hamiltonian $\mathsf{H}(t)$ for open system plus primary and secondary environment reads (omitting tensor products with unity for brevity)

$$\mathsf{H}(t) = \underbrace{\mathsf{H}_{\mathrm{S}}(t) + \mathsf{H}^{(1)}_{\mathrm{E}}(t) + \mathsf{H}^{(1)}_{\mathrm{I}}(t)}_{\mathsf{H}^{\mathrm{eff}}_{\mathrm{S}}(t)} + \mathsf{H}^{(2)}_{\mathrm{E}}(t) + \mathsf{H}^{(2)}_{\mathrm{I}}(t), \tag{2.24}$$

where $\mathsf{H}_{\mathrm{S}}(t)$, $\mathsf{H}^{(1)}_{\mathrm{E}}(t)$ and $\mathsf{H}^{(2)}_{\mathrm{E}}(t)$ are the Hamiltonians for open system, primary and

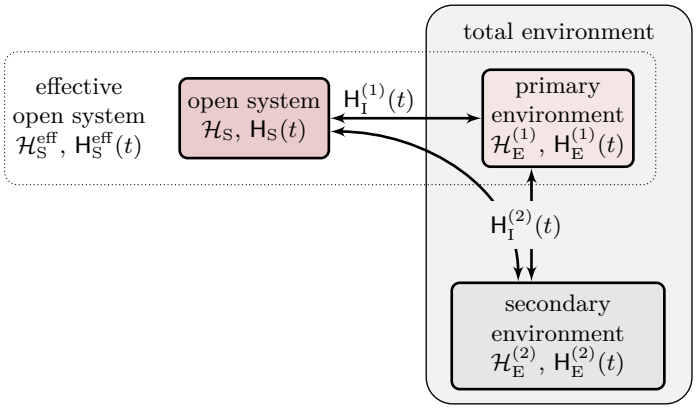

Figure 2.1: Sketch of the partitioning of the total environment in a primary (strongly coupled) and secondary (weakly coupled) environment. When the Born-Markov approximations are satisfied, the dynamics of the effective open system composed of actual open system with Hilbert space $\mathcal{H}_S$ and primary environment with Hilbert space $\mathcal{H}_E^{(1)}$ becomes Markovian and can again be modeled by a Lindblad master equation.

secondary environment, respectively, $\mathsf{H}_I^{(1)}(t)$ the interaction between open system an primary environment and $\mathsf{H}_I^{(2)}(t)$ the interaction of the secondary environment with both of the other two. Since the secondary environment usually satisfies all requirements for the Born-Markov approximations to hold, we can model the entire dynamics with an effective open system composed of $\mathcal{H}_S$ and $\mathcal{H}_E^{(1)}$ and its Hamiltonian $\mathsf{H}_S^{\text{eff}}(t)$ as defined in Eq. (2.24). Its dynamics is Markovian and we can model it by the Lindblad master equation (2.21). However, note that the actual open system of interest will always be $\mathcal{H}_S$ and any physical objective, for instance in a control problem, needs to be met there. Figure 2.1 depicts the partitioning of the environment schematically.

In the remainder of the thesis, we will always consider a Lindblad description for the dynamics of the effective open quantum systems (including potential ancilla systems that render the dynamics of the actual open system non-Markovian). We drop the subscript "S" for the quantities of the open system in the following.

2.3 Quantum Optimal Control Theory

As briefly mentioned at the end of Sec. 2.1, the key idea of quantum control [11] is to take additional control fields $\{\mathcal{E}_k(t)\}$ into account, e.g. laser and microwave fields or any time-dependent, controllable quantity, that interacts with the system as

$$\mathsf{H}(t) = \mathsf{H}_0 + \sum_k \mathsf{H}_k \mathcal{E}_k(t), \tag{2.25}$$

where H_0 is the time-independent drift Hamiltonian and H_k the drive Hamiltonian describing the coupling of control field $\mathcal{E}_k(t)$ to the system. While quantum control usually refers to the general concept of controlling/steering the dynamics of any quantum system via external control fields, quantum optimal control theory (OCT) aims at finding those fields $\{\mathcal{E}_k^{\mathrm{opt}}(t)\}$ that carry out a predefined task in an optimal fashion [8]. While the actual meaning of the term "optimal" depends on the context and the given control task, OCT generally aims at designing specific dynamical maps $\mathcal{D}_{t,t_0}$ on-demand — either at a given time, e.g. some final time $t = T$, or at all times $t \in [t_0, T]$. Such a control problem can typically not be solved analytically due to the possibility of (almost) arbitrarily complex fields $\{\mathcal{E}_k(t)\}$ that prevent an analytical expression for $\mathcal{D}_{t,t_0}$, cf. Eq. (2.23). Hence, most optimal control tasks are solved numerically. Nevertheless, in order to introduce OCT and its methodological challenges, we start with the mathematical and analytical framework first.

2.3.1 Controllability

Before asking the question *how* to optimally choose $\{\mathcal{E}_k(t)\}$ for a given control task, we should first ask which tasks *can* be done at all, i.e., which set $\{\mathcal{D}_{t,t_0}\}$ of dynamical maps *can* be generated by the available control fields $\{\mathcal{E}_k(t)\}$ within their experimental limitations. For simplicity, we start by addressing controllability in closed quantum systems, i.e., we ask which set [11]

$$\mathcal{U} = \bigcup_{t \geq t_0} \mathcal{U}(t), \qquad \mathcal{U}(t) = \left\{ \mathsf{U}_{t,t_0} \middle| \forall \mathcal{E}_k \in \mathcal{M}_k \right\} \tag{2.26}$$

of time-evolution operators can be realized in general. $\mathcal{U}(t)$ is thereby the set of all time-evolution operators that can be physically realized at time t by at least one choice of $\{\mathcal{E}_k(\tau)\}$, $t_0 \leq \tau \leq t$. Each field $\mathcal{E}_k(t)$ must thereby be an element from its corresponding set of conceivable control fields $\mathcal{M}_k$, i.e., the function set $\mathcal{M}_k$ captures the fact that each $\mathcal{E}_k(t)$ can not assume arbitrary time-dependent function due to physical limitations, e.g. in amplitude and/or frequency. Let $N = \dim\{\mathcal{H}\}$ such that $\mathsf{U}_{t,t_0} \in \mathrm{SU}(N)$[1] and we thus have $\mathcal{U} \subseteq \mathrm{SU}(N)$. The quantum system is said to be fully controllable iff $\mathcal{U} = \mathrm{SU}(N)$ and partially controllable otherwise. Full controllability implies that for all $\mathsf{O} \in \mathrm{SU}(N)$ there exists at least one time $t' \geq t_0$ and one choice of control fields $\{\mathcal{E}'_k(\tau)\}$, $t_0 \leq \tau \leq t'$, such that $\mathsf{O} = \mathsf{U}_{t',t_0} \in \mathcal{U}$.

Controllability of closed quantum systems can be fully determined on the level of the

[1] We consider $\mathrm{SU}(N)$ instead of $\mathrm{U}(N)$, since their elements only differ by a global phase which is irrelevant in quantum mechanics.

Hamiltonian $\mathsf{H}(t)$ that generates the dynamics. Mathematically, $\mathcal{U}$ is a Lie group and, thus, can always be written as $\mathcal{U} = \exp\{\mathfrak{g}\}$ with $\mathfrak{g}$ the corresponding Lie algebra that generates $\mathcal{U}$. As the exponential map suggests, cf. Eq. (2.7), $\mathfrak{g}$ is closely connected to $\mathsf{H}(t)$. The details can be expressed via the following theorem [11].

Theorem 2.1. *Let $\{\mathcal{E}_k(t)\}$ be a set of control fields that interact with a closed quantum system via Hamiltonian (2.25) and let $\bar{\mathcal{M}}_k$ be the set of scalar values that $\mathcal{E}_k(t)$ can physically assume at any time t, i.e., $\mathcal{E}_k(t) \in \bar{\mathcal{M}}_k$ for all t. The set of reachable unitaries $\mathcal{U} \subseteq \mathrm{SU}(N)$ is given by $\mathcal{U} = \exp\{\mathfrak{g}\}$, where $\mathfrak{g} \subseteq \mathfrak{su}(N)$ is the Lie algebra generated by $\mathfrak{g} = \mathrm{span}_{\mathcal{E}_k \in \bar{\mathcal{M}}_k}\{-\mathrm{i}\mathsf{H}[\{\mathcal{E}_k\}]\}$.*

While $\mathcal{U} \subseteq \mathrm{SU}(N)$ is a subgroup of the Lie group $\mathrm{SU}(N)$, the dynamical Lie algebra $\mathfrak{g} \subseteq \mathfrak{su}(N)$ which generates $\mathcal{U}$ is always a subalgebra of the Lie algebra $\mathfrak{su}(N)$ which generates $\mathrm{SU}(N)$. We can utilize the dimension of $\mathfrak{g}$ as an indicator for full or partial controllability, since $\dim\{\mathfrak{g}\} = N^2 - 1$ implies $\mathfrak{g} = \mathfrak{su}(N)$ and thus $\mathcal{U} = \exp\{\mathfrak{g}\} = \mathrm{SU}(N)$. Conversely, $\dim\{\mathfrak{g}\} < N^2 - 1$ implies $\mathfrak{g} \subset \mathfrak{su}(N)$ and thus $\mathcal{U} = \exp\{\mathfrak{g}\} \subset \mathrm{SU}(N)$.

The dynamical Lie algebra $\mathfrak{g}$ can be obtained by a recursive procedure [11]. Let $\{\mathsf{B}_1, \ldots, \mathsf{B}_S\}$ be a basis for $\mathrm{span}_{\mathcal{E}_k \in \bar{\mathcal{M}}_k}\{-\mathrm{i}\mathsf{H}[\{\mathcal{E}_k\}]\}$[2]. The procedure requires the calculation of repeated nested commutators of basis elements, i.e., $[\mathsf{B}_i, [\mathsf{B}_j, [\mathsf{B}_k, \ldots]]]$, until no new elements, which are linearly independent of $\{\mathsf{B}_1, \ldots, \mathsf{B}_S\}$ and all previous commutators, can be obtained anymore. We label all new and linearly independent elements, that can be obtained by this procedure, by $\mathsf{B}_{S+1}, \ldots, \mathsf{B}_K$ and ignore all linearly depend ones. The dynamical Lie algebra is then given by $\mathfrak{g} = \mathrm{span}\{\mathsf{B}_1, \ldots, \mathsf{B}_K\}$ and we have $\dim\{\mathfrak{g}\} = K$. It is therefore an easy procedure to determine the degree of controllability. However, note that even in case of full controllability, $\dim\{\mathfrak{g}\} = N^2 - 1$, this analysis does not provide any information about *how* to choose the control fields $\{\mathcal{E}_k(t)\}$ in order to realize a specific unitary $\mathsf{O} \in \mathrm{SU}(N)$. Nevertheless, it tells us that a solution exists for every unitary, or, in case of partial controllability, that there exists certain unitaries that can not be realized at all — no matter on how we choose the control fields $\{\mathcal{E}_k(t)\}$.

The task to analyze controllability becomes significantly more complex for open quantum systems. In order to sketch the emerging difficulties, it is already sufficient to consider purely Markovian dynamics, where the Hermitian Hamiltonian $\mathsf{H}(t)$ gets replaced by the non-Hermitian Liouvillian $\boldsymbol{\mathcal{L}}(t)$. In consequence, the set of reachable unitaries $\mathcal{U} \subseteq \mathrm{SU}(N)$ gets replaced by a set of non-unitary dynamical maps $\{\mathcal{D}_{t,t_0}\} \subseteq \mathcal{B}(\mathfrak{L}_{\mathcal{H}})$ for which the standard tools of controllability analysis do not apply anymore. An overview and ansatz to tackle the problem can be found in Ref. [54].

[2] Note that the trace of $\mathsf{H}[\{\mathcal{E}_k\}]$, which purely affects the global phase, needs to be removed first for the following procedure to work. This ensures $\mathsf{H}(\{\mathcal{E}_k\}) \in \mathfrak{su}(N)$ which would otherwise be $\mathfrak{u}(N)$.

2.3.2 Analytical Optimal Control

Optimal control problems range far beyond the realm of quantum physics. To this end, we start introducing them from their mathematical roots. We consider the general equation of motion

$$\dot{\boldsymbol{x}} = \boldsymbol{f}(\boldsymbol{x}, \boldsymbol{u}), \tag{2.27}$$

where $\boldsymbol{x} : \mathbb{R} \to \mathbb{R}^n$ represents the time-dependent state of a system and $\boldsymbol{u} : \mathbb{R} \to \mathbb{R}^m$ a time-dependent control function. An optimal control problem can be expressed as follows [11].

Definition 2.2. *(Optimal Control Problem) Let $\mathcal{X}$ be a set of state functions and $\mathcal{M}$ be a set of control functions. An optimal control problem is given by the task of finding the minimum of a cost function $\mathcal{J} : \mathcal{X} \times \mathcal{M} \times \mathbb{R} \to \mathbb{R}$ such that the solution still satisfies the dynamical constraints, i.e., the equation of motion* (2.27)*.*

The most general expression for the cost function $\mathcal{J}$, which is mathematically a functional, reads

$$\mathcal{J}[\boldsymbol{x}, \boldsymbol{u}, T] = \mathcal{J}_T[\boldsymbol{x}, T] + \int_0^T g[\boldsymbol{x}(t), \boldsymbol{u}(t), t]\,\mathrm{d}t, \tag{2.28}$$

where $\mathcal{J}_T$ defines the cost at final time T and the integral over g captures time-dependent running costs. For instance, $\mathcal{J}_T$ is often chosen to quantify the mismatch of the final state $\boldsymbol{x}(T)$ with some target state $\boldsymbol{x}^{\mathrm{trgt}}$, e.g. $\mathcal{J}_T = \|\boldsymbol{x}(T) - \boldsymbol{x}^{\mathrm{trgt}}\|^2$. While $\mathcal{J}_T$ is typically the relevant figure of merit within $\mathcal{J}$, the running costs g often influence the way the system reaches its goal. For instance, the choice $g = \|\boldsymbol{u}(t)\|^2$ would penalize the field intensity and solutions with high intensities would be strongly suppressed. How $\mathcal{J}$ needs to be chosen in practice depends mainly on the actual control problem at hand. We will discuss this in more detail in Chap. 3, when discussing its application in quantum control.

An optimal control problem, cf. definition 2.2, is solved by finding the minimum of functional (2.28). In order to tackle the problem analytically, the Pontryagin maximum principle (PMP) [11] can be used.

Theorem 2.2. *(Pontryagin Maximum Principle) Let $\boldsymbol{x}^* \in \mathcal{X}$ be the optimal state trajectory and $\boldsymbol{u}^* \in \mathcal{M}$ the optimal control function. Then, there exists a costate $\boldsymbol{p}^* \in \mathcal{X}$ such that*

$$H(t, \boldsymbol{x}^*, \boldsymbol{p}^*, \mu, \boldsymbol{u}^*) \geq H(t, \boldsymbol{x}^*, \boldsymbol{p}^*, \mu, \boldsymbol{u}) \qquad \forall\, \boldsymbol{u} \in \mathcal{M} \tag{2.29}$$

with the PMP pseudo-Hamiltonian [55]

$$H(t, \boldsymbol{x}, \boldsymbol{p}, \mu, \boldsymbol{u}) = \boldsymbol{p}^\top \boldsymbol{f}(\boldsymbol{x}, \boldsymbol{u}) + \mu g, \tag{2.30}$$

where μ is a constant which is chosen to ensure that both terms in Eq. (2.30) *never vanish simultaneously. Moreover, the costate satisfies*

$$\dot{\boldsymbol{p}}^\top = -\nabla_{\boldsymbol{x}} H(t, \boldsymbol{x}, \boldsymbol{p}, \mu, \boldsymbol{u})\Big|_{\boldsymbol{x}=\boldsymbol{x}^*, \boldsymbol{p}=\boldsymbol{p}^*, \boldsymbol{u}=\boldsymbol{u}^*} \quad \text{with} \quad \boldsymbol{p}^\top(T) = -\nabla_{\boldsymbol{x}} \mathcal{J}_T\left[\boldsymbol{x}, T\right]\Big|_{\boldsymbol{x}=\boldsymbol{x}(T)}. \tag{2.31}$$

Albeit its rather complicated formulation, the PMP simplifies the search for the optimal control $\boldsymbol{u}^*$ to a maximization of the pseudo-Hamiltonian $H(t, \boldsymbol{x}, \boldsymbol{p}, \mu, \boldsymbol{u})$. For low dimensional problems, this maximization can be carried out analytically and the optimal field can be determined in the process as well. It should be noted that solutions due to the PMP are even time-optimal, i.e., it guarantees that no other solution exists that reaches the same objective in shorter time. In the language of quantum physics, a time-optimal solution for a given control problem is said to operate at the quantum speed limit (QSL). The PMP has been successfully applied to two-level systems [55–57], three-level systems [58] and coupled spins [59] to name a few examples, which have a low dimensional Hilbert space in common. For more complex systems, which cover most high dimensional physical systems, the minimization of $\mathcal{J}$ needs to be performed numerically. However, it should be stressed that even some numerical approaches, especially the gradient-based algorithms discussed in Subsec.2.3.4, can be traced back to the PMP.

2.3.3 Numerical Optimal Control

In the language of quantum physics, functional (2.28) becomes

$$\mathcal{J}\left[\{\rho_l\}, \{\mathcal{E}_k\}, T\right] = \mathcal{J}_T\left[\{\rho_l\}, T\right] + \int_0^T g_a\left[\{\mathcal{E}_k(t)\}, t\right] \mathrm{d}t + \int_0^T g_b\left[\{\rho_l(t)\}, t\right] \mathrm{d}t, \tag{2.32}$$

where $\{\rho_l(t)\}$ is a set of density matrices and $\{\mathcal{E}_k(t)\}$ a set of control fields. Note that we have divided the running costs g into two contributions, where g_a and g_b capture field and state related costs, respectively. The task remains to find the global minimum of $\mathcal{J}$ such that all $\rho_l(t)$ still satisfy the equation of motion, e.g. the Lindblad master equation (2.21) in our case. Functional $\mathcal{J}$, and especially $\mathcal{J}_T$, captures the physics of the problem and it should be minimal iff the dynamics behaves exactly as desired. It is of crucial importance to choose it appropriately in view of the optimal control problem at hand. However, note that even with an appropriate choice, the minimum might not be unique as several solutions, i.e., different sets of control fields, might exist that give rise

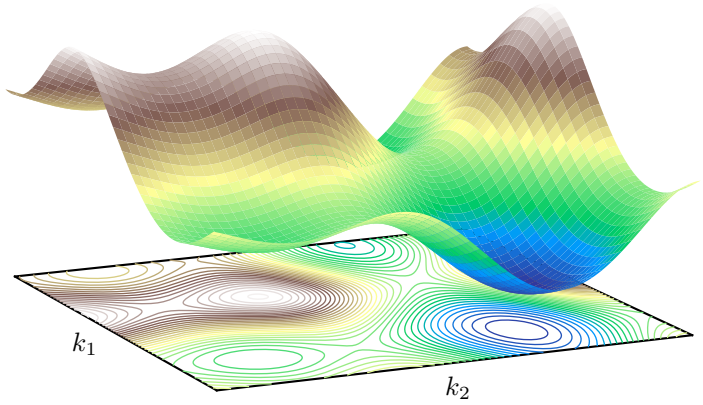

Figure 2.2: Illustration of a quantum control landscape with two control parameters k_1 and k_2. They define a three dimensional landscape where the third dimension corresponds to the functional value $\mathcal{J}$ for that particular combination of k_1 and k_2.

to the same functional value. Despite its importance for the optimal control problem, we postpone the discussion of general rules for choosing $\mathcal{J}$, and especially $\mathcal{J}_T$, to Chap. 3 and focus in the remainder entirely on how to find the minimum of a given functional $\mathcal{J}$.

The Pontryagin maximum principle, cf. theorem 2.2, can be used to derive the optimal control fields analytically when the quantum system and control problem is sufficiently simple. Unfortunately, the complexity of most physical systems only allows for a numerical treatment of their dynamics. In consequence, also the minimization of $\mathcal{J}$ needs to be carried out numerically and we can no longer search for completely arbitrary time-dependent control fields. In contrast, we need to parametrize each control field $\mathcal{E}_k(t)$ by N_k control parameters, e.g. $\mathcal{E}_{k,1}, \ldots, \mathcal{E}_{k,N_k} \in \mathbb{R}$, which then determine the control field $\mathcal{E}_k(t)$ entirely. We will discuss typical parametrizations in Subsec. 2.3.4. For the ease of notation, we can write functional $\mathcal{J}$ as a function of those parameters

$$\mathcal{J} \to \mathcal{J}\left[\{\rho_l\}, \{\ldots, \mathcal{E}_{k,1}, \ldots, \mathcal{E}_{k,N_k}, \ldots\}, T\right]. \tag{2.33}$$

Any minimization of $\mathcal{J}$ then simply corresponds to an optimization of all control parameters $\{\ldots, \mathcal{E}_{k,1}, \ldots, \mathcal{E}_{k,N_k}, \ldots\}$, i.e., a search for the set of control parameters that gives the smallest $\mathcal{J}$. The problem, albeit in general difficult to solve, allows for a simple geometric interpretation. Let $K = \sum_k N_k$ be the number of total control parameters. These parameters define a $K+1$ dimensional quantum control landscape [60], i.e., a high dimensional landscape of "mountains and valleys" where the optimization task corresponds to the figurative task of finding the deepest valley. Figure 2.2 visualizes the

problem for $K = 2$. An optimization algorithm thus tries to find the global minimum of $\mathcal{J}$. Note that such a minimum, albeit unique in Fig.2.2, does not have to be unique in practice. The search gets even more complicated by the presence of local minima. The general problem of optimal control theory is, however, that the landscape is in almost all cases unknown. It furthermore depends heavily on the choice of $\mathcal{J}$ and the parametrization of the control fields. Hence, the optimization tasks can be interpreted with the geographic search for the deepest valley despite the lack of a map while being blind besides. Nevertheless, effort has been put into exploring topological and structural properties of quantum control landscapes just by means of analyzing the functional dependence of $\mathcal{J}$ from the control fields $\{\mathcal{E}_k(t)\}$. This has revealed insights regarding the existence of traps [61], unitary transformations in closed [62] or open quantum systems [63], the influence of constraints on the fields [64] and many more. While most of these approaches are primarily theoretical, quantum control landscapes have also been charted experimentally [65]. However, none of these theoretical methods can readily yield the optimal set of control fields. Thus, in order to identify these fields, various numerical optimization techniques have been developed.

2.3.4 Gradient-Free and Gradient-Based Optimization

Numerical optimization algorithms for minimizing Eq. (2.33) can be roughly divided into two categories, namely gradient-free and gradient-based methods [11]. While gradient-free methods just rely on a systematic evaluation of the functional $\mathcal{J}$ in order to search for its minimum, gradient-based methods incorporate gradient information with respect to $\mathcal{J}$ in order to move in the direction of decreasing $\mathcal{J}$ within the control landscape. Gradient-free methods are especially efficient when the number of control parameters K is sufficiently small, i.e., $K \lesssim 20$ [66]. For significantly larger sets of control parameters, gradient-free methods become quickly stuck and gradient-based methods and their gradient information are required in order to ensure "moving" into the right direction [66]. It is important to stress out that besides the mere optimization method, the general success of an optimization depends strongly on the right choice of $\mathcal{J}$ as well as the right parametrization of the control fields.

Nelder-Mead or downhill simplex [67] is one of the most prominent representative of gradient-free algorithms. As such, it is restricted to only a few control parameters. Thus, typical parametrizations often employ an expansion of each control field $\mathcal{E}_k(t)$ in terms of a set of functions f_n,

$$\mathcal{E}_k(t) = \bar{S}_k(t) \sum_n c_n^{(k)} f_n(t). \tag{2.34}$$

In order to keep the number of control parameters small, the optimization is then artificially restricted by allowing it to only explore the function space determined by just a couple expansion coefficients $\{c_n^{(k)}\}$ — the set of control parameters. $\bar{S}_k(t) \in [0,1]$ is a shape function that is used to ensure a smooth switching on and off in the beginning and end of the control field. As a specific version of Eq. (2.34), a possible choice in view of *physical* control fields and the experimental hardware that generates them, is the expansion in terms of a superposition of various oscillating components, i.e.,

$$\mathcal{E}_k(t) = \bar{S}_k(t) \sum_n a_n^{(k)} \sin\left(\omega_n^{(k)} t + \phi_n^{(k)}\right). \tag{2.35}$$

The control parameters in such an optimization are a small number of amplitudes $a_n^{(k)}$, frequencies $\omega_n^{(k)}$ and phases $\phi_n^{(k)}$. The advantage of Eqs. (2.34) and (2.35) — or any parametrization in the same spirit — is that the control fields always remain simple and smooth. However, the limited set of functions that can be expressed by the choice of control parameters severely constrains the optimization. Every solution that can not be expressed by that choice can not be accessed by the optimization and therefore not be found. Hence, particular care needs to be taken when choosing the control parameters. The chopped random basis (CRAB) algorithm [68–70] has been developed explicitly to overcome this problem. It obviates the original rigid choice of control parameters by adding a randomization scheme and hence allows to explore a virtually larger parameter space. A similar effect can be achieved by increasing the number of control parameters subsequently [71].

When there is no clear or obvious choice of parametrization for the control fields $\{\mathcal{E}_k(t)\}$, the least restrictive parametrization is to discretize each field $\mathcal{E}_k(t)$ by N_t time steps within which the field is assumed to be approximately constant — a procedure that is anyway necessary for solving the dynamics numerically [72, 73]. In this parametrization, the control parameters are simply the field values/amplitudes in each time step, i.e., $\mathcal{E}_{k,m} \approx \mathcal{E}_k(t)$ for $t \in [t_{m-1}, t_{m-1} + dt)$ where t_{m-1} and dt define the start and width of the mth time step. Note that in order to minimize the error, we usually assume the field amplitude to be exact in the middle of each time step, i.e., $\mathcal{E}_{k,m} = \mathcal{E}_k(t_{m-1} + dt/2)$. This allows the definition of a time-independent Liouvillian $\boldsymbol{\mathcal{L}}_m$ within each time step, i.e., $\boldsymbol{\mathcal{L}}_m \approx \boldsymbol{\mathcal{L}}(t)$ for $t \in [t_{m-1}, t_m)$ and hence the dynamical map within each time step is given by $\mathcal{D}_m \equiv \mathcal{D}_{t_m, t_{m-1}} = \exp\{\boldsymbol{\mathcal{L}}_m dt\}$, cf. Eq. (2.10), such that the total dynamical map (2.23) can be written as

$$\mathcal{D}_{T,t_0} \approx \prod_{m=1}^{N_t} \mathcal{D}_m = \mathcal{D}_{N_t} \ldots \mathcal{D}_1. \tag{2.36}$$

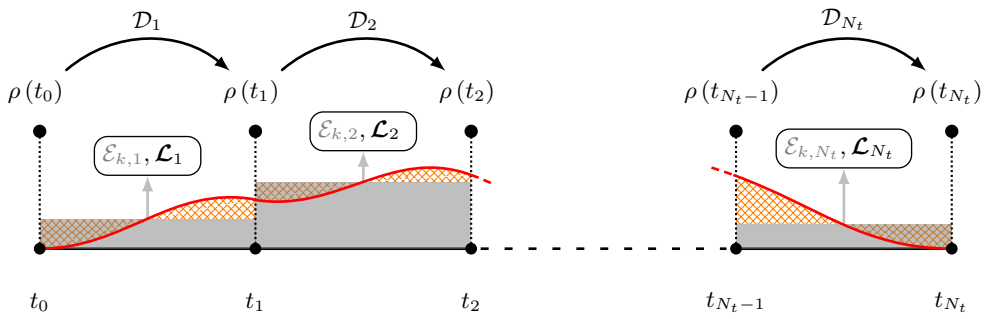

Figure 2.3: Sketch of the piecewise-constant representation of the control field $\mathcal{E}_k(t)$ (red solid line). The field is assumed to be approximately constant within each time step $[t_{m-1}, t_m)$ and given by the value $\mathcal{E}_{k,m}$. The orange area indicates the error within each time step due to the piecewise-constant approximation. Note that the state $\rho(t_m)$ is only defined on the $N_t + 1$ time grip points $t_0, \ldots, t_{N_t}$, which define the N_t time steps.

Figure 2.3 sketches this piecewise-constant representation of $\mathcal{E}_k(t)$ as well as the time-evolution according to Eq. (2.36). Note that the error caused by this piecewise-constant approximation can be kept sufficiently small by choosing sufficiently small time steps dt, i.e., sufficiently large N_t. The significant advantage of this parametrization is its possibility to represent almost arbitrary time-dependent control fields. It just requires the piecewise-constant discretization to hold in the sense that also rapidly oscillating parts are smoothly resolved. The flexibility of this parametrization comes at the expense of $N_t \gg 1$, typically $\mathcal{O}(N_t) \gtrsim 10^3$, and thus requires gradient-based methods for minimizing $\mathcal{J}$.

The gradient ascent pulse engineering (GRAPE) algorithm [74] is one of the most common representative of gradient-based optimization techniques. It calculates the gradient of $\mathcal{J}$ with respect to all $K = \sum_k N_t$ control parameters that define the control fields $\{\mathcal{E}_k(t)\}$, i.e.,

$$\nabla_{\{\mathcal{E}_{k,m}\}} \mathcal{J}\left[\ldots, \mathcal{E}_{k,1}, \ldots, \mathcal{E}_{k,N_t}, \ldots\right] = \left(\ldots, \frac{\partial \mathcal{J}}{\partial \mathcal{E}_{k,1}}, \ldots, \frac{\partial \mathcal{J}}{\partial \mathcal{E}_{k,N_t}}, \ldots\right). \tag{2.37}$$

The individual derivatives $\partial \mathcal{J} / \partial \mathcal{E}_{k,m}$ can have an explicit contribution from $\partial g_a / \partial \mathcal{E}_{k,m}$ if $g_a \neq 0$, cf. Eq. (2.32), but otherwise only depend (potentially via the chain rule) on $\partial \rho_l(t) / \partial \mathcal{E}_{k,m}$. In the piecewise-constant parametrization, cf. Eq. (2.36), the latter derivative reads

$$\frac{\partial \rho_l(t_{m'})}{\partial \mathcal{E}_{k,m}} = \mathcal{D}_{m'} \ldots \mathcal{D}_{m+1} \frac{\partial \mathcal{D}_m}{\partial \mathcal{E}_{k,m}} \mathcal{D}_{m-1} \ldots \mathcal{D}_1 \rho_l(t_0), \qquad \frac{\partial \mathcal{D}_m}{\partial \mathcal{E}_{k,m}} = \mathcal{D}_m \frac{\partial \mathcal{L}_m}{\partial \mathcal{E}_{k,m}}. \tag{2.38}$$

Since the states are only represented at the time grid points $t_0, \ldots, t_{N_t}$, cf. Fig. 2.3, it follows that $\partial\rho_l(t_{m'})/\partial\mathcal{E}_{k,m} = 0$ if $m' < m$. For a minimization of $\mathcal{J}$, each control parameter is updated via $\mathcal{E}_{k,m} \to \mathcal{E}_{k,m} - \lambda(\partial\mathcal{J}/\partial\mathcal{E}_{k,m})$, where $\lambda > 0$ quantifies the update magnitude. It is determined by a line search along the total update direction $\nabla_{\{\mathcal{E}_{k,m}\}}\mathcal{J}$. Unfortunately, as the optimization approaches the minimum of $\mathcal{J}$ its gradient starts to vanish, which, in consequence, causes the convergence to slow down severely. In order to improve the performance close to the minimum, GRAPE can be extended to incorporate information form the Hessian $\Delta_{\{\mathcal{E}_{k,m}\}}\mathcal{J}$, i.e., the second order derivatives [75, 76]. However, since the computational cost for evaluating the exact Hessian is substantial, the BFGS quasi-Newton method should be employed in practice [77–80]. It replaces the exact calculation of the Hessian by an approximated version built from successive gradients. This procedure can even be realized memory efficiently — a method known as LBFGS-B [81, 82].

Two approaches, which aim at merging the numerical advantages of gradient-based methods with the advantages and simplicity provided by analytically parametrized control fields, have been brought forth recently. The gradient optimization using parametrization (GROUP) algorithm [83] employs a control field parametrization as in Eq. (2.34) while it calculates the gradient of $\mathcal{J}$ with respect to the coefficients $\{c_n^{(k)}\}$. In comparison to GRAPE, the latter results in a more complicated but still solvable expression for the gradient. A similar approach is given by the gradient optimization of analytical controls (GOAT) method [84], which relies on a mathematical trick that allows forward-mode differentiation to calculate the gradient. While both algorithms show significant speedups when compared to gradient-free methods such as Nelder-Mead or CRAB and even allow for larger sets of control parameters, they both rely on a fixed parameterization when expanding the control fields. This still limits the set of accessible control fields and might prevent the optimization from finding any solution.

In this thesis, we will use Krotov's method as the primarily optimization algorithm. Like GRAPE, it relies on a piecewise-constant parametrization of the control fields, as illustrated in Fig. 2.3, but comes — in contrast to GRAPE and all other optimization methods – with the guarantee of monotonic convergence.

2.3.5 Krotov's Method

Krotov's method [85–88] was originally developed in the context of classical control theory and later translated to quantum mechanics [89, 90], where its first application has been the control of molecular dynamics [91–93]. The central idea of Krotov's method is the replacement of the actual optimization functional $\mathcal{J}[\{\rho_l\}, \{\mathcal{E}_k\}, T]$ by an auxiliary functional $L[\{\rho_l\}, \{\mathcal{E}_k\}, T, \Phi]$, augmented by an additional scalar function $\Phi[\{\rho_l(t)\}, t]$,

such that $\mathcal{J} = L$ for all Φ. The motivation for is that, while minimizing L is still equivalent to minimizing $\mathcal{J}$, the freedom to choose Φ can then be utilized to construct monotonic convergence [94], which is a favorable feature for an optimization algorithm. In an iterative scheme, monotonic convergence implies

$$L\left[\left\{\rho_l^{(i+1)}\right\},\left\{\mathcal{E}_k^{(i+1)}\right\},T,\Phi\right] \leq L\left[\left\{\rho_l^{(i)}\right\},\left\{\mathcal{E}_k^{(i)}\right\},T,\Phi\right], \tag{2.39}$$

where i denotes the iteration.

In order to understand, why monotonic convergence poses a difficult challenge for any optimization algorithm, it should be noted that functional $\mathcal{J}$, respectively L, change due to two effects. On the one hand, the functional changes individually when the control fields $\{\mathcal{E}_k^{(i)}(t)\} \to \{\mathcal{E}_k^{(i+1)(t)}\}$ or states $\{\rho_l^{(i)}(t)\} \to \{\rho_l^{(i+1)}(t)\}$ change, as the functional depends directly on both. On the other hand, however, the control fields and states are also intertwined, since the states depend on the control fields and the changes of the control fields depend on the states. Krotov's method allows to disentangle this interdependence by virtue of the freedom to choose Φ. To this end, $\Phi\left[\{\rho_l(t)\},t\right]$ is first chosen such that in iteration i, i.e., for states $\{\rho_l^{(i)}(t)\}$, it is the worst possible choice with respect to L such that *every* conceivable change in the states $\{\rho_l^{(i)}(t)\} \to \{\rho_l^{(i+1)}(t)\}$ — irrespective of what causes it — will necessarily improve L. To this end, L can be written as [94]

$$\begin{aligned} L\left[\{\rho_l\},\{\mathcal{E}_k\},T,\Phi\right] = {} & G\left[\{\rho_l(T)\},T,\Phi\right] - \Phi\left[\{\rho_l(t_0)\},t_0\right] \\ & - \int_{t_0}^{T} R\left[\{\rho_l(t)\},\{\mathcal{E}_k(t)\},t,\Phi\right]\mathrm{d}t, \end{aligned} \tag{2.40}$$

where

$$G\left[\{\rho_l(T)\},T,\Phi\right] = \mathcal{J}_T\left[\{\rho_l(T)\},T\right] + \Phi\left[\{\rho_l(T)\},T\right], \tag{2.41}$$

$$\begin{aligned} R\left[\{\rho_l(t)\},\{\mathcal{E}_k(t)\},t,\Phi\right] = {} & -g_a\left[\{\mathcal{E}_k(t)\},t\right] - g_b\left[\{\rho_l(t)\},t\right] + \frac{\partial\Phi\left[\{\rho_l(t)\},t\right]}{\partial t} \\ & + \sum_l \Big\langle\!\Big\langle \nabla_{\rho_l}\Phi\left[\{\rho_l(t)\},t\right] \Big| \mathrm{i}\boldsymbol{\mathcal{L}}\left(\{\mathcal{E}_k(t)\}\right)\left[\rho_l(t)\right] \\ & - \mathrm{i}\boldsymbol{\mathcal{L}}^{\dagger}\left(\{\mathcal{E}_k(t)\}\right)\left[\rho_l(t)\right] \Big\rangle\!\Big\rangle. \end{aligned} \tag{2.42}$$

In order to make Φ the worst possible choice for the states $\{\rho_l^{(i)}(t)\}$, we need to find Φ

such that

$$\left\{\rho_l^{(i)}(t)\right\} = \underset{\{\rho_l(t)\}}{\operatorname{argmax}}\left\{G\left[\{\rho_l(T)\}, T, \Phi\right]\right\} = \underset{\{\rho_l(t)\}}{\operatorname{argmin}}\left\{R\left[\{\rho_l(t)\}, \{\mathcal{E}_k(t)\}, t, \Phi\right]\right\}. \tag{2.43}$$

This will maximize L and might therefore appear counter-intuitive at first glance, since the general goal is still to minimize L. However, it ensures that any change of the control fields $\{\mathcal{E}_k^{(i)}(t)\} \to \{\mathcal{E}_k^{(i+1)}(t)\}$ does not cause its accompanying and implicit change of the states $\{\rho_l^{(i)}(t)\} \to \{\rho_l^{(i+1)}(t)\}$ to increase L. Hence, in a second step, the task of minimizing L now simplifies to finding conditions that minimize L when changing the control fields $\{\mathcal{E}_k^{(i)}(t)\} \to \{\mathcal{E}_k^{(i+1)}(t)\}$. Together with the maximum condition required by the first step, this second step translates into conditions regarding the first and second order derivatives of G and R, which can be satisfied by constructing Φ to second order in the states [94]. The disentanglement of the interdependence of control fields and states constitutes the general philosophy and ansatz of Krotov's method and ultimately leads to monotonic convergence, cf. Eq. (2.39). Nevertheless, instead of delving further into the mathematical detail of Krotov's method, which can be found in Ref. [94], we now proceed with its final steps that lead to an update equation for the fields $\{\mathcal{E}_k(t)\}$.

In order to obtain the actual update equation for control field $\mathcal{E}_k(t)$, we need to evaluate the derivative of the running costs $g = g_a + g_b$ with respect to the fields. For field $\mathcal{E}_k(t)$ it reads [94]

$$\begin{aligned}\frac{\partial g}{\partial \mathcal{E}_k}\Big|_{\left\{\mathcal{E}_{k'}^{(i+1)}(t)\right\}} = 2\mathfrak{Re}\Bigg\{&\sum_l \left\langle\!\!\left\langle \chi_l^{(i)}(t)\middle|\frac{\partial \boldsymbol{\mathcal{L}}\left(\{\mathcal{E}_{k'}(t)\}\right)}{\partial \mathcal{E}_k}\Big|_{\left\{\mathcal{E}_{k'}^{(i+1)}(t)\right\}}\rho_l^{(i+1)}(t)\right\rangle\!\!\right\rangle \\ &+\frac{\sigma(t)}{2}\sum_l \left\langle\!\!\left\langle \rho_l^{(i+1)}(t) - \rho_l^{(i)}(t)\middle|\frac{\partial \boldsymbol{\mathcal{L}}\left(\{\mathcal{E}_{k'}(t)\}\right)}{\partial \mathcal{E}_k}\Big|_{\left\{\mathcal{E}_{k'}^{(i+1)}(t)\right\}}\rho_l^{(i+1)}(t)\right\rangle\!\!\right\rangle\Bigg\},\end{aligned} \tag{2.44}$$

where $\sigma(t)$ is a scalar function, see Ref. [94] for details, and the states $\{\rho_l^{(i+1)}(t)\}$ are solutions to

$$\frac{\mathrm{d}}{\mathrm{d}t}\rho_l^{(i+1)}(t) = \boldsymbol{\mathcal{L}}\left(\left\{\mathcal{E}_{k'}^{(i+1)}(t)\right\}\right)\left[\rho_l^{(i+1)}(t)\right], \tag{2.45a}$$

$$\rho_l^{(i+1)}(0) = \rho_l(0) \tag{2.45b}$$

whereas the co-states $\{\chi_l^{(i)}(t)\}$ are solutions to

$$\frac{\mathrm{d}}{\mathrm{d}t}\chi_l^{(i)}(t) = -\boldsymbol{\mathcal{L}}^\dagger\left(\left\{\mathcal{E}_{k'}^{(i)}(t)\right\}\right)\left[\chi_l^{(i)}(t)\right] + \nabla_{\{\rho_l\}} g_b\Big|_{\left\{\rho_l^{(i)}(t)\right\}}, \tag{2.46a}$$

$$\chi_l^{(i)}(T) = -\nabla_{\rho_l} \mathcal{J}_T\big|_{\{\rho_{l'}^{(i)}(T)\}}. \tag{2.46b}$$

As a final step for obtaining the update equation for the fields $\{\mathcal{E}_k(t)\}$, we need to choose an explicit form for the field and state dependent cost functions g_a and g_b, respectively. A common choice is

$$g_a\left[\{\mathcal{E}_k(t)\}, t\right] = \sum_k \frac{\lambda_k}{S_k(t)} \left(\mathcal{E}_k(t) - \mathcal{E}_k^{\text{ref}}(t)\right)^2, \qquad g_b\left[\{\rho_l(t)\}, t\right] = 0, \tag{2.47}$$

where $\lambda_k \in \mathbb{R}_+$ is a numerical parameter, $S_k(t) \in (0,1]$ a shape function and $\mathcal{E}_k^{\text{ref}}(t)$ a reference field. Note that $S_k(t)$ can, in principle, differ from the physical shape $\bar{S}_k(t)$, cf. Eqs. (2.34) or (2.35), although they are often identical in practice. Plugging Eq. (2.47) into Eq. (2.44) yields the final update equation,

$$\begin{aligned}\mathcal{E}_k^{(i+1)}(t) = \mathcal{E}_k^{\text{ref}}(t) + \frac{S(t)}{\lambda_k} \mathfrak{Re}\Bigg\{ &\sum_l \left\langle\!\!\left\langle \chi_l^{(i)}(t) \middle| \frac{\partial \boldsymbol{\mathcal{L}}\left(\{\mathcal{E}_{k'}(t)\}\right)}{\partial \mathcal{E}_k}\Big|_{\{\mathcal{E}_{k'}^{(i+1)}(t)\}} \rho_l^{(i+1)}(t) \right\rangle\!\!\right\rangle \\ &+ \frac{\sigma(t)}{2} \sum_l \left\langle\!\!\left\langle \rho_l^{(i+1)}(t) - \rho_l^{(i)}(t) \middle| \right. \right. \\ &\left. \left. \frac{\partial \boldsymbol{\mathcal{L}}\left(\{\mathcal{E}_{k'}(t)\}\right)}{\partial \mathcal{E}_k}\Big|_{\{\mathcal{E}_{k'}^{(i+1)}(t)\}} \rho_l^{(i+1)}(t) \right\rangle\!\!\right\rangle \Bigg\}, \end{aligned} \tag{2.48}$$

where λ_k acts as inverse update magnitude and the shape function $S_k(t)$ suppresses updates where $S_k(t) = 0$. The reference field $\mathcal{E}_k^{\text{ref}}(t)$ is usually taken to be the control field $\mathcal{E}_k^{(i)}(t)$ from the previous iteration i and serves as reference for the current iteration $i+1$. Due to this choice, g_a and its contribution to the total functional $\mathcal{J}$ vanishes as the control fields converge to their final forms and $\mathcal{J}_T$ becomes the dominant term in $\mathcal{J}$. Equation (2.48) can be divided into a first order term (first line) and a second order term (second and third line). While the first order term is sufficient to ensure monotonic convergence in most cases, the second order term becomes mathematically necessary for some cases, for instance if $\mathcal{J}_T$ depends higher than quadratically on the states [94].

Equation (2.48) constitutes the central update equation for any control field within this thesis. Hence, its main characteristics should be mentioned — namely that it is mathematically only valid for time-continuous, non-discretized control fields $\{\mathcal{E}_k(t)\}$. Unfortunately, discretization is inevitable in order to evaluate Eq. (2.48) due to another interdependence of the control fields and states. In detail, the field update $\mathcal{E}_k^{(i+1)}(t)$ depends on the states $\{\rho_l^{(i+1)}(t)\}$, which are, in fact, not known yet, as they can only be computed when $\{\mathcal{E}_k^{(i+1)}(t)\}$ is already known. This interdependence can be resolved

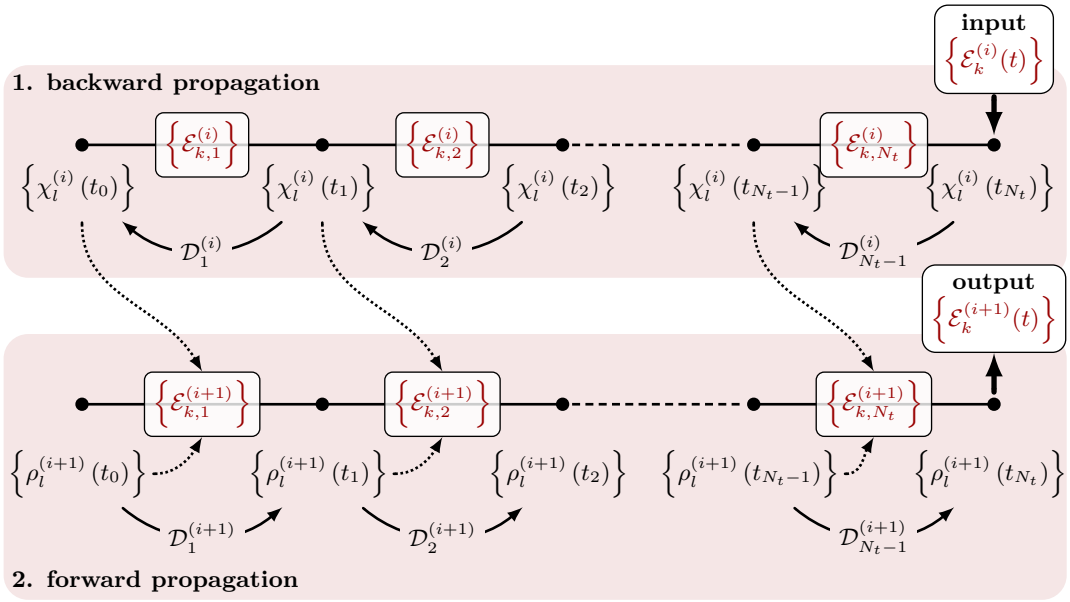

Figure 2.4: Sketch of Krotov's update scheme due to Eq. (2.48).

approximately by the piecewise-constant discretization $\mathcal{E}_k(t) \to \{\mathcal{E}_{k,1}, \ldots, \mathcal{E}_{k,N_t}\}$ sketched in Fig. 2.3. While the states are defined at the time grid points $t_0, \ldots, t_{N_t}$, the field values $\{\mathcal{E}_{k,m}\}$ are defined for the intervals $[t_{m-1}, t_m)$, $m = 1, \ldots, N_t$, between those grid points. We assume them to be exact at the center of the interval, i.e., $\mathcal{E}_{k,m} = \mathcal{E}_k(t_{m-1} + dt/2)$, cf. Fig. 2.3. When ensuring a sufficiently smooth discretization, the states $\{\rho_l^{(i+1)}(t_{m-1} + dt/2)\}$, which are required for calculating $\mathcal{E}_{k,m} = \mathcal{E}_k(t_{m-1} + dt/2)$, can be approximated by the known states $\{\rho_l^{(i+1)}(t_{m-1})\}$.

An iteration in Krotov's method, i.e., an evaluation of Eq. (2.48) for all control fields $\mathcal{E}_k(t)$, proceeds as follows.

1. (backward propagation) Calculate $\{\chi_l^{(i)}(T)\}$ via Eq. (2.46b) and solve equation of motion (2.46a) while storing $\{\chi_l^{(i)}(t_m)\}$ for all m and l.

2. (forward propagation) Use $\{\chi_l^{(i)}(t_0)\}$ and $\{\rho_l^{(i+1)}(t_0)\}$ to calculate $\{\mathcal{E}_{k,1}^{(i+1)}\}$ for all k; use $\{\mathcal{E}_{k,1}^{(i+1)}\}$ to propagate $\{\rho_l^{(i+1)}(t_0)\} \to \{\rho_l^{(i+1)}(t_1)\}$ one time step further; use $\{\chi_l^{(i)}(t_1)\}$ and $\{\rho_l^{(i+1)}(t_1)\}$ to calculate $\{\mathcal{E}_{k,2}^{(i+1)}\}$ for all k; continue to $\{\mathcal{E}_{k,N_t}^{(i+1)}\}$.

Figure 2.4 sketches Krotov's update scheme. The second step reveals the sequential nature of Krotov's method, where the control fields are updated sequentially in time. The sequential update is an important difference compared to GRAPE, where the control fields are updated concurrently for all time steps at once. A detailed discussion of the

numerical details of Krotov's method as well as pseudo-code for its implementation can be found in Ref. [66]. A comparison of GRAPE and Krotov's method in terms of performance can be found in Refs. [95, 96].

In order to mitigate the deviation from fully time-continuous control fields, Krotov's method can also be combined with a high accuracy propagation scheme that incorporates information about the actual intermediate time-dependency of the control fields within each time step [97]. The study has, unfortunately, yielded rather inconclusive results regarding its effectiveness [98]. In contrast to that, Krotov's method has been combined very successfully with, e.g., spectral [99, 100] and state-dependent constrains [101, 102]. Such constraints can help to keep the optimized fields in an experimentally feasible regime or to generally guide the optimization through the control problem's field or state space.

3

Quantum Optimal Control for Mixed State Squeezing

In the previous chapter, especially in Sec. 2.3, we have introduced the general idea and concept of optimal control. There, we have mainly focused on the parametrization of control fields and on various analytical and mathematical methods to minimize a given optimization functional $\mathcal{J}$. In contrast to that, we will now concentrate on what actually defines an appropriate functional. In detail, this implies that we will focus on the physical aspects of a control problem. This is due to the fact that an appropriate functional — besides being mathematically reliable — needs to capture the physics of a control problem and must therefore always be chosen in view of the control problem's physical context. To this end, we will illustrate the subject with the help of an example from cavity optomechanics, where the control task is to prepare a mechanical oscillator in a squeezed state by means of driving an optical cavity to which it is coupled to. Interestingly, the target state in this example is a mixed state, which is unusual for most optimizations and therefore constitutes an interesting control problem. The mixedness of the target state can here be utilized to pinpoint to problems that common optimization functionals face.

Section 3.1 starts by defining the mathematical conditions that any functional needs to fulfill. It thus builds the foundation for the definition of every functional within this thesis. In Sec. 3.2, we will then focus on a specific class of optimization targets — namely

those that can be expressed in terms of a set of target states. These require a reliable functional to assess the distance between final and target states. We will analyze common optimization functionals that employ state overlaps as indicators for the closeness between final and target states. Their failure in case of mixed target states will be illustrated by a toy optimization problem as well as by a geometric picture derived from the Bloch sphere. In the subsequent Sec. 3.3, we will use the insights from the previous section and examine if and how proper distance metrics can be used as distance measures and thus as functionals. This will emphasize a second property that any functional needs to fulfill besides being reliable: It needs to be derivable with respect to the states in order to be compatible with gradient-based optimization techniques. We then use this knowledge to construct a new and quite general functional that is reliable even for mixed target states and also derivable with respect to the states. In the final Sec. 3.4, we then apply this new functional to speed up the generation of mixed state squeezing in cavity optomechanics. This example will not only be interesting from a physical perspective but will also serve as an illustration of the subtleties in the application of optimal control — especially when optimizing towards a mixed target state.

Reference [103] builds the foundation for this chapter.

3.1 Optimization Functionals

An appropriate choice of functional $\mathcal{J}$, cf. Eq. (2.32), is vital for the success of any optimization and its importance should not be underestimated. In the literature, a great deal of effort is put into creating new optimization algorithms as well as improving existing ones, cf. Sec. 2.3, in order to improve their performance and accelerate their convergence, i.e., to find solutions faster and more efficiently. In contrast, the same benefits can often be achieved by simply exchanging the functional with a more appropriate one. In the worst case, an ill-chosen functional immediately causes the control landscape to become treacherous as the minima might no longer correspond to the desired optimal solutions — a problem that can not be detected or corrected by the choice of the optimization algorithm. We will sketch what *appropriate* means in the following.

First, note that the problem of choosing $\mathcal{J}$ appropriately usually only affects its final-time part $\mathcal{J}_T$, as the running costs g_a or g_b are typically used to guide the optimization while the important figure of merit is given by $\mathcal{J}_T$. This pertains within this thesis and especially for Krotov's method, where the running costs vanish as the optimization converges. Hence, we will restrict the further discussion to $\mathcal{J}_T$, which is a function of a set of time-evolved states $\{\rho_l(T)\}$ at final time T, for which we define the following

mathematical conditions.

Let $\mathfrak{L}_\mathcal{H}$ be the Liouville space over Hilbert space $\mathcal{H}$ and $\mathcal{S}_\mathcal{H} \subset \mathfrak{L}_\mathcal{H}$ the corresponding state space of density matrices. Any final-time functional $\mathcal{J}_T$ that allows the optimization target to be expressed in terms of a set of target states $\{\rho_l^{\text{trgt}}\}$ — not to be confused with the time-evolved states $\{\rho_l(T)\}$ — needs to satisfy

$$\forall \rho_1, \rho_2, \ldots \in \mathcal{S}_\mathcal{H} : \mathcal{J}_T\left[\{\rho_l\}\right] \in \mathbb{R}, \tag{3.1a}$$

$$\mathcal{J}_T\left[\left\{\rho_l^{\text{trgt}}\right\}\right] = \inf_{\rho_1,\rho_2,\ldots\in\mathcal{S}_\mathcal{H}} \mathcal{J}_T\left[\{\rho_l\}\right] \quad \Leftrightarrow \quad \rho_l^{\text{trgt}} = \rho_l \; \forall l. \tag{3.1b}$$

While the first condition just ensures an order relation, the second one guarantees that the infimum of $\mathcal{J}_T$ (typically $\mathcal{J}_T = 0$) is attained iff all time-evolved states $\{\rho_l(T)\}$ perfectly coincide with their respective target states $\{\rho_l^{\text{trgt}}\}$. It might appear rather peculiar that we emphasize the fact that the optimization target needs to be expressible in terms of target states $\{\rho_l^{\text{trgt}}\}$ in order for Eq. (3.1) to apply. However, it is important to note that some optimization targets can not be expressed in terms of a set of target states $\{\rho_l^{\text{trgt}}\}$. We will present some examples for this at the end of this section. In the following, we start with the majority of optimization targets that are in fact expressible in terms of target states. Note that we discarded $\mathcal{J}_T$'s explicit dependence on the final time T in Eq. (3.1).

A very general optimization target is an optimization towards a certain dynamical map, i.e., we want $\mathcal{D}_{T,t_0} \stackrel{!}{=} \mathcal{D}^{\text{trgt}} \in \mathcal{B}(\mathfrak{L}_\mathcal{H})$. Let $\{\rho_1, \ldots, \rho_{N^2}\}$ be a basis for $\mathfrak{L}_\mathcal{H}$ with $N = \dim\{\mathcal{H}\}$. Since $\mathcal{B}(\mathfrak{L}_\mathcal{H})$ defines the set of bounded operators on the set of bounded Hilbert space operators $\mathfrak{L}_\mathcal{H}$, elements from $\mathcal{B}(\mathfrak{L}_\mathcal{H})$ are sometimes referred to as superoperators. Formally, any $\mathcal{D} \in \mathcal{B}(\mathfrak{L}_\mathcal{H})$ can be identified uniquely by its dynamical or process matrix $\mathcal{X} \in \mathbb{C}^{N^2\times N^2}$ whose elements are given by $\mathcal{X}_{l,l'} = \langle\!\langle \rho_l | \mathcal{D}\left[\rho_{l'}\right] \rangle\!\rangle$, $l, l' = 1, \ldots, N^2$ [2]. Therefore, we can ensure that an optimization targets $\mathcal{D}^{\text{trgt}}$ by ensuring that $\mathcal{X}_{l,l'}(T) = \langle\!\langle \rho_l | \mathcal{D}_{T,t_0}\left[\rho_{l'}\right] \rangle\!\rangle \stackrel{!}{=} \langle\!\langle \rho_l | \mathcal{D}^{\text{trgt}}\left[\rho_{l'}\right] \rangle\!\rangle$ for all $l, l' = 1, \ldots, N^2$. The latter can be ensured by taking the final time functional $\mathcal{J}_T$ to read

$$\mathcal{J}_T\left[\{\rho_l\}, T\right] = \sum_{l=1}^{N^2} w_l d\left(\rho_l^{\text{trgt}}, \rho_l(T)\right), \qquad \rho_l^{\text{trgt}} = \mathcal{D}^{\text{trgt}}\left[\rho_l\right], \quad \rho_l(T) = \mathcal{D}_{T,t_0}\left[\rho_l\right], \tag{3.2}$$

where $d(\rho_l^{\text{trgt}}, \rho_l(T)) \geq 0$ quantifies the distance between ρ_l^{trgt} and $\rho_l(T)$ and $w_l > 0$ is a weight.

Equation (3.2) constitutes a very general expression for all optimization targets that rely on a set of target states. For instance, in case of a simple state-to-state optimization, the functional simplifies to $\mathcal{J}_T[\rho, T] = d\left(\rho^{\text{trgt}}, \rho(T)\right)$ and the index l can be omitted. Such

an optimization puts less constraints on the general dynamical map $\mathcal{D}_{T,t_0}$ as it vanishes when the initial state $\rho(t_0) = \rho^{\text{in}}$ gets correctly mapped onto $\rho^{\text{trgt}} \stackrel{!}{=} \rho(T) = \mathcal{D}_{T,t_0}[\rho(t_0)]$, independent of what happens to other states $\rho(t_0) \neq \rho^{\text{in}}$. The same concept holds if the target operation is defined on a subspace $\mathcal{H}' \subseteq \mathcal{H}$ of Hilbert space, $\mathcal{H} = \mathcal{H}' \oplus \mathcal{H}'^{\perp}$, where $M = \dim\{\mathcal{H}'\} \leq \dim\{\mathcal{H}\} = N$, respectively a subspace $\mathfrak{L}_{\mathcal{H}'} \subseteq \mathfrak{L}_{\mathcal{H}}$ of Liouville space. In that case, we require a dynamical map $\mathcal{D}^{\text{trgt}} \in \mathcal{B}(\mathfrak{L}_{\mathcal{H}})$ that ensures $\mathcal{D}^{\text{trgt}}[\mathfrak{L}_{\mathcal{H}'} \oplus 0] \subseteq \mathfrak{L}_{\mathcal{H}'} \oplus 0$ with $0 \in \mathfrak{L}_{\mathcal{H}'^{\perp}}$ the zero operation. Note that states $\rho \notin \mathcal{S}_{\mathcal{H}'} \oplus 0$, i.e., states that start initially outside of this subspace, do not have any specific target state, i.e., $\mathcal{D}^{\text{trgt}}$ is only defined partially. Let $\{\rho'_1, \ldots, \rho'_{M^2}\}$ be a basis for $\mathfrak{L}_{\mathcal{H}'}$ and let $\{\rho_1^{\text{trgt}}, \ldots, \rho_{M^2}^{\text{trgt}}\}$ specify the desired target operation within $\mathfrak{L}_{\mathcal{H}'}$ completely. It is then sufficient to minimize Eq. (3.2) for the M^2 states $\{\rho'_1 \oplus 0, \ldots, \rho'_{M^2} \oplus 0\}$ and $\{\rho_1^{\text{trgt}} \oplus 0, \ldots, \rho_{M^2}^{\text{trgt}} \oplus 0\}$, since it ensures the correct behavior within $\mathfrak{L}_{\mathcal{H}'}$ and leaves the behavior in the remaining Liouville space unspecified. Such an optimization target is a very common scenario in quantum information, where the actual Hilbert space $\mathcal{H}$ is often larger but an operation needs to be realized on an M dimensional subspace $\mathcal{H}' \subseteq \mathcal{H}$, e.g. $M = 2$ or $M = 4$ for one- or two-qubit operations. For instance, an optimization towards a specific unitary process within $\mathfrak{L}_{\mathcal{H}'}$ would target a dynamical map $\mathcal{D}^{\text{trgt}}$ that ensures $\mathcal{D}^{\text{trgt}}[\mathfrak{L}_{\mathcal{H}'} \oplus 0] = U^{\text{trgt}}\mathfrak{L}_{\mathcal{H}'}U^{\text{trgt}\dagger} \oplus 0$, where $U^{\text{trgt}} \in \mathrm{SU}(M) \subset \mathfrak{L}_{\mathcal{H}'}$ is the desired unitary operation on subspace $\mathcal{H}'$. Interestingly, depending on the operation that should be realized, the optimization does not always have to be performed with M^2 states. In the important and common example of an optimization towards a unitary operation on $\mathfrak{L}_{\mathcal{H}'} \subseteq \mathfrak{L}_{\mathcal{H}}$ it is sufficient to evaluate the dynamics of only three appropriately chosen states $\rho'_1, \rho'_2, \rho'_3 \in \mathcal{S}_{\mathcal{H}'}$ [104]. In detail, it is possible to ascertain $\mathcal{D}^{\text{trgt}}[\mathfrak{L}_{\mathcal{H}'} \oplus 0] = U^{\text{trgt}}\mathfrak{L}_{\mathcal{H}'}U^{\text{trgt}\dagger} \oplus 0$ just by means of ensuring $\mathcal{D}_{T,t_0}[\rho_l{}' \oplus 0] \equiv \rho_l(T) \stackrel{!}{=} \rho_l^{\text{trgt}} \oplus 0 \equiv U^{\text{trgt}}\rho'_l U^{\text{trgt}\dagger} \oplus 0$ for $l = 1, 2, 3$, i.e., $\mathcal{J}_T = 0$ in Eq. (3.2). This holds for arbitrary dimensions M.

As is evident from Eq. (3.2), all these optimization tasks that are characterized by a set of target states $\{\rho_l^{\text{trgt}}\}$ boil down to a set of state-to-state optimizations. In detail, each initial state $\rho_l = \rho_l(t_0)$ needs to be transferred into $\rho_l(T) \stackrel{!}{=} \rho_l^{\text{trgt}}$ at final time T by the *same* set of control fields $\{\mathcal{E}_k(t)\}$. Thus, a reliable distance measure $d\left(\rho_l^{\text{trgt}}, \rho_l(T)\right)$ between any two states is vital. At least, such a measure needs to fulfill Eq. (3.1) in the sense that for two states $\rho_1, \rho_2 \in \mathcal{S}_{\mathcal{H}}$ it is real and its infimum unique, i.e.,

$$d(\rho_1, \rho_2) = \inf_{\rho'_1, \rho'_2 \in \mathcal{S}_{\mathcal{H}}} d\left(\rho'_1, \rho'_2\right) \quad \Leftrightarrow \quad \rho_1 = \rho_2. \tag{3.3}$$

These two conditions are naturally satisfied by any metric on $\mathfrak{L}_{\mathcal{H}}$, where the infimum coincides with the minimum $d = 0$. In addition, such a metric would be symmetric and

satisfy the triangle inequality. While the latter two properties are undoubtedly useful, they are strictly speaking not necessary for OCT. As consequence, various distance measures have been used in OCT whereas some do not even qualify as reliable indicator for the closeness of two states. Section 3.2 will demonstrate that distance measures which use state overlaps as indicators for closeness are not reliable in combination with mixed target states and non-unitary dynamics. Reliable distance measures for such a control task will be explored in Sec. 3.3 — also in view of their capability to build analytical derivatives with respect to the states. The latter is not a mathematical necessity like Eq. (3.3) but a practical requirement in order for the measure to be compatible with gradient-based optimization techniques.

As a final remark, it should be noted that the discussion regarding distance measures between states only affects optimization targets that can be expressed in terms of a set of target states $\{\rho_l^{\text{trgt}}\}$. If no specific target states exist, we also do not require a reliable distance measure d between the states of $\{\rho_l^{\text{trgt}}\}$ and $\{\rho_l(T)\}$. For instance, if the goal is to maximize the expectation value of an Hermitian operator $\mathsf{A} \in \mathfrak{L}_{\mathcal{H}}$, the corresponding final-time functional reads [89]

$$\mathcal{J}_T\left[\{\rho_l\}, T\right] = 1 - \frac{1}{\eta}\sum_l \langle\!\langle \mathsf{A}|\rho_l(T)\rangle\!\rangle\,, \tag{3.4}$$

where η normalizes the sum to one at maximum. Such functionals find e.g. application in optimizing molecular alignment [105]. An even more sophisticated example that goes beyond Eq. (3.4), is the optimization of the entangling content of a two-qubit gate [106–108]. In that case, no specific target unitary U^{trgt} and, thus, no specific target states $\{\rho_l^{\text{trgt}}\}$ exists and $\mathcal{J}_T$ is just a rather complicated expression of the time-evolved states $\{\rho_l(T)\}$.

3.2 Failure of Overlap-Based Functionals for Mixed States

In this section, we start to discuss how to reliable choose the distance measure d in Eq. (3.2). To this end, we first consider a specific type of distance measure — namely those that employ state overlaps as indicators for closeness. A standard choice to evaluate how close two states are within an optimization is given by the real and square modulus functionals [90]. In Hilbert and Liouville space, they respectively read

$$\begin{aligned} d_{\text{re}}^{\mathcal{H}}\left(|\psi_1\rangle, |\psi_2\rangle\right) &= 1 - \mathfrak{Re}\left\{\tau_{\mathcal{H}}\right\}, & d_{\text{re}}\left(\rho_1, \rho_2\right) &= 1 - \tau, \\ d_{\text{sm}}^{\mathcal{H}}\left(|\psi_1\rangle, |\psi_2\rangle\right) &= 1 - |\tau_{\mathcal{H}}|^2, & d_{\text{sm}}\left(\rho_1, \rho_2\right) &= 1 - \tau^2, \end{aligned} \tag{3.5}$$

where $\tau_{\mathcal{H}} = \langle\Psi_1|\Psi_2\rangle \in \mathbb{C}$ is the Hilbert space overlap of states $|\psi\rangle_1, |\psi\rangle_2 \in \mathcal{H}$ and $\tau = \langle\!\langle\rho_1|\rho_2\rangle\!\rangle \in \mathbb{R}$ the Liouville space overlap of states $\rho_1, \rho_2 \in \mathfrak{L}_{\mathcal{H}}$. In Hilbert space, these distance measures attain their minimum, zero, iff $|\psi_1\rangle = |\psi_2\rangle$ for $d_{\mathrm{re}}^{\mathcal{H}}$ or $|\psi_1\rangle = e^{\mathrm{i}\phi}|\psi_2\rangle$ for $d_{\mathrm{sm}}^{\mathcal{H}}$, respectively. While the real part functional is sensitive to the global phase $\phi \in \mathbb{R}$, the square modulus functional is not. Although this feature vanishes in Liouville space, in Hilbert space it serves as a perfect illustration for what we might call the "restrictiveness" of a functional — a property that goes beyond the mathematical reliability of a functional. To elaborate, let us assume the optimization target is a single state-to-state transfer. While $d_{\mathrm{re}}^{\mathcal{H}} = 0$ requires perfect equivalence of $|\psi_1\rangle$ and $|\psi_2\rangle$, $d_{\mathrm{sm}}^{\mathcal{H}} = 0$ still allows for an arbitrary global phase difference ϕ between the two states. Since the global phase is typically irrelevant, we can argue that $d_{\mathrm{re}}^{\mathcal{H}}$ unnecessarily excludes solutions from the optimization. Solutions with $d_{\mathrm{sm}}^{\mathcal{H}} = 0$, which are usually perfectly fine from a physical perspective, might be nonzero in $d_{\mathrm{re}}^{\mathcal{H}}$ and the optimization is not able to find them. Therefore, choosing $d_{\mathrm{sm}}^{\mathcal{H}}$ might be the better choice as a distance measure. Despite the example's simplicity, it illustrates that specific part in choosing an appropriate functional that can not be expressed in terms of mathematical requirements. In order to make an appropriate choice, it always requires knowledge of the actual optimization target and the underlying system's physical aspects. In most cases, functional $\mathcal{J}_T$ should be chosen — within the scope of Eq. (3.1) — such that it is the least restrictive with respect to conceivable solutions of the control problem.

Since we will primarily work with density matrices in this thesis, it should be noted that the "restrictiveness" of $d_{\mathrm{re}}^{\mathcal{H}}$ only affects its Hilbert space version. In Liouville space, the global phase ϕ vanishes as any state $e^{\mathrm{i}\phi}|\psi_1\rangle$ becomes the same pure density matrix $\rho_1 = |\psi_1\rangle\langle\psi_1|$, i.e., both d_{re} and d_{sm} are insensitive to global phases. Unfortunately, other problems arise in Liouville space. While for any two states $|\psi_1\rangle, |\psi_2\rangle \in \mathcal{H}$, respectively their *pure* density matrices $\rho_1 = |\psi_1\rangle\langle\psi_1|$ and $\rho_2 = |\psi_2\rangle\langle\psi_2|$, the Liouville space versions d_{re} and d_{sm} of $d_{\mathrm{re}}^{\mathcal{H}}$ and $d_{\mathrm{sm}}^{\mathcal{H}}$ fulfill Eq. (3.3) and are thus reliable, problems arise as soon as we consider *mixed* states. In detail, for density matrices ρ_1 and ρ_2, the state overlap $\tau = \langle\!\langle\rho_1|\rho_2\rangle\!\rangle$ becomes real and minimizing d_{re} and d_{sm} is equivalent to maximizing τ. Unfortunately, τ is no longer a reliable measure or indicator for closeness of ρ_1 and ρ_2 if *both* states are mixed.

We can illustrate the problem with the simplest example of a quantum system, a qubit. Representing the qubit state in the canonical basis, $\{|0\rangle, |1\rangle\}$, consider

$$\rho_1(\alpha) = \begin{pmatrix} \alpha & 0 \\ 0 & 1-\alpha \end{pmatrix}, \qquad \rho_2(\beta) = \begin{pmatrix} \beta & 0 \\ 0 & 1-\beta \end{pmatrix}, \tag{3.6}$$

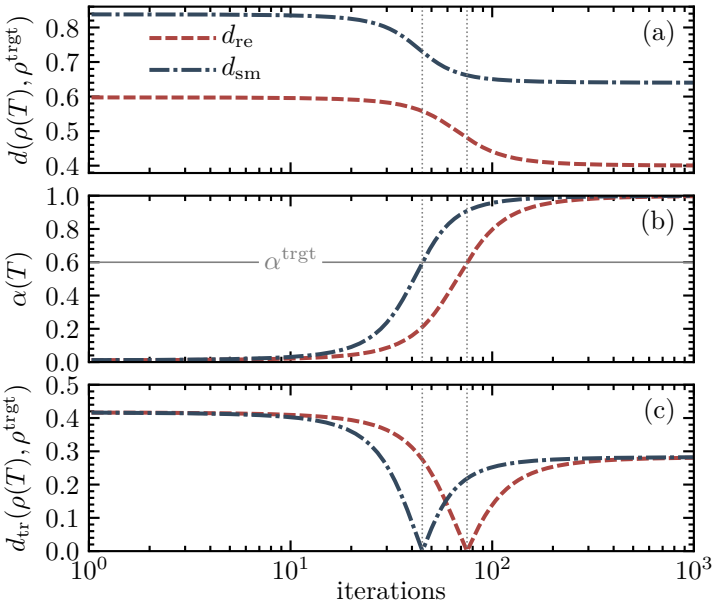

Figure 3.1: Optimization results for a qubit, where the dynamics is governed by Eq. (3.7). The initial state is $\rho(0) = |1\rangle\langle 1|$, the target state $\rho^{\mathrm{trgt}} = \mathrm{diag}\{0.6, 0.4\}$ and the initial field $u(t) = 0.01$ with total propagation time $T = 1$. (a) Final-time functionals d_{re} and d_{sm}, cf. Eq. (3.5), as a function of the number of iterations. (b) Population $\alpha(T)$ in $|0\rangle$ at final time. The horizontal line indicates the respective population of the target state ρ^{trgt}. (c) Trace distance d_{tr}, cf. Eq. (6.2), between propagated state $\rho(T)$ and target state ρ^{trgt}.

where $0 \leq \alpha, \beta \leq 1$. Both states are obviously equivalent iff $\alpha = \beta$ and correspond to an overlap of $\tau^{\mathrm{eq}} \equiv \langle\!\langle \rho_1(\beta) | \rho_2(\beta) \rangle\!\rangle = \beta^2 + (1-\beta)^2$ in Liouville space. However, for pure states such as $\rho_1(1)$ or $\rho_1(0)$, we find $\tau = \langle\!\langle \rho_1(1) | \rho_2(\beta) \rangle\!\rangle = \beta$ or $\tau = \langle\!\langle \rho_1(0) | \rho_2(\beta) \rangle\!\rangle = 1 - \beta$. This results in $\tau > \tau^{\mathrm{eq}}$ for $\beta \in (\frac{1}{2}, 1)$ or $\beta \in (0, \frac{1}{2})$, respectively. Hence, pure states maximize τ, respectively minimize d_{re} or d_{sm}, and therefore incorrectly indicate closeness of ρ_1 and ρ_2 even if they are actually less close. Moreover, for the completely mixed state $\rho_2(\frac{1}{2}) = \mathrm{diag}\{\frac{1}{2}, \frac{1}{2}\}$, we find $\tau = \langle \rho_1(\alpha), \rho_2(\frac{1}{2}) \rangle = \frac{1}{2}$ for all α. In this case, τ is not even able to indicate differences at all.

The ill-definedness of the overlap-based functionals (3.5) in case of mixed target states is easily demonstrated by a simple toy control problem, where $\rho_2 = \rho^{\mathrm{trgt}}$ plays the role of a target state and $\rho_1 = \rho(t)$ that of a time-evolved state that needs to be matched with ρ^{trgt} at final time T. We consider a qubit whose dynamics is determined by a purely dissipative master equation,

$$\frac{\mathrm{d}}{\mathrm{d}t}\rho(t) = -\mathrm{i}\mathcal{L}_{\mathrm{diss}}(u(t))[\rho(t)] = u(t)\left[\sigma_-\rho(t)\sigma_+ - \frac{1}{2}\{\sigma_+\sigma_-, \rho(t)\}\right], \tag{3.7}$$

where $\sigma_-(\sigma_+)$ are the standard lowering (raising) operators and $u(t) \geq 0$ is a time-dependent, controllable decay rate, cf. Eq. (2.21). We choose the initial state of the qubit to be $\rho(0) = |1\rangle\langle 1|$. Thus, we can reach any diagonal state $\rho(T) = \alpha(T)\,|0\rangle\langle 0| + (1-\alpha(T))\,|1\rangle\langle 1|$ with $\alpha(T) > 0$, since $\alpha(T)$ can be controlled by appropriately choosing $u(t)$ for $t \in [0, T]$. Figure 3.1 presents optimization results, employing Krotov's method, for a mixed state target, $\rho^{\mathrm{trgt}} = 0.6\,|0\rangle\langle 0| + 0.4\,|1\rangle\langle 1|$, employing the functionals (3.5). Figure 3.1(a) shows the monotonic decrease of both functionals over the number of iterations, while Fig. 3.1(b) plots the corresponding final time ground state population $\alpha(T)$. The optimization starts with a fairly low ground state population, $\alpha(T) \sim 0$, due to the non-optimal, i.e., too small, guess field $u(t)$. The decay rate is increased during the optimization such that $\alpha(T) \sim 1$ after convergence is reached. This result maximizes the overlap since $\tau^{\mathrm{opt}} \equiv \left\langle \rho_{\mathrm{opt}}(T), \rho^{\mathrm{trgt}} \right\rangle > \langle \rho^{\mathrm{trgt}}, \rho^{\mathrm{trgt}} \rangle \equiv \tau^{\mathrm{eq}}$ with $\rho_{\mathrm{opt}}(T) = |0\rangle\langle 0|$, and thus realizes smaller values of the functionals d_{re} and d_{sm}. However, this is not what the optimization is supposed to achieve. Figure 3.1(c) shows the trace distance d_{tr} (a reliable measure for the closeness of states, as we will discuss in Sec. 3.3) between $\rho(T)$ and ρ^{trgt} as a function of the number of iterations. A minimum is observed at the correct value $\alpha(T) = \alpha^{\mathrm{trgt}} = 0.6$. The increase of d_{tr} as the iterative algorithm proceeds, which is due to further minimization of d_{re} and d_{sm}, illustrates that the optimization misses the desired target.

The failure of measures (3.5) in Liouville space can be fully generalized and illustrated geometrically, even for arbitrary N level systems, when employing the Bloch vector representations of states ρ_1 and ρ_2. This representation can be obtained by choosing a basis of traceless, Hermitian $N \times N$ matrices, $\{\mathsf{A}_i\}$, with $\langle \mathsf{A}_i, \mathsf{A}_j \rangle = \delta_{i,j}$, that allows to expand the density matrix ρ as [109]

$$\rho = \frac{1}{N}\mathbb{1}_N + \sum_{i=1}^{N^2-1} r_i \mathsf{A}_i = \frac{1}{N}\mathbb{1}_N + \boldsymbol{r}\cdot\mathbf{A}, \qquad r_i = \langle\!\langle \rho | \mathsf{A}_i \rangle\!\rangle\,, \tag{3.8}$$

where $\boldsymbol{r} = (r_1, r_2, \dots)^\top$ is the generalized Bloch vector, containing the expansion coefficients for matrices $\mathbf{A} = (\mathsf{A}_1, \mathsf{A}_2, \dots)^\top$. In this picture, the purity (2.3) obtains a simple geometric interpretation as it becomes $\mathcal{P}(\rho) = \langle\!\langle \rho | \rho \rangle\!\rangle = 1/N + |\boldsymbol{r}|^2$ and is thus proportional to the length of the state's Bloch vector. A pure state $\mathcal{P}(\rho) = 1$ is therefore given by $|\boldsymbol{r}| = r_{\max} = \sqrt{(N-1)/N}$, whereas a mixed states has $|\boldsymbol{r}| < r_{\max}$ and the completely mixed state corresponds to $\boldsymbol{r} = 0$.

In the Bloch picture, the state overlap τ in Liouville space becomes

$$\tau = \langle\!\langle \rho_1 | \rho_2 \rangle\!\rangle = \frac{1}{N} + \boldsymbol{r}_1 \cdot \boldsymbol{r}_2 = \frac{1}{N} + |\boldsymbol{r}_1|\,|\boldsymbol{r}_2| \cos(\theta), \tag{3.9}$$

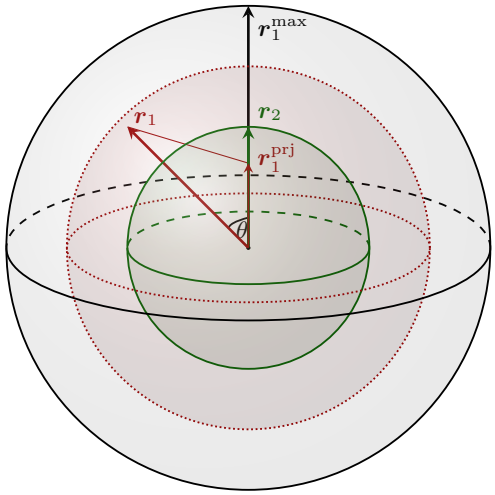

Figure 3.2: The overlap $\tau = \langle\!\langle \rho_1 | \rho_2 \rangle\!\rangle$ visualized geometrically in terms of their Bloch vectors $\boldsymbol{r}_1$ and $\boldsymbol{r}_2$. The overlap, cf. Eq. (3.9), is equivalent to the projection of $\boldsymbol{r}_1$ onto $\boldsymbol{r}_2$, which means that the maximal overlap is always achieved by $\boldsymbol{r}_1^{\max}$.

with θ the geometric angle between the two vectors $\boldsymbol{r}_1$ and $\boldsymbol{r}_2$. Let $\boldsymbol{r}_2$ again constitute the target state of an optimization and let $\boldsymbol{r}_1$ represent a state that needs to be matched with with $\boldsymbol{r}_2$. Thus, any minimization with d_{re} or d_{sm}, cf. Eq. (3.5), necessarily maximizes τ. The latter can only be achieved with $\theta = 0$ and by maximizing $|\boldsymbol{r}_1|$. Geometrically, this means that the optimization maximizes the projection of $\boldsymbol{r}_1$ onto $\boldsymbol{r}_2$, which physically corresponds to an optimization towards a pure state $\boldsymbol{r}_1$ that has the same angular orientation on the Bloch sphere as $\boldsymbol{r}_2$, irrespective of whether $\boldsymbol{r}_2$ is actually pure or not. In fact, if the target state $\boldsymbol{r}_2$ is mixed, the optimization targets inevitably the wrong state. Figure 3.2 visualizes the problem geometrically. This readily explains the optimization results of Fig. 3.1.

We can therefore conclude that the overlap-based functionals d_{re} and d_{sm}, cf. Eq. (3.5), are not reliable when optimizing towards mixed target states in combination with non-unitary dynamics. This conclusion holds for every other functional that employs τ as an indicator for closeness. Even though most target states in an optimization are pure [8, 9] and the problems outlined above do therefore not apply, exceptions exist, as we will see in Sec. 3.4. In any such case, d_{re} or d_{sm} need to be replaced by a reliable distance measure. We will analyze possible alternatives in the following.

3.3 Construction of a New Geometric Functional

In the last section, we have illustrated that the overlap-based functionals d_{re} and d_{sm}, cf. Eq. (3.5), are not reliable for an optimization targeting a mixed state. In contrast to that, a reliable distance measure between any two density matrices, independent on whether they are mixed or not, is naturally given by a proper metric on $\mathfrak{L}_{\mathcal{H}}$. Conceivable metrics are the trace distance [2],

$$d_{\mathrm{tr}}(\rho_1,\rho_2) = \frac{1}{2}\left\|\rho_1-\rho_2\right\|_{\mathrm{tr}}, \qquad \left\|\rho\right\|_{\mathrm{tr}} = \mathrm{tr}\left\{\sqrt{\rho^\dagger\rho}\right\}, \tag{3.10}$$

the Bures distance [110],

$$d_{\mathrm{bures}}(\rho_1,\rho_2) = \sqrt{1-F(\rho_1,\rho_2)}, \qquad F(\rho_1,\rho_2) = \mathrm{tr}\left\{\sqrt{\sqrt{\rho_1}\rho_2\sqrt{\rho_1}}\right\} \tag{3.11}$$

with $F(\rho_1,\rho_2)$ the Uhlmann fidelity [111], the Hellinger distance [112],

$$d_{\mathrm{hellinger}}(\rho_1,\rho_2) = \sqrt{1-A(\rho_1,\rho_2)}, \qquad A(\rho_1,\rho_2) = \mathrm{tr}\left\{\sqrt{\rho_1}\sqrt{\rho_2}\right\} \tag{3.12}$$

with $A(\rho_1,\rho_2)$ the quantum affinity, the Jensen-Shannon divergence [113],

$$d_{\mathrm{JS}}(\rho_1,\rho_2) = \sqrt{E\left(\frac{\rho_1+\rho_2}{2}\right)-\frac{1}{2}E(\rho_1)-\frac{1}{2}E(\rho_2)}, \qquad E(\rho) = \mathrm{tr}\{\rho\ln(\rho)\} \tag{3.13}$$

with $E(\rho)$ the von Neumann entropy [114], and the Hilbert-Schmidt distance [115],

$$d_{\mathrm{HS}}(\rho_1,\rho_2) = \frac{1}{2}\mathrm{tr}\left\{(\rho_1-\rho_2)^2\right\} = \frac{1}{2}\left\langle\!\left\langle\rho_1-\rho_2|\rho_1-\rho_2\right\rangle\!\right\rangle, \tag{3.14}$$

to name a few. Note that some of these metrics have been adapted from their definitions in the literature to satisfy $d \in [0,1]$.

Each of these metrics is a reliable distance measure between any two states. It fulfills Eq. (3.3) and is therefore a reliable choice for d in Eq. (3.2). However, in order to be useful in practice, d needs to fulfill another property — namely to be derivable with respect to the states. This is an important property that was trivially satisfied by d_{re} or d_{sm} but becomes non-trivial for the metrics in Eqs. (6.2)-(3.14). For instance, in Krotov's method, a gradient with respect to the states appears in Eq. (2.46b). The availability of an analytical derivative can thus be seen as a prerequisite for any metric in order to be compatible with gradient-based OCT. The only metric from Eqs. (6.2)-(3.14), that allows for an analytical gradient is the Hilbert-Schmidt distance (3.14). It has therefore already been utilized for OCT, see e.g. Ref. [116].

Motivated by the simple geometric picture of state mismatches, cf. Fig. 3.2, we will now construct a new functional based on this geometric picture, which is suitable for mixed target states and compatible with gradient-based OCT. To this end, we first analyze the Hilbert-Schmidt distance (3.14). In the Bloch picture, it takes the simple geometric form $d_{\mathrm{HS}}(\boldsymbol{r}_1, \boldsymbol{r}_2) = \frac{1}{2}|\boldsymbol{r}_1 - \boldsymbol{r}_2|^2$, i.e., it essentially coincides with the squared Euclidean distance of the two Bloch vectors $\boldsymbol{r}_1, \boldsymbol{r}_2$. It is thus trivial to see that $d_{\mathrm{HS}} = 0$ iff $\boldsymbol{r}_1 = \boldsymbol{r}_2$. Based on this geometric picture, the idea in the following is to create separate distance measures for the length and angle mismatch of $\boldsymbol{r}_1$ and $\boldsymbol{r}_2$, respectively. In the Bloch picture, these individual measures take the form

$$d_{\mathrm{angle}}(\boldsymbol{r}_1, \boldsymbol{r}_2) = \frac{\theta^2}{\pi^2}, \tag{3.15a}$$

$$d_{\mathrm{length}}(\boldsymbol{r}_1, \boldsymbol{r}_2) = \frac{N}{N-1}\Big(|\boldsymbol{r}_1| - |\boldsymbol{r}_2|\Big)^2 \tag{3.15b}$$

with θ the angle between the vectors $\boldsymbol{r}_1$ and $\boldsymbol{r}_2$, cf. Eq. (3.9). In the state space $\mathcal{S}_{\mathcal{H}} \subset \mathfrak{L}_{\mathcal{H}}$ of density matrices they read

$$d_{\mathrm{angle}}(\rho_1, \rho_2) = \frac{1}{\pi^2}\arccos^2\left(\frac{\xi_{12}}{\sqrt{\xi_{11}\xi_{22}}}\right), \tag{3.16a}$$

$$d_{\mathrm{length}}(\rho_1, \rho_2) = \frac{N}{N-1}\left(\sqrt{\xi_{11}} - \sqrt{\xi_{22}}\right)^2, \tag{3.16b}$$

with $\xi_{ij} \equiv \langle\!\langle \rho_i | \rho_j \rangle\!\rangle - 1/N$ and $N = \dim\{\mathcal{H}\}$. Their derivatives with respect to the states read

$$\nabla_{\rho_1} d_{\mathrm{angle}}(\rho_1, \rho_2) = -\frac{2}{\pi^2}\arccos\left(\frac{\xi_{12}}{\sqrt{\xi_{11}\xi_{22}}}\right)\frac{\rho_2 - \frac{\xi_{12}}{\xi_{11}}\rho_1}{\sqrt{\xi_{11}\xi_{22} - \xi_{12}^2}}, \tag{3.17a}$$

$$\nabla_{\rho_1} d_{\mathrm{length}}(\rho_1, \rho_2) = \frac{2N}{N-1}\frac{\sqrt{\xi_{11}} - \sqrt{\xi_{22}}}{\sqrt{\xi_{11}}}\rho_1. \tag{3.17b}$$

Note that the normalization is chosen such that $d_{\mathrm{angle}}, d_{\mathrm{length}} \in [0, 1]$. Combining both measures allows to build the new distance measure,

$$d_{\mathrm{split}}(\rho_1, \rho_2) = \alpha_1 d_{\mathrm{angle}}(\rho_1, \rho_2) + \alpha_2 d_{\mathrm{length}}(\rho_1, \rho_2), \tag{3.18}$$

where $\alpha_1, \alpha_2 \geq 0$, $\alpha_1 + \alpha_2 = 1$, are numerical parameters that allow to weight the contributions individually while ensuring $d_{\mathrm{split}} \in [0, 1]$. Like the Hilbert-Schmidt distance d_{HS}, the minimum, $d_{\mathrm{split}} = 0$, can be reached iff $\rho_1 = \rho_2$ and d_{split} thus fulfills Eq. (3.3). However, compared to d_{HS}, it provides some conceptual advantages. It naturally allows to

resolve the mismatch into an angle or length mismatch and thus provides information on the actual origin of the mismatch. This can be especially informative as it corresponds to the coherent (i.e., angle) or dissipative (i.e., length) mismatch of the states, respectively, and tells the user whether the optimization has difficulties to match the angle or the purity of the time-evolved state with its corresponding target. Moreover, it allows to weight the contributions individually within an optimization and thus to set the importance of their individual minimization. The latter can also be automatized within an optimization by dynamically adjusting the two weights α_1 and α_2 after each iteration, e.g. via

$$\alpha_1^{(i+1)} = \frac{d_{\text{angle}}^{(i)}}{d_{\text{angle}}^{(i)} + d_{\text{length}}^{(i)}}, \qquad \alpha_2^{(i+1)} = \frac{d_{\text{length}}^{(i)}}{d_{\text{angle}}^{(i)} + d_{\text{length}}^{(i)}}. \tag{3.19}$$

This effectively causes the dominating term from iteration i to become preferentially minimized within the next iteration $i+1$. For an optimization algorithm, this implies that a different functional is optimized in each iteration. However, for Krotov's method, this still yields better convergence as though the same functional with fixed weights is used in each iteration [103]. In fact, it is straightforward to generalize this numerical trick of regularly updating weights to any functional consisting of multiple terms, holding the promise for a similar speedup in convergence.

So far we have used this geometric picture to construct a distance measure for two states $\rho_1, \rho_2 \in \mathcal{S}_{\mathcal{H}}$, where one of the states is typically the target state in an optimization while the other is the respective time-evolved initial state. However, the underlying geometric picture can be applied beyond the scope of a state-to-state optimization. To this end, we can write the generalized Bloch vector $\boldsymbol{r} = (r_1, \ldots, r_{N^2-1})^\top \in \mathbb{R}^{N^2-1}$, corresponding to a state ρ, in terms of the generalized spherical coordinates ($K = N^2 - 1$),

$$\begin{aligned}
r_1 &= r\cos(\phi_1),\\
r_2 &= r\sin(\phi_1)\cos(\phi_2),\\
r_3 &= r\sin(\phi_1)\sin(\phi_2)\cos(\phi_3),\\
&\vdots\\
r_{K-1} &= r\sin(\phi_1)\sin(\phi_2)\cdot\cdots\cdot\cos(\phi_{K-1}),\\
r_K &= r\sin(\phi_1)\sin(\phi_2)\cdot\cdots\cdot\sin(\phi_{K-1}),
\end{aligned} \tag{3.20}$$

where the set $\{r, \phi_1, \ldots, \phi_{K-1}\}$ uniquely determines the state ρ. Conversely, given the

coefficients $r_1, \ldots, r_K$, the spherical representation can be obtained via

$$\begin{aligned}
r &= \sqrt{r_1^2 + \cdots + r_K^2}, \\
\phi_1 &= \arccos\left(\frac{r_1}{\sqrt{r_1^2 + \cdots + r_K^2}}\right), \\
\phi_2 &= \arccos\left(\frac{r_2}{\sqrt{r_2^2 + \cdots + r_K^2}}\right), \\
&\vdots \\
\phi_{K-2} &= \arccos\left(\frac{r_{K-2}}{\sqrt{r_{K-2}^2 + r_{K-1}^2 + r_K^2}}\right), \\
\phi_{K-1} &= 2\mathrm{arccot}\left(\frac{r_{K-1} + \sqrt{r_{K-1}^2 + r_K^2}}{x_K}\right).
\end{aligned} \tag{3.21}$$

Since $r_i = \langle\!\langle \rho | \mathsf{A}_i \rangle\!\rangle$ with $i = 1, \ldots, N^2 - 1$ and A_i a Hermitian matrix, cf. Eq. (3.8), it is straightforward to evaluate the gradient of r_i with respect to ρ analytically, which yields $\nabla_\rho r_i = \mathsf{A}_i$. Hence, the entire derivation of $\boldsymbol{r}$ with respect to ρ can be done accordingly. Therefore, the spherical representation can be easily used in order to formulate an optimization functional targeting a complicated subspace of the Bloch sphere. Such a functional reads

$$\mathcal{J}_{\mathrm{bloch}}[\rho] = \alpha_0 \underbrace{\lambda_0 \left(r - r^{\mathrm{trgt}}\right)^2}_{d_0(\rho)} + \alpha_1 \underbrace{\lambda_1 \left(\phi_1 - \phi_1^{\mathrm{trgt}}\right)^2}_{d_1(\rho)} + \cdots + \alpha_{K-1} \underbrace{\lambda_{K-1} \left(\phi_{K-1} - \phi_{K-1}^{\mathrm{trgt}}\right)^2}_{d_{K-1}(\rho)}, \tag{3.22}$$

where each λ_k ensures that the respective measure d_k is normalized to $[0, 1]$ and the additional weights $\alpha_k \geq 0$ with $\sum_k \alpha_k = 1$ ensure $\mathcal{J}_{\mathrm{bloch}}[\rho] \in [0, 1]$. An optimization towards a subspaces of the Bloch sphere would simply require to define the geometric parameters of that subspace by defining its target radius and/or angles and set the weights for all irrelevant coefficients to zero. With such a functional we can, for instance, optimize towards an arbitrary state on the equator of the Bloch sphere. More sophisticated targets are of course conceivable. In case of all weights being non-zero, i.e., $\alpha_k > 0$ for all k, the optimization targets a single state and is conceptually equivalent to d_{split} in its action. Hence, Eq. (3.22) can be viewed as a generalization of d_{split}. Technically, it can be even further generalized to any optimization problem where the optimization target is a

subspace of a general hyperball (not necessarily the Bloch sphere). The only requirement for this to work is that the function, that maps the state ρ to a vector $(r_1, r_2, \dots)^\top$ in this hyperball, and that vector to a real number (the functional value), must remain derivable with respect to the states, i.e., each r_i must remain derivable with respect to ρ.

3.4 Generation of Mixed State Squeezing in Cavity Optomechanics

In this last section, we will use optimal control to accelerate the preparation of a mixed, squeezed state. It is an excellent example to highlight the importance of reliable optimization functionals and, besides, also constitutes an interesting physical control problem in itself. We start with motivating and introducing the physical context.

We will consider a system consisting of a mechanical mode, e.g. a mechanical resonator, which is coupled to an optical mode, e.g. an optical cavity, via radiation pressure. This fairly general setting is at the heart of cavity optomechanics [117, 118], which is a prominent field to explore e.g. quantum-enhanced sensing — one of the key endeavors of quantum metrology. Although quantum-enhanced sensing can be realized in multiple ways [119, 120], squeezed states play an important role as they allow to substantially increase the sensitivity of the sensing protocols [121, 122] and detectors, e.g. for the detection of gravitational waves [123, 124]. While squeezed states can in general be generated on a variety of physical platforms [125], cavity optomechanics in combination with driven-dissipative evolutions constitute a very promising combination in that respect. In a nutshell, the fundamental idea of driven-dissipative evolutions is to apply constant driving fields to the system such that the system's driven steady state coincides with the desired target state [126]. Such a strategy is advantageous as it is inherently robust against dissipation and is therefore favorable in view of experimental feasibility. It can be used for preparing all kinds of non-classical states [19, 127–133]. Nevertheless, since quantum reservoir engineering utilizes dissipation in order to drive the system's state into the desired target state, it also depends intrinsically on the time scale of the dissipation. This time scale can be long and hence causes the state preparation to be slow. In our example from cavity optomechanics, the interplay of two constant drives and the system's dissipation allows to engineer a strongly squeezed steady state by virtue of choosing the amplitudes and frequencies of two continuous-wave (cw) fields appropriately [134, 135]. Due to the non-zero temperature of the environment, this steady state will be mixed. Since we want to accelerate the preparation of this state by means of optimal control, it requires an optimization with a mixed target state. It therefore constitutes an excellent

example to apply and examine the performance of d_{split} that has been introduced in Sec. 3.3.

3.4.1 Model and Control Problem

In the following, we consider an optomechanical system consisting of an optical cavity and a mechanical resonator that couple via radiation pressure. The cavity interacts with two driving fields. The Hamiltonian describing such a system reads [134]

$$\mathsf{H}(t) = \omega_{\text{cav}}\mathsf{a}^\dagger\mathsf{a} + \Omega\mathsf{b}^\dagger\mathsf{b} - g_0\mathsf{a}^\dagger\mathsf{a}\left(\mathsf{b}+\mathsf{b}^\dagger\right) + \left[\left(\alpha_+ e^{-\mathrm{i}\omega_+ t} + \alpha_- e^{-\mathrm{i}\omega_- t}\right)\mathsf{a}^\dagger + \text{H.c.}\right], \tag{3.23}$$

where ω_{cav} and Ω are the frequencies of the optical cavity and mechanical oscillator, respectively, and g_0 is their coupling strength. Moreover, $\alpha_\pm$ and $\omega_\pm$ are the amplitudes and frequencies of the two driving fields that exclusively interact with the cavity. a and b are the photon and phonon annihilation operators for the optical and mechanical mode, respectively. The Hamiltonian can be simplified by first applying the displacement transformation $\mathsf{a} \to \mathsf{a} + \bar{\alpha}_+ e^{-\mathrm{i}\omega_+ t} + \bar{\alpha}_- e^{-\mathrm{i}\omega_- t}$ and secondly assuming the two drives to satisfy $\omega_\pm = \omega_{\text{cav}} \pm \Omega$. The latter implies that the two control fields drive a red (ω_-) and blue (ω_+) detuned sideband of the cavity with the detuning given by the resonator's frequency Ω. In the interaction picture and linearized regime, the resulting Hamiltonian takes the simple form [134]

$$\mathsf{H}(t) = -\left[\mathsf{a}^\dagger\left(G_+\mathsf{b}^\dagger + G_-\mathsf{b}\right) + \text{H.c.}\right] - \left[\mathsf{a}^\dagger\left(G_+\mathsf{b}e^{-2\mathrm{i}\Omega t} + G_-\mathsf{b}^\dagger e^{2\mathrm{i}\Omega t}\right) + \text{H.c.}\right], \tag{3.24}$$

where $G_\pm$ are the effective optomechanical coupling rates corresponding to the red (ω_-) and blue (ω_+) detuned sideband drives. Note that, in the following, we will ignore the counter-rotating terms in Eq. (3.24), as we will never explore parameter regimes where they become relevant. In order to take the environment into account, three Lindblad operators are required [134],

$$\mathsf{L}_1 = \sqrt{\kappa}\mathsf{a}, \tag{3.25a}$$

$$\mathsf{L}_2 = \sqrt{\Gamma_{\text{M}}\left(n_{\text{th}}+1\right)}\mathsf{b}, \tag{3.25b}$$

$$\mathsf{L}_3 = \sqrt{\Gamma_{\text{M}} n_{\text{th}}}\mathsf{b}^\dagger, \tag{3.25c}$$

with κ and Γ_{M} the photon and phonon decay rates of the optical and mechanical mode and n_{th} the thermal occupation of the latter, cf. Eq. (2.16). Note that the decay rates, termed γ_k in Eq. (2.12), have been absorbed into the Lindblad operators here. The total physical setup of optical and mechanical mode, the two control fields and the environment

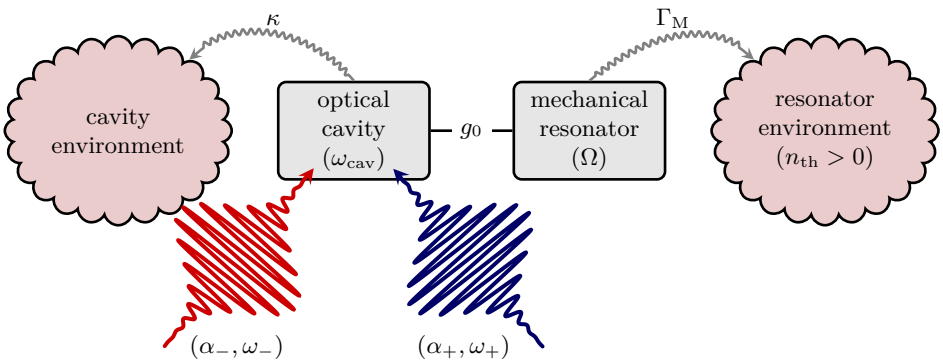

Figure 3.3: Sketch of the optomechanical system, which is given by an optical cavity (with frequency ω_{cav}) that couple with strength g_0 to a mechanical resonator (with frequency Ω), while both are interacting with their respective environments (with decay rates κ and Γ_{M}, respectively). The cavity is furthermore driven by two laser fields (with amplitudes $\alpha_\pm$ and frequencies $\omega_\pm$).

is sketched in Fig. 3.3.

The key idea of the driven-dissipative protocol is that if the time-independent (effective) amplitudes $G_\pm$ of the two driving fields are chosen appropriately, it allows to generate a strongly squeezed state of the mechanical mode in the steady state limit. To this end, it should be noted that the system's steady state ρ^{th} will be approached from every initial state, i.e., $\rho(t_0) \to \rho^{\mathrm{th}}$ for $t \to \infty$ for all $\rho(t_0)$. However, note that ρ^{th} will depend on $G_\pm$. In detail, by appropriately choosing G_- and the relative strength $G_+/G_- < 1$, a squeezed thermal steady states of the mechanical resonator is generated. The reduced state $\rho_{\mathrm{res}}^{\mathrm{th}} = \mathrm{tr}_{\mathrm{cav}}\left\{\rho^{\mathrm{th}}\right\}$ of the mechanical resonator can be calculated by tracing out the optical cavity. Its squeezing strength is quantified by the expectation value $\langle \mathsf{X}_1^2 \rangle$ of the mechanical quadrature $\mathsf{X}_1 = (\mathsf{b} + \mathsf{b}^\dagger)/\sqrt{2}$. Interestingly, it has been observed in Ref. [134] that larger squeezing of $\rho_{\mathrm{res}}^{\mathrm{th}}$ is usually accompanied by a decrease in purity and vice versa. The purity of the joint system's steady state ρ^{th} depends, besides $G_\pm$, on κ, Γ_{M} and n_{th}. In cavity optomechanics, the joint effect of these parameters is typically captured by a single quantity — the cooperativity $\mathcal{C} = 4G_-^2/(\kappa\Gamma_{\mathrm{M}})$. It serves as an important figure of merit for any optomechanical system and quantifies the exchange of photons and phonons, i.e., the coupling between optical cavity and mechanical resonator [117, 136].

We are interested in minimizing the time T it takes to reach, with sufficient accuracy, the mixed steady state ρ^{th} — our target state in the following optimizations. On the one hand, we know that T is determined by the dissipation rates and the distance of the initial state $\rho(t_0)$ from ρ^{th}. On the other hand, however, in the time-independent protocol proposed in Ref. [134], T is also determined to a large extent by the cooperativity $\mathcal{C}$ and

the optomechanical coupling rates $G_\pm$. Thus, we can take the intensities of the blue and red sideband drives to be controllable, which is experimentally easy to realize and results in time-dependent, effective coupling rates $G_\pm(t)$. While, for the sake of simplicity, we will directly optimize $G_\pm(t)$ instead of the actual time-dependent field intensities that give rise to them, the latter can always be calculated given $G_\pm(t)$.

A simple, yet sufficient final-time functional for this control problem, i.e., the preparation of the steady state ρ^{th}, is given by

$$\mathcal{J}_T\left[\rho, T\right] = d\left(\rho^{\text{th}}, \rho(T)\right), \tag{3.26}$$

where d needs to be a reliable distance measure between the time-evolved state $\rho(T)$ and the target state ρ^{th}, i.e., d needs to satisfy Eq. (3.3). Since the target state ρ^{th} is mixed and we we will use Krotov's method to minimize d, this leaves us with two reliable choices for d — namely the Hilbert-Schmidt distance d_{HS}, cf. Eq. (3.14), and the newly constructed measure d_{split}, cf. Eq. (3.18). In the following we will use these two reliable distance measures and compare them in terms of the physical solutions they yield and their general numerical performance. However, we will also use the unreliable measures d_{re} and d_{sm} from Eq. (3.5) in order to demonstrate their failure. Since we are moreover interested in accelerating the approach towards ρ^{th}, we will also check how the control solutions change when we decrease T. For the optimization we will use Krotov's method as described in Subsec. 2.3.5.

3.4.2 Speeding Up the Approach towards the Steady State

We take the initial state $\rho(t_0) = \rho_{\text{cav}}(t_0) \otimes \rho_{\text{res}}(t_0)$ of the bipartite system to be a product state of the thermal equilibrium states of cavity and resonator, respectively. For the cavity, this amounts to the ground state $\rho_{\text{cav}}(t_0) = |0\rangle\langle 0|$, whereas the initial state of the resonator is characterized by the resonator's thermal occupancy $n_{\text{th}} = [\exp\{\beta\Omega\} - 1]^{-1}$ via $\rho_{\text{res}}(t_0) = \exp\{-\beta\Omega \mathsf{b}^\dagger \mathsf{b}\}/Z$, where Z is the partition function. We assume $n_{\text{th}} = 2$ in the following. The remaining parameters are given by $\kappa/2\pi = 450\,\text{kHz}$ and $\Gamma_M/2\pi = 3\,\text{Hz}$ and taken from the experiment reported in Ref. [135]. Furthermore, we choose G_+ and G_- such that $\mathcal{C} = 100$ and $G_+/G_- = 0.7$, since this yields a steady state that shows a good trade-off between the steady state's squeezing strength and mixedness. With this choice, it takes roughly $T \approx 15\,\text{ms}$ to get sufficiently close to the actual steady state ρ^{th} and, in terms of squeezing strength, this leads to $\langle \mathsf{X}_1^2\rangle / \langle \mathsf{X}_1^2\rangle_{\text{ZPF}} \approx 0.27$. The index ZPF denotes the zero-point fluctuations, which coincide with the squeezing strength of the ground state. Values of $\langle \mathsf{X}_1^2\rangle / \langle \mathsf{X}_1^2\rangle_{\text{ZPF}}$ below 0.5 correspond to squeezing strengths

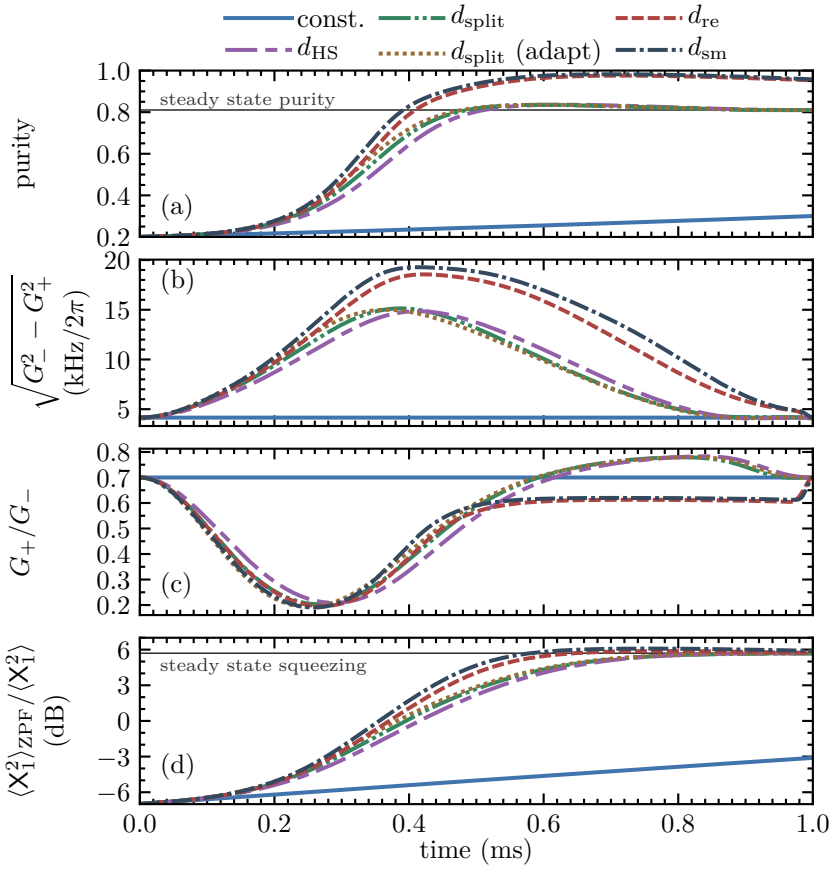

Figure 3.4: Comparison of the time evolution obtained with constant (blue solid lines) and optimized drives, using the target functionals indicated in the legend, cf. Eqs. (3.5), (3.14) and (3.18). (a) Joint state purity, (b) and (c) optimized field shapes, (d) squeezing $\langle X_1^2\rangle$ in units of the zero-point fluctuations $\langle X_1^2\rangle_{\mathrm{ZPF}}$. "$d_{\mathrm{split}}$ (adapt)" represents an optimization using an adaptive choice for the weights of angle and length, cf. Eq. (3.19).

beyond the relevant 3 dB limit and therefore to a regime where interesting effects can be observed [137–139].

Figure 3.4 compares the dynamics of the time-independent protocol with constant drives (blue solid lines) to those induced by optimized drives for a total time of $T = 1$ ms. For the sake of comparison, several target functionals, i.e., distance measures d, have been employed in the optimization. While d_{HS} and d_{split} are reliable distance measures even in case of mixed state targets, d_{re} and d_{sm} are not reliable. However, we still use and show them here in order to highlight their failure and emphasize the importance of reliability for the distance measure d. The joint state purity and resonator squeezing are analyzed in Fig. 3.4(a) and (d), respectively. Moreover, while Fig. 3.4(b) shows the difference $\sqrt{G_-^2(t) - G_+^2(t)}$, which determines an effective cooling rate into the squeezed

state, Fig. 3.4(c) shows the ratio $G_+(t)/G_-(t)$, which effectively determines the squeezing strength of the final steady state, cf. Ref. [134]. Fields optimized using d_{HS} or d_{split} result in an acceleration of the thermalization process, cf. the blue solid vs. purple double-dashed, brown dotted and green dashed-double dotted lines in Fig. 3.4(a). These lines all converge to the correct joint state purity — in contrast to those optimized with d_{re} and d_{sm}. Similarly, the resonator squeezing reaches the desired value for the corresponding curves in Fig. 3.4(d) and does so significantly faster for all optimized fields.

Figure 3.4(b) and (c) unravel the control strategy behind this acceleration. It consists, independently on the actual target functional, in an increase of the effective cooling rate $\sqrt{G_-^2(t) - G_+^2(t)}$ in order to speed up the transition into the squeezed target state. One might naively argue that ramping up G_- and G_+ is always beneficial as it accelerates the coherent part of the dynamics due to an increase of the Hamiltonian's norm, cf. Eq. (3.24). However, ramping up the coupling also changes the steady state of the driven-dissipative dynamics and thus the target in our optimization. Hence, the increase of $\sqrt{G_-^2(t) - G_+^2(t)}$, which is primarily achieved by an increase of $G_-(t)$, needs to be balanced by a modulation of $G_+(t)/G_-(t)$ to ensure steering the system towards the correct target state. Interestingly, the optimizations with both d_{HS} (purple double-dashed lines) and d_{split} (green dashed-double dotted and brown dotted lines) find almost identical control fields. This is not at all guaranteed due to the typical non-uniqueness of control solutions and different control landscapes that each measure gives rise to.

From an experimental perspective, it should be noted that the optimized control fields of Fig. 3.4(b) and (c) only require a slow modulation of the drive amplitudes while their frequencies are kept constant. This makes them experimentally easily feasible with existing technology such as arbitrary waveform generators that allow amplitude modulations on timescales down to sub-nanoseconds [140] and even significantly more complex field shapes [141].

Figure 3.5(a) provides a closer look at the asymptotic squeezing dynamics of Fig. 3.4(d), showing that only fields optimized with d_{HS} and d_{split} reach the correct squeezing at final time T, cf. the purple double-dashed and brown dotted lines. In contrast, the fields optimized with d_{re} and d_{sm} (red dashed and dark blue dot-dashed lines in Fig. 3.4) fail to steer the system towards a state with the correct squeezing and purity. Instead, they act so as to increase the purity at final time T as much as possible, albeit failing to reach completely pure states which are not attainable at finite temperature ($n_{\mathrm{th}} > 0$). Figures 3.4 and 3.5(a) thus illustrate that the target functionals d_{re} and d_{sm} should not be used for mixed target states and emphasize the requirement to employ reliable functionals.

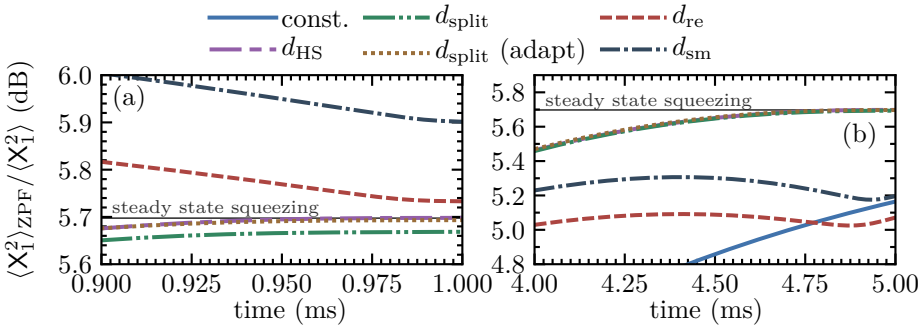

Figure 3.5: (a) The relevant part of the squeezing dynamics as shown in Fig. 3.4(d). (b) A similar dynamics as in (a) but for a different optimization with final time $T = 5\,\mathrm{ms}$.

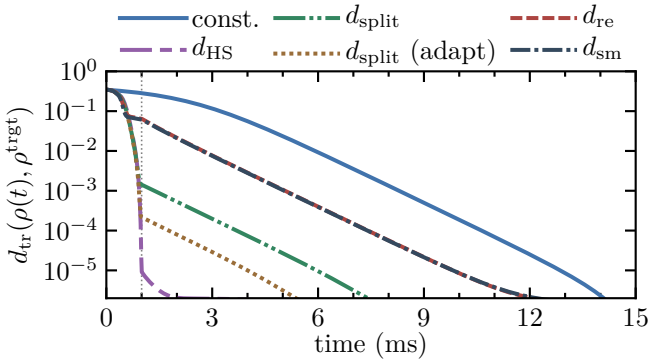

Figure 3.6: Dynamics of the trace distance d_{tr}, cf. Eq. (6.2), under the guess and optimized fields of Fig. 3.4. Beyond $T = 1\,\mathrm{ms}$ (indicated by the vertical line) all optimized fields are extended by the constant fields of the original, time-independent protocol.

Interestingly, the dynamics shown in Fig. 3.5(a) all result in a comparable amount of squeezing with the final values $\langle X_1^2\rangle / \langle X_1^2\rangle_{\mathrm{ZPF}}$ obtained with d_{re} and d_{sm} even below the intended steady state squeezing of roughly 0.27, cf. the red dashed and dark blue dot-dashed lines in Fig. 3.5(a). This indicates a larger squeezing to be possible than the one set by the steady state with its corresponding trade-off between squeezing and purity. These apparently "good" optimization results with respect to the final-state squeezing obtained with d_{re} and d_{sm} in Fig. 3.5(a) can most likely be explained by the fact that squeezing of any state is mainly determined by the direction of its Bloch vector on the generalized Bloch sphere rather than its lengths. Therefore, the optimization seems to benefit from the fact that d_{re} and d_{sm} still try to match the final state directions. However, this is not always the case, as illustrated in Fig. 3.5(b) showing the squeezing dynamics for a similar optimization as in Fig. 3.4 but with a final time of $T = 5\,\mathrm{ms}$.

If the state preparation errors obtained with the optimized fields after $T = 1\,\mathrm{ms}$ are not yet sufficient, one might ask whether it is possible to continue approaching the steady

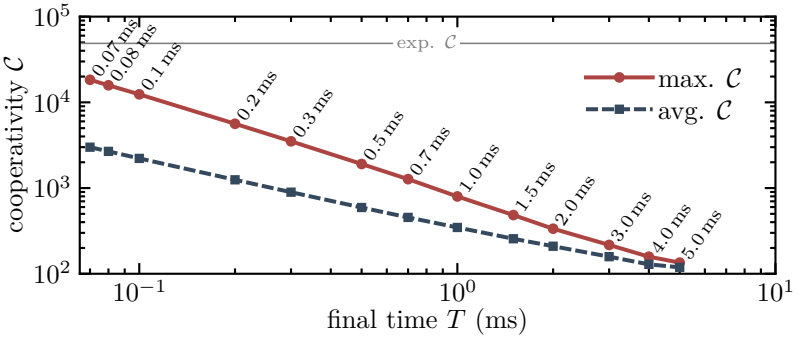

Figure 3.7: Peak and average cooperativity $\mathcal{C}$, calculated from the optimized fields $G_-(t)$, required to achieve a state preparation error of at most $d_{\mathrm{tr}} < 10^{-4}$, as function of the total optimization time T (employing d_{HS} for all optimizations). The horizontal line indicates the static cooperativity used in the experiment reported in Ref. [135].

state using the original protocol of constant drives [134]. This is demonstrated in Fig. 3.6, which shows the evolution of the trace distance d_{tr}, cf. Eq. (6.2), under the constant drives and optimized fields from Fig. 3.4(b) and (c), if the driving fields are switched back to the constant drives at $T = 1\,\mathrm{ms}$. In that case, we observe that d_{tr} continues to decrease for times larger than the switching time $T = 1\,\mathrm{ms}$, i.e., the final time used in the optimization. A monotonous decrease of d_{tr} after the switching time, as observed in Fig. 3.6, is expected for the fields optimized with d_{split} and d_{HS}, as they are both reliable for the considered optimization task. Form a mathematical perspective, this does not need to be the case for the fields optimized with d_{re} or d_{sm}, as these two measures are not reliable to quantify the distance towards the target state. Nevertheless, at the switching time $T = 1\,\mathrm{ms}$, we observe an improvement of d_{tr} with respect to the intended steady state for all states — independent on the distance measure d used in the optimization — and observe that d_{tr} continues to improve in all cases under constant drives, as we would expect for an asymptotic behavior. Figure 3.6 thus provides an alternative illustration of the speedup in preparing the squeezed steady state.

Figure 3.7 illustrates by how much the approach of the steady state can be accelerated. The price for speedup is cooperativity, or, in other words, drive intensity. It shows the peak and average cooperativity $\mathcal{C}$, determined by the optimized field $G_-(t)$, as a function of the total optimization time T. Given an experimental bound on the feasible cooperativity $\mathcal{C}$, one can thus easily determine the required time T to reach the target state. Taking the experimental value of the cooperativity reported in Ref. [135], we observe a speedup of at least two orders of magnitude compared to the original protocol employing constant drives [134]. Conversely, fixing a certain duration T determines the required cooperativity or drive power. Durations as short as $T = 0.07\,\mathrm{ms}$ are feasible,

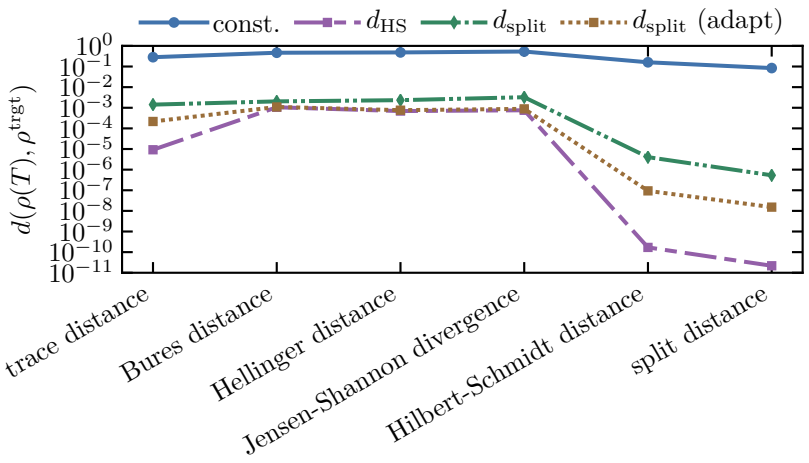

Figure 3.8: Comparison between changes in various distance measures, cf. Eqs. (6.2)-(3.14) and Eq. (3.18), under optimization with d_{HS} and d_{split}, cf. Fig. 3.4.

while the state preparation errors, i.e., distance to the actual steady states, are still sufficiently small with $d_{\mathrm{tr}} < 10^{-4}$ for all points in Fig. 3.7. Moreover, the optimized field shapes corresponding to the data from Fig. 3.7 all look quite similar to the ones presented in Fig. 3.4(b) and (c). Both peak and average cooperativity of the optimized field increase with decreasing duration T, as one would expect for reaching the same target in less time. We observe an almost perfect power law dependence of the cooperativity $\mathcal{C}$ as a function of the duration T. This power law scales similarly as the intrinsic scaling of the system due to its non-linearity, which suggests the latter to be the defining feature even in the case of time-dependent and optimized drives, cf. Ref. [103].

At last, Fig. 3.8 compares the value of several reliable distance measures for the final state obtained with the fields optimized using d_{HS} and d_{split} and with constant driving. The latter thus corresponds to the non-optimized, i.e., guess, values. Inspection of Fig 3.8 shows that all measures decrease under optimization with d_{HS} and d_{split} with the Hilbert-Schmidt distance (purple double-dashed line) yielding the smallest state preparation errors for itself as well as all other distance measures. While the smallest value of the Hilbert-Schmidt distance correctly indicates the smallest *physical* state preparation error, the *absolute* value of any distance measure d, or, to be more general, of a any functional $\mathcal{J}_T$, does not necessarily say much about how well the dynamics actually performs. For instance, if $d \in [0, 1]$ is a reliable distance measure for any physical process so is $d^2 \in [0, 1]$ and the latter will naturally yield smaller values despite describing identical physical results. While this might appear trivial from a mathematical point of view, it is an important fact to keep in mind when assessing optimization results. In that respect,

Fig 3.8 provides another important insight. Upon minimizing d_{HS} and d_{split}, all other distance measures are minimized as well. Although this seems intuitive, it does not need to hold in general. For instance, if $d(\rho_2, \rho^{\mathrm{trgt}}) > d(\rho_1, \rho^{\mathrm{trgt}}) > 0$ holds for two states ρ_1, ρ_2, a desired target state ρ^{trgt} and a reliable measure d, it does not imply the same to hold for another measure d'. In other words, two reliable measures can still disagree on which of the two states ρ_1, ρ_2 is closer to the target ρ^{trgt} even though both correctly assess when a state becomes identical to the target. However, Fig. 3.8 demonstrates that it is usually a good assumption to expect any reliable distance measures to decrease in the process of minimizing another. Conceptually, this constitutes an important example for optimal control as it demonstrates that it is sometimes worth exploring auxiliary quantities that are related to the quantity that should be optimized in the first place but which can not be expressed via a functional and therefore not directly optimized.

In conclusion, the results in this chapter have shown that care needs to be taken when choosing an optimization functional — especially when optimizing towards mixed target states. To this end, we have introduced a new, reliable distance measure d_{split}, where we have employed the geometric picture of the Bloch sphere. In addition, this new measure is designed such as to be compatible with gradient-based optimization technique. It has been successfully used to accelerate the preparation of a mixed squeezed state in cavity optomechanics. However, in this particular example, it has not shown, better performance compared to the Hilbert-Schmidt distance d_{HS}.

4

Identification of Decoherence-Free Subspaces via Optimal Control

Beating dissipation is one of the toughest yet most important challenges for quantum technologies [6]. The presence of a detrimental but ubiquitous environment renders the dynamics of any quantum device non-unitary and causes it to lose its quantum properties over time, thus causing it to behave classical. The problem to counteract the environment's impact can be tackled in several ways. A quite natural and straightforward approach is to shield the device from any unwanted interaction as best as possible. One possibility to achieve this is to appropriately engineer the device and its materials. For instance, this has been successfully achieved for superconducting devices [142–146], spin-based platforms [147–149] as well as trapped ions [150, 151] to name a few examples. However, besides improvements originating from better physical properties of the device, also quantum control techniques can assist in improving the coherence time. Dynamical decoupling, for instance, decreases the effective coupling strength between the device and its environment and thus helps boosting the coherence times substantially [152–154].

Although all of these methods are crucial in minimizing dissipation, none of them can completely avoid it and thus give rise to truly unitary dynamics. Hence, some environmental interaction and induced errors will always prevail. Therefore, an approach taking this into account is given by quantum error correction (QEC), which accepts the remaining errors as being unavoidable in the first place and then thinks about ways

to correct them upon occurrence [2, 155]. To this end, QEC relies crucially on error syndrome measurements, i.e., ways to detect errors non-invasively without affecting the stored quantum information. The syndrome measurements tell if and which kind of error occurred such that it can be corrected subsequently. The general feasibility of QEC has already been demonstrated in practice, initially for NMR [156] and later also for e.g. superconducting qubits [157, 158], trapped ions [159, 160] and NV centers in diamond [161, 162]. Unfortunately, these QEC schemes typically require a severe overhead of physical resources and an error rate below a certain threshold [163] — both of which is still challenging for current quantum information platforms [6].

Decoherence-free subspaces (DFSs) are another prominent concept for avoiding dissipation [164, 165]. Their main idea is to identify unitary, i.e., decoherence-free, subspaces in the total Hilbert space of the device and subsequently use these subspaces for encoding information and performing operations. Unfortunately, the task to determine whether a DFS exists at all or its particular form is a non-trivial problem. Their existence typically originates form symmetries in the system-environment interaction, where these symmetries cause errors to cancel each other advantageously within certain subspaces. DFSs have been experimentally confirmed with photons [166–168] and trapped ions [169] shortly after their initial prediction [164, 165] and later also for e.g. quantum dots [170] and NV centers [23]. However, while they are excellent memories for quantum information [169, 171], implementing quantum gates within any DFS, i.e., exploit them for e.g. quantum computing and other related quantum technologies, requires special care [172–176].

In order to present a simple example and get some intuitive understanding of DFSs, let us consider a qubit with Hamiltonian $\mathsf{H} = \sigma_z$ embedded in an environment that gives rise to pure dephasing described by the Lindblad operator $\mathsf{L} = \sigma_z$, cf. Eq. (2.13). This system has two separate DFSs, namely both the ground and excited state, $|0\rangle$ and $|1\rangle$. This is because both $|0\rangle\langle 0|$ and $|1\rangle\langle 1|$ are invariants of the dynamics and thus evolve unitarily. In contrast, each superposition $|\Psi\rangle\langle\Psi|$ with $|\Psi\rangle = \alpha|0\rangle + \beta|1\rangle$ evolves non-unitary as it loses its coherence and therefore becomes mixed over time. Albeit this model gives rise to two individual one dimensional DFSs, it is important to note that it does not have a two dimensional DFS, since this would require any state to evolve unitarily. In general, while the existence of an M dimensional DFS always implies the existence of at least M one dimensional DFSs, the converse statement does not hold in general as the example shows. Continuing with the example, by including environmentally induced cooling via the Lindblad operator $\mathsf{L} = \sigma_-$ it immediately follows that the excited state is no longer a DFS and only the ground state remains as DFS. If we would also include

environmentally induced heating via $\mathsf{L} = \sigma_+$, no DFS would exists anymore. However, especially for interacting multi qubit systems these relaxation and dephasing processes can sometimes cancel each other favorably and therefore give rise to more complex DFSs than illustrated in this simple example.

In this chapter, we will focus on the identification of DFSs by means of optimal control. To this end, we start by introducing an optimization functional for DFSs in Sec. 4.1. Since we will search for subspaces in this chapter — and not for time-dependent control fields like in the rest of the thesis — we also need to find an appropriate parametrization for subspaces that is compatible with gradient-based optimal control. We will construct such a parametrization of arbitrary subspaces in Sec. 4.2 and subsequently explain how to use it within an optimization procedure in Sec. 4.3. We will then investigate the performance of the introduced method in Sec. 4.4, where we will apply it to multi qubit systems exposed to typical environmental noise. At last, Sec. 4.5 points out how the optimization procedure towards DFSs can be further generalized to also work for other subspaces, i.e., other than DFSs, which might be similarly interesting for quantum technologies.

4.1 Functionals for Decoherence-Free Subspaces

We start this chapter and section with the formal definition of decoherence-free subspaces.

Definition 4.1. *Let $\mathcal{H}$ be an N dimensional Hilbert space and $\mathfrak{L}_\mathcal{H}$ its corresponding Liouville space. Let $\mathcal{D}_{t,t_0}$ be the dynamical map within $\mathfrak{L}_\mathcal{H}$, i.e., $\mathcal{D}_{t,t_0} : \mathfrak{L}_\mathcal{H} \to \mathfrak{L}_\mathcal{H}; \rho(t_0) \mapsto \rho(t) = \mathcal{D}_{t,t_0}[\rho(t_0)]$. Let $\mathcal{H}' \subseteq \mathcal{H}$ be an $M \leq N$ dimensional subspace such that $\mathcal{H} = \mathcal{H}' \oplus \mathcal{H}'^{\perp}$ and let $\mathfrak{L}_{\mathcal{H}'}$ be its corresponding Liouville space. $\mathcal{H}'$ is called decoherence-free subspace (DFS) of the dynamics $\mathcal{D}_{t,t_0}$ if $\mathcal{D}_{t,t_0}[\mathfrak{L}_{\mathcal{H}'} \oplus 0] = \mathsf{U}_{t,t_0} \mathfrak{L}_{\mathcal{H}'} \mathsf{U}_{t,t_0}^\dagger \oplus 0$ for all $t \geq t_0$, where $0 \in \mathfrak{L}_{\mathcal{H}'^{\perp}}$ is the zero operation and $\mathsf{U}_{t,t_0} \in \mathrm{SU}(M)$ a time-evolution operator in $\mathcal{H}'$.*

In order to target a DFS in an optimization, we first need to introduce a reliable functional $\mathcal{J}_{\mathrm{dfs}}[\mathcal{H}']$ such that it reaches its extremum, i.e., maximum in the following, iff $\mathcal{H}' \subseteq \mathcal{H}$ is a DFS. In detail, this requires a reliable measure for unitarity within $\mathcal{H}'$.

The problem to formulate a DFS functional has first been tackled in Ref. [177] and we will thus briefly review the approach taken there. It is based on the following theorem [178].

Theorem 4.1. *Let $\{|\psi_1\rangle, \ldots, |\psi_M\rangle\}$ be a basis for subspace $\mathcal{H}' \subseteq \mathcal{H}$ of Hilbert space $\mathcal{H}$, where $M \leq N = \dim\{\mathcal{H}\}$ and $\mathcal{H} = \mathcal{H}' \oplus \mathcal{H}'^{\perp}$, and let $\mathfrak{L}_{\mathcal{H}'}$ and $\mathfrak{L}_\mathcal{H}$ be their respective Liouville spaces. The dynamical map $\mathcal{D}_{t,t_0} : \mathfrak{L}_\mathcal{H} \to \mathfrak{L}_\mathcal{H}$ gives rise to unitary evolution in $\mathcal{H}'$, respectively $\mathfrak{L}_{\mathcal{H}'}$, iff $\mathcal{D}_{t,t_0}$ maps the set $\mathcal{P} = \{|\psi_1\rangle\langle\psi_1| \oplus 0, \ldots, |\psi_M\rangle\langle\psi_M| \oplus 0\}$ of one*

dimensional projectors in $\mathfrak{L}_{\mathcal{H}'} \oplus 0$ *onto a set of one dimensional projectors in* $\mathfrak{L}_{\mathcal{H}'} \oplus 0$. *In addition, it needs to map the totally rotated projector* $|\psi_{\mathrm{tr}}\rangle\langle\psi_{\mathrm{tr}}| \oplus 0$ *in* $\mathfrak{L}_{\mathcal{H}'} \oplus 0$ *with* $|\psi_{\mathrm{tr}}\rangle = \frac{1}{\sqrt{M}} \sum_{m=1}^{M} |\psi_m\rangle$ *onto a one dimensional projector in* $\mathfrak{L}_{\mathcal{H}'} \oplus 0$.

This theorem provides a straightforward way to check unitarity in subspace $\mathcal{H}'$ under the dynamical map $\mathcal{D}_{t,t_0}$ by means of only evaluating the images of $M+1$ projectors. However, in order for $\mathcal{H}'$ to become an actual DFS, theorem 4.1 needs to hold for all times $t \geq t_0$. Based on theorem 4.1, two functionals, $\mathcal{J}_1, \mathcal{J}_2 \in [0,1]$, that become maximal iff $\mathcal{H}'$ is a DFS, have been formulated [177],

$$\mathcal{J}_1\left[\mathcal{H}'\right] = \min_t \left\{ \min_{m=1,\ldots,M+1} \{P_m(t)\} \right\}, \qquad \mathcal{J}_2\left[\mathcal{H}'\right] = \frac{1}{M+1} \sum_{m=1}^{M+1} \min_t \{P_m(t)\}, \tag{4.1}$$

where $\rho_m(t) = \mathcal{D}_{t,t_0}\left[|\psi_m\rangle\langle\psi_m| \oplus 0\right]$ and

$$P_m(t) = \mathrm{Tr}_{\mathcal{H}'}\left\{\rho_m^2(t)\right\} = \sum_{m=1}^{M} \left\langle \psi_m \middle| \rho_m^2(t) \middle| \psi_m \right\rangle \in [0,1] \tag{4.2}$$

measures the deviation of $\rho_m(t)$ from being a one dimensional projector within $\mathfrak{L}_{\mathcal{H}'} \oplus \rho$. Physically, this corresponds to measuring both loss of population from $\mathfrak{L}_{\mathcal{H}'}$ into $\mathfrak{L}_{\mathcal{H}'^{\perp}}$ as well as loss of purity within $\mathfrak{L}_{\mathcal{H}'}$. Although we will only start discussing parametrizations of $\mathcal{H}'$ in Sec. 4.2, it is already evident from the definition of the functionals in Eq. (4.1) that due to the minimum no analytical gradients of $\mathcal{J}_1$ or $\mathcal{J}_2$ can be calculated with respect to any set of states that parametrizes $\mathcal{H}'$. To overcome this issue, we will introduce a new functional that is compatible with gradient-based optimization techniques in the following.

Let $\{\sigma_1, \ldots, \sigma_{N^2}\}$ be a basis for Liouville space $\mathfrak{L}_{\mathcal{H}}$ and let $\hat{\mathcal{D}}_{t,t_0}$ be the superoperator matrix for the dynamical map $\mathcal{D}_{t,t_0}$, i.e., $(\hat{\mathcal{D}}_{t,t_0})_{nm} = \langle\!\langle \sigma_m | \mathcal{D}_{t,t_0}[\sigma_n] \rangle\!\rangle$, $m,n = 1,\ldots,N^2$. This gives rise to the measure [179]

$$\mathcal{J}_{\mathrm{unitary},t}\left[\mathcal{H}\right] = \frac{1}{N^2} \left\| \hat{\mathcal{D}}_{t,t_0} \right\|_2^2 = \frac{1}{N^2} \sum_{m,n=1}^{N^2} \langle\!\langle \sigma_m | \mathcal{D}_{t,t_0}\left[\sigma_n\right] \rangle\!\rangle^2, \qquad \left\| \hat{\mathcal{A}} \right\|_2 = \sqrt{\mathrm{tr}\left\{\hat{\mathcal{A}}\hat{\mathcal{A}}^{\dagger}\right\}}, \tag{4.3}$$

which yields, at maximum, $\mathcal{J}_{\mathrm{unitary},t} = 1$ iff $\mathcal{D}_{t,t_0}$ is unitary on $\mathfrak{L}_{\mathcal{H}}$, or, at minimum, $\mathcal{J}_{\mathrm{unitary},t} = 1/N^2$ for the completely depolarizing channel that maps every state to the completely mixed state. The latter can be interpreted as the most non-unitary dynamical map $\mathcal{D}_{t,t_0}$.

This measure can be straightforwardly generalized to arbitrary subspaces. Let $\{|\psi_1\rangle, \ldots, |\psi_M\rangle\}$ be a basis for subspace $\mathcal{H}' \subseteq \mathcal{H}$ and let $\{\lambda_1, \ldots, \lambda_{M^2}\}$ be a basis for its

corresponding Liouville space $\mathfrak{L}_{\mathcal{H}'}$. We can calculate the corresponding superoperator matrix $\hat{\mathcal{D}}'_{t,t_0}$ in this reduced space in the same sense as before and a unitary measure, defined as in Eq. (4.3), becomes (including normalization)

$$\mathcal{J}_{\text{unitary},t}\left[\mathcal{H}'\right] = \frac{1}{M^2}\left\|\hat{\mathcal{D}}'_{t,t_0}\right\|_2^2 = \frac{1}{M^2}\sum_{m,n=1}^{M^2}\left\langle\!\left\langle \lambda_m \oplus 0 | \mathcal{D}_{t,t_0}\left[\lambda_n \oplus 0\right]\right\rangle\!\right\rangle^2, \tag{4.4}$$

where $0 \in \mathfrak{L}_{\mathcal{H}'^{\perp}}$ is the zero operation. It yields $\mathcal{J}_{\text{unitary},t} = 1$ iff $\mathcal{D}_{t,t_0}$ is unitary in $\mathfrak{L}_{\mathcal{H}'}$, i.e., in the subspace $\mathcal{H}'$. However, note that its minimum changes to $\mathcal{J}_{\text{unitary},t} = 0$, since this reduced version of Eq. (4.3) also captures loss of population from $\mathfrak{L}_{\mathcal{H}'}$ into $\mathfrak{L}_{\mathcal{H}'^{\perp}}$.

Equations (4.3) and (4.4) are reliable measures for unitarity in $\mathfrak{L}_{\mathcal{H}}$ and $\mathfrak{L}_{\mathcal{H}'}$, i.e., in $\mathcal{H}$ and $\mathcal{H}'$, respectively. However, in order for Eq. (4.4) to be a reliable DFS functional, it needs to yield unitarity for all $t \geq t_0$. Hence, the final DFS functional reads

$$\mathcal{J}_{\text{dfs}}\left[\mathcal{H}'\right] = \frac{1}{T}\int_{t_0}^{T}\mathcal{J}_{\text{unitary},t}\left[\mathcal{H}'\right]\mathrm{d}t \in [0,1], \tag{4.5}$$

which yields $\mathcal{J}_{\text{dfs}}[\mathcal{H}'] = 1$ iff $\mathcal{H}'$ is a DFS and is strictly smaller otherwise. It should be noted that evaluation of $\mathcal{J}_{\text{dfs}}$ requires the propagation of M^2 states, which needs to be compared to the evaluation of $M+1$ states required for calculating $\mathcal{J}_1$ and $\mathcal{J}_2$ in Eq. (4.1). However, in contrast to $\mathcal{J}_1$ and $\mathcal{J}_2$, functional $\mathcal{J}_{\text{dfs}}$ is not only a reliable measure for unitarity in $\mathcal{H}'$ but also a reliable measure for non-unitarity. This is due to the fact that $\mathcal{J}_{\text{dfs}}$ decreases smoothly the more non-unitary the dynamics becomes. Conversely, $\mathcal{J}_1$ and $\mathcal{J}_2$ do not smoothly decrease when the dynamics becomes non-unitary, since none of them incorporates information from all states and all times due to the presence of the minimum in both definitions, cf. Eq. (4.1). As a consequence, the latter will cause the control landscape to become less smooth, which makes it harder for the optimization to find solutions. The fact that M^2 instead of $M+1$ states need to be propagated will not even be of relevance in practice as we will see in Sec. 4.3.

However, before proceeding, we will extend functional (4.5), respectively the unitarity measure of Eq. (4.4), to tensor Hilbert spaces. Let $\mathcal{H}$ be an $N = N_{\text{A}}N_{\text{B}}$ dimensional Hilbert space composed out of two subsystems (A and B with dimensions N_{A} and N_{B}, respectively) such that $\mathcal{H} = \mathcal{H}_{\text{A}} \otimes \mathcal{H}_{\text{B}}$. The task in the following will be to search for an $M_{\text{A}} \leq N_{\text{A}}$ dimensional subspace $\mathcal{H}'_{\text{A}} \subseteq \mathcal{H}_{\text{A}}$ in subsystem A. Hence, if $\mathcal{H}'_{\text{A}}$ is a DFS, every state $\rho_{\text{A}} \in \mathfrak{L}_{\mathcal{H}'_{\text{A}}}$ needs to evolve unitarily. Let $\mathcal{H}_{\text{A}} = \mathcal{H}'_{\text{A}} \oplus \mathcal{H}'^{\perp}_{\text{A}}$ and $\{|\psi_{\text{A},1}\rangle, \ldots, |\psi_{\text{A},M_{\text{A}}}\rangle\}$ be a basis for $\mathcal{H}'_{\text{A}}$ and let $\{\lambda_{\text{A},1}, \ldots, \lambda_{\text{A},M_{\text{A}}^2}\}$ be as basis for its corresponding Liouville space $\mathfrak{L}_{\mathcal{H}'_{\text{A}}}$. We have to distinguish between two possible scenarios. On the one hand, we may demand $\mathcal{H}'_{\text{A}}$ to be a DFS provided that subsystem B is initially in the specific state

$\rho_{\mathrm{B}}(t_0) \in \mathfrak{L}_{\mathcal{H}_{\mathrm{B}}}$. In that case, Eq. (4.4) becomes

$$\mathcal{J}_{\mathrm{unitary},t,\rho_{\mathrm{B}}(t_0)}\left[\mathcal{H}'_{\mathrm{A}}\right] = \frac{1}{M_{\mathrm{A}}^2}\sum_{m,n=1}^{M_{\mathrm{A}}^2}\left\langle\!\left\langle \lambda_{\mathrm{A},m}\oplus 0\middle|\mathrm{tr}_{\mathrm{B}}\left\{\mathcal{D}_{t,t_0}\left[\left(\lambda_{\mathrm{A},n}\oplus 0\right)\otimes\rho_{\mathrm{B}}(t_0)\right]\right\}\right\rangle\!\right\rangle^2, \quad (4.6)$$

where $0 \in \mathfrak{L}_{\mathcal{H}'^{\perp}_{\mathrm{A}}}$ is the zero operation and $\rho_{\mathrm{B}}(t_0)$ defines a parameter for the functional. This unitarity measure for $\mathcal{H}_{\mathrm{A}'}$ at time t can be turned into a functional for DFS by performing the integral over all times like in Eq. (4.5). This functional yields $\mathcal{J}_{\mathrm{dfs},\rho_{\mathrm{B}}(t_0)}[\mathcal{H}'_{\mathrm{A}}] = 1$ iff $\mathcal{H}'_{\mathrm{A}}$ is a DFS and subsystem B is initially in state $\rho_{\mathrm{B}}(t_0)$. In view of optimal control, $\rho_{\mathrm{B}}(t_0)$ can either be held fixed or be parametrized and optimized as well. In the latter case, an optimization would then try to optimize the parametrization of $\mathcal{H}'_{\mathrm{A}}$ in parallel to optimizing $\rho_{\mathrm{B}}(t_0)$. In other words, it searches for an appropriate initial state $\rho_{\mathrm{B}}(t_0)$ in subsystem B such that $\mathcal{H}'_{\mathrm{A}}$ becomes a DFS in subsystem A. On the other hand, a stricter choice would demand that $\mathcal{H}'_{\mathrm{A}}$ needs to be a DFS independent on the initial state $\rho_{\mathrm{B}}(t_0)$ of subsystem B. In that case, functional (4.6) needs to include an integral over all conceivable initial states $\rho_{\mathrm{B}}(t_0)$ and reads

$$\mathcal{J}_{\mathrm{unitary},t}\left[\mathcal{H}'_{\mathrm{A}}\right] = \frac{1}{M_{\mathrm{A}}^2}\sum_{m,n=1}^{M_{\mathrm{A}}^2}\int_{\rho_{\mathrm{B}}(t_0)\in\mathfrak{L}_{\mathcal{H}_{\mathrm{B}}}}\left\langle\!\left\langle \lambda_{\mathrm{A},m}\oplus 0\middle|\mathrm{tr}_{\mathrm{B}}\left\{\mathcal{D}_{t,t_0}\left[\left(\lambda_{\mathrm{A},n}\oplus 0\right)\otimes\rho_{\mathrm{B}}(t_0)\right]\right\}\right\rangle\!\right\rangle^2. \quad (4.7)$$

The assumption of separability in Eqs. (4.6) and (4.7) is reasonable, since we are only interested in pure states $\rho_{\mathrm{A}} \in \mathfrak{L}_{\mathcal{H}'_{\mathrm{A}}}$ which can therefore not be correlated to any state in $\mathfrak{L}_{\mathcal{H}_{\mathrm{B}}}$ at any time.

4.2 Subspace Parametrization

The maximization of Eq. (4.5), respectively Eq. (4.4), via optimal control requires a clever parametrization of the subspace $\mathcal{H}' \subseteq \mathcal{H}$, i.e., a clever parametrization of its basis states $\{|\psi_1\rangle, \ldots, |\psi_M\rangle\}$. The challenge for the parametrization is to choose it such that the change of any of its parameters will always maintain orthogonality and norm of all states, i.e., any change needs to preserve the mathematical structure of an orthonormal basis. Let $\{|e_1\rangle, \ldots, |e_N\rangle\}$ be a fixed basis for $\mathcal{H}$. Thus, every basis state $|\psi_m\rangle$, $m = 1, \ldots, M$, where $\mathrm{span}\{|\psi_1\rangle, \ldots, |\psi_M\rangle\} = \mathcal{H}'$, can be expanded in this basis,

$$|\psi_m(\alpha)\rangle = \sum_{n=1}^{N}\alpha_{m,n}|e_n\rangle, \qquad \alpha \in \mathbb{C}^{M\times N}. \quad (4.8)$$

If the basis $\{|\psi_1\rangle, \ldots, |\psi_M\rangle\}$, determined by the set of coefficients $\{\alpha_{m,n}\}$, is an orthonormal basis, the coefficient matrix $\alpha \in \mathbb{C}^{M\times N}$ fulfills $\alpha\alpha^\dagger = \mathbb{1}_M$. The intuitive choice made in Ref. [177] is to take the coefficients $\{\alpha_{m,n}\}$ as the set of optimization parameters. This corresponds to an optimization with the constraint $\alpha\alpha^\dagger = \mathbb{1}_M$ if orthonormality should be maintained. Unfortunately, this constraint goes far beyond simple bounds for each individual parameter but gives rise to a rather complicated interdependence between all parameters. It therefore yields an optimization problem that is typically difficult to solve. In first applications employing functionals (4.1), orthonormality has been ensured in a two step process [177]. First, the coefficients $\{\alpha_{m,n}\}$ have been allowed to change freely in each iteration such that functionals (4.1) are maximized. Secondly, each iteration has been followed by an orthonormalization process, e.g. using the Gram-Schmidt algorithm, which ensured that the next iteration again starts with a correct orthonormal basis. Unfortunately, this two step process comes at the expense that the manual orthonormalization during the second step usually decreases the functional value. In the worst scenario, it might even completely negate the gain of the first optimization step and might cause the functional to stagnate over several iterations or even indefinitely. In any case, it makes the optimization procedure prone of being stuck at local extrema and often prevents any further progress at all. It is usually advisable to avoid such non-trivial constraints if possible.

In the following, we will show how the orthonormality constraint can be completely avoided in the optimization procedure by a clever choice of the parametrization. In a nutshell, the trick is to use spherical coordinates and parametrize each state $|\psi_m\rangle$, $m = 1, \ldots, M$, recursively, i.e., the state $|\psi_m\rangle$ will depend on the parameters of all previous states $|\psi_1\rangle, \ldots, |\psi_{m-1}\rangle$. Although this might sound complicated, it is rather straightforward in practice. The details are as follows.

First State We start the representation of the first state $|\psi_1\rangle$ in the spirit of Eq. (4.8). However, we split the complex coefficients into their real and imaginary part and write $|\psi_1\rangle$ as

$$|\psi_1\rangle = \sum_{n=1}^{N} \left(a_n^{(1,\mathrm{re})} + \mathrm{i}a_n^{(1,\mathrm{im})}\right)|e_n\rangle\,, \tag{4.9}$$

where $a_n^{(1,\mathrm{re})}$ and $a_n^{(1,\mathrm{re})}$ are the real and imaginary part of coefficient $\alpha_{1,n}$. While the state $|\psi_1\rangle$ can be interpreted as the normalized vector $(\alpha_{1,1}, \ldots, \alpha_{1,N})^\mathsf{T} \in \mathbb{C}^N$, we can also uniquely map it to the normalized real vector

$$\boldsymbol{a}_1 = \left(a_1^{(1,\mathrm{re})}, \ldots, a_N^{(1,\mathrm{re})}, a_1^{(1,\mathrm{im})}, \ldots, a_N^{(1,\mathrm{im})}\right)^\mathsf{T} \in \mathbb{R}^{2N}, \tag{4.10}$$

$|\boldsymbol{a}_1| = 1$. This vector can subsequently be expanded in spherical coordinates, cf. Eq. (3.21), with angles $\phi_1^{(1)}, \ldots, \phi_{2N-1}^{(1)}$ and a fixed radius $r = 1$. These angles determine $|\psi_1\rangle$ completely and uniquely,

$$|\psi_1\rangle = \left|\psi_1\left(\phi_1^{(1)}, \ldots, \phi_{2N-1}^{(1)}\right)\right\rangle. \tag{4.11}$$

Second State We know that $|\psi_2\rangle$ is orthonormal to $|\psi_1\rangle$ on input, i.e., at the start of the optimization, since both are basis elements from the orthonormal basis $\mathrm{span}\{|\psi_1\rangle, \ldots, |\psi_M\rangle\} = \mathcal{H}'$. Hence, we must ensure that changing any optimization parameter maintains orthonormality. In order to achieve this, we do not expand $|\psi_2\rangle$ in the same basis $\{|e_1\rangle, \ldots, |e_N\rangle\}$ of $\mathcal{H}$ used for state $|\psi_1\rangle$. Instead, we use a rotated basis. In order to determine the latter, we first introduce the auxiliary state

$$|\psi_1'\rangle = \begin{cases} \frac{|\tilde{\psi}_1'\rangle}{\sqrt{\langle\tilde{\psi}_1'|\tilde{\psi}_1'\rangle}} & \langle\tilde{\psi}_1'|\tilde{\psi}_1'\rangle \neq 0, \\ 0 & \langle\tilde{\psi}_1'|\tilde{\psi}_1'\rangle = 0, \end{cases} \qquad |\tilde{\psi}_1'\rangle = |\psi_1\rangle - \langle e_1|\psi_1\rangle |e_1\rangle, \tag{4.12}$$

such that $|\tilde{\psi}_1'\rangle$ is the component of $|\psi_1\rangle$ that is orthogonal to $|e_1\rangle$. Furthermore, we define $\eta_1 = \arg\{\langle e_1|\psi_1\rangle\}$, the complex phase between $|e_1\rangle$ and $|\psi_1\rangle$, which ensures $e^{-\mathrm{i}\eta_1}\langle e_1|\psi_1\rangle \in \mathbb{R}$ and allows us to define the angle

$$\alpha_1 = \arccos\left(e^{-\mathrm{i}\eta_1}\langle e_1|\psi_1\rangle\right). \tag{4.13}$$

With this, we can define the unitary transformation

$$\begin{aligned} \mathsf{O}_1 = e^{-\mathrm{i}\eta_1}\Bigg[& \mathbb{1} + \left(|e_1\rangle\langle\psi_1'|e^{\mathrm{i}\eta_1} - e^{-\mathrm{i}\eta_1}|\psi_1'\rangle\langle e_1|\right)\sin(\alpha_1) \\ & + \left(|e_1\rangle\langle e_1| - |\psi_1'\rangle\langle\psi_1'|\right)(\cos(\alpha_1) - 1)\Bigg], \end{aligned} \tag{4.14}$$

which rotates $|e_1\rangle$ onto $|\psi_1\rangle$, i.e., $\mathsf{O}_1|e_1\rangle = |\psi_1\rangle$. Thus, we obtain a rotated basis $\{\mathsf{O}_1|e_1\rangle, \ldots, \mathsf{O}_1|e_N\rangle\}$ of $\mathcal{H}$, where $\mathsf{O}_1|e_1\rangle = |\psi_1\rangle$ and every other basis state being orthonormal to $|\psi_1\rangle$, i.e., $\mathsf{O}_1|e_n\rangle \perp |\psi_1\rangle$ for all $n \geq 2$. Hence, all orthonormal states with respect to $|\psi_1\rangle$, and in particular $|\psi_2\rangle$, can be written as

$$|\psi_2\rangle = \sum_{n=2}^{N}\left(a_n^{(2,\mathrm{re})} + \mathrm{i}a_n^{(2,\mathrm{im})}\right)\mathsf{O}_1|e_n\rangle, \tag{4.15}$$

where $a_n^{(2,\mathrm{re})}$ and $a_n^{(2,\mathrm{re})}$ are the real and imaginary part of the coefficients for basis state $\mathsf{O}_1 |e_n\rangle$. We can again write state $|\psi_2\rangle$ as a normalized real vector

$$\boldsymbol{a}_2 = \left(a_2^{(2,\mathrm{re})}, \ldots, a_N^{(2,\mathrm{re})}, a_2^{(2,\mathrm{im})}, \ldots, a_N^{(2,\mathrm{im})}\right)^\mathsf{T} \in \mathbb{R}^{2N-2}, \tag{4.16}$$

$|\boldsymbol{a}_2| = 1$. However, note that in contrast to Eq. (4.10), its dimension is reduced by two as one complex coefficient less is required. Formally, Eq. (4.15) just describes an arbitrary state $|\psi_2\rangle$ in the orthogonal, $N-1$ dimensional Hilbert space $\mathcal{H}_1 \equiv \mathcal{H} \backslash \mathrm{span}\{|\psi_1\rangle\}$. Nevertheless, Eq. (4.16) can again be expanded in spherical coordinates with angles $\phi_1^{(2)}, \ldots, \phi_{2N-3}^{(2)}$. Since the rotated basis $\{\mathsf{O}_1 |e_1\rangle, \ldots, \mathsf{O}_1 |e_N\rangle\}$ depends on O_1, which depends on $|\psi_1\rangle$ and thus from the angles $\phi_1^{(1)}, \ldots, \phi_{2N-1}^{(1)}$, we find the dependence of $|\psi_2\rangle$ to read

$$|\psi_2\rangle = \left|\psi_2\left(\phi_1^{(1)}, \ldots, \phi_{2N-1}^{(1)}, \phi_1^{(2)}, \ldots, \phi_{2N-3}^{(2)}\right)\right\rangle. \tag{4.17}$$

These new $2N-3$ angles describe $|\psi_2\rangle$ completely and uniquely — albeit viewed from a rotated frame where $|\psi_1\rangle$ corresponds to one of the basis states.

mth State This procedure can be continued recursively. In the following, we will assume that we have already obtained the spherical representation of states $|\psi_1\rangle, \ldots, |\psi_{m-1}\rangle$, $m \leq M$, in the same fashion as before. In detail, this implies that we have already obtained the unitary transformations $\mathsf{O}_1, \ldots, \mathsf{O}_{m-2}$ required to obtain the basis sets $\{\mathsf{O}_1 |e_1\rangle, \ldots, \mathsf{O}_1 |e_N\rangle\}, \ldots, \{\prod_{j=1}^{m-2} \mathsf{O}_j |e_1\rangle, \ldots, \prod_{j=1}^{m-2} \mathsf{O}_j |e_N\rangle\}$ for expressing states $|\psi_2\rangle, \ldots, |\psi_{m-1}\rangle$, respectively. In order to understand how these recursive basis sets work, the following needs to be taken into account. While O_1, necessary to represent $|\psi_2\rangle$, rotates $|e_1\rangle$ onto $|\psi_1\rangle$, i.e, $\mathsf{O}_1 |e_1\rangle = |\psi_1\rangle$, the unitary transformation O_2, necessary to represent $|\psi_3\rangle$, fulfills two properties. On the one hand, it leaves $|\psi_1\rangle$ invariant, i.e, $\mathsf{O}_2 |\psi_1\rangle = \mathsf{O}_2(\mathsf{O}_1 |e_1\rangle) = |\psi_1\rangle$, therefore it leaves the first state of the previous basis set $\{\mathsf{O}_1 |e_1\rangle, \ldots, \mathsf{O}_1 |e_N\rangle\}$ invariant. On the other hand, it rotates its second element $\mathsf{O}_1 |e_2\rangle$ onto $|\psi_2\rangle$, i.e., $\mathsf{O}_2(\mathsf{O}_1 |e_2\rangle) = |\psi_2\rangle$. Hence, we obtain the new basis $\{\mathsf{O}_2\mathsf{O}_1 |e_1\rangle, \ldots, \mathsf{O}_2\mathsf{O}_1 |e_N\rangle\}$, where the first two basis states, $\mathsf{O}_2\mathsf{O}_1 |e_1\rangle$ and $\mathsf{O}_2\mathsf{O}_1 |e_2\rangle$, coincide with $|\psi_1\rangle$ and $|\psi_2\rangle$, respectively. Thus, the state $|\psi_3\rangle$ can be expressed by only using all remaining basis elements, since due to initial orthonormality we have $|\psi_3\rangle \perp |\psi_1\rangle, |\psi_2\rangle$. For state $|\psi_m\rangle$, we assume that this concept has already been applied recursively to all further states up to $|\psi_{m-1}\rangle$. Therefore, we already have the basis $\{\prod_{j=1}^{m-2} \mathsf{O}_j |e_1\rangle, \ldots, \prod_{j=1}^{m-2} \mathsf{O}_j |e_N\rangle\}$ in which $|\psi_{m-1}\rangle$ is represented and can assume that its first $m-2$ basis states fulfill $\prod_{j=1}^{m-2} \mathsf{O}_j |e_k\rangle = |\psi_k\rangle$,

$k = 1, \ldots, m-2$.

Now, in order to obtain the spherical representation of state $|\psi_m\rangle$, we first need to find the basis $\{\prod_{j=1}^{m-1} \mathsf{O}_j |e_1\rangle, \ldots, \prod_{j=1}^{m-1} \mathsf{O}_j |e_N\rangle$, where the first $m-1$ basis elements coincide with $|\psi_1\rangle, \ldots, |\psi_{m-1}\rangle$, respectively. This implies that we need to find the unitary transformation O_{m-1} such that $|\psi_{m-1}\rangle$ becomes an basis element of the basis $\{\prod_{j=1}^{m-1} \mathsf{O}_j |e_1\rangle, \ldots, \prod_{j=1}^{m-1} \mathsf{O}_j |e_N\rangle\}$. To this end, we first define the auxiliary state

$$|\psi'_{m-1}\rangle = \begin{cases} \frac{|\tilde{\psi}'_{m-1}\rangle}{\sqrt{\langle\tilde{\psi}'_{m-1}|\tilde{\psi}'_{m-1}\rangle}} & \langle\tilde{\psi}'_{m-1}|\tilde{\psi}'_{m-1}\rangle \neq 0, \\ 0 & \langle\tilde{\psi}'_{m-1}|\tilde{\psi}'_{m-1}\rangle = 0, \end{cases} \tag{4.18a}$$

$$|\tilde{\psi}'_{m-1}\rangle = |\psi_{m-1}\rangle - \left\langle e_{m-1} \middle| \prod_{j=1}^{m-2} \mathsf{O}_j \middle| \psi_{m-1} \right\rangle |e_{m-1}\rangle . \tag{4.18b}$$

With its help we can define the necessary unitary transformation to read

$$\begin{aligned} \mathsf{O}_{m-1} = e^{-\mathrm{i}\eta_{m-1}} \Big[\mathbb{1} &+ \Big(|e_{m-1}\rangle \langle\psi'_{m-1}| \, e^{\mathrm{i}\eta_{m-1}} - e^{-\mathrm{i}\eta_{m-1}} |\psi'_{m-1}\rangle \langle e_{m-1}| \Big) \sin(\alpha_{m-1}) \\ &+ \Big(|e_{m-1}\rangle \langle e_{m-1}| - |\psi'_{m-1}\rangle \langle\psi'_{m-1}| \Big) (\cos(\alpha_{m-1}) - 1) \Big] \end{aligned} \tag{4.19}$$

with

$$\eta_{m-1} = \arg\{\langle e_{m-1}|\psi_{m-1}\rangle\}, \qquad \alpha_{m-1} = \arccos\left(e^{-\mathrm{i}\eta_{m-1}} \langle e_{m-1}|\psi_{m-1}\rangle\right). \tag{4.20}$$

O_{m-1} is constructed such that it rotates the $(m-1)$th basis vector of the previous basis set $\{\prod_{j=1}^{m-2} \mathsf{O}_j |e_1\rangle, \ldots, \prod_{j=1}^{m-2} \mathsf{O}_j |e_N\rangle\}$, onto $|\psi_{m-1}\rangle$, i.e., $\mathsf{O}_{m-1}(\prod_{j=1}^{m-2} \mathsf{O}_j |e_{m-1}\rangle) = |\psi_{m-1}\rangle$. The first $m-2$ basis states remain invariant as they already correspond to the states $|\psi_1\rangle, \ldots, |\psi_{m-2}\rangle$. Using the new basis $\{\prod_{j=1}^{m-1} \mathsf{O}_j |e_1\rangle, \ldots, \prod_{j=1}^{m-1} \mathsf{O}_j |e_N\rangle\}$ of $\mathcal{H}$, we thus can write any state that is orthogonal to $|\psi\rangle_1, \ldots, |\psi_{m-1}\rangle$, which in particular includes $|\psi_m\rangle$, as

$$|\psi_m\rangle = \sum_{n=m}^{N} \left(a_n^{(m,\mathrm{re})} + \mathrm{i} a_n^{(m,\mathrm{im})}\right) \left(\prod_{j=1}^{m-1} \mathsf{O}_j\right) |e_n\rangle . \tag{4.21}$$

As before, we can convert this state into a normalized real vector,

$$\boldsymbol{a}_m = \left(a_m^{(m,\mathrm{re})}, \ldots, a_N^{(m,\mathrm{re})}, a_m^{(m,\mathrm{im})}, \ldots, a_N^{(m,\mathrm{im})}\right)^\top \in \mathbb{R}^{2N-2(m-1)}, \tag{4.22}$$

$|\boldsymbol{a}_m| = 1$, which can be expanded in spherical coordinates with angles $\phi_1^{(m)}, \ldots, \phi_{2N-2(m-1)-1}^{(m)}$. Note that the dimension of this vector is reduced by $2(m-1)$, as it formally parametrizes an arbitrary state in the orthogonal, $N-(m-1)$ dimensional Hilbert space

$$\mathcal{H}_{m-1} \equiv \mathcal{H} \backslash \mathrm{span}\{|\psi_1\rangle, \ldots, |\psi_{m-1}\rangle\}. \tag{4.23}$$

Since all rotation matrices $\mathsf{O}_1, \ldots, \mathsf{O}_{m-1}$ depend on the angles of all previous states $|\psi_1\rangle, \ldots, |\psi_{m-1}\rangle$, we find the dependence of $|\psi_m\rangle$ to read

$$|\psi_m\rangle = \left|\psi_m\left(\phi_1^{(1)}, \ldots, \phi_{2N-1}^{(1)}, \phi_1^{(2)}, \ldots, \phi_{2N-3}^{(2)}, \ldots, \phi_1^{(m)}, \ldots, \phi_{2N-2(m-1)-1}^{(m)}\right)\right\rangle. \tag{4.24}$$

The $2N-2(m-1)-1$ new angles describe the state $|\psi_m\rangle$ completely and uniquely as viewed from a frame where the states $|\psi_1\rangle, \ldots, |\psi_{m-1}\rangle$ coincide with basis states.

The total set of all angles

$$\left\{\phi_1^{(1)}, \ldots, \phi_{2N-1}^{(1)}, \phi_1^{(2)}, \ldots, \phi_{2N-3}^{(2)}, \ldots, \phi_1^{(M)}, \ldots, \phi_{2N-2(M-1)-1}^{(M)}\right\}, \tag{4.25}$$

which is obtained by continuing this recursive procedure up to state $|\psi_M\rangle$, uniquely specifies an arbitrary $M \leq N$ dimensional subspace $\mathcal{H}' \subseteq \mathcal{H}$. While this parametrization might appear unnecessarily cumbersome at first glance, it has the crucial advantage that, by construction, changing any angle can never lead to non-normalized and non-orthogonal states. Hence, the structure of an orthonormal basis is a built-in feature of this parametrization. We will take the angles (4.25) as our optimization parameters in the following. For an M dimensional subspace this amounts to

$$\sum_{m=1}^{M}\Big[2N-2(m-1)-1\Big] = 2NM - M^2 \tag{4.26}$$

real parameters. This is in contrast to the $2NM$ real parameters that describe the complex $M \times N$ coefficient matrix α, cf. Eq. (4.8), that has been used before and where orthonormality has not been a built-in feature [177].

It is important to note that this recursive procedure is fully reversible. Given a set of angles describing the M dimensional subspace $\mathcal{H}'$, one can uniquely calculate its orthonormal basis states $\{|\psi_1\rangle, \ldots, |\psi_M\rangle\}$. The reverse process again starts at state $|\psi_1\rangle$, which can be fully constructed with the angles $\phi_1^{(1)}, \ldots, \phi_{2N-1}^{(1)}$. These angles also allow to calculate the unitary transformation O_1. With O_1 and angles $\phi_1^{(2)}, \ldots, \phi_{2N-3}^{(2)}$ we can subsequently construct $|\psi_2\rangle$ and O_2 and so forth.

4.3 Optimization Procedure

We have introduced the parametrization of an arbitrary M dimensional subspace $\mathcal{H}' \subseteq \mathcal{H}$ in the last section. Hence, the next question is how to use this parametrization in an actual optimization. To this end, we first observe that the number of optimization parameters, cf. Eq. (4.26), scales linearly with the dimension N of Hilbert space $\mathcal{H}$. For larger Hilbert spaces, the number of parameters quickly leaves the realm where gradient-free optimization is an option. Therefore, we will focus on gradient-based optimization in the following. Moreover, it is important to note that in contrast to all previous and remaining applications of optimal control in this thesis, we will not optimize time-dependent control fields. Instead, we will optimize a set of initial states such that their dynamics obey certain rules. In detail, we will optimize the set of basis states $\{|\psi_1\rangle, \ldots, |\psi_M\rangle\}$ such that $\mathrm{span}\{|\psi_1\rangle, \ldots, |\psi_M\rangle\} = \mathcal{H}'$ becomes a DFS. In consequence, we can not employ Krotov's method for this purpose as it only works for time-dependent control fields. However, we can in fact adapt the GRAPE algorithm [74] for this purpose as we will show in the following.

However, before discussing in detail how to do this in practice, we need to comment on the recursive nature of our parametrization as it has some non-trivial implications for the optimization procedure. By construction, the $m$the state $|\psi_m\rangle$ of the basis $\{|\psi_1\rangle, \ldots, |\psi_M\rangle\}$ depends on all previous states $|\psi_1\rangle, \ldots, |\psi_{m-1}\rangle$, since this ensures and maintains orthonormality of all states within the optimization. Although this is an advantageous feature for the parametrization, it implies that by changing any angle $\phi_k^{(m)}$, $1 \leq k \leq 2N - 2(m-1) - 1$, on which $|\psi_m\rangle$ depends on, not only that particular state changes but also all remaining states $|\psi_{m+1}\rangle, \ldots, |\psi_M\rangle$. This might cause problems in the optimization and also makes the calculation of gradients highly non-trivial (although not impossible). To overcome this, we employ sequential searches for one dimensional DFSs instead of a single search for an M dimensional DFS. The entire optimization procedure works as follows.

1. We start by optimizing $\phi_1^{(1)}, \ldots, \phi_{2N-1}^{(1)}$, which parametrizes an arbitrary state $|\psi_1\rangle \in \mathcal{H}$, by maximizing $\mathcal{J}_{\mathrm{dfs}}[\mathrm{span}\{|\psi_1\rangle\}]$. If we succeed, i.e., find a state $|\psi_1\rangle \in \mathcal{H}$ such that $\mathcal{J}_{\mathrm{dfs}}[\mathrm{span}\{|\psi_1\rangle\}] = 1$, we know that $\mathrm{span}\{|\psi_1\rangle\}$ is a one dimensional DFS. Hence, we fix the parameters $\phi_1^{(1)}, \ldots, \phi_{2N-1}^{(1)}$ and proceed.

2. In the next step we optimize $\phi_1^{(2)}, \ldots, \phi_{2N-3}^{(2)}$, which parametrizes an arbitrary state in $\mathcal{H}_1 = \mathcal{H} \backslash \mathrm{span}\{|\psi_1\rangle\}$, again by maximizing $\mathcal{J}_{\mathrm{dfs}}[\mathrm{span}\{|\psi_2\rangle\}]$. If we succeed, we know that $\mathrm{span}\{|\psi_2\rangle\}$ is another one dimensional DFS. Hence, we fix $\phi_1^{(2)}, \ldots, \phi_{2N-3}^{(2)}$ and proceed.

3. In the mth step we maximize $\mathcal{J}_{\text{dfs}}\left[\text{span}\{|\psi_m\rangle\}\right]$ by optimizing $\phi_1^{(m)},\ldots,\phi_{2N-2(m-1)-1}^{(m)}$, which parametrizes an arbitrary state in $\mathcal{H}_{m-1}=\mathcal{H}\backslash\text{span}\{|\psi_1\rangle,\ldots,|\psi_{m-1}\rangle\}$. If successful, we again fix $\phi_1^{(m)},\ldots,\phi_{2N-2(m-1)-1}^{(m)}$ and proceed.

4. We continue this procedure until no new one dimensional DFS can be found anymore. Let M be the number of one dimensional DFSs that have been identified this way. Finally, in order to check whether any combination of these M one dimensional DFSs builds a higher dimensional DFS, we only need to evaluate functional (4.5) for each combination. For instance, evaluating $\mathcal{J}_{\text{dfs}}\left[\text{span}\{|\psi_1\rangle,|\psi_2\rangle\}\right]$ immediately answers whether $\text{span}\{|\psi_1\rangle,|\psi_2\rangle\}$ is a two dimensional DFS.

This procedure has the advantage that we do not need to specify the dimension M of the desired DFS in advance. In contrast, provided that we have identified all one dimensional DFSs, subsequently exploring all conceivable combinations of these one dimensional DFSs guarantees that we also identify all higher dimensional DFSs if any exist.

As mentioned before, we will employ the GRAPE algorithm for the actual optimization in each step, i.e., maximization of $\mathcal{J}_{\text{dfs}}\left[\text{span}\{|\psi_m\rangle\}\right]$ in the mth step. To this end, we first need to rewrite the original GRAPE gradient (2.37) to read

$$\nabla_{\left\{\phi_1^{(m)},\ldots,\phi_{2N-2(m-1)-1}^{(m)}\right\}}\mathcal{J}_{\text{dfs}}\left[\text{span}\{|\psi_m\rangle\}\right]=\left(\frac{\partial\mathcal{J}_{\text{dfs}}}{\partial\phi_1^{(m)}},\ldots,\frac{\partial\mathcal{J}_{\text{dfs}}}{\partial\phi_{2N-2(m-1)-1}^{(m)}}\right). \tag{4.27}$$

From this, it is straightforward to see that we only need to provide the derivatives of $\mathcal{J}_{\text{dfs}}\left[\text{span}\{|\psi_m\rangle\}\right]$ with respect to the angles $\phi_k^{(m)}$, $k=1,\ldots,2N-2(m-1)-1$. These are given by, cf. Eqs. (4.5) and (4.4),

$$\begin{aligned}\frac{\partial\mathcal{J}_{\text{dfs}}\left[\text{span}\{|\psi_m\rangle\}\right]}{\partial\phi_k^{(m)}}&=\frac{1}{T}\int_{t_0}^{T}\frac{\partial\left\langle\!\left\langle\lambda_m|\mathcal{D}_{t,t_0}\left[\lambda_m\right]\right\rangle\!\right\rangle^2}{\partial\phi_k^{(m)}}\mathrm{d}t\\&\approx\frac{1}{N_t}\sum_{i=0}^{N_t}\frac{\partial\left\langle\!\left\langle\lambda_m|\mathcal{D}_{t_i,t_0}\left[\lambda_m\right]\right\rangle\!\right\rangle^2}{\partial\phi_k^{(m)}}\\&=\frac{2}{N_t}\sum_{i=0}^{N_t}\left[\left\langle\!\left\langle\frac{\partial\lambda_m}{\partial\phi_k^{(m)}}\middle|\mathcal{D}_{t_i,t_0}\left[\lambda_m\right]\right\rangle\!\right\rangle+\left\langle\!\left\langle\lambda_m\middle|\mathcal{D}_{t_i,t_0}\Big[\frac{\partial\lambda_m}{\partial\phi_k^{(m)}}\Big]\right\rangle\!\right\rangle\right]\end{aligned} \tag{4.28}$$

with $\lambda_m=|\psi_m\rangle\langle\psi_m|$ and

$$\frac{\partial\lambda_m}{\partial\phi_k^{(m)}}=\frac{\partial|\psi_m\rangle}{\partial\phi_k^{(m)}}\langle\psi_m|+|\psi_m\rangle\frac{\partial\langle\psi_m|}{\partial\phi_k^{(m)}}. \tag{4.29}$$

Note that in the second line of Eq. (4.28) we have approximated the integral-based

time averaging by a sum, which we anyway need for numerically solving the equation of motion. The derivative of state $|\psi_m\rangle$, cf. Eq. (4.21), with respect to all angles $\phi_1^{(m)}, \ldots, \phi_{2N-2(m-1)-1}^{(m)}$ is given by

$$\frac{\partial |\psi_m\rangle}{\partial \phi_k^{(m)}} = \sum_{n=m}^{N} \left(\frac{\partial a_n^{(m,\mathrm{re})}}{\partial \phi_k^{(m)}} + \mathrm{i} \frac{\partial a_n^{(m,\mathrm{im})}}{\partial \phi_k^{(m)}} \right) \left(\prod_{j=1}^{m-1} \mathsf{O}_j \right) |e_n\rangle \,. \tag{4.30}$$

Fortunately, the unitary transformations O_j, $j = 1, \ldots, m-1$, only depend on the angles up to $m-1$, which are fixed in the mth step, and their derivations with respect to $\phi_k^{(m)}$ thus vanish. From the spherical representation of $|\psi_m\rangle$, cf. Eq. (4.22), the remaining derivatives with respect to the coefficients $a_n^{(m,\mathrm{re})}$ and $a_n^{(m,\mathrm{im})}$ are straightforward to compute. However, for the ease of notation, we first rename its vector representation, cf. Eq. (4.22),

$$\boldsymbol{a}_m = \left(a_m^{(m,\mathrm{re})}, \ldots, a_N^{(m,\mathrm{re})}, a_m^{(m,\mathrm{im})}, \ldots, a_N^{(m,\mathrm{im})} \right)^{\mathsf{T}} \equiv \left(x_1^{(m)}, \ldots, x_{2N-2(m-1)}^{(m)} \right) \in \mathbb{R}^{2N-2(m-1)}. \tag{4.31}$$

Employing the spherical representation of this normalized vector, $K = 2N - 2(m-1)$,

$$\begin{aligned}
x_1^{(m)} &= r \cos\left(\phi_1^{(m)}\right), \\
x_2^{(m)} &= r \sin\left(\phi_1^{(m)}\right) \cos\left(\phi_2^{(m)}\right), \\
x_3^{(m)} &= r \sin\left(\phi_1^{(m)}\right) \sin\left(\phi_2^{(m)}\right) \cos\left(\phi_3^{(m)}\right), \\
&\vdots \\
x_{K-1}^{(m)} &= r \sin\left(\phi_1^{(m)}\right) \sin\left(\phi_2^{(m)}\right) \ldots \cos\left(\phi_{K-1}^{(m)}\right), \\
x_K^{(m)} &= r \sin\left(\phi_1^{(m)}\right) \sin\left(\phi_2^{(m)}\right) \ldots \sin\left(\phi_{K-1}^{(m)}\right),
\end{aligned} \tag{4.32}$$

we find the derivative of the spherical representation with respect to angle $\phi_k^{(m)}$ as

$$\frac{\mathrm{d}x_j^{(m)}}{\mathrm{d}\phi_k^{(m)}} = \begin{cases} \cos\left(\phi_k^{(m)}\right) \cos\left(\phi_j^{(m)}\right) \left[\prod_{\substack{l=1 \\ l \neq k}}^{j-1} \cos\left(\phi_l^{(m)}\right) \right], & k < j, \\ -\prod_{l=1}^{j-1} \sin\left(\phi_l^{(m)}\right), & k = j, \\ 0, & k > j. \end{cases} \tag{4.33}$$

These derivatives can be easily mapped back to Eq. (4.30).

Some remarks regarding the different notations in Eq. (4.4), respectively Sec. 4.1, and Eq. (4.28) are required. In Sec. 4.1, we consistently use a tensor sum representation of

the Hilbert space, namely $\mathcal{H} = \mathcal{H}' \oplus \mathcal{H}'^{\perp}$, which implies that the first M basis states from the basis of $\mathcal{H}$ span $\mathcal{H}'$ entirely. Thus, if $\mathcal{H}'$ is given, we can simply choose a basis for $\mathcal{H}$ that gives rise to such a tensor sum representation. However, the optimization is done with the fixed basis $\{|e_1\rangle, \ldots, |e_N\rangle\}$ of $\mathcal{H}$ and we need to express an arbitrary subspace $\mathcal{H}' \subseteq \mathcal{H}$ within this basis. Hence, instead of expressions like $\lambda_m \oplus 0$ with $\lambda_m \in \mathfrak{L}_{\mathcal{H}'}$ and $0 \in \mathfrak{L}_{\mathcal{H}'^{\perp}}$, we have the general $\lambda_m \in \mathfrak{L}_{\mathcal{H}}$ in practice.

At last, in contrast to the optimization of time-dependent control fields, where the guess fields for an optimization can and should be chosen based on physical intuition, the choice of a guess state $|\psi_m\rangle$ form where to start the optimization of $\mathcal{J}_{\mathrm{dfs}}[\mathrm{span}\{|\psi_m\rangle\}]$ is not straightforward. However, in contrast to time-dependent control fields, the parametrization of $|\psi_m\rangle$ contains much less parameters and using random guess states is a solid option to ensure unbiased optimization results. Even though random initial states can sometimes cause the gradient-based optimization to become stuck, we overcome this problem by employing swarm optimization. In detail, the mth optimization step, i.e., the search for the mth one dimensional DFS by maximizing $\mathcal{J}_{\mathrm{dfs}}[\mathrm{span}\{|\psi_m\rangle\}]$, is performed with several random initial states in parallel until one of them succeeds. Typically, the number of parallel optimization in the swarm will increase as the Hilbert space dimension and hence the number of optimization parameters increases.

4.4 Decoherence-Free Subspaces in Qubit Networks

In order to test the optimization procedure that has been introduced so far, we will first consider a system, where the DFS is known and check, whether we can reliably identify it. To this end, we consider a multi qubit network embedded in an environment consisting of an infinite number of bosonic modes [164]. Let S be the number of qubits. The Hamiltonian for system and environment is given by

$$\mathsf{H}_{\mathrm{S}} = \sum_{s=1}^{S} \omega^{(s)} \sigma_{\mathrm{z}}^{(s)}, \qquad \mathsf{H}_{\mathrm{E}} = \sum_{k} \Omega^{(k)} \mathsf{b}^{(k)\dagger} \mathsf{b}^{(k)}, \tag{4.34}$$

where $\omega^{(s)}$ is the level spacing of qubit s and $\Omega^{(k)}$ the frequency of the kth bosonic mode. Their interaction reads [164]

$$\begin{aligned} \mathsf{H}_{\mathrm{I}} = \sum_{s=1}^{S} \sum_{k} \Big[& g^{(s,k)} \left(\sigma_{+}^{(s)} \mathsf{b}^{(k)} + \sigma_{-}^{(s)} \mathsf{b}^{(k)\dagger} \right) + f^{(s,k)} \left(\sigma_{+}^{(s)} \mathsf{b}^{(k)\dagger} + \sigma_{-}^{(s)} \mathsf{b}^{(k)} \right) \\ & + h^{(s,k)} \sigma_{\mathrm{z}}^{(s)} \left(\mathsf{b}^{(k)} + \mathsf{b}^{(k)\dagger} \right) \Big], \end{aligned} \tag{4.35}$$

where $g^{(s,k)}$ describes the exchange of excitations between qubit s and mode k, wheres and $f^{(s,k)}$ describes simultaneous excitation and de-excitation of both. The term $h^{(s,k)}$ causes the qubit s to pick up a relative phase depending on its state. If we assume that all theses interaction processes happen with the same intensity for all qubits, i.e., when $g^{(s,k)}$, $f^{(s,k)}$ and $h^{(s,k)}$ are independent of s, and $\omega^{(s)} = \omega$, the bosonic environment gives rise to collective noise for the network of qubits. In that case, we can model the qubits' open system dynamics by a Lindblad master equation, cf. Eq. (2.13), where we only need three Lindblad operators,

$$\mathsf{L}_+ = \gamma_+ \sum_{s=1}^{S} \sigma_+^{(s)}, \qquad \mathsf{L}_- = \gamma_- \sum_{s=1}^{S} \sigma_-^{(s)}, \qquad \mathsf{L}_\mathrm{z} = \gamma_\mathrm{z} \sum_{s=1}^{S} \sigma_\mathrm{z}^{(s)}, \tag{4.36}$$

with γ_+, γ_- and γ_z their respective decay rates. By inspecting these Lindblad operators, the collective nature of this noise becomes evident. None of these operators does allow any qubit to be affected individually by any of these noise processes, since the latter always act on all qubits at the same time and with the same intensity.

For an even number S of qubits, the above model gives rise to a single DFS with dimension [164]

$$M(S) = \frac{S!}{(S/2+1)!(S/2)!}. \tag{4.37}$$

For instance, for $S = 2$ we find $M(2) = 1$. This one dimensional DFS is defined by $|\psi_1\rangle = (|01\rangle - |10\rangle)/\sqrt{2}$. Unfortunately, a one dimensional DFS is not very helpful for quantum information, as it can neither be used as quantum memory for a qubit state nor for quantum computing. Thus, we skip this case and immediately proceed to $S = 4$ qubits, where we have $M(4) = 2$. This two dimensional DFS is given by $\mathcal{H}' = \mathrm{span}\{|\psi_1\rangle, |\psi_2\rangle\}$ with

$$\begin{aligned} |\psi_1\rangle &= \frac{1}{2}\left(|0101\rangle - |0110\rangle - |1001\rangle + |1010\rangle\right), \\ |\psi_2\rangle &= \frac{1}{2\sqrt{3}}\left(2\,|0011\rangle - |0101\rangle - |0110\rangle - |1001\rangle - |1010\rangle + 2\,|1100\rangle\right). \end{aligned} \tag{4.38}$$

These two states can be interpreted as the basis of a new logical qubit, e.g. with basis states $|\bar{0}\rangle \equiv |\psi_1\rangle$ and $|\bar{1}\rangle \equiv |\psi_2\rangle$, and can therefore be used both for storing information as well as computing. In the following application of our optimization procedure, we chose the fixed basis $\{|e_1\rangle, \ldots, |e_N\rangle\}$ for $\mathcal{H}$ to be the standard logical basis $\{|00\ldots00\rangle, \ldots, |11\ldots11\rangle\}$.

Figure 4.1(a-c) show the basis states $|\psi_1\rangle$ and $|\psi_2\rangle$ that we find in three individual runs of the entire optimization procedure with $S = 4$ qubits. It is straightforward to

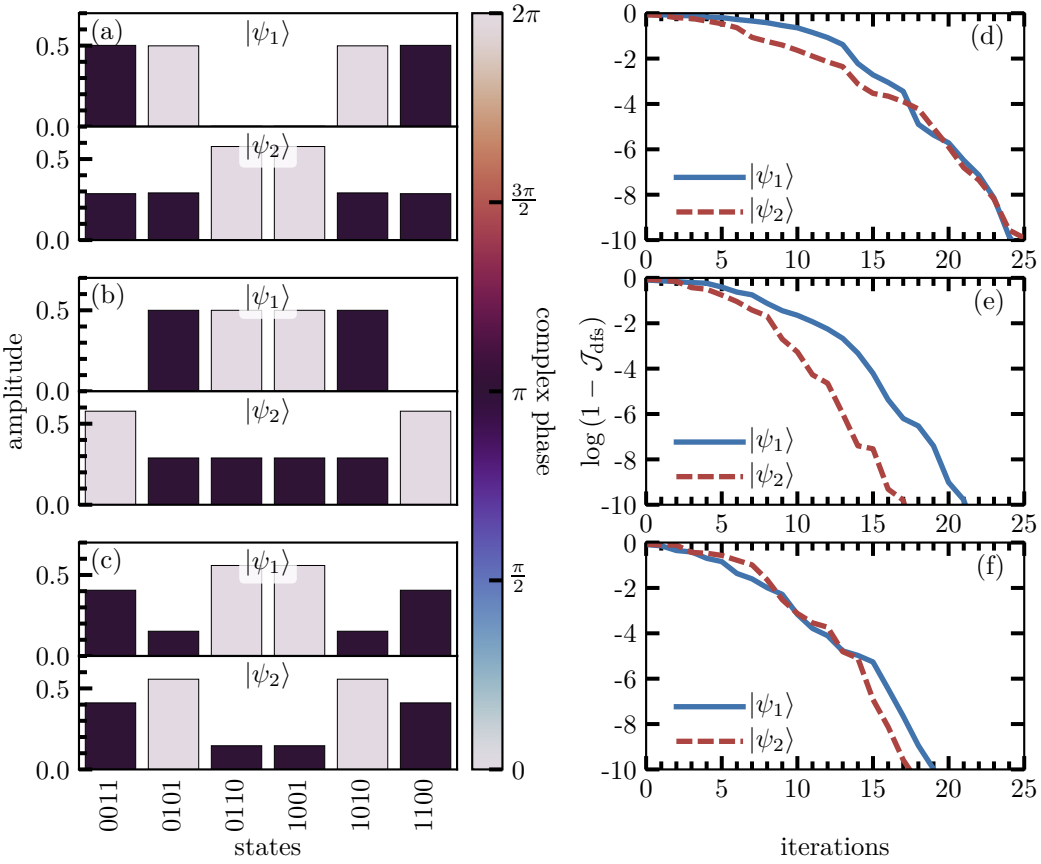

Figure 4.1: Optimization results for $S = 4$ qubits that are exposed to collective noise. Panels (a-c) show the one dimensional DFS states $|\psi_1\rangle$ and $|\psi_2\rangle$, which we obtain by applying the entire optimization procedure described in Sec. 4.3 three separate times. The histograms show the complex coefficient for their components in the respective basis states indicated at the bottom. The height of each bar shows the magnitude of each coefficient while the color indicates its complex phase. Panels (d-f) show the functional value $\mathcal{J}_{\rm dfs}[\text{span}\{|\psi_m\rangle\}]$ in terms of GRAPE iterations. The qubits' level splitting is $\omega = 1$ and the collective decay rates are $\gamma_+ = 0, \gamma_- = 0.1$ and $\gamma_z = 0.1$.

check that each state obtained this way describes a one dimensional DFS, both states are orthogonal to each other and indeed give rise to a two dimensional DFS as expected from Eq. (4.37). It should be noted that due to the randomness in the guess states, cf. Sec. 4.3, the solutions differ in each panel, i.e, in each individual run of the entire optimization procedure. Moreover, the DFS states $|\psi_1\rangle$ and $|\psi_2\rangle$ obtained in each run do not necessarily coincide exactly with the ones presented in Eq. (4.38). However, all states presented in Fig. 4.1(a-c) have still in common that they are indeed basis states for the same DFS, namely $\mathcal{H}' = \text{span}\{|\psi_1\rangle, |\psi_2\rangle\}$. This confirms that the optimization towards

DFSs works as intended. The differences in the solutions are because the basis for each subspace remains a basis under unitary transformations within this subspace, i.e., even though $\mathcal{H}'$ is unique, its basis states $|\psi_1\rangle$ and $|\psi_2\rangle$ are not. Hence, there is no unique solution and even $|\psi_1\rangle$ and $|\psi_2\rangle$ in Eq. (4.38) should be merely viewed as one possible choice among many.

Figure 4.1(d-f) show the performance of the optimization procedure in terms of required GRAPE iterations necessary to obtain the states presented in Fig. 4.1(a-c). It takes at maximum 25 iterations to find any of the one dimensional DFS in any of the three runs — even for functional values as small as $1 - \mathcal{J}_{\text{dfs}} \sim 10^{-10}$. Even though the latter error might appear unnecessarily small, such small errors are at least helpful for the entire optimization procedure to work out smoothly. This is because after state $|\psi_m\rangle$ gets fixed, every subsequent search for further one dimensional DFSs is tied to the states $|\psi_1\rangle, \ldots, |\psi_{m-1}\rangle$ that are already fixed basis vectors and only the reduced space $\mathcal{H}_{m-1} = \mathcal{H} \backslash \text{span}\{|\psi_1\rangle, \ldots, |\psi_{m-1}\rangle\}$ can be furthermore explored. Hence, insufficiently characterized previous DFS states can potentially give rise to undesired artifacts in later searches, for instance if they do not evolve sufficiently unitarily.

Next, we consider $S = 6$ qubits for which Eq. (4.37) predicts the existence of an $M(6) = 5$ dimensional DFS. In this case, it becomes already rather cumbersome to write down an exemplary basis $\text{span}\{|\psi_1\rangle, \ldots, |\psi_5\rangle\} = \mathcal{H}'$ like in Eq. (4.38) for $S = 4$. However, Fig. 4.2(a-c) show the optimization results again for three individuals runs of the entire optimization procedure. Each panel shows the five one dimensional DFS, $|\psi_1\rangle, \ldots, |\psi_5\rangle$, that the optimization is able to find. As before, all the states are mutually orthogonal and together give rise to the same five dimensional DFS $\mathcal{H}'$. Hence, we can confirm that the algorithm has no problems to identify the DFS $\mathcal{H}' = \text{span}\{|\psi_1\rangle, \ldots, |\psi_5\rangle\}$ in all cases, and does so with only slightly more iterations compared to $S = 4$, cf. Fig. 4.2.

At last, we consider the case of $S = 8$ qubits, where the DFS increases to dimension $M(8) = 14$. Even in this case, the optimization reliably identifies a 14 dimensional basis of the corresponding DFS. However, due to the size of the Hilbert space and the DFS, the corresponding states $|\psi_1\rangle, \ldots, |\psi_{14}\rangle$ become rather lengthy expressions and we do not present them here. Nevertheless, Fig. 4.3 again shows the performance for three individual executions of the entire optimization procedure. A somewhat general observation from Figs. 4.1 to 4.3 is that the number required iterations does not seem to depend on the number m of the state $|\psi_m\rangle$ that is being optimized for. Intuitively, we might expect states with larger m to take more iterations on average. The rationale behind this is as follows. Consider the case with $S = 8$ qubits where an $M(8) = 14$ dimensional DFS exists and the Hilbert space has dimension $N = 2^S = 256$. In the first step of the optimization

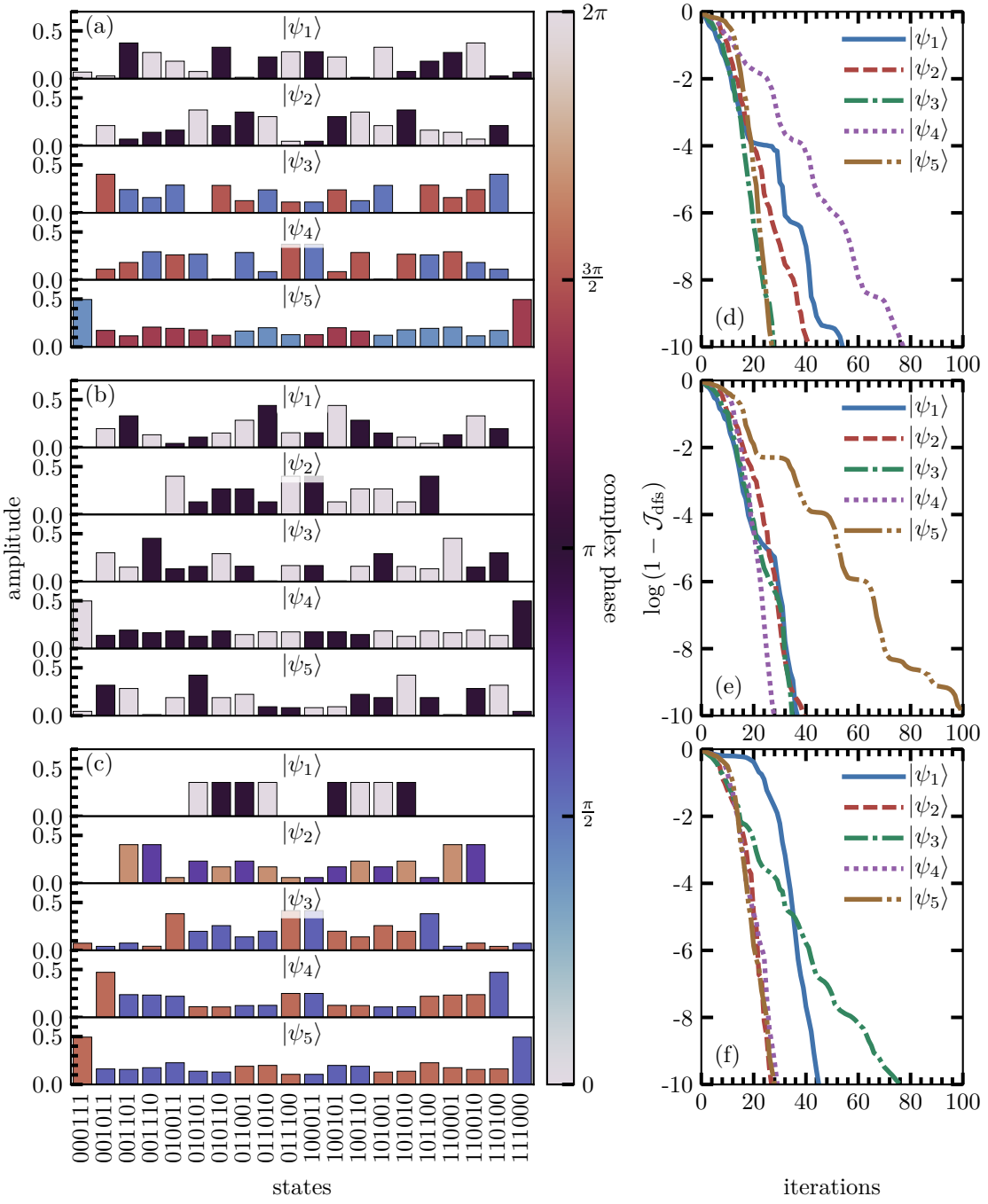

Figure 4.2: Identical to Fig. 4.1 but for $S = 6$ qubits. Panels (a-c) show the optimization results in terms of the obtained states $|\psi_1\rangle, \ldots, |\psi_5\rangle$ again for three individual runs of the entire optimization procedure. Panels (d-f) show $\mathcal{J}_{\rm dfs}[\text{span}\{|\psi_m\rangle\}]$ and the number of required iterations. The parameters are identical to Fig. 4.1.

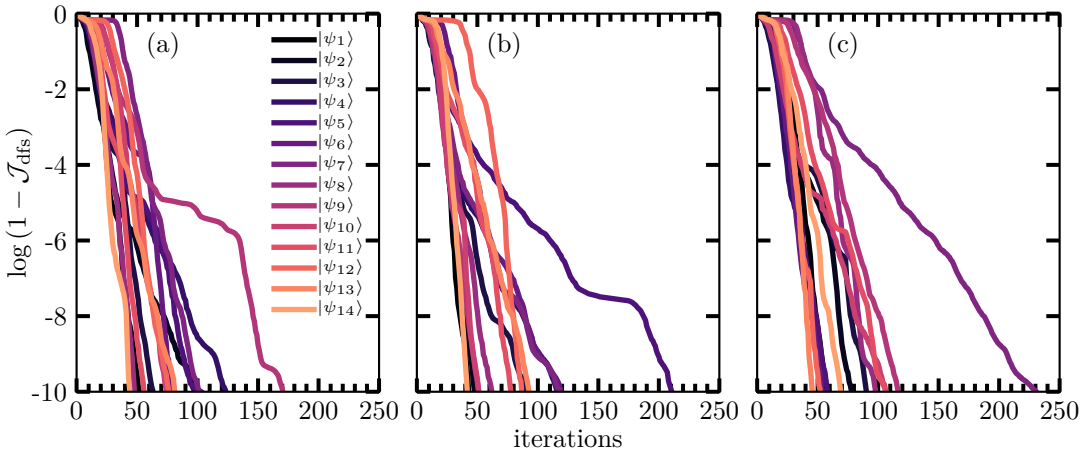

Figure 4.3: Performance in terms of required GRAPE iterations for the optimizations of the $M(8) = 14$ one dimensional DFSs with $S = 8$ qubits and for three separate runs of the entire optimization procedure. The parameters are identical to Fig. 4.1.

procedure we search for a one dimensional DFS spanned by $|\psi_1\rangle$ in $\mathcal{H}$, hence 14 out of 256 dimensions are solutions to this inquire. In the next step, we then search for $|\psi_2\rangle$ in $\mathcal{H}_1 \equiv \mathcal{H}\backslash\mathrm{span}\{|\psi_1\rangle\}$ and therefore 13 out of 255 dimensions are solutions. Continuing this procedure, for the last state $|\psi_M\rangle$ only one in $256 - 13 = 243$ dimensions is a solution. Hence, it would be intuitive to expect this optimization to be more challenging (on average) than previous ones. Surprisingly, this seems not to be that case as the iterations in Fig. 4.3 confirm.

In conclusion, the entire optimization procedure derived in Secs. 4.1 to 4.3 works excellent in terms of performance and reliability for our model system of non-interacting qubits under collective noise. Thus, as a next step, we will deviate from the original model and consider two kinds of interactions between the qubits. In detail, we consider the two system Hamiltonians

$$\mathsf{H}_{\mathrm{S}}^{\mathrm{full}} = \sum_{s=1}^{S} \omega \sigma_{\mathrm{z}}^{(s)} + \sum_{\substack{s,s'=1 \\ s\neq s'}}^{S} J \sigma_{\mathrm{x}}^{(s)} \sigma_{\mathrm{x}}^{(s')}, \tag{4.39}$$

$$\mathsf{H}_{\mathrm{S}}^{\mathrm{chain}} = \sum_{s=1}^{S} \omega \sigma_{\mathrm{z}}^{(s)} + \sum_{s=1}^{S-1} J \sigma_{\mathrm{x}}^{(s)} \sigma_{\mathrm{x}}^{(s+1)}, \tag{4.40}$$

where $\mathsf{H}_{\mathrm{S}}^{\mathrm{full}}$ corresponds to a model where every qubit interacts with every other qubit and $\mathsf{H}_{\mathrm{S}}^{\mathrm{chain}}$ describes a linear chain of interacting qubits. Similar to the assumption of identical level splittings ω for all qubits, we also assume identical coupling strength J between all qubits. In addition to introducing interactions, we also vary the present

noise forms, i.e., whether both collective energy relaxation, described by γ_+ and γ_-, and collective dephasing, described by γ_z, or just one of these processes acts at the same time.

We start with discussing the fully interacting model, described by $\mathsf{H}_S^{\text{full}}$, where the optimization procedure yields (data not shown) that for even number S of qubits the interactions neither change the dimension $M(S)$ of the DFSs nor their particular form. Both are identical to the interaction free case, cf. Eq. (4.37), if we consider both collective energy relaxation and dephasing or, for instance, only collective relaxation. However, if we consider only collective dephasing, i.e., $\gamma_+ = \gamma_- = 0$ and $\gamma_z \neq 0$, the DFS dimensions increase from $M(2) = 1$ and $M(4) = 2$ to $M(2) = 2$ and $M(4) = 5$ for $S = 2$ and $S = 4$ qubits. This might be explained by the missing relaxation process, which causes new symmetries to emerge and therefore causes new subspaces to become decoherence-free. Unfortunately, how the missing energy relaxation affects DFSs in the larger systems with $S = 6$ or $S = 8$ qubits is not clear from the optimization results and can also not be straightforwardly extrapolated from the changes observed for $S = 2$ and $S = 4$ qubits. To this end, it should be generally noted that in order to determine the DFS dimension in an unknown system, we always need to acquire sufficient statistical data such that we can confidently identify the correct DFS dimension. This implies that we need to run the entire optimization procedure repeatedly. Although this is not a general problem for our method, it becomes numerically more expensive with increasing Hilbert space and DFS dimension.

Next, we consider the chain of interacting qubits, described by $\mathsf{H}_S^{\text{chain}}$. In contrast to the fully interacting model, these interactions change the symmetries between the qubits substantially. We observe that, in combination with collective energy relaxation as only dissipative process, this does not allow for any DFS in case of more than $S = 2$ qubits (the case $S = 2$ is identical to the fully interacting model, cf. Eqs. (4.39) and (4.40)). However, with collective dephasing as the only dissipative process, we find $M(S) = 2$ for every even number S of qubits. Although the obtained DFS basis states $|\psi_1\rangle$ and $|\psi_2\rangle$ look different in each individual run of the optimization procedure due to the random nature of the guess states, we can deduce a general rule for every even S by closely inspecting the structure of the obtained states $|\psi_1\rangle$ and $|\psi_2\rangle$. Both states can be generated analytically by the recursive formula

$$\begin{aligned}
\left|\psi_1^{(S)}\right\rangle &= \frac{1}{\sqrt{2}}\left(|0\rangle \otimes \left|\psi_2^{(S-2)}\right\rangle \otimes |1\rangle + |1\rangle \otimes \left|\psi_2^{(S-2)}\right\rangle \otimes |0\rangle\right), \qquad \left|\psi_1^{(2)}\right\rangle = \frac{1}{\sqrt{2}}\left(|01\rangle + |10\rangle\right), \\
\left|\psi_2^{(S)}\right\rangle &= \frac{1}{\sqrt{2}}\left(|0\rangle \otimes \left|\psi_1^{(S-2)}\right\rangle \otimes |1\rangle - |1\rangle \otimes \left|\psi_1^{(S-2)}\right\rangle \otimes |0\rangle\right), \qquad \left|\psi_2^{(2)}\right\rangle = \frac{1}{\sqrt{2}}\left(|01\rangle - |10\rangle\right).
\end{aligned} \tag{4.41}$$

For $S = 2$ qubits, the two states $|\psi_1^{(2)}\rangle$ and $|\psi_2^{(2)}\rangle$ coincide with the Bell states $|\Psi^{\pm}\rangle = (|01\rangle \pm |10\rangle)/\sqrt{2}$, which are maximally entangled two qubit states. Interestingly, for larger S, the structure of the Bell states is somewhat preserved by the recursive formula. For instance, the states $|\psi_1^{(4)}\rangle$ and $|\psi_2^{(4)}\rangle$ can be interpreted as "Bell states of Bell states". Therefore, the states $|\psi_1^{(S)}\rangle$ and $|\psi_2^{(S)}\rangle$ will be, in general, highly non-local states and will most likely be multipartite entangled. The latter is unfortunately very difficult to quantify [180, 181].

Our findings show that under certain conditions DFSs exist in qubit chains and that we can reliably identify them employing the introduced optimization procedure. Especially the combination of numerical optimization and the manual analysis of the structure of the optimized states allows to deduce analytical formulas, which can afterwards easily be verified numerically. The fact that we are able to obtain such a general analytical formula in case of the qubit chain is exactly what numerical OCT hopes to achieve. To this end, recall that numerical OCT is typically applied when the problem does not allow for an analytical treatment. Hence, the ideal result of any numerical optimization is that its results provide enough fundamental insights into the problem such that a solution can afterwards be constructed analytically. We can therefore confirm that the introduced optimization procedure works well and as intended.

It should be emphasized that searching for DFSs via OCT has some advantages in contrast to determining them analytically. In general, OCT allows to tackle arbitrarily complex systems and environments with the only restriction that the numerical costs need to remain manageable. It can therefore tackle problems that might be intractable analytically. Besides, another crucial advantages is that the optimization procedure introduced in this chapter can even be used in systems where no DFS exists. In that case, it allows to identify those states or subspaces, which are least affected by dissipation — something the analytical approach is not capable of. This is interesting from two different perspectives. On the one hand, the least dissipating subspace would be the natural choice for encoding information and performing operations as it constitutes the best available protection in a system where dissipation is inevitable. Moreover, the least dissipating states, called pointer states [182], are for instance also relevant to understand measurements in quantum mechanics [183] and are therefore interesting by themselves. On the other hand, the non-existence of DFSs immediately raises the question how the dynamics, determined by $\mathcal{D}_{t,t_0}$, needs to change such that a DFS can exist. This latter question can in principle be tackle in several ways. One possibility is to control the open system's Hamiltonian in such a way that missing symmetries are added manually such that a DFS starts to exist. These controls can for instance be

static or time-dependent control fields, as e.g. for dynamical decoupling [153, 154], or any other controllable quantity of the system. First ideas in this direction can be found in Ref. [184]. Alternatively, we can also try to alter the incoherent, i.e., dissipative, part of the dynamics by controlling — in realistic limits — the environment's impact in the same spirit of quantum reservoir engineering [126]. Although we can not simply diminish the environment's interaction strength, since we can assume that this would otherwise have already been done, we can usually add or adapt selective dissipative processes on purpose such as to "symmetrize" the noise. As an example, let us consider the qubit network described by Eq. (4.34), where the DFS originates due to the collective nature of the noise. However, different qubits have typically different decay rates and collective noise might therefore be unrealistic in practice. Nevertheless, by artificially enforcing collective noise on all qubits, it could be possible to create a DFS manually. Conceptually, this would mean that we deliberately deteriorate the dissipation in most parts of the Hilbert space but improve it substantially in a small subspace. Numerical OCT would again constitute a promising approach in order to identify the coherent control fields or incoherent control knobs of the dynamics to achieve this. However, it would require us to combine the current optimization procedure towards DFSs with a second optimization loop for all kinds of control parameters that determine the coherent and incoherent part of the dynamics. In case of time-dependent, coherent control fields, this second optimization loop would require us to combine the DFS search with e.g. the GRAPE or Krotov algorithm.

4.5 Functional Variations beyond Decoherence-Free Subspaces

In order to provide some possible future application of this algorithm, we generalize it to also work for states and subspaces other than DFSs in the following. The main motivation for this is that the identification of certain states and subspaces is relevant beyond the search for DFSs and the subspace parametrization developed in Sec. 4.2 constitutes an excellent starting point for that. In fact, to use the optimization procedure introduced so far for subspaces other than DFSs, we only need to define appropriate and reliable functionals for these subspaces in order to quantify the success.

As one particular example, we formulate a functional that quantifies population conserving subspaces (PCSs). These can be viewed as weaker forms of DFSs. While a DFS requires conservation of the population within the subspace $\mathcal{H}' \subseteq \mathcal{H}$ as well as unitary evolution for all states within it, a PCS is solely determined by the first property. Hence, it is in general more likely to find a PCS in any system than to find a DFS. The

former are especially interesting for quantum reservoir engineering, where dissipative processes can be engineered such as to have a desired impact on a subspace and steer its dynamics within it in a certain way. However, loss of population from the subspace is rather difficult to counteract via engineered dissipation [185]. Hence, identifying PCSs for a given system might be beneficial for creating quantum reservoir engineering protocols.

Starting from Eq. (4.4), we can easily modify it to read

$$\mathcal{J}_{\mathrm{pcs},t}\left[\mathcal{H}'\right] = \frac{1}{M^2}\left\|\hat{\mathcal{D}}'_{t,t_0}\right\|_1 = \frac{1}{M^2}\sum_{m,n=1}^{M^2}\left|\langle\!\langle \lambda_m \oplus 0|\mathcal{D}_{t,t_0}\left[\lambda_n \oplus 0\right]\rangle\!\rangle\right|, \tag{4.42}$$

i.e., we replace the squared l^2 norm by the l^1 norm. By virtue of this, we effectively replace $\langle\!\langle \ldots \rangle\!\rangle^2$ by $|\langle\!\langle \ldots \rangle\!\rangle|$ in the sum, which in fact only measures population loss form $\mathcal{H}' \subseteq \mathcal{H}$ and is insensible for purity loss of the states $\lambda_n \in \mathfrak{L}_{\mathcal{H}'}$. As long as the population gets transferred for every initial state λ_n to any of the other states $\lambda_m \in \mathfrak{L}_{\mathcal{H}'}$, the term $\sum_{m=1}^{M^2}|\langle\!\langle \lambda_m \oplus 0|\mathcal{D}_{t,t_0}[\lambda_n \oplus 0]\rangle\!\rangle|$ becomes one and is strictly smaller iff population is lost into $\mathfrak{L}_{\mathcal{H}'^{\perp}}$.

Another possible application is the identification of subspaces for quantum error correction (QEC). The latter can be seen as a different approach to negate the environment's detrimental influence. While DFSs avoid errors completely, QEC allows errors to occur in certain subspaces. The latter subspaces need to fulfill the QEC criteria [186]

$$\left\langle \psi_i \middle| \mathsf{E}_l^{\dagger}\mathsf{E}_k \middle| \psi_j \right\rangle = \Xi_{lk}\delta_{ij}, \tag{4.43}$$

where Ξ_{lk} is a Hermitian matrix and $\mathsf{E}_l, \mathsf{E}_k \in \mathcal{E}_{\mathrm{err}}$ with $\mathcal{E}_{\mathrm{err}}$ the set of possible errors. For quantum computing, a two dimensional subspaces is sufficient and we can restrict our search to two states, $|\psi_1\rangle$ and $|\psi_2\rangle$, that fulfill the above criteria. A functional that indicates how well any subspace $\mathcal{H}' = \mathrm{span}\{|\psi_1\rangle, |\psi_2\rangle\}$ performs in view of Eq. (4.43), needs to measure (i) the Hermiticity of Ξ_{lk}, (ii) that Ξ_{lk} has no individual dependence on the states $|\psi_1\rangle, |\psi_2\rangle$ and (iii) whether the left hand side of Eq. (4.43) vanishes for $i \neq j$. A possible functional $\mathcal{J}_{\mathrm{qec}}$ that is zero iff these criteria are fulfilled reads

$$\begin{aligned}\mathcal{J}_{\mathrm{qec}}\left[\mathrm{span}\left\{|\psi_1\rangle, |\psi_2\rangle\right\}\right] = -\Delta_{\mathrm{herm}}&\left[\left\|\Xi_{\psi_1} - \Xi_{\psi_1}^{\dagger}\right\|_2^2 + \left\|\Xi_{\psi_2} - \Xi_{\psi_2}^{\dagger}\right\|_2^2\right] \\ &- \Delta_{\mathrm{eq}}\left\|\Xi_{\psi_1} - \Xi_{\psi_2}\right\|_2^2 - \Delta_{\mathrm{diff}}\left\|\Xi_{\psi_1,\psi_2}\right\|_2^2\end{aligned} \tag{4.44}$$

where the three matrices $\Xi_{\psi_1}, \Xi_{\psi_2}$ and Ξ_{ψ_1,ψ_2} are defined as

$$\left(\Xi_{\psi_1}\right)_{lk} = \left\langle \psi_1 \middle| \mathsf{E}_l^\dagger \mathsf{E}_k \middle| \psi_1 \right\rangle, \quad \left(\Xi_{\psi_2}\right)_{lk} = \left\langle \psi_2 \middle| \mathsf{E}_l^\dagger \mathsf{E}_k \middle| \psi_2 \right\rangle, \quad \left(\Xi_{\psi_1,\psi_2}\right)_{lk} = \left\langle \psi_1 \middle| \mathsf{E}_l^\dagger \mathsf{E}_k \middle| \psi_2 \right\rangle \tag{4.45}$$

and $\Delta_{\text{herm}}, \Delta_{\text{eq}}, \Delta_{\text{diff}} \geq 0$ are weights for the individual terms in $\mathcal{J}_{\text{qec}}$. Note that in contrast to the functionals presented previously, Eq. (4.44) is a time-independent quantity without any information about the dynamics of the system. Nevertheless, it contains all information about the type and structure of the noise via $\mathcal{E}_{\text{err}}$ and thus might provide a suitable starting point for exploring the error correction capabilities of any subspace fulfilling $\mathcal{J}_{\text{qec}} = 0$.

In a next step, a more sophisticated ansatz would require us to extend the functional to also include information about the subspace's capability to perform error syndrome measurements. While a subspace $\mathcal{H}' = \text{span}\{|\psi_1\rangle, |\psi_2\rangle\}$ that fulfills Eq. (4.43) is in general capable of correcting errors, syndrome measurements need to be available in order to detect the occurrence of errors in the first place. Hence, more terms are in general required in $\mathcal{J}_{\text{qec}}$ to quantify this.

In order to conclude this chapter, we have introduced a new optimization procedure that allows to search for decoherence-free subspaces by means of optimal control. We have introduced a functional that quantifies whether a subspace $\mathcal{H}' \subseteq \mathcal{H}$ is a DFS and furthermore introduced a parametrization for arbitrary subspaces $\mathcal{H}' \subseteq \mathcal{H}$ — both designed such that they are compatible with gradient-based optimization techniques. We have successfully demonstrated the method's performance by identifying DFSs in a network of qubits and have moreover outlined the method's capabilities to identify subspaces other than DFSs.

5

Time-Optimal Qubit Reset

The availability of on-demand qubit reset is essential for any quantum technology [187]. Qubit reset — also referred to as qubit purification or initialization — describes the process of transferring a qubit's current state to a known pure state, usually its ground state, which then defines the starting point for its further usage. This process needs to be performed prior to any quantum technological application, if they are based on qubits, and occasionally also during runtime as part of the quantum algorithm itself. Examples for the latter are quantum computing [188–193] or quantum thermodynamical machines [194–198]. Especially the requirement that a quantum device needs to start from a known pure initial state of all qubits can be understood quite intuitively. Since the outcome of a quantum technological application is typically stored in the final state of all qubits and the entire dynamics is supposed to be unitary, this final state can only provide meaningful information if its initial state is pure and known.

The fact that resetting a single qubit requires its dynamics to transfer every possible qubit state, independent on whether it is mixed or pure, to the same pure target state already emphasizes the strong non-unitary nature of this operation. Hence, this simple observation immediately tells us that, in order to perform such an operation, some sort of auxiliary system that renders the qubit dynamics non-unitary is needed. The necessity for an auxiliary system can be explained very easily in the language of quantum thermodynamics. Since the qubit's purity can be regarded as its effective temperature — with a pure state corresponding to zero temperature — the process of resetting a qubit

basically describes thermodynamical cooling, i.e., export of entropy. Such an export can not occur in closed systems nor can, for instance, the purity change under unitary dynamics. Hence, we need the auxiliary system as an entropy dump and as a source of non-unitarity. The equivalence of entropy export and purification can also be seen in typical measures of quantum entropy, for instance like the von Neumann entropy [114], its generalization the Rényi entropy [199] or the Tsallis entropy [200] to name a few. While they differ in general, all these entropic measures become minimal iff they are evaluated for a pure state.

Formally, the auxiliary system, required for resetting the qubit, is given by the anyway ubiquitous environment or by a part of it. This makes qubit reset a very unique and complex task compared to other quantum technological tasks. On the one hand, it requires that, on a fundamental level, all qubits actively couple to their individual environments such that resetting becomes feasible. On the other hand, however, this coupling minimal still needs to be kept minimal such as not to impair any other qubit properties due to ensuing environmental noise. Moreover, since the entropy needs to flow from the qubit into the environment, their mutual coupling strength will determine the overall time scale for this process. This raises another problem. While weak coupling is advantageous as it minimizes environmentally induced noise on the qubits, it also promotes very time consuming resets that, if these reset times start to dominate other operations substantially, will slow down the operational speed of the entire quantum technological application. Unfortunately, a large coupling between qubit and environment is typically even worse, as it severely impairs the qubit and all of its operations due to the ensuing substantial increase of dissipation.

One way out of this dilemma is to utilize an interaction between qubit and its environment that can be controlled effectively, i.e., which is large when need and sufficiently small otherwise. Conceptually, this can be done in two ways. Given a generally weak coupling between the qubit and its environment, one possibility is to use tunable environments [201–205]. In that case, the natural thermalization of the qubit with its environment is artificially accelerated by enhancing the effective environmental coupling strength and thus the qubit's decay rates. The thermal steady state would thereby coincide with the qubit's pure target state. This approach is therefore related to quantum reservoir engineering [126]. Instead of using the qubit's total environment as auxiliary system, a slightly different approach is to selectively use only a single, strongly coupling mode [206–208]. As long as the effective coupling between qubit and this auxiliary mode can be controlled sufficiently well, this allows to exploit the fast time scale set by the strong coupling and does not require the qubit to undergo any thermalization process,

which is typically slower.

In practice, both variants, i.e., qubit reset that employs a tunable environment as well as qubit reset that utilize a strongly coupled ancilla, require control over an open quantum system. In detail, this on-demand qubit reset intrinsically relies on control fields that activate and deactivate the reset process by controlling the environment's effective interaction with the qubit. Moreover, since qubit reset should in practice be executed in minimal time and with highest fidelity, it constitutes an excellent problem for optimal control.

In the this chapter, we will explore qubit reset from the perspective of optimal control. In detail, we will be interested in bounds and limits in terms of minimal time and maximally achievable qubit purity. In Sec. 5.1 we will consider a qubit reset protocol that is based on a tunable environment. We will start from an analytical control scheme for that purpose and, in the course of the section, replace this protocol by an optimized and improved version. This will also allow us to identify its limits in time and fidelity. In the remaining Secs. 5.2 and 5.3 we will then turn towards ancilla-based reset protocols. The focus in Sec. 5.2 will be on the influence of initial correlations between qubit and ancilla and how those can be turned into an asset for the reset protocol. In contrast, Sec. 5.3 will assume uncorrelated initial qubit-ancilla states and thoroughly explore how the particular type of qubit-ancilla interaction and local qubit control affects the fundamental limits of the reset process. While we will identify those combinations of interaction and local control which do not allow for qubit purification at all, we will also provide time-optimal solutions for all remaining combinations.

Note that all results presented in this chapter are in stark contrast to close loop feedback control techniques that can also be used to increase the purification rate of the qubit in an iterative feedback loop [209–212]. However, such techniques do not allow to identify fundamental limits.

5.1 Qubit Reset with a Tunable Environment

In this section, we will explore qubit reset via a tunable environment. To this end, we will consider a model based on a physical setup introduced in Refs. [203, 213]. We will furthermore use its proposed analytical reset scheme, which uses a single time-dependent and tunable level splitting as control field, as a starting point for optimal control. By subsequently lifting the restriction to a single control field, i.e., by extending the set of controls, optimal control will allow us to explore the fundamental limits of qubit reset in this particular setup.

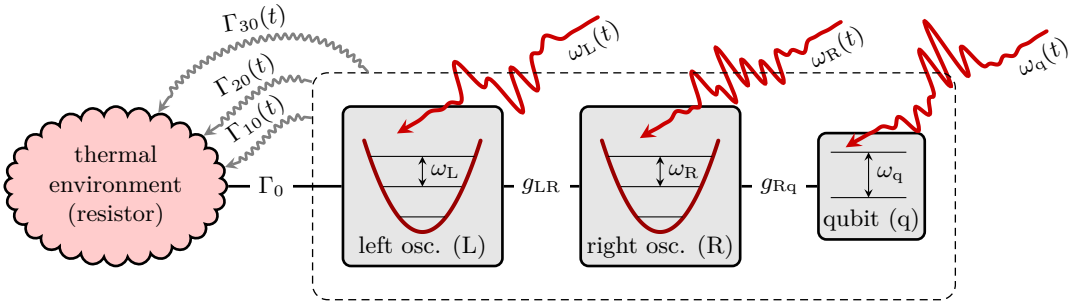

Figure 5.1: Schematic diagram of the physical scenario consisting of a qubit (q) linearly coupled to a harmonic oscillator (R), which in turn is linearly coupled to a second harmonic oscillator (L) that is in direct contact with a thermal environment. By temporally controlling the level splittings $\omega_{q/L/R}(t)$ of the qubit, the right and the left oscillator, we can effectively tune the coupling strength of the environment and change the decay rates over several orders of magnitude.

The results presented in this section have been published in Ref. [214].

5.1.1 Model and Control Problem

The physical setup is given by a tripartite system consisting of two harmonic oscillators, named left (subscript L) and right (subscript R) oscillator, and a qubit (subscript q) as sketched in Fig. 5.1. We assume the two oscillators to be linearly coupled to each other and the qubit to be exclusively coupled to the right oscillator. This scenario is modeled by the Hamiltonian [213]

$$\begin{aligned} \mathsf{H}(t) = {} & \omega_{\mathrm{L}}(t)\mathsf{a}_{\mathrm{L}}^{\dagger}\mathsf{a}_{\mathrm{L}} + \omega_{\mathrm{R}}(t)\mathsf{a}_{\mathrm{R}}^{\dagger}\mathsf{a}_{\mathrm{R}} + \omega_{\mathrm{q}}(t)\sigma_{+}\sigma_{-} \\ & + g_{\mathrm{LR}}(t)\left(\mathsf{a}_{\mathrm{L}}^{\dagger} + \mathsf{a}_{\mathrm{L}}\right)\left(\mathsf{a}_{\mathrm{R}}^{\dagger} + \mathsf{a}_{\mathrm{R}}\right) - \mathrm{i}g_{\mathrm{Rq}}(t)\left(\mathsf{a}_{\mathrm{R}}^{\dagger} + \mathsf{a}_{\mathrm{R}}\right)(\sigma_{+} - \sigma_{-})\,, \end{aligned} \tag{5.1}$$

where $\mathsf{a}_{\mathrm{L}}^{\dagger}$, $\mathsf{a}_{\mathrm{R}}^{\dagger}$ and σ_{+} are the creation operators for the left oscillator, right oscillator and qubit, respectively. The first three terms in Eq. (5.1) describe the free evolution of the three subsystems, with $\omega_{q/L/R}(t)$ being the time-dependent and controllable level splittings of the qubit, the left and the right oscillator, respectively. The fourth and fifth term describe how the right oscillator is coupled to the left oscillator and to the qubit, respectively. Their time-dependent interaction strengths are given by

$$g_{\mathrm{LR}}(t) = g_{\mathrm{LR}}^{0}\sqrt{\frac{\omega_{\mathrm{L}}(t)}{\omega_{\mathrm{R}}(t)}}, \qquad g_{\mathrm{Rq}}(t) = \sqrt{g_{\mathrm{Rq}}^{0}\omega_{\mathrm{R}}(t)}, \tag{5.2}$$

where g^0_{LR} is the resonant coupling strength between the two oscillators and g^0_{Rq} is a static coupling between the right oscillator and the qubit.

The Hamiltonian (5.1) can be simplified by applying a rotating-wave approximation (RWA), assuming $g_{\mathrm{Rq}}(t) < g^0_{\mathrm{LR}} \ll \omega_{\mathrm{R}}(t)$. This results in [213]

$$\begin{aligned}\mathsf{H}(t) \approx{}& \omega_{\mathrm{L}}(t)\mathsf{a}_{\mathrm{L}}^\dagger\mathsf{a}_{\mathrm{L}} + \omega_{\mathrm{R}}(t)\mathsf{a}_{\mathrm{R}}^\dagger\mathsf{a}_{\mathrm{R}} + \omega_{\mathrm{q}}(t)\sigma_+\sigma_- \\ &+ g_{\mathrm{LR}}(t)\left(\mathsf{a}_{\mathrm{L}}^\dagger\mathsf{a}_{\mathrm{R}} + \mathsf{a}_{\mathrm{R}}^\dagger\mathsf{a}_{\mathrm{L}}\right) + \mathrm{i}g_{\mathrm{Rq}}(t)\left(\mathsf{a}_{\mathrm{R}}^\dagger\sigma_- - \mathsf{a}_{\mathrm{R}}\sigma_+\right). \end{aligned} \tag{5.3}$$

Within this approximation, the number of excitations is a conserved quantity under unitary evolution. Therefore, the total Hilbert space $\mathcal{H}$ of the system can be conveniently divided into subspaces $\mathcal{H}_N$ where the number of excitations N is constant, i.e., $\mathcal{H} = \mathcal{H}_0 \oplus \mathcal{H}_1 \oplus \ldots$. A state belonging to a subspace $\mathcal{H}_N$ will thus remain within this subspace during any coherent dynamics that is solely governed by Hamiltonian (5.3).

However, we consider the tripartite system to be open in the sense that it interacts with an environment through one of its subsystems. Specifically, we take the left oscillator to be linearly coupled to a thermal reservoir as sketched in Fig. 5.1. Since we want this coupling to be relatively strong (compared to other environmental couplings), the right oscillator is needed as an intermediate component in order to allow for decoupling the qubit sufficiently well from the reservoir when it is used otherwise, e.g. in a computation. This deliberate and strong interaction of the left oscillator with the resistor allows us to safely neglect all other environments, e.g. those of the right oscillator and the qubit. The argument is that other environments interact much weaker and therefore induce a dynamics that occurs on a much slower time scale and thus do not contribute on the faster time scale of the reset. Hence, the system-environment interaction Hamiltonian is of the form [213]

$$\mathsf{H}_{\mathrm{I}} = \alpha\left(\mathsf{a}_{\mathrm{L}}^\dagger + \mathsf{a}_{\mathrm{L}}\right)\mathsf{V}_{\mathrm{R}}, \tag{5.4}$$

where V_{R} is an operator of the reservoir and α plays the role of an effective coupling strength. In order to derive a master equation for the open system, we utilize its instantaneous eigenbasis $\{|\Psi_n(t)\rangle\}$, defined by $\mathsf{H}(t)\,|\Psi_n(t)\rangle = \omega_n(t)\,|\Psi_n(t)\rangle$, with $\{\omega_n(t)\}$ being the respective eigenvalues. In this representation, the system-environment interaction can be rewritten as

$$\mathsf{H}_{\mathrm{I}} = \alpha\sum_{m,n} v_{mn}\,|\Psi_m(t)\rangle\langle\Psi_n(t)|\,\mathsf{V}_{\mathrm{R}}, \qquad v_{mn}(t) = \left\langle\Psi_m(t)\middle|\,\mathsf{a}_{\mathrm{L}}^\dagger + \mathsf{a}_{\mathrm{L}}\,\middle|\Psi_n(t)\right\rangle. \tag{5.5}$$

Using the standard techniques based on a weak-coupling hypothesis and the Born-Markov

and secular approximations, cf. Subsec. 2.2.1, it is possible to derive a Markovian master equation for the open system, i.e., the tripartite system. The decay rates, responsible for dissipation, are given by

$$\Gamma_{mn}(t) = \alpha^2 |v_{mn}(t)|^2 S_{\mathrm{R}}\big[\omega_{mn}(t)\big], \tag{5.6}$$

where $\omega_{mn}(t) = \omega_m(t) - \omega_n(t)$ and $S_{\mathrm{R}}(\omega)$ is the real part of the Fourier transform of the reservoir correlation function,

$$S_{\mathrm{R}}(\omega) = \int_{-\infty}^{+\infty} \mathrm{d}s\, e^{\mathrm{i}\omega s} \langle \mathsf{V}_{\mathrm{R}}(s)\mathsf{V}_{\mathrm{R}}(0)\rangle_{\mathrm{R}}\,, \tag{5.7}$$

where the average $\langle \ldots \rangle_{\mathrm{R}}$ is taken over the thermal state of the reservoir and the operators are expressed in the interaction picture with respect to the environment's Hamiltonian. This derivation yields a Lindblad master equation, cf. Eq. (2.21), that reads

$$\frac{\mathrm{d}}{\mathrm{d}t}\rho(t) = -\mathrm{i}\,[\mathsf{H}(t), \rho(t)] + \sum_{m,n} \Gamma_{mn}(t) \left(\mathsf{L}_{mn}(t)\rho(t)\mathsf{L}_{mn}^{\dagger}(t) - \frac{1}{2}\left\{ \mathsf{L}_{mn}^{\dagger}(t)\mathsf{L}_{mn}(t), \rho(t) \right\} \right), \tag{5.8}$$

where the Lindblad operators are given by $\mathsf{L}_{mn}(t) = |\Psi_m(t)\rangle\langle\Psi_n(t)|$ and describe transitions among different eigenstates. Note that a more detailed derivation of the master equation can be found in Refs. [213, 214]. The Hamiltonian $\mathsf{H}(t)$ can be controlled directly by tuning the level splittings $\omega_{\mathrm{q/L/R}}(t)$. Most importantly, the Lindblad operators and decay rates inherit the temporal dependence from the instantaneous eigenstates and eigenvalues, which in fact depend on $\omega_{\mathrm{q/L/R}}(t)$. As a consequence, Eq. (5.8) goes beyond the description based on static decay channels with constant rates that is used for most engineered protocols [130, 215–217]. It is thus one particular example for a time-local Lindblad master equation (2.21).

Unfortunately, solving the full master equation (5.8) is numerically rather challenging. In the following, we will therefore limit our calculations to a finite number of subspaces $\mathcal{H}_N$. In detail, we will consider the dynamics of the open system in the two subspaces $\mathcal{H}_0$ and $\mathcal{H}_1$, i.e., the subspace with no excitations, $\mathcal{H}_0 = \mathrm{span}\{|0,0,g\rangle\}$, and that with a single excitation, $\mathcal{H}_1 = \mathrm{span}\{|0,0,e\rangle, |0,1,g\rangle, |1,0,g\rangle\}$, where we have used the conventional short notation $|i,j,k\rangle = |i\rangle_{\mathrm{L}} \otimes |j\rangle_{\mathrm{R}} \otimes |k\rangle_{\mathrm{q}}$. In the reduced Hilbert space $\mathcal{H} = \mathcal{H}_0 \oplus \mathcal{H}_1$ and

its basis $\{|0,0,g\rangle, |0,0,e\rangle, |0,1,g\rangle, |1,0,g\rangle\}$, Hamiltonian (5.3) reads

$$H(t) = \begin{pmatrix} 0 & 0 & 0 & 0 \\ 0 & \omega_{\mathrm{q}}(t) & -\mathrm{i}g_{\mathrm{Rq}}(t) & 0 \\ 0 & \mathrm{i}g_{\mathrm{Rq}}(t) & \omega_{\mathrm{R}}(t) & g_{\mathrm{LR}}(t) \\ 0 & 0 & g_{\mathrm{LR}}(t) & \omega_{\mathrm{L}}(t) \end{pmatrix}. \tag{5.9}$$

This simplified model of the tripartite system can be solved analytically in the basis of the instantaneous eigenstates $|\Psi_1(t)\rangle, |\Psi_2(t)\rangle, |\Psi_3(t)\rangle \in \mathcal{H}_1$ and the ground state $|\Psi_0\rangle = |0,0,g\rangle$.

In the following, we will exclusively account for population decay from the excited states in $\mathcal{H}_1$ to the ground state $|\Psi_0\rangle$ as the only incoherent process. Since we can in general assume the environmental temperature to be sufficiently low such that other incoherent processes are strongly suppressed, we will neglect them. This especially involves the reverse process of thermal excitation. Due to restricting the Hilbert space and assuming low environmental temperature, we obtain a simplified version of Eq. (5.8),

$$\begin{aligned} \frac{\mathrm{d}}{\mathrm{d}t}\rho(t) &= \boldsymbol{\mathcal{L}}(t)\left[\rho(t)\right], \\ &= -\mathrm{i}\left[\mathsf{H}(t), \rho(t)\right] + \underbrace{\sum_{n=1}^{3} \Gamma_{n0}(t)\left(\mathsf{L}_n(t)\rho(t)\mathsf{L}_n^\dagger(t) - \frac{1}{2}\left\{\mathsf{L}_n^\dagger(t)\mathsf{L}_n(t), \rho(t)\right\}\right)}_{\boldsymbol{\mathcal{L}}_{\mathrm{diss}}(t)[\rho(t)]} \end{aligned} \tag{5.10}$$

where the only three remaining time-dependent Lindblad operators are given by $\mathsf{L}_n(t) = |\Psi_0\rangle\langle\Psi_n(t)|$, $n = 1,2,3$.

The model, as introduced so far, is quite general. In order to proceed with the derivation and to obtain analytical formulas for the Lindblad operators and the decay rates, we need to make specific assumptions. Therefore, we will now sketch a possible experimental realization. It will imply certain constraints and specific functional dependencies between the bare frequencies of the three subsystems, $\omega_{\mathrm{L}}(t), \omega_{\mathrm{R}}(t), \omega_{\mathrm{q}}(t)$, and their respective couplings. The model described by Hamiltonian (5.1) can for instance be realized by means of a superconducting qubit coupled to two LC resonators [213]. The resonators behave effectively as quantum harmonic oscillators, the tunable frequencies of which are determined by the capacitance C and a controllable, time-dependent inductance $L(t)$, i.e., $\omega_{L/R}(t) = 1/\sqrt{L_{L/R}(t)C_{L/R}}$. In this implementation, the couplings between the components can be expressed as functions of the physical parameters of the system and the bare resonator frequencies [213]. The assumption of sufficiently cold environments is also well fulfilled for superconducting qubits [218].

The reservoir is realized by connecting a resistor to the left resonator, cf. Fig. 5.1, with V_R in the interaction Hamiltonian (5.4) describing voltage fluctuations over the resistor. The resistor can be modeled as a thermal environment of bosonic modes [12] with the environmental correlation function (5.7) corresponding to the Johnson-Nyquist spectrum,

$$S_\mathrm{R}(\omega) = \frac{2R\omega}{1 - e^{-\omega/k_\mathrm{B}T_\mathrm{env}}}, \tag{5.11}$$

where R is the resistance of the resistor and T_env denotes its temperature [12]. At low temperature, the spectral function (5.11) strongly suppresses emission of thermal excitations from the resistor so that indeed the population decay is the leading-order dissipative process. The decay rates can be expressed as [213]

$$\Gamma_{n0}(t) = \Gamma_0 \left| \left\langle \Psi_0(t) \middle| \mathsf{a}_\mathrm{L}^\dagger + \mathsf{a}_\mathrm{L} \middle| \Psi_n(t) \right\rangle \right|^2 \frac{\omega_\mathrm{L}(t)\omega_n(t)}{\omega_\mathrm{R}(t)^2} \frac{1}{1 - e^{-\omega_n(t)/k_\mathrm{B}T_\mathrm{env}}}, \tag{5.12}$$

where Γ_0 plays the role of a static decay rate. Note that the decay rates fulfill the detailed balance condition [213]

$$\Gamma_{mn}(t) = \exp\left\{ -\frac{\omega_{mn}(t)}{k_\mathrm{B}T_\mathrm{env}} \right\} \Gamma_{nm}(t), \tag{5.13}$$

which implies suppression of thermal excitations at low temperatures and therefore constitutes just another justification that we only need to account for thermal decay processes.

With Hamiltonian (5.9) and analytical expressions for the Lindblad operators and decay rates, cf. Eq. (5.10), we can now have a closer look at the actual qubit reset problem. From an optimal control perspective, we want the qubit to be in its ground state $|g\rangle$ at final time T — independent on its initial state. While this is sufficient for a standard reset task, it is unfortunately not enough in the current case. Since resetting the qubit implies export of entropy from the qubit into the thermal environment, i.e., the resistor, it also implies that the entropy necessarily needs to pass through both harmonic oscillators during the reset process. Hence, we must ensure that the entropy is not only removed from the qubit but actually from the entire tripartite system. Otherwise the entropy might get transferred back to the qubit in an uncontrolled fashion later on. This can be avoided by ensuring that all excitations from $\mathcal{H}_1$, i.e., no matter in which subsystem they are initially located, are transferred to the total ground state $|\Psi_0\rangle = |0, 0, g\rangle$. It therefore corresponds to a full reset of the entire tripartite system. In terms of optimal control, we can ensure this by choosing the final-time functional $\mathcal{J}_T$ to

read

$$\mathcal{J}_T\left[\{\rho_l\}, T\right] = 1 - \frac{1}{3}\sum_{l=1}^{3}\left\langle\!\left\langle \rho^{\mathrm{trgt}} | \mathcal{D}_{T,t_0}[\rho_l(t_0)]\right\rangle\!\right\rangle, \qquad \rho^{\mathrm{trgt}} = |\Psi_0\rangle\langle\Psi_0|, \tag{5.14}$$

where the set of initial states $\{\rho_l(t_0)\}$ is given by the three basis states $\{|0,0,e\rangle, |0,1,g\rangle, |1,0,g\rangle\}$ for $\mathcal{H}_1$ converted to density matrices. Since $\mathcal{J}_T \in [0,1]$ measures the remaining population in $\mathcal{H}_1$ at final time T, it corresponds to the error of the reset protocol. Hence, an ideal protocol is given by $\mathcal{J}_T = 0$.

We will minimize the final-time functional $\mathcal{J}_T$ employing Krotov's method, cf. Subsec. 2.3.5, in the following. Note that this optimization problem is also particularly interesting from a control theoretical perspective, since it is modeled by a time-local master equation with an explicitly time-dependent dissipative part. The latter allows to actively modify both the Hamiltonian, which controls the coherent part of the dynamics, as well as the dissipator, which is typically time-independent and can therefore not be modified actively [9]. In order to use Krotov's method for this purpose, we need to be able to calculate the analytical derivatives of the Liouvillian $\boldsymbol{\mathcal{L}}(t)$ with respect to the control fields $\{\mathcal{E}_k\}$, i.e., $\{\omega_{\mathrm{L}}, \omega_{\mathrm{R}}, \omega_{\mathrm{q}}\}$ in our case. Since both the Hamiltonian $\mathsf{H}(t)$ and the dissipator $\boldsymbol{\mathcal{L}}_{\mathrm{diss}}(t)$ depend on the control fields, this derivative reads, cf. Eq. (5.10),

$$\frac{\partial \boldsymbol{\mathcal{L}}\left(\{\mathcal{E}_{k'}\}\right)}{\partial \mathcal{E}_k}\rho = -\mathrm{i}\left[\frac{\partial \mathsf{H}\left(\{\mathcal{E}_{k'}\}\right)}{\partial \mathcal{E}_k}, \rho\right] + \frac{\partial \boldsymbol{\mathcal{L}}_{\mathrm{diss}}\left(\{\mathcal{E}_{k'}\}\right)}{\partial \mathcal{E}_k}\rho. \tag{5.15}$$

While the derivative of the Hamiltonian with respect to ω_{L}, ω_{R} and ω_{q} is straightforward to calculate, cf. Eq. (5.9), the derivative of the dissipator $\boldsymbol{\mathcal{L}}_{\mathrm{diss}}(t)$ with respect to those fields is rather complicated to evaluate. This is due to the dependence of the decay rates $\Gamma_{n0}(t)$ and Lindblad operators $\mathsf{L}_n(t)$ on the instantaneous eigenvalues $\omega_n(t)$ and eigenstates $|\Psi_n(t)\rangle$, which are themselves complicated functions of $\omega_{\mathrm{L}}, \omega_{\mathrm{R}}$ and ω_{q}. However, the required derivatives of $\omega_n(t)$ and $|\Psi_n(t)\rangle$ with respect to ω_{L}, ω_{R}, and ω_{q} can be evaluated analytically employing computer software.

5.1.2 Optimization of the Original Protocol

We start exploring the reset problem by considering the analytical protocol that has been derived for the setup sketched in Fig. 5.1 and introduced in Ref. [213]. In this original protocol, only the left oscillator frequency $\omega_{\mathrm{L}}(t)$ has been time-dependent and controllable. The frequencies of the right oscillator and qubit, ω_{R} and ω_{q}, have been constant and we will keep them constant within this subsection. This analytical protocol is based on a simple choice for $\omega_{\mathrm{L}}(t)$, which consists of two stages, namely $\omega_{\mathrm{L}}(t) = \omega_+$

initial left oscillator frequency	$\omega_{\mathrm{L}_0}/2\pi$	11.5 GHz
right oscillator frequency	$\omega_{\mathrm{R}}/2\pi$	10.0 GHz
qubit frequency	$\omega_{\mathrm{q}}/2\pi$	9.5 GHz
static coupling between right oscillator and qubit	$g^0_{\mathrm{Rq}}/2\pi$	68 MHz
static coupling between left and right oscillator	$g^0_{\mathrm{LR}}/2\pi$	74 MHz
static decay rate	Γ_0	31 MHz
environmental temperature	T_{env}	10 mK

Table 5.1: Parameters used in the calculations for the setup shown in Fig. (5.1). The parameters are taken from Ref. [213] and correspond to an experimentally feasible circuit QED realization. T_{env} is a typical temperature for dilution refrigerators used to operate superconducting qubits [218].

and $\omega_{\mathrm{L}}(t) = \omega_-$, and the condition $\omega_{\mathrm{L}}(t_0) = \omega_{\mathrm{L}}(T) = \omega_{\mathrm{L}_0}$ for its initial and final value. The value of $\omega_{\mathrm{L}}(t)$ between different stages is changed by smooth ramps. The entire protocol reads

$$\omega_{\mathrm{L}}(t) = \begin{cases} \omega_{\mathrm{L}_0} \to \omega_+, & t_0 & \leq t < t_{\mathrm{R}}; \\ \omega_+, & t_{\mathrm{R}} & \leq t < T/2; \\ \omega_+ \to \omega_-, & T/2 & \leq t < T/2 + t_{\mathrm{R}}; \\ \omega_-, & T/2 + t_{\mathrm{R}} & \leq t < T - t_{\mathrm{R}}; \\ \omega_- \to \omega_{\mathrm{L}_0}, & T - t_{\mathrm{R}} & \leq t \leq T; \end{cases} \tag{5.16}$$

where $T/2$ is the hold time at each stage, and $t_{\mathrm{R}} \ll T$ is the ramping duration. The individual ramps follow the formula

$$\omega_{\mathrm{L}}(t) = \omega_{\mathrm{in}} + (\omega_{\mathrm{out}} - \omega_{\mathrm{in}})\, f\left(\frac{t - t_{\mathrm{in}}}{t_{\mathrm{out}} - t_{\mathrm{in}}}\right) \tag{5.17}$$

with $f(x) = 6x^5 - 15x^4 + 10x^3$, which ramps $\omega_{\mathrm{L}}(t)$ smoothly from its respective initial value ω_{in} to the intended final value ω_{out} as time t goes from t_{in} to t_{out}. The operational points ω_+ and ω_- in Eq. (5.16) have been chosen such that $\Gamma_{20}(t) \approx \Gamma_{30}(t)$ in the case of ω_+ and $\Gamma_{10}(t) \approx \Gamma_{20}(t)$ for ω_-, where the two identical rates are always as large as possible [213]. This choice guarantees that any excitation in $\mathcal{H}_1$ decays at some point during the protocol, since $\Gamma_{n0}(t)$ describes the decay from $|\Psi_n(t)\rangle$ into the target state $|\Psi_0\rangle$. We will refer to this scheme as protocol of sequential resonances (SR). The physical parameters for the tripartite system are summarized in Table 5.1.

We start by inspecting the performance of the original, analytical and non-optimized version of the SR scheme [213]. The solid blue line in Fig. 5.2 shows its performance as function of the protocol duration T. It shows a rapid approach towards errors $\mathcal{J}_T$ as small as 10^{-6} for $T = 2000\,\mathrm{ns}$. Although this is sufficiently small for most applications, the

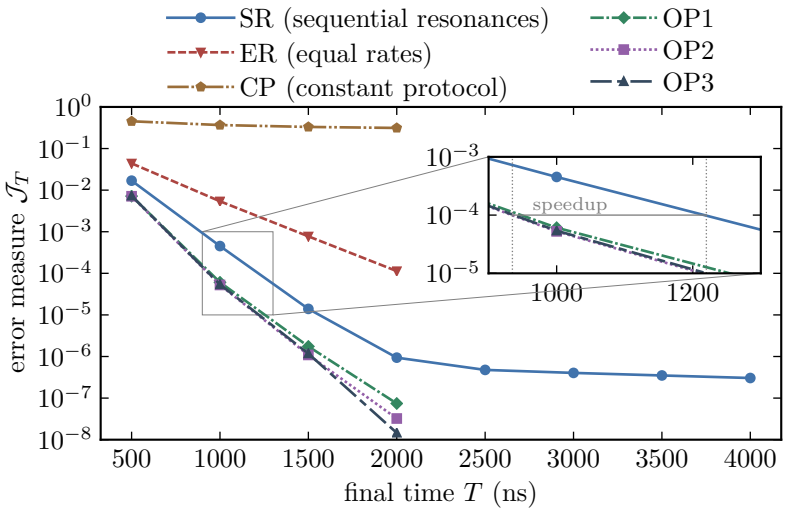

Figure 5.2: Excited state population $\mathcal{J}_T$, Eq. (5.14), as a function of the protocol duration T for different control fields. SR denotes the original protocol utilizing sequential resonances with the resistive environment [213], CP refers to a protocol with only constant fields, and OP1, OP2, and OP3 are results obtained with SR or CP as guess control fields to start the optimization (see main text for detailed explanations). An optimization targeting equal dissipation rates, cf. Eq. (5.18), instead of minimizing $\mathcal{J}_T$ is labeled by ER. The inset highlights the speedup due to the optimization, by comparing the durations for which the optimized protocols and the SR reach an error of $\mathcal{J}_T = 10^{-4}$. All physical parameters are summarized in Table 5.1.

SR exhibits a plateau for longer durations, which prevents it from reaching significantly smaller errors. This plateau is caused by population being locked in the excited state of the right oscillator — an unfavorable feature that is apparently not resolvable by simply extending the protocol duration T. However, taking Eq. (5.16) as the initial guess field for an optimization using Krotov's method, the green dashed double-dotted line in Fig. 5.2 shows that, depending on T, an improvement of up to two orders of magnitude in the error $\mathcal{J}_T$ compared to the SR is possible. In addition, this optimized protocol (referred to as OP1) even resolves the issue of the plateau by reaching errors $\mathcal{J}_T < 10^{-7}$. However, the improvement with respect to the original protocol duration is comparatively modest as the inset of Fig. 5.2 illustrates. Taking e.g. $\mathcal{J}_T = 10^{-4}$ as a sufficiently small error, the speedup with respect to the SR is roughly $\Delta T \approx 280\,\mathrm{ns}$.

Figure 5.3 compares the dynamics of the original protocol SR and its optimized version OP1 for a protocol duration of $T = 1500\,\mathrm{ns}$. It shows the population of the excited eigenstates in Figs. 5.3(a), their respective decay rates in Fig. 5.3(b) and the control field $\omega_\mathrm{L}(t)$ that generates the dynamics in Fig. 5.3(c). However, before having a closer look at the dynamics under the optimized field, it is instructive to understand

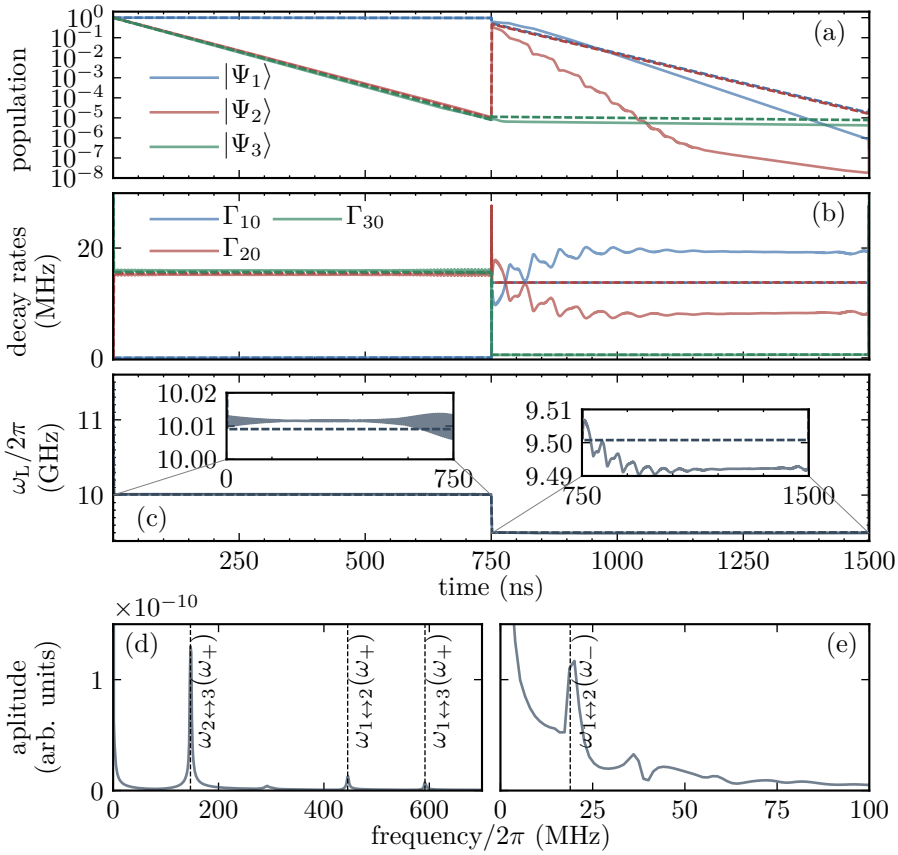

Figure 5.3: Dynamics for the SR (dashed lines) and its optimized version OP1 (solid lines) for a protocol duration of $T = 1500\,\text{ns}$, cf. Fig. 5.2. (a) Population in the three eigenstates of the excited subspace $\mathcal{H}_1$. (b) Decay rates $\Gamma_{n0}(t)$, cf. Eq. (5.12), from $\mathcal{H}_1$ into the total ground state $|\Psi_0\rangle$. (c) Left oscillator frequency $\omega_L(t)$ following the original two stage protocol of Eq. (5.16). The two stages are still visible in the optimized version, with modulations on top, as highlighted by the two insets. The shaded area in the left inset corresponds to fast oscillations, which are not resolved due to the linewidth. (d) and (e) show the frequency spectra of the optimized level splitting $\omega_L(t)$ from the left and right insets of (c), respectively. The vertical lines indicate frequency differences, $\omega_{i\leftrightarrow j} \equiv |\omega_i - \omega_j|$ with $\omega_i = \omega_i(\omega_L)$ being the instantaneous eigenvalues.

the dynamics under the analytical field (5.16), shown as dashed lines in Fig. 5.3. We find that the original two-stage protocol (SR) acts as intended, i.e., the population decays from all three eigenstates of $\mathcal{H}_1$. However, it is important to note that the intermediate ramp from ω_+ to ω_- transfers a significant amount of population from $|\Psi_1(t)\rangle$ to $|\Psi_2(t)\rangle$. Hence, $\Gamma_{20}(t)$ needs to be sufficiently large also during the second stage, which is guaranteed by the choice of ω_- and ω_+ that ensures $\Gamma_{20}(t)$ to be large in both stages. Such a population transfer between different eigenstates within $\mathcal{H}_1$ occurs due to non-adiabatic transitions caused by changes of those particular eigenstates.

The origin of these non-adiabatic transitions is that the Hamiltonian (5.9), if expressed in its eigenbasis $\{|\Psi_0\rangle, |\Psi_1(t)\rangle, |\Psi_2(t)\rangle, |\Psi_3(t)\rangle\}$ and adapted to satisfy the Lindblad master equation (5.10), contains terms like $-\mathrm{i}\,|\Psi_n(t)\rangle\langle\dot{\Psi}_m(t)|$, which describe an effective coupling between $|\Psi_n(t)\rangle$ and $|\Psi_m(t)\rangle$. These couplings become small for adiabatic, i.e., slow, changes in the eigenstates or vanish completely if they are constant. However, the relatively fast ramps of $\omega_\mathrm{L}(t)$ necessarily cause the eigenstates to change rapidly and therefore give rise to significant non-adiabatic couplings and the observed population transfer. It should nevertheless be noted that the population transfer between different eigenstates due to non-adiabatic transitions is always accompanied by a contribution originating from the change in the eigenstates themselves.

A similar reasoning readily explains the structure of the optimized control field in case of OP1, shown as solid line in Fig. 5.3(c). Compared to the SR, the optimization effectively shifts the base levels of ω_L at both stages and adds oscillations on top. This results in an increase of $\Gamma_{10}(t)$ and a decrease of $\Gamma_{20}(t)$, cf. Fig. 5.3(b) — in particular during the protocol's second stage. This directly causes the population of $|\Psi_1(t)\rangle$ ($|\Psi_2(t)\rangle$) to decay faster (slower). The additional oscillations, even though having small amplitude, drive non-adiabatic transitions between $|\Psi_1(t)\rangle$ and $|\Psi_2(t)\rangle$, which primarily transfer population from the slow decaying state $|\Psi_2(t)\rangle$ to the fast decaying state $|\Psi_1(t)\rangle$, cf. Fig. 5.3(a). This becomes even more clear by inspecting Figs. 5.3(d) and 5.3(e), which show the spectra corresponding to the insets of Fig. 5.3(c). In both cases, the frequencies match the differences between various eigenvalues ω_n, evaluated for $\omega_\mathrm{L} = \omega_+$ and $\omega_\mathrm{L} = \omega_-$ in the left and right inset, respectively. Whereas the spectrum shown in Fig. 5.3(d) is dominated by a peak at $\omega_{2\leftrightarrow 3}$, which does not seem to have a noticeable impact on the dynamics, Fig. 5.3(e) exhibits a peak at $\omega_{1\leftrightarrow 2}$ and is responsible for the above-mentioned population transfer between $|\Psi_1(t)\rangle$ and $|\Psi_2(t)\rangle$. The combination of increasing decay rates and engineered population transfer results in the excitation to decay more efficiently from both states. The required control of the left oscillator frequency $\omega_\mathrm{L}(t)$ can, for instance, be achieved by Josephson parametric amplifiers [219].

In summary, the optimization studied in Fig. 5.3 changes both the coherent and dissipative part of the evolution compared to the SR, creating non-adiabatic transitions by suitably modulating $\omega_\mathrm{L}(t)$ and adapting the decay rates $\Gamma_{n0}(t)$ accordingly. Both effects are necessary to explain the observed improvement with respect to the SR. In order to demonstrate that this interplay of adapting the decay rates and driving non-adiabatic transitions between the eigenstates is crucial for the success of the reset protocol, Fig. 5.2 also shows optimization results where the dynamics has been completely ignored in the optimization process. In this case, the minimization of Eq. (5.14) via minimizing the total

functional (2.32) with Krotov's method has been replaced by a total functional targeting equal dissipation rates (ER). In detail, $\omega_{\mathrm{L}}(t)$ has been optimized to yield $R_1 \approx R_2 \approx R_3$ (with each R_i as large as possible), where

$$R_n = \int_0^T \Gamma_{n0}(t)\mathrm{d}t, \qquad i = 1,2,3, \tag{5.18}$$

are the time-integrated dissipation rates which are independent of the system dynamics. Since we have analytical expressions for the decay rates, such an optimization does not require any information from the time-evolved states. The naive assumption behind this optimization is that, since all states ρ_1, ρ_2, ρ_3 are equally important and weighted in Eq. (5.14), equal dissipation from all of them may be a good choice to decrease the error $\mathcal{J}_T$. However, this is not the case as Fig. 5.2 demonstrates. This emphasizes the crucial interplay of coherent and dissipative dynamics for the problem at hand.

5.1.3 Optimization with an Extended Set of Control Fields

So far, only the left oscillator frequency $\omega_{\mathrm{L}}(t)$ has been utilized for the reset protocol, as it has been the only time-dependent, controllable field in the analytical SR as well as its optimized version OP1. In the following, we therefore assume the frequencies of the right oscillator and of the qubit, $\omega_{\mathrm{R}}(t)$ and $\omega_{\mathrm{q}}(t)$, to be time-dependent and controllable as well. The rationale is that this will readily extend the general possibilities of the reset protocol, since the eigenvalues $\omega_n(t)$ and eigenstates $|\Psi_n(t)\rangle$, $n = 1,2,3$, depend non-trivially on all three frequencies, ω_{L}, ω_{R} and ω_{q}. Thus, changing any of the two newly time-dependent fields may affect the dynamics and reset task beneficially. In other words, more control fields give the optimization more flexibility to steer the dynamics in the desired way and engineer the dissipation rates more appropriately.

Since we already know that the reset protocol crucially depends on the interplay of coherent dynamics and engineered dissipation rates, we first inspect in Fig. 5.4 how the decay rates change as a function of the three level splittings ω_{L}, ω_{R}, and ω_{q}. In general, with ω_{L} being the only time-dependent field and ω_{R} and ω_{q} being fixed with their parameters as in Table 5.1, any optimization with these restrictions can only access decay rates described by the lower axes of the middle column of Fig. 5.4. The two spots of the SL are marked by a blue cross for $\omega_{\mathrm{L}} = \omega_+$ and an orange cross for $\omega_{\mathrm{L}} = \omega_-$ and deviating from these spots, i.e., changing ω_{L}, implies moving on this lower axis. However, with ω_{R} and ω_{q} now being time-dependent as well, the optimization can access the full space of decay rates. Two important observations can be made from Fig. 5.4 in that respect. On the one hand, we observe that the decay rates are still mutually exclusive in

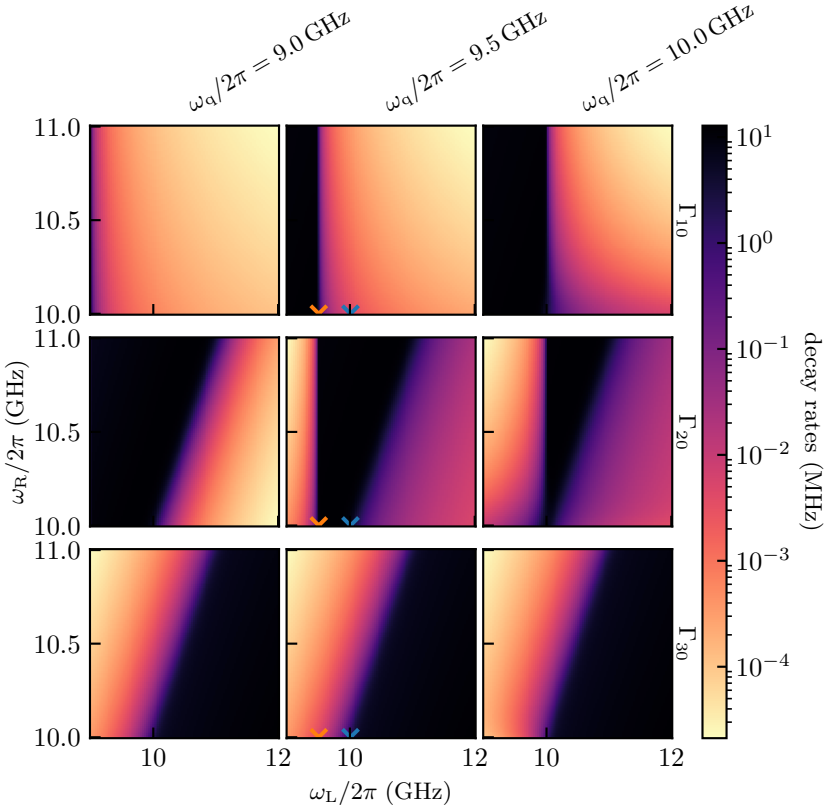

Figure 5.4: Decay rates Γ_{n0} from the excited subspace $\mathcal{H}_1$ into the total ground state $|\Psi_0\rangle$, cf. Eq. (5.12), as a function of level splittings ω_L and ω_R and for three different values of ω_q (as indicated on top of each column). The decay rates for the two stages $\omega_L = \omega_+$ and $\omega_L = \omega_-$ of the SL are marked by a blue and orange cross, respectively.

the sense that there exists no combination such that two or more of them are maximal at the same time. It is only possible that two of them are simultaneously large but not maximal. An example for the latter is given by the two stages ω_+ and ω_-. On the other hand, the attainable total maximum of each individual decay rate as a function of all three controls ω_L, ω_R and ω_q does not change. Hence, adjusting ω_R or ω_q in addition to ω_L does not yield essentially larger rates, and there will not be a significantly faster decay to the ground state. Nevertheless, although no direct improvement is to be expected from simply increasing the decay rates, i.e., due to the dissipative part of the dynamics, one may still achieve an improvement by more appropriately steering the coherent part.

Figure 5.2 also includes optimization results (referred to as OP2) for the case where all three frequencies are time-dependent. The initial guess fields have been chosen according to the SR, i.e., taking Eq. (5.16) for $\omega_L(t)$ and constant values for $\omega_R(t)$, $\omega_q(t)$. As

evidenced by Fig. 5.2, despite the extended set of controls, the optimization does not yield errors $\mathcal{J}_T$ significantly below the case where $\omega_\mathrm{L}(t)$ is the only time-dependent control field. This finding is reproducible even when using different sets of controls, for instance such as only using $\omega_\mathrm{q}(t)$ and $\omega_\mathrm{L}(t)$ or only using $\omega_\mathrm{q}(t)$ and $\omega_\mathrm{R}(t)$. Therefore, we expect that using further control fields beyond $\omega_\mathrm{L}(t)$ does not allow us to steer the coherent part of the dynamics more efficiently.

In order to study and justify this expectation in more detail and evaluate the general impact of the guess fields, it is necessary and instructive to conduct further optimizations with all three possible controls. However, since the optimized solution depends strongly on the initial guess fields, we will now choose guess fields that differ substantially from the SR. To this end, the right oscillator and qubit frequencies, $\omega_\mathrm{R}(t)$ and $\omega_\mathrm{q}(t)$, can initially again be chosen constant. Conversely, in order for $\omega_\mathrm{L}(t)$ to differ from the two stages of the SR, we can choose it effectively constant, namely as $\omega_\mathrm{L}(t) = (\omega_+ + \omega_-)/2$ with additional ramps in the beginning and end to ensure that ω_L starts and ends at ω_{L_0}. Due to this choice, $\Gamma_{20}(t)$ is almost maximal during the entire protocol, whereas $\Gamma_{10}(t)$ and $\Gamma_{30}(t)$ are both orders of magnitude smaller. In terms of Fig. 5.4, this operational point is just the middle between the blue and orange cross. In consequence, only population in $|\Psi_2(t)\rangle$ decays fast while the population in the other two excited eigenstates $|\Psi_1(t)\rangle$ and $|\Psi_3(t)\rangle$ is almost conserved, since, due to the constancy of the guess fields, no non-adiabatic transitions reshuffle the population. Hence, extending the protocol duration T will obviously not resolve the problem. The performance of this constant protocol (CP) is included in Fig. 5.2 and yields, as expected, very large reset errors $\mathcal{J}_T$. We might therefore call this a rather bad choice. Nevertheless, by taking the constant fields as guess fields, the optimization (referred to as OP3) is again able to find optimized control fields that yield similarly small errors $\mathcal{J}_T$ as before, cf. OP3 with OP1 and OP2 in Fig. 5.2.

We again analyze an exemplary dynamics for $T = 1500\,\mathrm{ns}$ in Fig. 5.5. Figure 5.5(a) shows the population dynamics. As expected, the population in $|\Psi_2(t)\rangle$ decays rapidly under the constant guess fields, while $|\Psi_3(t)\rangle$ exhibits only slow decay and the population in $|\Psi_1(t)\rangle$ is almost constant. The respective decay rates and control fields are shown in Figs. 5.5(b) and 5.5(c). Interestingly, the optimization OP3 leaves the base levels of each control field unchanged while again only adding small oscillations on top. In consequence, the decay rates do not change in magnitude but exhibit small oscillations as well. Thus, since $\Gamma_{20}(t)$ is essentially already maximal by choice of the constant guess fields, cf. Fig. 5.4, there is no possibility for the optimization to further increase it. Instead, the optimization ensures that all excitations are coherently transferred, again via

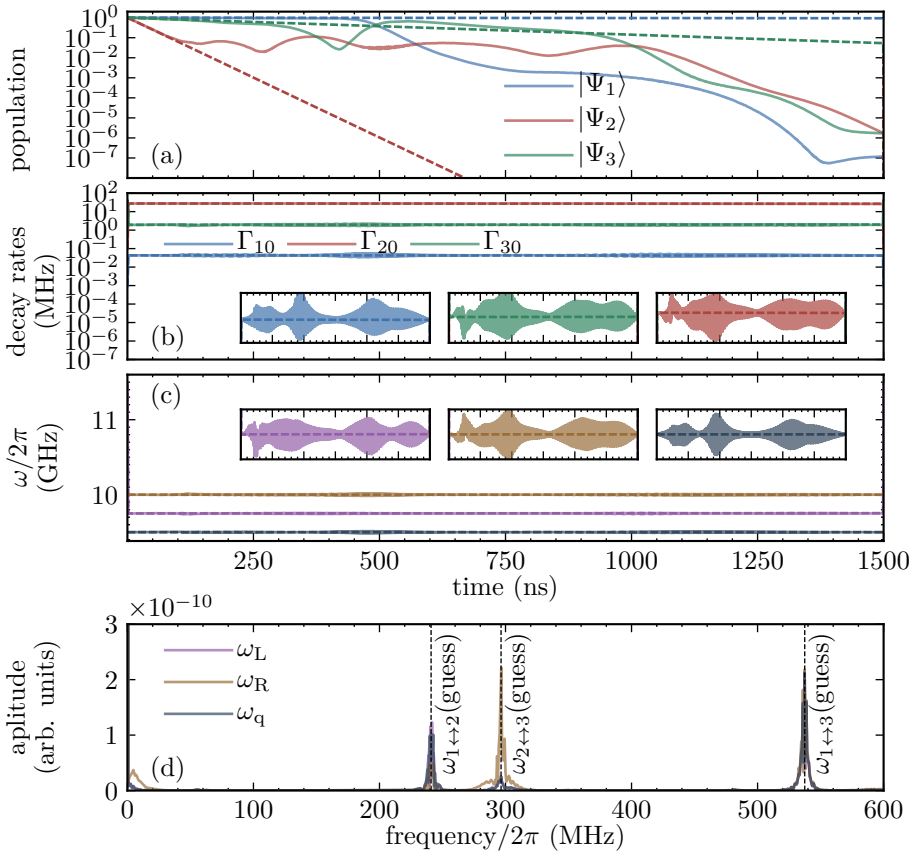

Figure 5.5: Dynamics obtained with the constant protocol CP (dashed lines) as guess and its optimized version OP3 (solid lines). The panels are as in Fig. 5.3 with the small insets in (b) and (c) providing a closer look at the shapes of the optimized fields, respectively decay rates, compared to their non-optimized, constant counterparts. Panel (d) shows the spectra of all optimized fields from panel (c).

engineered non-adiabatic transitions, to this strongly decaying state — in our example from $|\Psi_1(t)\rangle$ and $|\Psi_3(t)\rangle$ to $|\Psi_2(t)\rangle$, as evident from Fig. 5.5(a). Thus, we find a similar reset strategy as in Fig. 5.3: The control fields are tailored such that a single decay rate (at least in theory not necessarily the same at different times) is maximal and population is transferred coherently into this strongly decaying state.

Especially with the insights from the control strategies of OP1 and OP3, illustrated in Figs. 5.3 and 5.5, we expect the same unique reset strategy to be feasible for essentially any combination of control fields and choice of guess fields. This follows from the decay rates being mutually exclusive, cf. Fig. 5.4, i.e., if one state from the set $\{|\Psi_1(t)\rangle, |\Psi_2(t)\rangle, |\Psi_3(t)\rangle\}$ has a maximal decay rate, the other two states necessarily decay much slower. Hence, all that is required is to ensure coherent population transfer into

this state, which seems to be always possible by tailoring the control fields appropriately via optimal control.

Another interesting result from extending the set of control fields is that the addition of further control fields beyond $\omega_{\mathrm{L}}(t)$ does not result in significantly smaller errors $\mathcal{J}_T$, cf. Fig. 5.2. In fact, our results suggest that $\omega_{\mathrm{L}}(t)$ alone is already sufficient to fully control the decay rates and engineer the required population transfer for the identified strategy to work. Nevertheless, while additional control fields beyond $\omega_{\mathrm{L}}(t)$ might not be necessary from a control theoretical perspective, we have demonstrated that the same small reset error can also be achieved with different sets of controls. This observation is still valuable as it increases the flexibility for its realization and is thus potentially beneficial in experiments — especially if certain control fields are experimentally more convenient to implement than others.

Finally, inspecting Fig. 5.2 suggests that we have actually identified the quantum speed limit for the reset protocol for the tripartite scenario sketched in Fig. 5.1. While it should be kept in mind that numerical optimal control can never provide a rigorous mathematical proof of (time-)optimality, our numerical results strongly support this assumption. On the one hand, all different sets of control fields and guess choices (even those not shown in Fig. 5.2) converge to roughly the same final error $\mathcal{J}_T$ which is only defined by the protocol duration T. On the other hand, the structure of the decay rates, cf. Fig. 5.4, only allows for large decay rates if they are mutually exclusive. Hence, the identified control strategy that reshuffles the population of all excited states into the only strongly decaying one seems to be quite general.

To briefly conclude this section, we have investigated a reset protocol that utilizes a tunable environment. Starting from an analytical reset scheme proposed in Ref. [213], we have demonstrated that the reset can be improved in fidelity and time when optimized control fields are used. We have furthermore shown that similarly small reset errors can be achieved with various combinations of conceivable control fields and are therefore convinced that we have identified the quantum speed limit for the considered physical setting.

5.2 Qubit Reset with an Ancilla System

In contrast to a reset protocol that utilizes a tunable environment for qubit reset, in this section we will now switch to qubit reset employing a single ancilla system from the environment. While both reset strategies rely on an effectively controllable coupling to an environment or environmental mode, qubit reset via an ancilla system typically allows

for a larger variety in the qubit's dynamics. This is due to the ancilla's strong coupling to the qubit, which, for instance, allows the qubit dynamics to become non-Markovian. This has not been possible for the reset task considered in the last section or for driven-dissipative dynamics in general [126, 220–222]. Another aspect that can be ignored for weakly coupled environments, independent on whether their effective coupling is static or tunable due to a drive, but becomes relevant for strongly coupled ancillas, is that such strong couplings between system and ancilla, i.e., between system and environment, are usually accompanied by an increasing chance for these modes to become correlated. While correlations, and especially entanglement, between qubits are a key feature and advantage for many quantum technologies, correlations of a qubit — or more generally an open quantum system — with its environment typically cause problems when using it. Hence, a reliable qubit reset does not only need to map the qubit to a pure state but should also erase all initial correlations with the environment or any other mode. In terms of reset fidelity, this problem is solved if we are able to reset the qubit to a pure state, since a pure state implies vanishing correlations with any other mode. However, the problem raised by initial correlations is rather whether we are able to erase them at all and how their presence at initial time influences the reset protocol's fidelity and time. Thus, in the following section we will focus on resetting an initially correlated qubit using optimized control fields. The results in this section are based on Ref. [223].

5.2.1 Model and Control Problem

The open system considered in the following consists of a single qubit in interaction with an external field. Its Hamiltonian reads

$$\mathsf{H}_{\mathrm{Q}}(t) = -\frac{\omega_{\mathrm{Q}}}{2}\sigma_{\mathrm{z}}^{\mathrm{Q}} - \frac{\mathcal{E}(t)}{2}\sigma_{\mathrm{z}}^{\mathrm{Q}}, \tag{5.19}$$

where ω_{Q} is the qubit's level splitting and $\mathcal{E}(t)$ a control field that can be used to steer the qubit's dynamics and that we will optimize via optimal control. σ_i, $i = \mathrm{x}, \mathrm{y}, \mathrm{z}$, are the usual Pauli matrices.

We assume the qubit to interact with an environment that, in general, gives rise to non-Markovian dynamics. Although such an environment can take various forms, we will take a very simple realization where it is given by a single mode that couples weakly to a large environment of harmonic modes [224]. This mode, which will act as our ancilla system for the reset, is taken to be another two-level system with Hamiltonian $\mathsf{H}_{\mathrm{A}} = -\omega_{\mathrm{A}}\sigma_{\mathrm{z}}^{\mathrm{A}}/2$ and level splitting ω_{A}. Figure 5.6 sketches the setup of qubit, ancilla and remaining environment. In this model, the ancilla is not necessarily weakly coupled

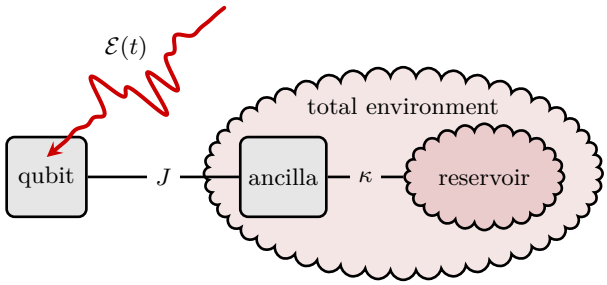

Figure 5.6: A sketch of the physical setup. We consider a qubit (Q) strongly coupled to an ancilla two-level system (A) that is in fact weakly coupled to a reservoir. The ancilla and reservoir together define the total environment for the qubit. Due to the strong coupling J between qubit and ancilla, the qubit dynamics may become non-Markovian. The ancilla and reservoir couple with strength κ. The qubit couples to the reservoir only indirectly.

to the open system. We therefore treat the interaction between the open system, i.e., the qubit, and the ancilla exactly, i.e., we do not employ an effective description of the reduced qubit dynamics in the spirit of a master equation. This allows us to fully capture the correlations between qubit and ancilla in whose influence on the reset process we are interested in. For the rest of the environment, i.e., the environment of harmonic oscillators, we employ the usual approximations, summarized in Subsec. 2.2.1, which lead to the standard Markovian master equation, cf. Eq. (2.21), for the joint state $\rho(t)$ of qubit and ancilla [49, 52, 224, 225],

$$\begin{aligned} \frac{\mathrm{d}}{\mathrm{d}t}\rho(t) &= -\mathrm{i}\left[\mathsf{H}(t), \rho(t)\right] + \boldsymbol{\mathcal{L}}_{\mathrm{diss}}\left[\rho(t)\right], \\ \boldsymbol{\mathcal{L}}_{\mathrm{diss}}\left[\rho(t)\right] &= \sum_{k=1,2} \kappa \left(\mathsf{L}_k \rho(t) \mathsf{L}_k^\dagger - \frac{1}{2}\left\{ \mathsf{L}_k^\dagger \mathsf{L}_k, \rho(t) \right\} \right), \end{aligned} \tag{5.20}$$

with the Hamiltonian for the bipartite system of qubit and ancilla given by

$$\mathsf{H}(t) = \mathsf{H}_{\mathrm{Q}}(t) \otimes \mathbb{1}_{\mathrm{A}} + \mathbb{1}_{\mathrm{Q}} \otimes \mathsf{H}_{\mathrm{A}} + \mathsf{H}_{\mathrm{I}} \tag{5.21}$$

and their static interaction by

$$\mathsf{H}_{\mathrm{I}} = J\left(\sigma_{\mathrm{x}}^{\mathrm{Q}} \otimes \sigma_{\mathrm{x}}^{\mathrm{A}}\right). \tag{5.22}$$

The Lindblad operators L_k in Eq. (5.20) model the thermal equilibration of the ancilla induced by the remaining reservoir and correspond to those of the optical master equation (2.16). In terms of operators on the bipartite Hilbert space $\mathcal{H} = \mathcal{H}_{\mathrm{Q}} \otimes \mathcal{H}_{\mathrm{A}}$ they

read

$$\mathsf{L}_1 = \sqrt{N+1}\left(\mathbb{1}_\mathrm{Q} \otimes \sigma_-^\mathrm{A}\right), \qquad \mathsf{L}_2 = \sqrt{N}\left(\mathbb{1}_\mathrm{Q} \otimes \sigma_+^\mathrm{A}\right), \tag{5.23}$$

where $N = 1/\left(e^{\beta\omega_\mathrm{A}} - 1\right)$ is the Planck distribution and β the inverse thermal energy of the reservoir. The state of the qubit $\rho_\mathrm{Q}(t)$, in which we are exclusively interested in, is obtained by tracing out the ancilla degrees of freedom. This model constitutes one of the simplest realization to describe the qubit's generally non-Markovian dynamics by using the separation of the total environment into a strongly and weakly coupled part, i.e., into a primary and secondary environment. This has been introduced in detail in Subsec. 2.2.2 and, for the general case, sketched in Fig. 2.1. Hamiltonian (5.21) is therefore equivalent to $\mathsf{H}_\mathrm{S}^\mathrm{eff}(t)$ in Eq. (2.24) and the influence of the secondary environment, here given by the reservoir, is described by the Lindblad master equation (5.20).

Resetting the qubit requires transferring its initial state to a pure target state. In the following, this pure target state will be the qubit's ground state, which is typically chosen and the reason why resetting the qubit is sometimes also referred to as cooling. Besides the quantum thermodynamical aspect of qubit reset, which already justifies the term "cooling", it can also be explained by inspecting the decay rates of the optical master equation, i.e., Eq. (2.16). They reveal that in case of cold environments with large β and thus vanishing N, the environment induces the desired incoherent decay into the qubit's ground state. Hence, bringing the qubit in contact with a cold environment is theoretically sufficient for resetting it. In the model described by Fig. 5.6 this is not an option, since we assume that the environment, and especially the reservoir, which describes the largest part of the total environment, is simply not sufficiently cold for this to work. Moreover, we want to explore the fast time scale set by the strong coupling to the ancilla and not the slow one induced by the remaining environment. This is possible, since we assume an exchange interaction between qubit and ancilla of the form $\mathsf{H}_\mathrm{I} = J(\sigma_\mathrm{x}^\mathrm{Q} \otimes \sigma_\mathrm{x}^\mathrm{A})$, which allows the exchange of entropy. On the one hand, we assume the coupling J between qubit and ancilla to be much larger than the coupling κ. Otherwise the dynamics of the qubit would be Markovian and its reset would again be a simple thermalization process. On the other hand, J is still small with respect to the level splittings ω_Q and ω_A of qubit and ancilla. The corresponding timescale separation ensures detailed balance and accordance with the second law of thermodynamics [226].

As a remark, note that both the interaction $\mathsf{H}_\mathrm{I} = J(\sigma_\mathrm{x}^\mathrm{Q} \otimes \sigma_\mathrm{x}^\mathrm{A})$, cf. Eq. (5.22), and the type of local control $\mathsf{H}_\mathrm{ctrl}(t) = -\mathcal{E}(t)\sigma_\mathrm{z}^\mathrm{Q}/2$, cf. Eq. (5.19), can also be chosen differently and still give rise to an entropy exchange between qubit and ancilla. We will delve deeper

into different interactions and local controls in Sec. 5.3. For the moment, however, we will restrict ourselves to these choices.

Our main goal in this section will be to analyze the impact of initial correlations between qubit and environment, i.e., between qubit and ancilla, on the reset protocol. We will therefore take several initial states for the qubit and the ancilla into account. Since the ancilla is physically part of the total environment, we always assume it to be initially in thermal equilibrium with the reservoir. In order to fully understand the role of initial correlations between qubit and ancilla, we first start by understanding qubit reset if both systems are initially uncorrelated, i.e., are factorized, and generalize it to correlated states later. For the sake of comparability, we will assume that the initial state of the qubit is quasi-thermalized with the reservoir as well. The respective initial state for qubit or ancilla reads

$$\rho_\alpha^{\mathrm{th}} = \frac{e^{x_\alpha}\left|0\right\rangle\left\langle 0\right| + e^{-x_\alpha}\left|1\right\rangle\left\langle 1\right|}{2\cosh\left(x_\alpha\right)}, \qquad x_\alpha = \frac{\omega_\alpha \beta}{2}, \tag{5.24}$$

with $\alpha \in \{\mathrm{Q}, \mathrm{A}\}$. In the factorized case, the joint state of qubit and ancilla at initial time t_0, i.e., the initial state of the bipartite system for which we then need to find the dynamics that resets the qubit into its ground state, reads

$$\rho_1^{\mathrm{init}} = \rho_{\mathrm{Q}}^{\mathrm{th}} \otimes \rho_{\mathrm{A}}^{\mathrm{th}}. \tag{5.25}$$

For non-factorizing initial conditions, we will also investigate the fully thermalized state of qubit and ancilla, which is the steady state of the bipartite system and therefore a natural choice. In the standard two qubits basis $\{\left|00\right\rangle, \left|01\right\rangle, \left|10\right\rangle, \left|11\right\rangle\}$, it reads

$$\rho_2^{\mathrm{init}} = \rho^{\mathrm{th}} = \frac{1}{Z}\begin{pmatrix} \lambda_+ & 0 & 0 & \zeta_+ \\ 0 & \mu_+ & \zeta_- & 0 \\ 0 & \zeta_- & \mu_- & 0 \\ \zeta_+ & 0 & 0 & \lambda_- \end{pmatrix}, \tag{5.26}$$

where $Z = 2\left[\cosh\left(x_+\right) + \cosh\left(x_-\right)\right]$ is the partition function and

$$\begin{aligned} \delta_\pm &= \omega_{\mathrm{Q}} \pm \omega_{\mathrm{A}}, & \lambda_\pm &= \cosh\left(x_+\right) \pm \frac{\delta_+}{\Omega_+}\sinh\left(x_+\right), \\ x_\pm &= \frac{\Omega_\pm \beta}{2}, & \mu_\pm &= \cosh\left(x_-\right) \pm \frac{\delta_-}{\Omega_-}\sinh\left(x_-\right), \\ \Omega_\pm &= \sqrt{\delta_\pm^2 + 4J^2}, & \zeta_\pm &= -\frac{2J}{\Omega_\pm}\sinh\left(x_\pm\right). \end{aligned} \tag{5.27}$$

Since the thermal equilibrium state (5.26) can always be reached by waiting sufficiently long, the control problem of resetting the qubit is theoretically solved if we can solve it for this particular initial state. For any realistic choice of parameters, the initial correlations between qubit and ancilla for this thermalized state are present but rather small. Therefore, in order to examine the impact of initial correlations for the reset in more detail, we artificially add correlations to the factorizing initial state (5.25),

$$\rho_3^{\text{init}} = \rho_{\text{Q}}^{\text{th}} \otimes \rho_{\text{A}}^{\text{th}} + \begin{pmatrix} 0 & 0 & 0 & 0 \\ 0 & 0 & \gamma & 0 \\ 0 & \gamma^* & 0 & 0 \\ 0 & 0 & 0 & 0 \end{pmatrix}. \tag{5.28}$$

Although γ can theoretically be an arbitrary complex number, motivated by Eq. (5.26) we choose $0 > \gamma \in \mathbb{R}$ where we only need to ensure that ρ_3^{init} is still a valid density matrix. Mathematically, this just implies that there is, depending on $\rho_{\text{Q}}^{\text{th}}$ and $\rho_{\text{A}}^{\text{th}}$, a maximum $|\gamma| \leq \gamma_{\text{max}}$ beyond which ρ_3^{init} looses its positive semi-definiteness. Conceptually, it is also important to note that the addition of correlations via γ does not change the reduced states of both the qubit and the ancilla, i.e., $\rho_{\text{Q}}^{\text{th}} = \text{tr}_{\text{A}}\{\rho_3^{\text{init}}\}$ and $\rho_{\text{A}}^{\text{th}} = \text{tr}_{\text{Q}}\{\rho_3^{\text{init}}\}$ for all γ, but increases the purity of their bipartite state ρ_3^{init}.

The total amount of correlations between qubit and ancilla can be quantified in terms of the mutual information $\mathcal{I} = \mathcal{C} + \mathcal{Q}$ [227]. The latter measures the total amount of correlations, both classical $\mathcal{C}$ and quantum $\mathcal{Q}$, between system and ancilla, i.e., between system and environment. The mutual information can be calculated via the von Neumann entropy $E(\rho)$, cf. Eq. (3.13) and Ref. [114]. For a general bipartite system with Hilbert space $\mathcal{H} = \mathcal{H}_{\text{Q}} \otimes \mathcal{H}_{\text{A}}$ and subsystems Q and A with respective Hilbert spaces $\mathcal{H}_{\text{Q}}$ and $\mathcal{H}_{\text{A}}$, it reads

$$\mathcal{I}\left(\rho_{\text{QA}}\right) = E\left(\rho_{\text{Q}}\right) + E\left(\rho_{\text{A}}\right) - E\left(\rho_{\text{QA}}\right) \geq 0, \tag{5.29}$$

where ρ_{Q} and ρ_{A} are the reduced states of subsystems Q and A. If their joint state ρ_{QA} is uncorrelated, i.e., $\rho_{\text{QA}} = \rho_{\text{Q}} \otimes \rho_{\text{A}}$, we find $\mathcal{I} = 0$, i.e., the entropy stored in ρ_{QA} is equivalent to that stored in both local states ρ_{Q} and ρ_{A} together. The argument can also be viewed from an information theoretical perspective, since the von Neumann entropy $E(\rho)$ can be related to the classical Shannon entropy [228], which quantifies the amount of information stored in an entity, i.e., a density matrix in our case. This information argument becomes more clear for correlated states with $\mathcal{I} > 0$ where it implies that the entropy of the two local states ρ_{Q} and ρ_{A} together is larger than that of their joint state

ρ_{QA}. Conversely, this implies that the combined information stored in the two local states is less than what is stored in their joint state. Thus, some of the information needs to be stored in the non-local part of ρ_{QA}. Unfortunately, the mutual information itself does not distinguish between quantum correlations $\mathcal{Q}$ and classical correlations $\mathcal{C}$. Hence, in order to distinguish between these, various concepts and measures have been introduced [229]. In the following, we will use quantum discord [230] as one particular measure to quantify $\mathcal{Q}$. It has the advantage of being analytically computable [231] for all states accessible by the dynamics governed by Eq. (5.20). In addition to quantum discord, we also calculate the amount of entanglement, as one of the most prominent representative of quantum correlations, in terms of the concurrence [232]

$$C(\rho) = \max\left\{0, \sqrt{\lambda_1} - \sqrt{\lambda_2} - \sqrt{\lambda_3} - \sqrt{\lambda_4}\right\}, \tag{5.30}$$

where $\lambda_1 \geq \cdots \geq \lambda_4 \geq 0$ are the ordered eigenvalues of $\rho \mathsf{Y} \rho^* \mathsf{Y}$ with $\mathsf{Y} = \sigma_{\mathrm{y}} \otimes \sigma_{\mathrm{y}}$. Note that Eq. (5.30) is only defined for two qubit states.

For the qubit reset task, we utilize the control field $\mathcal{E}(t)$ that interacts with the qubit, cf. Eq. (5.19), i.e., we have local control only over the qubit and no direct control over any part of the environment. The control task will be to reset the qubit into its ground state. Since we are exclusively interested in the final state of the qubit, irrespective of the final state of the ancilla, the final-time functional reads [233]

$$\mathcal{J}_T\left[\rho, T\right] = 1 - \left\langle \Psi_{\mathrm{Q}}^{\mathrm{trgt}} \middle| \mathrm{tr}_{\mathrm{A}}\left\{\rho(T)\right\} \middle| \Psi_{\mathrm{Q}}^{\mathrm{trgt}} \right\rangle \tag{5.31}$$

and we choose the target state $|\Psi_{\mathrm{Q}}^{\mathrm{trgt}}\rangle$ to be the bare ground state of the qubit. Functional $\mathcal{J}_T$ therefore directly measure the error of the reset protocol. We will search for optimized field shapes for $\mathcal{E}(t)$ that minimize $\mathcal{J}_T$ via Krotov's method, cf. Subsec. 2.3.5.

In the following and if not stated otherwise we assume and $\omega_{\mathrm{A}} > \omega_{\mathrm{Q}}$. We set $\omega_{\mathrm{Q}} = 1$ which defines the units for time and energy. The relations of the remaining parameters with respect to ω_{Q} are typical for superconducting qubits [142]. Hence, our model system can, for instance, be readily implemented by two superconducting qubits in an RLC circuit [197], where a resistor acts as a thermal reservoir, or by two superconducting qubits with one of them coupled to a lossy cavity [234]. An alternative realization would be closer to the model sketched in Fig. 5.6, where the ancilla is given by a strongly coupled defect in the environment of superconducting qubits, which are mainly given by well characterized two-level defects [235]. Hence, the theoretical model introduced so far can be straightforwardly realized experimentally.

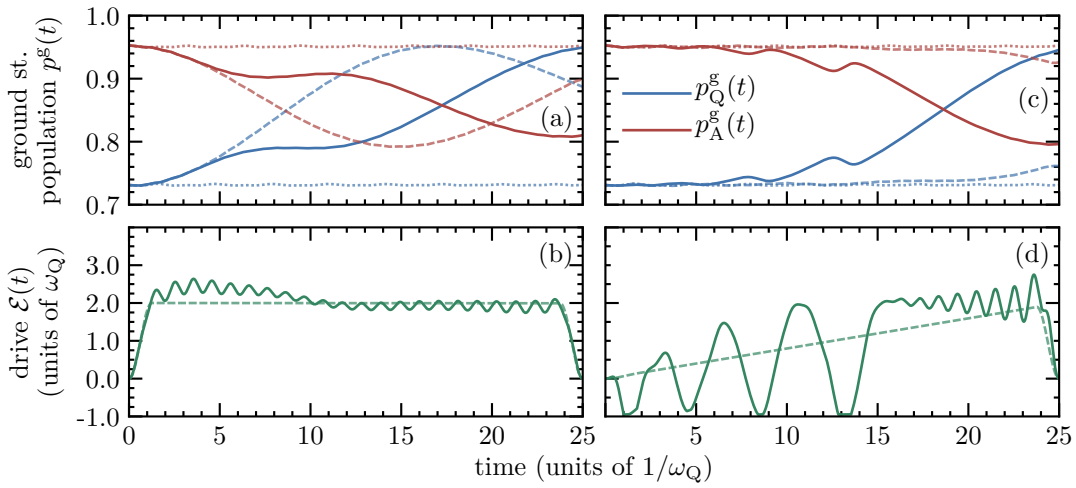

Figure 5.7: (a,c) Population dynamics induced by the optimized fields (solid lines) for the factorizing initial state (5.25). The corresponding fields are shown in (b,d). The dotted lines illustrate the free evolution of the system, the dashed lines the guess field and its evolution. Left and right hand side correspond to different guess fields for the optimization. Parameters are $\omega_Q = 1.0$, $\omega_A = 3.0$, $J = 0.1$, $\kappa = 0.04$ and $\beta = 1.0$.

5.2.2 Factorizing Initial States

In order to obtain some intuition about the reset protocol, we first consider the factorizing initial state (5.25), i.e., the uncorrelated state of system and environment and derive an optimized reset protocol for it. Since we need to export entropy from the qubit, the ancilla will be our target system to absorb it. Thus, it is important that it contains less entropy initially, i.e., has a higher initial purity. This requirement is the reason why we choose the level splittings of qubit and ancilla to be unequal and $\omega_A > \omega_Q$. Together with the identical temperature of qubit and ancilla, i.e., identical β, the inequality $\omega_A > \omega_Q$ results in a higher von Neumann entropy of the qubit than the ancilla, i.e., $E(\rho_Q^{th}) > E(\rho_A^{th})$, cf. Eq. (5.24). According to the second law of thermodynamics, one would expect the best cooling to be achieved by an entropy exchange between qubit and ancilla. This has been observed before [206, 207].

For the chosen parameters, entropy exchange can be realized by simply swapping the initial ground state populations of qubit and ancilla, i.e., $p_Q^g(t_0)$ and $p_A^g(t_0)$. One possibility to achieve this is to put qubit and ancilla in resonance. As evident from Eq. (5.19), the control field $\mathcal{E}(t)$ effectively changes the frequency, i.e., the level splitting ω_Q, of the qubit. Therefore an educated guess is to ramp qubit and ancilla rapidly into resonance and stay there just long enough for a full swap operation to complete. Figure 5.7(a) shows the dynamics for this particular guess field (dashed lines), as well as

the free evolution (dotted lines) and the dynamics under the optimized field (solid lines). With the optimized field, we indeed obtain the anticipated swap of the ground state populations at the final time $T = 25$ chosen for the optimization. In contrast, for the guess field, the maximum of the qubit's ground state population $p_{\mathrm{Q}}^{\mathrm{g}}(t)$ is already achieved at $t \approx 17$. Hence, although the optimization fulfills its task and minimizes the error at final time T, there obviously exists a faster solution with identical error. The optimized field and its corresponding dynamics are therefore not time-optimal. For the parameters of Fig. 5.7, the initial ground state populations of qubit and ancilla are $p_{\mathrm{Q}}^{\mathrm{g}}(t_0) = 0.731$ and $p_{\mathrm{A}}^{\mathrm{g}}(t_0) = 0.953$. The final value for the qubit's ground state population is specified by the error $\mathcal{J}_T = 5.04\%$.

To understand the idea of resetting the qubit by means of an ancilla conceptually, it is important to note that for as long as qubit and ancilla are out of resonance, their effective coupling is almost vanishing. This is evidenced by their populations being almost constant up to small oscillations in the field-free (dotted) dynamics in Fig. 5.7(a). This shows that this setup allows to tune the qubit into resonance with the ancilla for the purpose of resetting it and proves that, if tuned out of resonance, the qubit is almost negligibly influenced by the ancilla. Note that tuning the qubit out of resonance after its entropy has been dumped into the ancilla is crucial as the entropy otherwise flows back to the qubit. The latter can be seen in the dynamics under the resonant guess field in Fig. 5.7(a) for times $t > 17$.

As will be shown analytically in Subsec. 5.2.4, the swap of populations under a constant resonant drive $\mathcal{E}(t) = \mathcal{E} = \omega_{\mathrm{A}} - \omega_{\mathrm{Q}}$ is even a time-optimal solution for all factorizing initial conditions when the ancilla is initially diagonal, i.e., has vanishing coherences. The analytical bounds for the minimal error $\mathcal{J}_T^{\min}$ and the shortest possible duration $T_{\min}$ in which this minimal error is reached, given the parameters used in Fig. 5.7, are

$$\mathcal{J}_T^{\min} = 1 - p_{\mathrm{A}}^{\mathrm{g,th}} = 4.74\%, \qquad T_{\min} = \frac{\pi}{2J} = 15.7. \tag{5.32}$$

The actual value of the minimal error $\mathcal{J}_T^{\min}$ is only determined by the initial ground state population $p_{\mathrm{A}}^{\mathrm{g}}(t_0) = p_{\mathrm{A}}^{\mathrm{g,th}}$ of the ancilla. It is therefore governed by the reservoir temperature and the ancilla level splitting ω_{A}. For instance, given an environment at zero temperature, the inverse thermal energy β would go to infinity and the ancilla would be initially in its ground state with $p_{\mathrm{A}}^{\mathrm{g,th}} = 1$, cf. Eq. (5.24). The same can, in principle, also be achieved by a sufficiently large ancilla level splitting ω_{A}, since in terms of Eq. (5.24) only $x_{\mathrm{A}} = \omega_{\mathrm{A}}\beta/2$ needs to be as large as possible for the ancilla to be initially as close as possible to its ground state. Thus, in order to get initially as close as possible to

$p_{\mathrm{A}}^{\mathrm{g,th}} = 1$, both β and ω_{A} should be engineered to their experimentally feasible maximum. Theoretically, with $p_{\mathrm{A}}^{\mathrm{g,th}} = 1$, swapping the ground state populations of qubit and ancilla would perfectly reset the qubit. The bound in fidelity, i.e., in $\mathcal{J}_T^{\mathrm{min}}$, originates therefore only from the experimental inaccessibility of $p_{\mathrm{A}}^{\mathrm{g,th}} = 1$. However, regarding the bound in time, one might wonder why the minimal time $t \approx 17$ observed for the swap in Fig. 5.7(a) is larger than $T^{\mathrm{min}} = 15.7$ in Eq. (5.32). This is due to the fact that, for the sake of experimentally feasible control signals, we need to allow $\mathcal{E}(t)$ to be smoothly switched on and off. If we would relax this constraint, the optimized control would indeed reach the quantum speed limit T_{min}.

For any time longer than T_{min}, there is always at least one control solution achieving maximal cooling, i.e. minimal $\mathcal{J}_T$. However, this solution is typically not unique, since usually several different fields $\mathcal{E}(t)$ exist that yield identical errors $\mathcal{J}_T$. Since we will only prove analytically in Subsec. 5.2.4 that the limits (5.32) are indeed fundamental, we might want to check first via numerical optimal control how the solution presented in Fig. 5.7(a,b) depends on the guess field. To this end, another exemplary dynamics and its generating control field is shown in Fig. 5.7(c,d). In that case, the guess field $\mathcal{E}(t)$ ramps qubit and ancilla slowly into resonance and we can again observe that both qubit and ancilla only start to significantly exchange entropy, i.e., interact effectively, as we get closer to the resonance condition. Since the guess field is chosen non-resonantly, the optimization tries to increase the resonant parts in the optimized control field, cf. the solid line in Fig. 5.7(d), and by doing so manages to reach a final error of $\mathcal{J}_T = 5.44\%$. Hence, it yields a very similar error compared to Fig. 5.7(a,b). Nevertheless, the non-uniqueness of the control solution is still valuable as it allows, for instance, to take into account further experimentally desirable features, such as restriction of the maximal amplitude of the control, without necessarily losing performance in terms of larger errors by doing so.

5.2.3 Correlated Initial States

An obvious choice for a correlated initial state is the joint thermal equilibrium state (5.26) of qubit and ancilla. For the parameters used in Fig. 5.7, the mutual information of this state is $\mathcal{I}^{\mathrm{init}} = 4.0 \cdot 10^{-3}$ and therefore rather small. The state is separable, i.e., it is non-entangled, but has finite quantum discord $\mathcal{Q} > 0$. This highlights the general concept of quantum discord as a measure for the amount of quantum correlations. It especially emphasizes the fact that not all quantum mechanically correlated states, i.e., states with $\mathcal{Q} > 0$, are necessarily entangled. However, the reverse statement always holds, since any entangled state implies $\mathcal{Q} > 0$. Although entanglement is the prevalent indicator for quantum correlations, it is by far not the most general one. In fact, all initial states

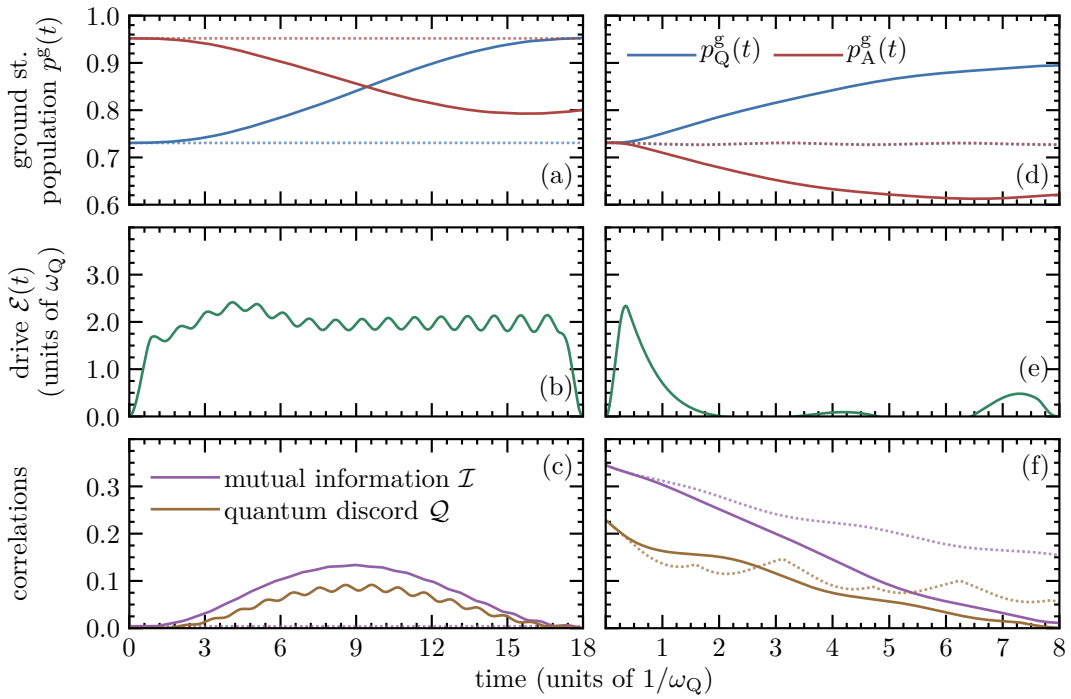

Figure 5.8: Same as Fig. 5.7 but with correlated, non-entangled initial states. For the left hand side, the initial state is given by Eq. (5.26). For the right hand side, the initial state is given by Eq. (5.28) with $\omega_{\rm Q} = \omega_{\rm A} = 1.0$ and $\gamma = -0.19$. In addition to Fig. 5.7, panel (c) and (f) show the evolution of the correlations.

studied within this subsection are non-entangled but have non-vanishing initial quantum discord.

Figure 5.8(a-c) show the dynamics when starting from the thermal equilibrium state (5.26) of qubit and ancilla in case of the field-free evolution (dotted lines) and under the optimized control field (solid lines). The figure reveals that both cooling and erasure of correlation is achieved by the optimized control field. With respect to the erasure of initial correlations it should be noted that, although its initial mutual information is already very small, its final value is still one order of magnitude smaller. Under the optimized control field, the final value of the error in Fig. 5.8(a) becomes $\mathcal{J}_T = 4.74\%$ and coincides with the minimal error $\mathcal{J}_T^{\rm min}$ for factorizing initial states, cf. Eq. (5.32).

Interestingly, in view of the reachable error $\mathcal{J}_T = 4.74\%$, optimal control seems to benefit from the presence of initial correlations, which might appear counter-intuitive at first glance. Thus, in order to further investigate the role of initial correlations we consider the extreme situation where qubit and ancilla are in resonance by virtue of their parameters, i.e., $\omega_{\rm Q} = \omega_{\rm A}$. For that case and given factorizing initial conditions, no cooling

would be possible at all, since both qubit and ancilla initially contain identical amounts of entropy. However, we use Eq. (5.28) as initial state in the following and are therefore able to add initial correlations artificially via $\gamma \neq 0$. For the case $\omega_\mathrm{Q} = \omega_\mathrm{A}$, Fig. 5.8(d-f) confirm that we are not only able to erase the correlations but even achieve cooling of the qubit, where it should otherwise not be possible. For the given parameters, the error limit for the factorizing thermal initial state (5.28) amounts to $\mathcal{J}_T^{\min} = 26.9\%$. However, with initial correlations, the error under the optimized field becomes $\mathcal{J}_T = 10.52\%$ and is thus much smaller than $\mathcal{J}_T^{\min}$, predicted for factorizing initial states. The initial state (5.28) gives rise to mutual information $\mathcal{I}^{\mathrm{init}} = 0.345$ and quantum discord $\mathcal{Q}^{\mathrm{init}} = 0.228$. The optimization roughly erases both at final time T. This actually strengthens the previous observation of an eased reset protocol and suggests that system-environment correlations might even act as a resource for cooling.

Even the quantum speed limit $T_{\min}$, which we have defined earlier for factorizing initial conditions, cf. Eq. (5.32), does not hold anymore in case of correlated initial states. In the dynamics presented in Fig. 5.8(d-f), i.e., for the extreme case $\omega_\mathrm{A} = \omega_\mathrm{Q}$, this feature is evidenced by the completion of the reset protocol with total time $T = 8 < T_{\min}$. However, the effect of reduced reset times can also be observed for the case $\omega_\mathrm{A} > \omega_\mathrm{Q}$. As can be seen in Fig. 5.9(a), with increasing total initial correlations, i.e., increasing mutual information $\mathcal{I}^{\mathrm{init}}$, the error threshold for the factorizing dynamics, $\mathcal{J}_T^{\min}$, can be reached in shorter times, i.e., the quantum speed limit effectively decreases. Each data point has been generated by a sequence of optimizations where the final time T has been reduced subsequently until the optimization has failed to find a solution with $\mathcal{J}_T \leq \mathcal{J}_T^{\min}$.

While Fig. 5.9(a) analyses the quantum speed limit for the error threshold $\mathcal{J}_T^{\min}$, Fig. 5.9(b) shows the minimally reachable error $\mathcal{J}_T$ for any time $T \leq 25$. The figure confirms a monotonic decrease of $\mathcal{J}_T$ with increasing initial correlations $\mathcal{I}^{\mathrm{init}}$. While each data point, i.e., each minimal error $\mathcal{J}_T$, is in general obtained with a different final time T, especially the smaller errors correspond to final times $T \leq T_{\min}$. Hence, initial correlations seem to improve the qubit reset twofold as they simultaneously minimize the error and protocol duration. It should again be emphasized that despite the increasing amount of initial correlations, none of the considered initial states in Fig. 5.9 is entangled. While identical simulations have been conducted for entangled initial states, their results do not differ qualitatively and the corresponding data is not presented here. In fact, this allows the conclusion that only the total amount of mutual information, i.e., the total amount of correlations, not the type, i.e., classical or quantum correlations, is responsible for the observed improvement of the reset task. Thus, in a nutshell, we have demonstrated that it is not only possible to reset the qubit in the presence of initial correlations, but

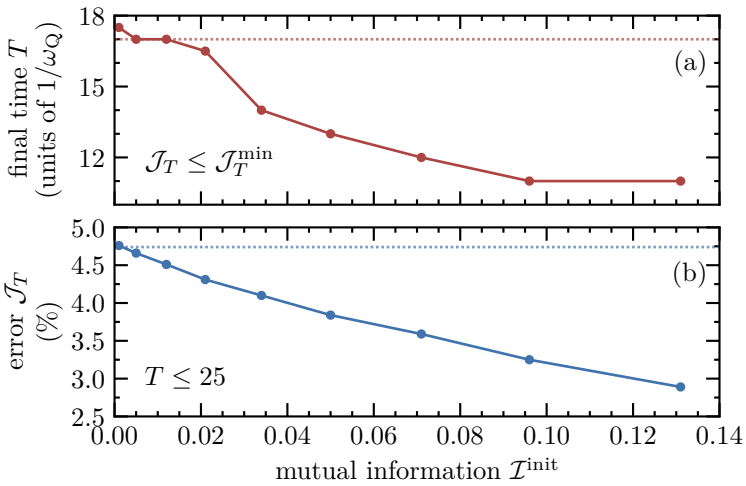

Figure 5.9: Quantum speed limit (a) and minimal error (b) for a parametrical variation of the strength of initial correlations $\mathcal{I}^{\text{init}}$ via Eq. (5.28). Note that upper and lower panel display results of different optimizations, only their initial states are identical. Panel (a) shows the smallest final time T, which still yields an error $\mathcal{J}_T \leq \mathcal{J}_T^{\min}$. The dashed line corresponds to the approximate minimal time for a swap operation for factorizing initial states, taking into account finite ramps of the field at the beginning and end, cf. Fig. 5.7(b). Panel (b) shows the smallest error $\mathcal{J}_T$ for any final time satisfying $T \leq 25$. The dashed line corresponds to the limit $\mathcal{J}_T^{\min}$ for factorizing initial states, cf. Eq. (5.32). The parameters are identical to those in Fig. 5.7.

have observed that initial correlations between system and environment can actually be used to enhance the performance of the reset protocol. Moreover, in the extreme case of Fig. 5.8(d-f), i.e., in the case where qubit and ancilla are in resonance even in the absence of a control field, initial correlations enable cooling that is impossible without their presence.

Similar observations where correlations assist in qubit reset have been found in parallel for another reset mechanism called algorithmic cooling [188, 236]. There, it has been shown that correlations that are being created dynamically by cross-relaxation [237] or by measurements of interacting qubits [238] allow to overcome a limit for algorithmic cooling that has been deemed fundamental [239]. However, the ancilla-based reset protocol presented here differs in two important ways. Although it depends on the initial state of the qubit-ancilla system if initial correlations should be exploited, it has even stronger advantages. In detail, it is time-optimal, requires controllability only over the qubit and not the environment and requires only a single application of the reset protocol. Algorithmic cooling does always requires several applications and is therefore significantly slower.

In the following Subsec. 5.2.4, we will analyze the dynamics with factorizing and

correlated initial states from an analytical perspective. However, as a closing remark for this and the last subsection, we will briefly analyze the dynamics regarding the presence and influence of non-Markovianity. As we have already mentioned earlier, the qubit dynamics will, in principle, behave non-Markovian due to the strong coupling between qubit and ancilla. Since no unique and analytical measure for non-Markovianity exists, cf. Subsec. 2.2.2, and for the sake of numerical efficiency, we take the qubit's accessible state space volume as an indicator for the presence of non-Markovianity [45]. This witness for non-Markovianity can be calculated by taking the qubit's dynamical map $\mathcal{D}^{\mathrm{Q}}_{t,t_0} : \mathfrak{L}_{\mathcal{H}_\mathrm{Q}} \to \mathfrak{L}_{\mathcal{H}_\mathrm{Q}}$, where $\mathcal{H}_\mathrm{Q}$ and $\mathfrak{L}_{\mathcal{H}_\mathrm{Q}}$ are the qubit's Hilbert and Liouville space, respectively, and convert it into its superoperator representation $\hat{\mathcal{D}}^{\mathrm{Q}}_{t,t_0}$. The determinant of the latter represents the qubit's accessible state space volume at any time t. An increases at any time indicates non-Markovian dynamics for the qubit. In the specific setup of Fig. 5.6, we observe that non-Markovianity seems to be linked to an entropy flow from the ancilla into the qubit. Conversely, a monotonic decrease in the qubit's state space volume can be observed when the entropy flows from the qubit into the ancilla. Although the qubit's state space volume is strictly speaking only a witness for non-Markovianity, an increase in the qubit's accessible state space volume at least hints towards Markovian dynamics. According to this observation, the dynamics of the time-optimal solution, cf. Eq. (5.32), turns out to be Markovian. In this case, the entropy of the qubit decreases monotonously until reaching its minimum at T_min. This corresponds to a maximum in its ground state population $p^{\mathrm{g}}_{\mathrm{Q}}(t)$. For longer times or non-optimal driving, the controlled dynamics becomes non-Markovian, cf. Fig. 5.7(c,d), as the entropy flows in both directions. This shows that even though non-Markovianity is not crucial for the qubit reset, it is also not harmful in the sense that the optimization does not try to actively suppress it.

5.2.4 Analytical Derivation of the Bounds

In the previous two subsections we have analyzed qubit reset for factorizing and correlated initial states from a numerical perspective. In this subsection, we now analyze the reset dynamics from an analytical perspective. In the following, we will justify the bounds of Eq. (5.32), identified for factorized initial states, as well as derive derive an intuitive understanding, why initial correlations turn out to be an asset for qubit reset. In addition to Ref. [223] the results presented in this subsection are also partly taken from Ref. [240].

As with most analytical derivations, it requires a simplification of the considered model to ease its analytical treatment. In our case, two approximations of the model and dynamics can be made, which are both in agreement with numerical observations.

On the one hand, solutions obtained under the rotating wave approximation (RWA) perform almost equally well in comparison to solutions that take the counter-rotating terms into account. Reference [223] discusses the influence of those terms in more detail. Interestingly, although the dynamics and optimized control fields differ in both cases, which actually highlights that the RWA is not a good approximation for the dynamics, the reachable error $\mathcal{J}_T$ is not affected by the presence or absence of the counter-rotating terms. Hence, since we are solely interested in the fundamental bounds for the reset protocol, neglecting these terms, i.e., applying the RWA, might still be a suitable simplification. On the other hand, two different timescales are relevant to characterize the interaction of the qubit with the environment — a fast one to dump the qubit's entropy into the ancilla, determined by the coupling strength J, and a slow one leading to equilibration with the larger environment of the reservoir, cf. Fig. 5.6, determined by the decay rate κ. It is important to note that the Markovian equilibration dynamics will never increase the purity of qubit or ancilla above their steady state values. Both the minimum error $\mathcal{J}_T^{\min}$ and time $T_{\min}$ for the qubit reset are therefore only determined by the fast dynamics and we can neglect the reservoir in the following. Hence, the dynamics of the joint qubit and ancilla system will be completely unitary. Starting from the equation of motion (5.20) and the Hamiltonian (5.21), if we neglect the counter-rotating terms and the slow equilibration due to the presence of the reservoir, the equation of motion becomes

$$\frac{\mathrm{d}}{\mathrm{d}t}\rho(t) = -\mathrm{i}\left[\mathsf{H}^{\mathrm{RWA}}(t), \rho(t)\right], \tag{5.33}$$

where

$$\begin{aligned} \mathsf{H}^{\mathrm{RWA}}(t) &= \mathsf{H}_{\mathrm{Q}}(t) \otimes \mathbb{1}_{\mathrm{A}} + \mathbb{1}_{\mathrm{Q}} \otimes \mathsf{H}_{\mathrm{A}} + \mathsf{H}_{\mathrm{I}}^{\mathrm{RWA}}(t), \\ \mathsf{H}_{\mathrm{I}}^{\mathrm{RWA}}(t) &= J(t)\left(\sigma_+^{\mathrm{Q}} \otimes \sigma_-^{\mathrm{A}} + \sigma_-^{\mathrm{Q}} \otimes \sigma_+^{\mathrm{A}}\right) \end{aligned} \tag{5.34}$$

is the Hamiltonian under the RWA. σ_- and σ_+ are the standard lowering and raising operators. Another simplification of the dynamics, which does not involve any further approximation, can be achieved by changing into the rotating frame. To this end, the transformation of state $\rho(t)$ and Hamiltonian $\mathsf{H}^{\mathrm{RWA}}(t)$ into the rotating frame reads

$$\begin{aligned} \rho'(t) &= \mathsf{O}^\dagger(t)\rho(t)\mathsf{O}(t), \\ \mathsf{H}'(t) &= \mathsf{O}^\dagger(t)\mathsf{H}^{\mathrm{RWA}}(t)\mathsf{O}(t) - \mathrm{i}\mathsf{O}^\dagger(t)\frac{\mathrm{d}\mathsf{O}(t)}{\mathrm{d}t}. \end{aligned} \tag{5.35}$$

If the transformation operator $\mathsf{O}(t)$ is chosen as

$$\mathsf{O}(t) = \exp\{-\mathrm{i}\mathsf{A}(t)t\}, \qquad \mathsf{A}(t) = \mathsf{H}_\mathrm{Q}(t) \otimes \mathbb{1}_\mathrm{A} + \mathbb{1}_\mathrm{Q} \otimes \mathsf{H}_\mathrm{A}, \tag{5.36}$$

the equation of motion (5.33) transforms into

$$\frac{\mathrm{d}}{\mathrm{d}t}\rho'(t) = -\mathrm{i}\left[\mathsf{H}'(t), \rho'(t)\right], \tag{5.37}$$

$$\mathsf{H}'(t) = \begin{pmatrix} \frac{\mathrm{d}\delta(t)}{\mathrm{d}t}\frac{t}{2} & 0 & 0 & 0 \\ 0 & \frac{\mathrm{d}\delta(t)}{\mathrm{d}t}\frac{t}{2} & J(t)e^{-\mathrm{i}\delta(t)t} & 0 \\ 0 & J(t)e^{\mathrm{i}\delta(t)t} & -\frac{\mathrm{d}\delta(t)}{\mathrm{d}t}\frac{t}{2} & 0 \\ 0 & 0 & 0 & -\frac{\mathrm{d}\delta(t)}{\mathrm{d}t}\frac{t}{2} \end{pmatrix}, \tag{5.38}$$

where $\delta(t) = \omega_\mathrm{Q} + \mathcal{E}(t) - \omega_\mathrm{A}$ is the time-dependent detuning of qubit and ancilla. Since it is uniquely determined by $\mathcal{E}(t)$, we can view it as the physical control field that we are interested in and for which we want to obtain a time-optimal solution in the following. For the sake of generality, we account for a possible time-dependence $J = J(t)$ of the coupling strength between qubit and ancilla.

The analytical treatment in this subsection is based on the ideas of geometric control theory [241]. The fundamental concept of the latter is to transform the system's equation of motion in such a way that the optimality condition can be expressed geometrically [242, 243]. Although this might sound rather vague at the moment, it will become clear in the following. For the numerical optimizations in the previous subsections, the optimization target has been to reset the qubit into its ground state, cf. Eq. (5.31). However, here we choose a more general target and strive to directly maximize the qubit's purity, i.e., to maximize

$$\mathcal{P}_\mathrm{Q} \equiv \mathcal{P}\left(\rho'_\mathrm{Q}(T)\right) = \mathrm{tr}\left\{\mathrm{tr}_\mathrm{A}\left\{\rho'(T)\right\}^2\right\}. \tag{5.39}$$

In order to start transforming the equation of motion in the spirit of geometric control theory, we first expand the state $\rho'(t)$ in terms of 16 real variables, $x_i(t) \in \mathbb{R}$. For the sake of brevity in the notation, we will drop using the prime to indicate the rotating frame as well as drop writing out time dependencies. The state ρ reads

$$\rho = \begin{pmatrix} x_1 & x_5 + \mathrm{i}x_6 & x_7 + \mathrm{i}x_8 & x_9 + \mathrm{i}x_{10} \\ x_5 - \mathrm{i}x_6 & x_2 & x_{11} + \mathrm{i}x_{12} & x_{13} + \mathrm{i}x_{14} \\ x_7 - \mathrm{i}x_8 & x_{11} - \mathrm{i}x_{12} & x_3 & x_{15} + \mathrm{i}x_{16} \\ x_9 - \mathrm{i}x_{10} & x_{13} - \mathrm{i}x_{14} & x_{15} - \mathrm{i}x_{16} & x_4 \end{pmatrix}. \tag{5.40}$$

Plugging Eq. (5.40) into the equation of motion (5.37) yields a new equation of motion which can be written in vector form,

$$\dot{\boldsymbol{x}} = J_1 \boldsymbol{f}_1(\boldsymbol{x}) + J_2 \boldsymbol{f}_2(\boldsymbol{x}) + \alpha \boldsymbol{f}_3(\boldsymbol{x}) \tag{5.41}$$

with $\boldsymbol{x} = (x_1, \ldots, x_{16})^\top \in \mathbb{R}^{16}$,

$$\begin{aligned}
\boldsymbol{f}_1(\boldsymbol{x}) &= \Big(0, -2x_{12}, 2x_{12}, 0, -x_8, x_7, -x_6, x_5, 0, 0, 0, x_2 - x_3, x_{16}, -x_{15}, x_{14}, -x_{13}\Big)^\top, \\
\boldsymbol{f}_2(\boldsymbol{x}) &= \Big(0, -2x_{11}, 2x_{11}, 0, -x_7, -x_8, x_5, x_6, 0, 0, x_2 - x_3, 0, -x_{15}, -x_{16}, x_{13}, x_{14}\Big)^\top, \\
\boldsymbol{f}_3(\boldsymbol{x}) &= \Big(0, 0, 0, 0, 0, 0, 2x_8, -2x_7, 2x_{10}, -2x_9, 2x_{12}, -2x_{11}, 2x_{14}, -2x_{13}, 0, 0\Big)^\top
\end{aligned} \tag{5.42}$$

and where J_1, J_2 and α are given by

$$J_1 = J\cos(\delta t), \qquad J_2 = J\sin(\delta t), \qquad \alpha = \frac{1}{2}\dot{\delta} t. \tag{5.43}$$

By analyzing Eq. (5.41), it becomes clear that the vector fields $\boldsymbol{f}_1(\boldsymbol{x}), \boldsymbol{f}_2(\boldsymbol{x})$ and $\boldsymbol{f}_3(\boldsymbol{x})$ govern the admissible directions for the evolution of state $\boldsymbol{x}$ within the vector space $\mathbb{R}^{16}$, whereas J_1, J_2 and α determine the "speed" for the evolution into these directions.

So far, we have transformed the original equation of motion (5.37) into the new form (5.41). However, as a next step we need to simplify it in view of the specific control task, i.e., the maximization of $\mathcal{P}_\mathrm{Q}$, cf. Eq. (5.39). In the coordinates $\{x_1, \ldots, x_{16}\}$, the latter reads

$$\mathcal{P}_\mathrm{Q} = (x_1 + x_2)^2 + (x_3 + x_4)^2 + 2\,(x_7 + x_{13})^2 + 2\,(x_8 + x_{14})^2\,. \tag{5.44}$$

This expression can be substantially simplified by introducing the following coordinate transformation from $\{x_1, \ldots, x_{16}\}$ to $\{z_1, \ldots, z_{16}\}$ with $z_i \in \mathbb{R}$, $i = 1, \ldots, 16$. The new coordinates are given by

$$\begin{aligned}
z_1 &\equiv x_1 + x_2 - 1/2, \\
z_2 &\equiv x_{12}, \\
z_3 &\equiv x_{11}, \\
z_4 &\equiv -2x_1 - x_2 - x_3, \\
z_5 &\equiv x_7 + x_{13}, \\
z_6 &\equiv x_6 - x_{16}, \\
z_7 &\equiv x_8 + x_{14},
\end{aligned}$$

$$z_8 \equiv x_5 - x_{15}. \tag{5.45}$$

Note that the remaining eight coordinates $z_9, \ldots, z_{16}$, which have not been specified in Eq. (5.45), are irrelevant for our analysis and can thus be chosen arbitrarily as long as they are linearly independent from each other and from $z_1, \ldots, z_8$.

In the new variables, the qubit purity $\mathcal{P}_\mathrm{Q}$ becomes

$$\mathcal{P}_\mathrm{Q} = \frac{1}{2} + 2\left(z_1^2 + z_5^2 + z_7^2\right). \tag{5.46}$$

While this readily simplifies the expression for the control target, the most important part is that the corresponding equation of motion for $z_1, \ldots, z_8$ decouple into two disjunct sets of variables, each with its own equation of motion. On the one hand, we have

$$\begin{pmatrix} \dot{z}_1 \\ \dot{z}_2 \\ \dot{z}_3 \end{pmatrix} = 2J_1 \begin{pmatrix} -z_2 \\ z_1 - c \\ 0 \end{pmatrix} + 2J_2 \begin{pmatrix} -z_3 \\ 0 \\ z_1 - c \end{pmatrix} + 2\alpha \begin{pmatrix} 0 \\ -z_3 \\ z_2 \end{pmatrix}, \tag{5.47}$$

which describes the dynamics of the qubit's ground state population, $p_\mathrm{Q}^\mathrm{g} = z_1 + 1/2$, within the three-dimensional subspace $S_{123} = \{z_1, z_2, z_3\}$, where c is a constant. On the other hand, the qubit's coherences, $\gamma_\mathrm{Q} = z_5 + \mathrm{i}z_7$, evolve within the four-dimensional subspace $S_{5678} = \{z_5, z_6, z_7, z_8\}$, which is governed by

$$\begin{pmatrix} \dot{z}_5 \\ \dot{z}_6 \\ \dot{z}_7 \\ \dot{z}_8 \end{pmatrix} = J_1 \begin{pmatrix} -z_6 \\ z_5 \\ z_8 \\ -z_7 \end{pmatrix} + J_2 \begin{pmatrix} z_8 \\ -z_7 \\ z_6 \\ -z_5 \end{pmatrix} + 2\alpha \begin{pmatrix} z_7 \\ 0 \\ -z_5 \\ 0 \end{pmatrix}. \tag{5.48}$$

It is straightforward to show that the dynamics within the subspaces S_{123} and S_{5678} is restricted to the surface of two spheres. For S_{123}, we find from Eq. (5.47) that

$$\frac{\mathrm{d}}{\mathrm{d}t} R_1 = 0, \qquad R_1^2 = (z_1 - c)^2 + z_2^2 + z_3^2, \tag{5.49}$$

with R_1 the radius of the sphere and its center being $(c, 0, 0)$. The center's shift from the origin is determined by the constant $c = -(z_4 + 1)/2$, cf. Eq. (5.45). Similarly for S_{5678}, Eq. (5.48) yields

$$\frac{\mathrm{d}}{\mathrm{d}t} R_2 = 0, \qquad R_2^2 = z_5^2 + z_6^2 + z_7^2 + z_8^2, \tag{5.50}$$

with radius R_2 and its center being the origin $(0,0,0,0)$. The values of R_1 and R_2 are exclusively determined by the initial values z_i^{init}, $i = 1,\ldots,8$. In other words, the accessible part of the entire state space is fully determined by the initial state ρ^{init}. Note that the initial state remains invariant when changing into the rotating frame, i.e., $\rho^{\text{init}} = \rho(t_0) = \rho'(t_0)$.

The feasibility to find a simplified expression for the control target in terms of Eq. (5.46), while at the same time simplifying the equations of motion, cf. Eqs. (5.47) and (5.48), is at the heart of geometric control theory. For the maximization of the qubit's purity $\mathcal{P}_{\text{Q}}$, this simplifies the control task by allowing us to discuss the maximization of z_1^2 on the sphere S_{123} and the maximization of z_5^2 and z_7^2 on the sphere S_{5678}. In the following, we will address factorized and correlated initial states separately.

Optimal Strategy for Thermal Factorizing Initial States

We start by considering the factorizing initial state (5.25) of qubit and ancilla, where both parts are in thermal equilibrium with the reservoir. Since this is a diagonal state, i.e., all its off-diagonal elements are zero, we can abstractly write it as

$$\rho^{\text{init}} = \rho_{\text{Q}}^{\text{th}} \otimes \rho_{\text{A}}^{\text{th}} = \begin{pmatrix} p_{\text{Q}}^{\text{g}} & 0 \\ 0 & p_{\text{Q}}^{\text{e}} \end{pmatrix} \otimes \begin{pmatrix} p_{\text{A}}^{\text{g}} & 0 \\ 0 & p_{\text{A}}^{\text{e}} \end{pmatrix}, \tag{5.51}$$

where p_{Q}^{g} (p_{A}^{g}) and p_{Q}^{e} (p_{A}^{e}) are the ground and exited state population for the qubit (ancilla), respectively, and we assume $\rho_{\text{A}}^{\text{th}}$ to be initially more pure than $\rho_{\text{Q}}^{\text{th}}$. This translates into $\mathcal{P}_{\text{A}}^{\text{init}} = (p_{\text{A}}^{\text{g}})^2 + (p_{\text{A}}^{\text{e}})^2 > (p_{\text{Q}}^{\text{g}})^2 + (p_{\text{Q}}^{\text{e}})^2 = \mathcal{P}_{\text{Q}}^{\text{init}}$, where $\mathcal{P}_{\text{Q}}^{\text{init}}$ ($\mathcal{P}_{\text{Q}}^{\text{init}}$) corresponds to the initial purity of the qubit (ancilla). Since Eq. (5.51) is diagonal, it follows from Eq. (5.45) that the coordinates $z_5^{\text{init}},\ldots,z_8^{\text{init}}$ are initially zero. As a consequence, we have $R_2 = 0$ for all t, as it is a constant and therefore defined by its initial value and no dynamics will occur in S_{5678}. This in turn implies that z_5 and z_7, which are the two coordinates from S_{5678} that are relevant for $\mathcal{P}_{\text{Q}}$, cf. Eq. (5.46), will remain zero no matter how δ, respectively $\mathcal{E}$, is chosen. The relevant subspace for the maximization of $\mathcal{P}_{\text{Q}}$ is therefore entirely given by S_{123} for which we find $z_2^{\text{init}} = x_{12} = \mathfrak{Im}\{\gamma\} = 0$ and $z_3^{\text{init}} = x_{11} = \mathfrak{Re}\{\gamma\} = 0$ due to the absence of initial correlations ($\gamma = 0$) and only z_1^{init} and c will be initially non-zero and are responsible for $R_1 > 0$, cf. Eq. (5.49). Hence, the control problem reduces to maximizing z_1^2.

In the following, we will show in three steps that the resonant case with $\delta = 0$ describes to a time-optimal reset protocol. First, we will show that $\delta = 0$ allows to reach the qubit purity $\mathcal{P}_{\text{Q}}^{\max} = \mathcal{P}_{\text{A}}^{\text{init}}$, i.e., that $\delta = 0$ gives rise to a swap of purities. Second, we will show

that allowing for $\delta \neq 0$ does not allow to reach qubit purities larger than $\mathcal{P}_{\mathrm{Q}}^{\max}$. At last, we will show that $\delta \neq 0$ also does not allow to reach $\mathcal{P}_{\mathrm{Q}}^{\max}$ faster. This will complete the proof that $\delta = 0$ is in fact time-optimal for resetting qubits that are initially factorized with the ancilla and are of the form (5.51).

The case $\delta = 0$ for all t implies $J_1 = J$ and $J_2 = \alpha = 0$, cf. Eq. (5.43). This allows us to further simplify the dynamics and convert it from the three dimensional sphere S_{123} and its equation of motion (5.47) to a two dimensional sphere $S_{12} = \{z_1, z_2\}$ and its corresponding equation of motion

$$\begin{pmatrix} \dot{z}_1 \\ \dot{z}_2 \end{pmatrix} = 2J \begin{pmatrix} -z_2 \\ z_1 - c \end{pmatrix}. \tag{5.52}$$

Figure 5.10 shows the accessible state space for the dynamics within S_{12} when starting in the initial state used in Fig. 5.7. The optimization target can be identified geometrically as the point with maximal z_1 on this curve, i.e., the point with maximal distance to the vertical gray line that indicates $z_1 = 0$. Assuming constant positive coupling $J > 0$, the state will evolve with constant speed along the green line in Fig. 5.10. It then takes $T_{\min} = \pi/(2J)$ to reach the rightmost point. This can be shown by integration along the green line. However, due to the geometric simplicity of this picture, it can be deduced immediately, that in case of a time-dependent coupling $J(t) \geq 0$, the minimal time is given by

$$\int_0^{T_{\min}} J(t)\mathrm{d}t = \frac{\pi}{2}. \tag{5.53}$$

Therefore, a time-optimal solution for constant $\delta = 0$ but time-dependent $J(t)$ is obviously to choose $J(t)$ maximal at every instance of time.

The point of maximum qubit purity $\mathcal{P}_{\mathrm{Q}}^{\max}$ is determined by the center $(c, 0, 0)$ of sphere S_{123} and its radius R_1,

$$\mathcal{P}_{\mathrm{Q}}^{\max} = \frac{1}{2} + 2\,(c + R_1)^2 = \left(p_{\mathrm{A}}^{\mathrm{g}}\right)^2 + \left(p_{\mathrm{A}}^{\mathrm{e}}\right)^2 = \mathcal{P}_{\mathrm{A}}^{\mathrm{init}}. \tag{5.54}$$

Note that Eqs. (5.53) and (5.54) hold for any factorizing initial state of the form (5.51) with the ancilla initially purer than the qubit.

It is straightforward to see that a non-vanishing and possibly time-dependent detuning $\delta \neq 0$ does not provide access to qubit states with purity higher than $\mathcal{P}_{\mathrm{Q}}^{\max}$. Although $\delta \neq 0$ gives access to the entire three dimensional sphere S_{123} instead of only S_{12}, since J_2 and α become non-zero, the dynamics is still confined to the surface of S_{123}, cf. Eq. (5.49),

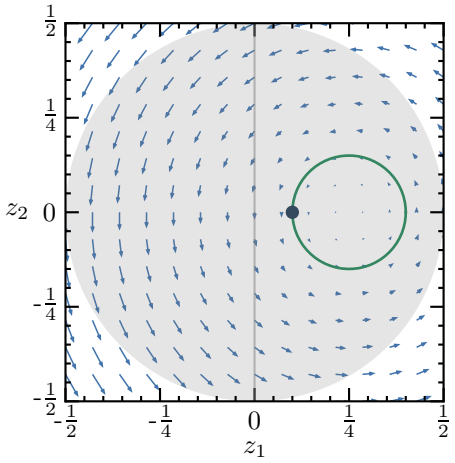

Figure 5.10: Evolution of the qubit ground state population $p_{\mathrm{Q}}^{\mathrm{g}} = z_1 + 1/2$ (green line) within the reduced subspace $S_{12} = \{z_1, z_2\}$ with the factorizing initial state (5.25) indicated by the large dot and the parameters as in Fig. 5.7. Qubit and ancilla are in resonance, i.e., $\delta = 0$ for all t, and the evolution of the state along the green line is determined by the vector field (5.52) (blue arrows). The gray vertical line corresponds to the qubit ground state population $p_{\mathrm{Q}}^{\mathrm{g}} = 1/2$. The gray sphere in the background visualizes the projection of the entire state space of valid density matrices onto the two-dimensional subspace S_{12}.

for which the point of maximal purity $\mathcal{P}_{\mathrm{Q}}^{\max}$ is unique and already accessible by $\delta = 0$.

Finally, we examine whether $\delta \neq 0$ allows to reach $\mathcal{P}_{\mathrm{Q}}^{\max}$ in shorter times, i.e., in times $T < T_{\min}$ with $T_{\min}$ according to Eq. (5.53). To this end, we transform the equations of motions once more. Since we are restricted to the surface of the three dimensional sphere S_{123}, a natural coordinate system is given by the spherical coordinates R_1, θ, ϕ, where R_1 is the radius of the sphere according to Eq. (5.49) and θ and ϕ are the standard azimuth and polar angle. In these coordinates, the qubit purity becomes [240]

$$\mathcal{P}_{\mathrm{Q}} = \frac{1}{2} + 2\left(R_1 \sin(\theta) + c\right)^2 \tag{5.55}$$

and the equations of motion (5.47) transforms into

$$\dot{\theta} = 2J\cos(u), \tag{5.56a}$$

$$\dot{\phi} = 2\alpha - J\tan(\theta)\sin(u), \tag{5.56b}$$

where we have introduced the new, abstract control field $u = \delta t - \phi$. In these spherical coordinates, the initial state of the qubit on S_{123} is given by its south pole $\theta^{\mathrm{init}} = -\pi/2$ and the target state by its north pole $\theta^{\mathrm{trgt}} = \pi/2$. Since radius R_1 and center c are constants, the purity $\mathcal{P}_{\mathrm{Q}}$ is exclusively determined by θ. Hence, the time-optimal solution to the

control problem is to maximize $\dot{\theta}$ for all t. On the one hand, by inspecting Eq. (5.56), this obviously requires us to choose $J(t) \geq 0$ maximal for all t. On the other hand, we need to ensure $\cos(u) = 1$, which can be straightforwardly achieved by setting $u = 0$ for all t. While u is just a virtual control field in Eq. (5.56), a possible solution for $u = 0$ is given by the physical control field $\delta = 0$. By integration of Eq. (5.56b), we again obtain $T_{\min} = J/(2\pi)$ in case of a constant coupling $J > 0$. This completes the proof that driving the qubit resonantly, i.e., $\delta = 0$, defines at least one time-optimal solution for the qubit reset protocol, as it reaches the maximally achievable qubit purity $\mathcal{P}_{\mathrm{Q}}^{\max}$ in the minimal time $T_{\min}$.

Optimal Strategy for Factorizing Initial States with Coherences

The most general factorizing initial state for qubit and ancilla is given by

$$\rho^{\mathrm{init}} = \rho_{\mathrm{Q}} \otimes \rho_{\mathrm{A}} = \begin{pmatrix} p_{\mathrm{Q}}^{\mathrm{g}} & \gamma_{\mathrm{Q}} \\ \gamma_{\mathrm{Q}}^{*} & p_{\mathrm{Q}}^{\mathrm{e}} \end{pmatrix} \otimes \begin{pmatrix} p_{\mathrm{A}}^{\mathrm{g}} & \gamma_{\mathrm{A}} \\ \gamma_{\mathrm{A}}^{*} & p_{\mathrm{A}}^{\mathrm{e}} \end{pmatrix}, \tag{5.57}$$

with $p_{\mathrm{Q}}^{\mathrm{g}}$ ($p_{\mathrm{A}}^{\mathrm{g}}$) and $p_{\mathrm{Q}}^{\mathrm{e}}$ ($p_{\mathrm{A}}^{\mathrm{e}}$) as in Eq. (5.51) and γ_{Q} (γ_{A}) the coherences of the qubit (ancilla). We will start the discussion with the case $\gamma_{\mathrm{A}} = 0$ but will comment on the case $\gamma_{\mathrm{A}} \neq 0$ later. From a physical perspective, $\gamma_{\mathrm{A}} = 0$ is a well justified initial state for the ancilla, since we assume it to be in permanent and direct contact with the reservoir and thus in thermal equilibrium. In contrast to the ancilla, non-zero coherences, $\gamma_{\mathrm{Q}} \neq 0$, are a realistic scenario for the qubit, e.g. as a result of its previous use in a quantum technological application. In this case, even though we again find $z_2^{\mathrm{init}} = z_3^{\mathrm{init}} = z_6^{\mathrm{init}} = z_8^{\mathrm{init}} = 0$, we also find that the coefficients $z_5^{\mathrm{init}} = \mathfrak{Re}\{\gamma_{\mathrm{Q}}\}$ and/or $z_7^{\mathrm{init}} = \mathfrak{Im}\{\gamma_{\mathrm{Q}}\}$ will be initially non-zero. Thus, we have $R_2 > 0$ and there will be dynamics within the subspace S_{5678}.

Assuming resonance in the following, i.e., $\delta = 0$ for all t, the dynamics within S_{123} is reduced to the two-dimensional subspace S_{12}, as discussed before. Fortunately, $\delta = 0$ also allows to simplify the dynamics on the four dimensional sphere S_{5678}, where it allows to decouple its equation of motion (5.48) into two separate equations of motion, each of them describing the dynamics on the two dimensional sphere $S_{56} = \{z_5, z_6\}$ and $S_{78} = \{z_7, z_8\}$, respectively. Their corresponding equations of motions are

$$\begin{pmatrix} \dot{z}_5 \\ \dot{z}_6 \end{pmatrix} = J \begin{pmatrix} -z_6 \\ z_5 \end{pmatrix}, \qquad \begin{pmatrix} \dot{z}_7 \\ \dot{z}_8 \end{pmatrix} = J \begin{pmatrix} z_8 \\ -z_7 \end{pmatrix}. \tag{5.58}$$

Figure 5.11 shows the evolution in the three subspaces S_{12}, S_{56} and S_{78} for an exemplary initial factorizing state with $\gamma_{\mathrm{Q}} \neq 0$ and $\gamma_{\mathrm{A}} = 0$. Due to $R_1 > 0$ and $R_2 > 0$, we now

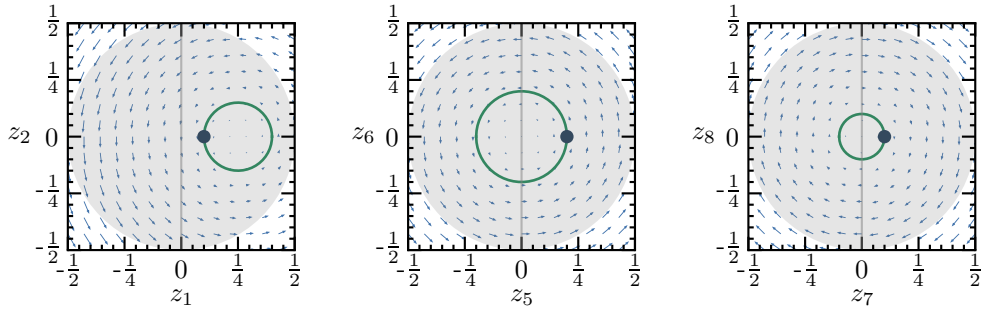

Figure 5.11: Time evolution (green lines) within the three subspaces S_{12}, S_{56} and S_{78} (from left to right) for a factorizing initial state (5.57) with $p_{\mathrm{Q}}^{\mathrm{g}} = 0.6$, $p_{\mathrm{Q}}^{\mathrm{e}} = 0.4$, $\gamma_{\mathrm{Q}} = 0.2 + \mathrm{i}0.1$ and $p_{\mathrm{A}}^{\mathrm{g}} = 0.9$, $p_{\mathrm{A}}^{\mathrm{e}} = 0.1$, $\gamma_{\mathrm{A}} = 0$. Qubit and ancilla are in resonance ($\delta = 0$ for all t). The dots indicate the initial state within the specific subspace, which then evolves along the vector fields (5.52) and (5.58), represented by the blue arrows. The gray vertical lines indicate the respective minimal contribution to the qubit's purity for each subspace, while the gray spheres visualize the projection of the entire state space onto the subspaces.

have dynamics in all three subspaces and thus have contributions to $\mathcal{P}_{\mathrm{Q}}$ from all of them. As before, maximizing the qubit's ground state population, $p_{\mathrm{Q}}^{\mathrm{g}} = z_1 + 1/2$, requires the time $T = \pi/(2J)$, which corresponds to an evolution in terms of a half circle in S_{12}. It is important to note that the motion within S_{12} is twice as fast as that in S_{56} and S_{78}. This can be easily seen by comparing Eqs. (5.52) and (5.58). Therefore, at time $T = \pi/(2J)$ when the qubit's ground state population is maximized, the qubit's coherences, $\gamma_{\mathrm{Q}} = z_5 + \mathrm{i}z_7$, vanish, since the evolution within S_{56} and S_{78} only runs through a quarter circle within the same time. However, due to the maximization of $p_{\mathrm{Q}}^{\mathrm{g}}$, we know that this state corresponds to $\mathcal{P}_{\mathrm{Q}}^{\mathrm{max}} = \mathcal{P}_{\mathrm{A}}^{\mathrm{init}}$. Since we know that a purity swap is the optimal solution in terms of fidelity, this tells us that also the minimal reset time is not changed when allowing for coherences in the initial qubit state. Hence, as long as the initial purities of qubit and ancilla satisfy $\mathcal{P}_{\mathrm{Q}}^{\mathrm{init}} < \mathcal{P}_{\mathrm{A}}^{\mathrm{init}}$, a time-optimal solution is given by Eqs. (5.53) and (5.54). This is true irrespective of the specific initial state of the qubit.

If we now also allow for coherences in the initial state of the ancilla, i.e., $\gamma_{\mathrm{A}} \neq 0$, the question whether $\delta = 0$ still determines a time-optimal solution is not as simple to answer anymore — at least not by the geometric picture established so far. In this case, some or all of the initial values z_2^{init}, z_3^{init}, z_6^{init} and z_8^{init}, which have been zero so far, can become non-zero. Geometrically, this implies that the initial dots in the three spheres S_{12}, S_{56} and S_{78} of Fig. 5.11, which indicate the initial starting position according to state (5.57), are then placed at arbitrary positions along the green curves. Thus, the evolution can not be synchronized easily in terms of half and quarter circles, since each contribution to $\mathcal{P}_{\mathrm{Q}}$ from the three spheres reaches its maximum at a different time. Thus, rather exact

knowledge of the initial state would be required to determine the optimal solution.

Optimal Strategy for Correlated Initial States

For correlated initial states, we consider states of the form (5.28), which here can be generalized to read

$$\rho^{\text{init}} = \begin{pmatrix} p_{\text{Q}}^{\text{g}} & 0 \\ 0 & p_{\text{Q}}^{\text{e}} \end{pmatrix} \otimes \begin{pmatrix} p_{\text{A}}^{\text{g}} & 0 \\ 0 & p_{\text{A}}^{\text{e}} \end{pmatrix} + \begin{pmatrix} 0 & 0 & 0 & 0 \\ 0 & 0 & \gamma & 0 \\ 0 & \gamma^{\star} & 0 & 0 \\ 0 & 0 & 0 & 0 \end{pmatrix}, \tag{5.59}$$

with p_{Q}^{g} (p_{A}^{g}) and p_{Q}^{e} (p_{A}^{e}) as in Eq. (5.51) and γ being responsible for the correlations between qubit and ancilla. For such an initial state, we again have that the coefficients $z_5^{\text{init}}, \ldots, z_8^{\text{init}}$ are initially vanishing, which yields $R_2 = 0$ and, as a consequence, the dynamics on S_{5678} is vanishing as well. We can therefore restrict our discussion to the three dimensional sphere S_{123} for which the dynamics will involve all three dimensions. The latter follows from our choice of $\gamma \in \mathbb{R}$ that implies $z_3^{\text{init}} \neq 0$. While the geometric analysis of the qubit reset does unfortunately not allow us to derive a time-optimal solution for this case, we will see that the geometric picture is still useful in order to obtain physical insights into the fundamental control mechanisms. In particular, it will explain why initial correlations allow us to obtain purities $\mathcal{P}_{\text{Q}} > \mathcal{P}_{\text{Q}}^{\max}$ in times $T < T_{\min}$, i.e., why initial correlations allow us to beat the limits (5.32) established for factorizing initial conditions.

For any initial state satisfying Eq. (5.59), it is straightforward to show that such correlated initial states allow to access qubit states with purity higher than $\mathcal{P}_{\text{Q}}^{\max}$. Since the reduced states of qubit and ancilla are unchanged by the presence of correlations, the center $(c, 0, 0)$ of the sphere in S_{123}, which is exclusively determined by these reduced states of qubit and ancilla, remains unchanged. However, the sphere's radius R_1 increases, which follows directly form Eq. (5.49) and the fact that z_3^{init}, which has been zero so far, becomes non-zero now. As a result, the set of accessible states that may be reached by the dynamics changes and now contains states with larger z_1 values and thus larger qubit purities than what has been accessible with factorizing initial states.

Figure 5.12(a) shows the evolution starting from a correlated initial state under a field designed by numerical optimization, cf. Fig. 5.12(b). It illustrates geometrically why the quantum speed limit $T_{\min}$ for factorizing initial states can be beaten. For the initial state in Fig. 5.12(a), we have $z_2^{\text{init}} = 0$ and $z_3^{\text{init}} = \gamma < 0$. The optimized field drives

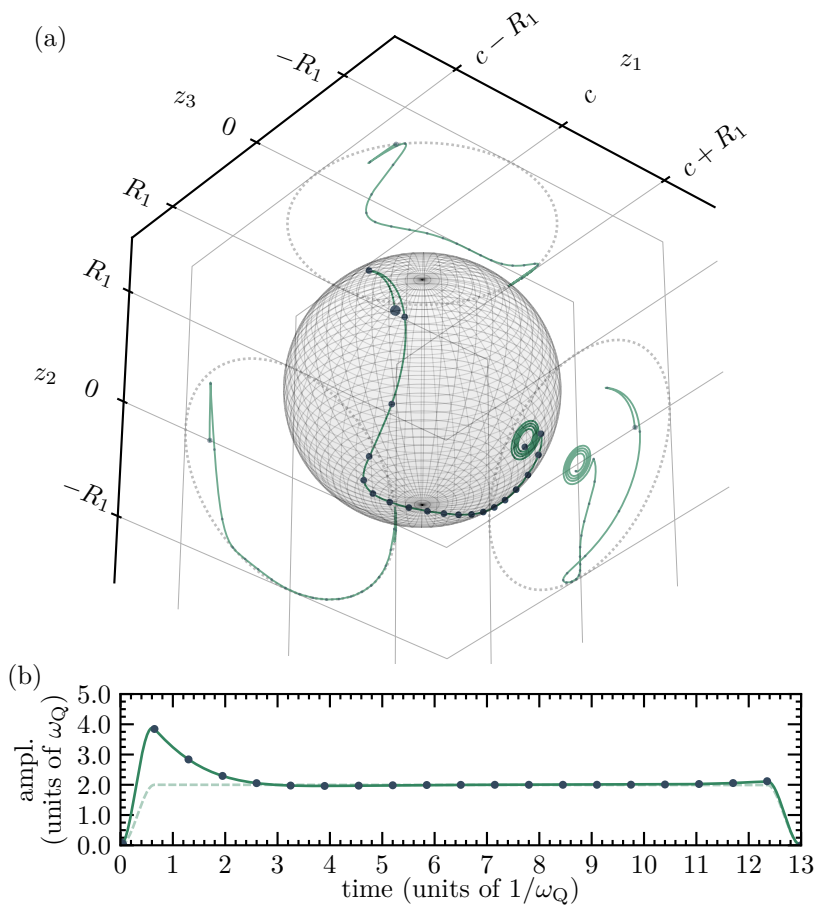

Figure 5.12: (a) Evolution within the subspace S_{123} for a correlated initial state of the form (5.59) under the optimized field shown in (b). The parameters are $\gamma = -0.09$ and all other as in Fig. 5.7. The large dot marks the initial point in state space, the small dots indicate the evolution in chunks of 5% of the total time $T = 13$. The final error is $\mathcal{J}_T = 1.6\%$.

the state rapidly towards the $z_3 = 0$ plane. This is achieved by the off-resonant peak in the optimized field between $t = 0$ and $t \approx 2$, cf. Fig. 5.12(b). The subsequent evolution with $\delta = 0$ becomes again two-dimensional within the z_1-z_2 plane. This evolution is conceptually equivalent to the evolution shown in Fig. 5.10. However, in contrast to the dynamics shown in Fig. 5.10, the motion in the z_1-z_2 plane has to overcome a reduced distance as a consequence of the initial transfer between $z_3 < 0$ and $z_3 = 0$. This can be seen from the projection of the entire motion onto the z_1-z_2 plane that is shown in the front left plane in Fig. 5.12(a). The position of the third small dot should be noted in particular, as it marks the point in time where the control field δ goes roughly back into resonance for the remainder of the reset protocol. However, less than a half circle has to

be overcome by the remaining evolution with $\delta = 0$ to reach the point of largest purity, $z_1^{\max} = c + R_1$. Since the initial transfer towards the $z_3 = 0$ plane is accomplished faster than any motion within this plane, the total reset duration is reduced below $T_{\min}$.

This reduction of $T_{\min}$ can also be demonstrated analytical. To this end, we again consider the equation of motion (5.47) and assume the coupling J to be constant and bounded, while there is no constraint on $\frac{\mathrm{d}\delta}{\mathrm{d}t}$, i.e., on $\alpha(t)$, cf. Eq. (5.43). Inspired by the numerical solution of Fig. 5.12, a presumably time-optimal solution can be decomposed into two stages. In a first stage, we can neglect the two terms with J_1 and J_2 on the right hand side of Eq. (5.47) as the α term can be tuned dominant and be used to move arbitrarily fast within the z_2-z_3 plane. This assumption is justified, since J_1 and J_2 are negligibly small compared to α which therefore effectively determines the dynamics. It can thus be used to drive the initial point as fast as possible into the $z_3 = 0$ plane. This motion is completed in the time T_α provided α satisfies the condition

$$\int_0^{T_\alpha} 2\alpha(t)\mathrm{d}t = \frac{\pi}{2}, \tag{5.60}$$

which, after integration by parts, leads to

$$\delta(T_\alpha) - \int_0^{T_\alpha} \delta(t)\mathrm{d}t = \frac{\pi}{2}. \tag{5.61}$$

A standard solution for δ is then given by a linear time evolution of the form

$$\delta(t) = \frac{\pi t}{2T_\alpha(1 - \frac{T_\alpha}{2})} \tag{5.62}$$

for $t \in [0, T_\alpha]$. The second stage of the presumably time-optimal solution is the meridian trajectory in the $z_3 = 0$ plane with $\delta = 0$. In fact, for constant δ, we recover the Grushin model [58] for which it can be shown analytically that the meridian trajectory is the solution minimizing the time to reach the state of largest purity, i.e., $z_1^{\max}$ in our case. The time required for the motion along the meridian is fixed by the initial point for this dynamics. It is given by $T_\theta = \theta^{\mathrm{init}}/(2J)$, where θ^{init} is again the azimuth angle within the sphere S_{123} given by $z_1^{\mathrm{init}} = R_1 \cos(\theta^{\mathrm{init}})$. Since we can assume that the time T_α to reach the $z_3 = 0$ plane to be arbitrarily small, as α can be made arbitrarily large, the total time $T_{\min}^{\mathrm{corr}} = T_\alpha + T_\theta$ required for both stages of the presumably time-optimal solution for correlated initial states is given by $T_{\min}^{\mathrm{corr}} \approx T_\theta < T_{\min}$ and therefore smaller than the minimal time $T_{\min} = \pi/(2J)$ obtained for factorizing initial states. This geometric analysis of the numerical solution in Fig. 5.12 explains and confirms the role of initial correlations for the speedup of the purification process.

In conclusion, although we can not prove time-optimality of the numerical solution presented in Fig. 5.12, we can find an explanation of the larger accessible purity and lower reset time by analyzing the numerical solution geometrically. Unfortunately, this improvement in fidelity and time comes at a cost, namely the control field must be optimized in dependence with the initial value $z_3^{\text{init}} = \gamma$. In other words, for correlated initial states, derivation of the time-optimal control strategy requires knowledge of the initial state.

Finally, it should be mentioned that the analytical model presented so far has been extended in Ref. [240] to also include the effects of the reservoir which we have neglected so far. There, it has been found that the reset time *including* the reservoir is actually lower bounded by the reset time $T_{\text{min}} = \pi/(2J)$ obtained here while *neglecting* the reservoir [240]. Physically, this implies that the reservoir is not assisting in terms of reducing the reset time, even though its presence is of course crucial for the protocol to work, as it is responsible for the equilibration of the ancilla after it receives the qubit's entropy. However, an interesting distinction can be made depending on whether $\Gamma/J > 4$ or $\Gamma/J < 4$ with $\Gamma = \kappa(2N+1)$, κ the coupling strength between ancilla and reservoir and N the Planck distribution, cf. Eq. (5.23). For $\Gamma/J > 4$, the dissipation becomes so strong that it renders the qubit dynamics Markovian despite the strong coupling between qubit and ancilla. As a consequence, the target state on the sphere can not be reached in finite time anymore as it becomes the steady state of a Markovian process that approaches this point only asymptotically. In contrast, for $\Gamma/J < 4$ the qubit dynamics is non-Markovian in which case the target state can always be reached in finite time. See Ref. [240] for details.

To summarize, in this section we have considered qubit reset that utilizes the strong coupling to a single ancilla mode of the environment. We have explored the impact of initial correlations between qubit and environment on the qubit reset. Employing optimized control fields, we have shown that initial correlations can be turned into an asset for the reset protocol. For uncorrelated initial states, we have derived a time-optimal reset protocol. The latter scenario will be investigated in more detail in the following.

5.3 Fundamental Bounds for Ancilla-Based Qubit Reset

In this last section, we will generalize the model for ancilla-based qubit reset, as it has been introduced in the last section. While the focus in the last section has been on the role of initial correlations between qubit and ancilla on the reset process, here we switch the focus and examine the influence of the type of qubit-ancilla interaction and local

qubit control on the reset process — both of which haven been fixed in Sec. 5.2. This is a quite natural question to ask, since many quantum information architectures, especially superconducting qubits, can be designed with great flexibility. In detail, traits like the local control mechanism and the type of interaction between different qubits or of a qubit and other modes can often be engineered to some extent. The influence of these traits is surprisingly non-trivial, as we will demonstrate in this section. From a theoretical perspective, each physically and mathematically conceivable combination of qubit-ancilla interaction and local qubit control gives rise to a different form of controllability for the combined qubit-ancilla system, i.e., each combination allows for a different set of realizable dynamical maps, cf. Subsec. 2.3.1. Therefore, each combination also gives rise to a different dynamics in the reduced system of the qubit and, as a consequence, each combination needs to be evaluated individually in view of its capability to reset the qubit, i.e., to export entropy from the qubit into the ancilla. It should be emphasized that even if the controllability for the qubit-ancilla system is identical for two different combinations of qubit-ancilla interaction and local qubit control, this does not necessarily imply that also the required reset time is identical. In terms of the qubit's dynamical map $\mathcal{D}^{\mathrm{Q}}_{t,t_0}$, the latter statement implies that, even though the same set of dynamical maps can be realized with two different sets of qubit-ancilla interaction and local qubit control, the necessary time t to implement it can still be very different in practice. Thus, in this section, we will examine the general feasibility of qubit reset as well as its bounds in fidelity and time in dependence of the types of qubit-ancilla interaction and local qubit control and provide a time-optimal solution for all cases. The results in this section are based on Ref. [244].

5.3.1 Model and Control Problem

Like in Sec. 5.2 we consider a qubit coupled to a two-level ancilla. Let $\mathcal{H}_{\mathrm{Q}}$ ($\mathfrak{L}_{\mathcal{H}_{\mathrm{Q}}}$) and $\mathcal{H}_{\mathrm{A}}$ ($\mathfrak{L}_{\mathcal{H}_{\mathrm{A}}}$) be the Hilbert (Liouville) spaces for qubit and ancilla, respectively. However, in contrast to Sec. 5.2, we consider a more general Hamiltonian for this bipartite system, which reads

$$\mathsf{H}(t) = \big(\mathsf{H}_{\mathrm{Q}} + \mathcal{E}(t)\mathsf{O}_{\mathrm{ctrl}}\big) \otimes \mathbb{1}_{\mathrm{A}} + \mathbb{1}_{\mathrm{Q}} \otimes \mathsf{H}_{\mathrm{A}} + J\big(\mathsf{O}_{\mathrm{Q}} \otimes \mathsf{O}_{\mathrm{A}}\big), \tag{5.63}$$

where H_{Q} and H_{A} are the static Hamiltonians for qubit and ancilla, respectively. $\mathcal{E}(t)$ is a time-dependent control field that interacts via operator $\mathsf{O}_{\mathrm{ctrl}} \in \mathfrak{L}_{\mathcal{H}_{\mathrm{Q}}}$ with the qubit. The interaction between qubit and ancilla is given by $\mathsf{O}_{\mathrm{Q}} \otimes \mathsf{O}_{\mathrm{A}} \in \mathfrak{L}_{\mathcal{H}_{\mathrm{Q}}} \otimes \mathfrak{L}_{\mathcal{H}_{\mathrm{A}}}$ with its interaction strength determined by J. Hamiltonian (5.63) therefore constitutes a

generalization of Hamiltonian (5.21). The latter is given by the special case of $\mathsf{O}_{\mathrm{ctrl}} = \sigma_{\mathrm{z}}/2$ and $\mathsf{O}_{\mathrm{Q}} = \mathsf{O}_{\mathrm{A}} = \sigma_{\mathrm{x}}$. What distinguishes Eq. (5.63) from the scenario considered in Sec. 5.2 is that we are not only interested in the solution of the reset task for one fixed Hamiltonian but rather on how this solutions depends on the actual characteristics of the Hamiltonian. This is interesting, since in view of Eq. (5.63), the Hamiltonian's characteristics change substantially depending on the operators $\mathsf{O}_{\mathrm{ctrl}}, \mathsf{O}_{\mathrm{Q}}, \mathsf{O}_{\mathrm{A}}$ — which here specify the type of local control and qubit-ancilla interaction. It is therefore not straightforward to answer, how these operators need to be chosen in order to ease or even fundamentally enable qubit reset. Their only restriction requires them to be Hermitian operators, i.e., their most general form would be $\mathsf{O}_{\mathrm{ctrl}}, \mathsf{O}_{\mathrm{Q}}, \mathsf{O}_{\mathrm{A}} \in \mathfrak{su}(2)$ with $\mathfrak{su}(2)$ the Lie algebra that generates the Lie group SU(2).

In our current model, which has been generalized with respect to the one used in Sec. 5.2 by using a more general Hamiltonian, we nevertheless neglect the reservoir to which the ancilla is weakly coupled to, cf. Fig. 5.6. Although its presence is crucial for the ancilla-based qubit reset to work physically, as it is responsible for the equilibration of the ancilla, it has no impact on the fast, time-optimal reset protocol which utilizes the strong coupling between qubit and ancilla. This is in agreement with the analytical calculations from Subsec. 5.2.4 and Refs. [223, 240]. Hence, we will neglect the reservoir in the following and the dynamics of the joint qubit-ancilla system will therefore be unitary. Furthermore, since in contrast to Sec. 5.2 the focus should not be on initial correlations between qubit and ancilla, we assume the initial state to be uncorrelated. It is given by $\rho(t_0) = \rho_{\mathrm{Q}}(t_0) \otimes \rho_{\mathrm{A}}(t_0)$, with $\rho_{\mathrm{Q}}(t_0)$ and $\rho_{\mathrm{A}}(t_0)$ the reduced states of qubit and ancilla, respectively. Its dynamics reads

$$\rho(t) = \mathsf{U}_{t,t_0}\big(\rho_{\mathrm{Q}}(t_0) \otimes \rho_{\mathrm{A}}(t_0)\big)\mathsf{U}_{t,t_0}^{\dagger}, \tag{5.64}$$

where $\mathsf{U}_{t,t_0} \in \mathrm{SU}(4)$ describes the time-evolution operator of the joint qubit-ancilla system. The time-evolved state of the qubit becomes

$$\rho_{\mathrm{Q}}(t) = \mathrm{tr}_{\mathrm{A}}\left\{\mathsf{U}_{t,t_0}\big(\rho_{\mathrm{Q}}(t_0) \otimes \rho_{\mathrm{A}}(t_0)\big)\mathsf{U}_{t,t_0}^{\dagger}\right\} = \mathcal{D}^{\mathrm{Q}}_{t,t_0;\rho_{\mathrm{A}}(t_0)}[\rho_{\mathrm{Q}}(t_0)], \tag{5.65}$$

where we have introduced the dynamical map $\mathcal{D}^{\mathrm{Q}}_{t,t_0;\rho_{\mathrm{A}}(t_0)} : \mathfrak{L}_{\mathcal{H}_{\mathrm{Q}}} \to \mathfrak{L}_{\mathcal{H}_{\mathrm{Q}}}$ for the reduced system of the qubit. Note that due to the strong coupling between qubit and ancilla, the dynamical map $\mathcal{D}^{\mathrm{Q}}_{t,t_0;\rho_{\mathrm{A}}(t_0)}$ will depend substantially on the ancilla's initial state $\rho_{\mathrm{A}}(t_0)$, which is the reason why indicate this dependence explicitly.

Besides the generalization of Hamiltonian (5.63) compared to Sec. 5.2, also the control task will be the most general one, namely to maximize the qubit's purity $\mathcal{P}_{\mathrm{Q}}(t)$ at final

time T. In terms of optimal control this implies minimization of the final-time functional

$$\mathcal{J}_T[\rho, T] = 1 - \mathcal{P}_{\mathrm{Q}}(T) = 1 - \mathrm{tr}\left\{\rho_{\mathrm{Q}}(T)^2\right\} \tag{5.66}$$

with $\rho_{\mathrm{Q}}(T)$ given by Eq. (5.65). In the following, we want to identify the time-optimal solution to do this. In contrast to Sec. 5.2, we will examine how this time-optimal solution depends on the operators O_{Q} and O_{A}, which specify the type of qubit-ancilla interaction, and on $\mathsf{O}_{\mathrm{ctrl}}$, which specifies the local qubit control.

5.3.2 A Lie Algebraic Analysis of the Reset Task

Before we will delve into the details how to optimally choose $\mathcal{E}(t)$ in dependence of $\mathsf{O}_{\mathrm{ctrl}}, \mathsf{O}_{\mathrm{Q}}$ and O_{A}, we can examine the question from an even more fundamental perspective. Let $\mathsf{U} = \mathsf{U}_{t,t_0} \in \mathrm{SU}(4)$ be the time-evolution operator for the qubit-ancilla system. In view of Eq. (5.65), the most fundamental question to ask is which requirements U needs to fulfill such that it allows purification of the qubit in the first place. The answer to this question is independent of the particular Hamiltonian and control field that generate U and therefore independent of the choice of $\mathsf{O}_{\mathrm{ctrl}}, \mathsf{O}_{\mathrm{Q}}$ and O_{A}. Hence, we will forget about Hamiltonian (5.63) for a moment. The question regarding the structural requirements for U can be answered by the Cartan decomposition of the Lie group SU(4). To this end, we will briefly summarize its basic concept [11].

Definition 5.1. *(Cartan Decomposition) Let $\mathfrak{g}$ be a semisimple Lie algebra. Its decomposition $\mathfrak{g} = \mathfrak{k} \oplus \mathfrak{p}$ with $\mathfrak{p} = \mathfrak{k}^{\perp}$ is called Cartan decomposition of $\mathfrak{g}$ if $[\mathfrak{k}, \mathfrak{k}] \subset \mathfrak{k}$, $[\mathfrak{p}, \mathfrak{k}] \subset \mathfrak{p}$ and $[\mathfrak{p}, \mathfrak{p}] \subset \mathfrak{k}$. A maximal Abelian subalgebra $\mathfrak{a} \subset \mathfrak{p}$ is called Cartan subalgebra.*

Let G be the Lie group generated by $\mathfrak{g}$. A Cartan decomposition of G is given by $G = K \exp\{\mathfrak{a}\} K$ with $K = \exp\{\mathfrak{k}\}$ the compact subgroup of G generated by $\mathfrak{k}$. If we now consider the case $\mathfrak{g} = \mathfrak{su}(4)$ that describes to the joint qubit-ancilla system, its Cartan decomposition is well known and takes the form [245]

$$\begin{aligned}
\mathfrak{k} &= \mathrm{span}\left\{\sigma_{\mathrm{x}}^{\mathrm{Q}} \otimes \mathbb{1}_{\mathrm{A}}, \sigma_{\mathrm{y}}^{\mathrm{Q}} \otimes \mathbb{1}_{\mathrm{A}}, \sigma_{\mathrm{z}}^{\mathrm{Q}} \otimes \mathbb{1}_{\mathrm{A}}, \mathbb{1}_{\mathrm{Q}} \otimes \sigma_{\mathrm{x}}^{\mathrm{A}}, \mathbb{1}_{\mathrm{Q}} \otimes \sigma_{\mathrm{y}}^{\mathrm{A}}, \mathbb{1}_{\mathrm{Q}} \otimes \sigma_{\mathrm{z}}^{\mathrm{A}}\right\}, \\
\mathfrak{p} &= \mathrm{span}\Big\{\sigma_{\mathrm{x}}^{\mathrm{Q}} \otimes \sigma_{\mathrm{x}}^{\mathrm{A}}, \sigma_{\mathrm{x}}^{\mathrm{Q}} \otimes \sigma_{\mathrm{y}}^{\mathrm{A}}, \sigma_{\mathrm{x}}^{\mathrm{Q}} \otimes \sigma_{\mathrm{z}}^{\mathrm{A}}, \\
&\qquad \sigma_{\mathrm{y}}^{\mathrm{Q}} \otimes \sigma_{\mathrm{x}}^{\mathrm{A}}, \sigma_{\mathrm{y}}^{\mathrm{Q}} \otimes \sigma_{\mathrm{y}}^{\mathrm{A}}, \sigma_{\mathrm{y}}^{\mathrm{Q}} \otimes \sigma_{\mathrm{z}}^{\mathrm{A}}, \\
&\qquad \sigma_{\mathrm{z}}^{\mathrm{Q}} \otimes \sigma_{\mathrm{x}}^{\mathrm{A}}, \sigma_{\mathrm{z}}^{\mathrm{Q}} \otimes \sigma_{\mathrm{y}}^{\mathrm{A}}, \sigma_{\mathrm{z}}^{\mathrm{Q}} \otimes \sigma_{\mathrm{z}}^{\mathrm{A}}\Big\},
\end{aligned} \tag{5.67}$$

from which it is evident that its Cartan decomposition separates operators that act locally on either qubit or ancilla into $\mathfrak{k}$ and operators responsible for qubit-ancilla interactions

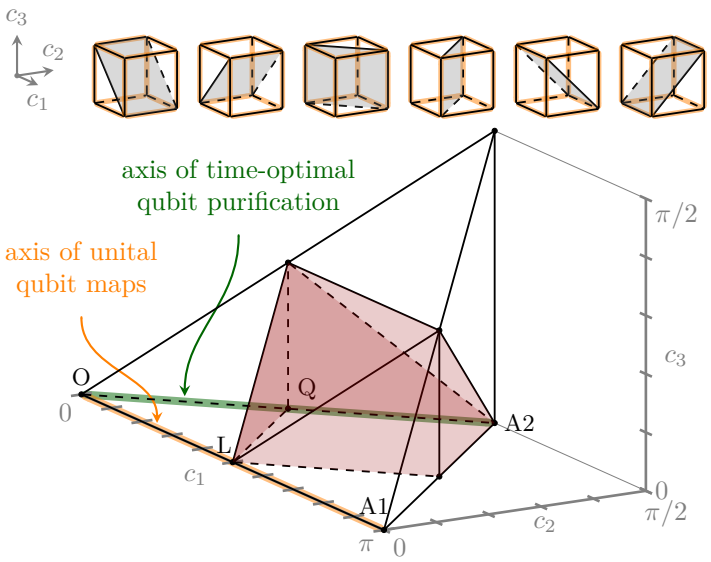

Figure 5.13: Symmetries (upper part) and construction of the Weyl chamber (lower part) for the characterization of the non-local part A of a two-qubit operation $\mathsf{U} \in \mathrm{SU}(4)$, cf. Eq. (5.69). The shaded polyhedron within the Weyl chamber describes all perfectly entangling operations. The orange lines highlight those U which lead to unital maps for the reduced system of the qubit. The green line anticipates a time-optimal path for qubit purification identified in the following. The letters mark specific points in the Weyl chamber.

into $\mathfrak{p}$. While a Cartan subalgebra $\mathfrak{a} \subset \mathfrak{g}$ is in general not unique, a possible choice in case of $\mathfrak{g} = \mathfrak{su}(4)$ is given by [245]

$$\mathfrak{a} = \mathrm{span}\{\sigma_x^{\mathrm{Q}} \otimes \sigma_x^{\mathrm{A}}, \sigma_y^{\mathrm{Q}} \otimes \sigma_y^{\mathrm{A}}, \sigma_z^{\mathrm{Q}} \otimes \sigma_z^{\mathrm{A}}\}. \tag{5.68}$$

In consequence, the Cartan decomposition of $\mathrm{G} = \mathrm{SU}(4)$ implies that we can write every element $\mathsf{U} \in \mathrm{SU}(4)$ as [245]

$$\mathsf{U} = \mathsf{K}\mathsf{A}\mathsf{K}', \qquad \mathsf{A} = \exp\left\{\frac{\mathrm{i}}{2}\left[c_1\left(\sigma_x^{\mathrm{Q}} \otimes \sigma_x^{\mathrm{A}}\right) + c_2\left(\sigma_y^{\mathrm{Q}} \otimes \sigma_y^{\mathrm{A}}\right) + c_3\left(\sigma_z^{\mathrm{Q}} \otimes \sigma_z^{\mathrm{A}}\right)\right]\right\}, \tag{5.69}$$

with $\mathsf{K} = \mathsf{K}_{\mathrm{Q}} \otimes \mathsf{K}_{\mathrm{A}} \in K$ and $\mathsf{K}' = \mathsf{K}'_{\mathrm{Q}} \otimes \mathsf{K}'_{\mathrm{A}} \in K$ with $K = \mathrm{SU}(2) \otimes \mathrm{SU}(2)$. The Cartan decomposition therefore allows us to decompose a general qubit-ancilla operator $\mathsf{U} \in \mathrm{SU}(4)$ into its local components K and K' and its non-local part A. The latter is exclusively determined by the coefficients $c_1, c_2, c_3 \in [0, \pi]$ cf. Eq. (5.69). In the following, we will refer to these coefficients as non-local (NL) coordinates. After reducing redundant symmetries within the full cube defined by $c_1, c_2, c_3 \in [0, \pi]$, sketched in the upper part of Fig. 5.13, we obtain the so-called Weyl chamber, sketched in lower part of Fig. 5.13.

The Weyl chamber constitutes a symmetry-reduced representation of the non-local part A of an arbitrary $\mathsf{U} \in \mathrm{SU}(4)$. See Ref. [245] for a more detailed explanation of the Cartan decomposition and the Weyl chamber.

The important implication of Eq. (5.69) with respect to resetting the qubit is that only the non-local part A of U can be responsible for any interaction between qubit and ancilla. It must therefore be responsible for the entropy exchange between qubit and ancilla. In contrast, the local operations $\mathsf{K}, \mathsf{K}' \in \mathrm{SU}(2) \otimes \mathrm{SU}(2)$ are only responsible for local unitary transformations and do therefore not change the entropy of neither qubit nor ancilla. Hence, in order to answer the original question regarding which $\mathsf{U} \in \mathrm{SU}(4)$ allow for qubit purification, we note that due to the Cartan decomposition of Eq. (5.69), the problem reduces to an analysis of only A. Hence, the question becomes how A needs to be structured in order to allow qubit purification.

A necessary condition for purification of the qubit is the non-unitality of its dynamical map [45]. A dynamical map is called unital if it maps the identity onto itself. In terms of Eq. (5.65), non-unitality therefore requires $\mathcal{D}^{\mathrm{Q}}_{t,t_0;\rho_{\mathrm{A}}(t_0)}[\mathbb{1}_{\mathrm{Q}}] \neq \mathbb{1}_{\mathrm{Q}}$, cf. Eq. (5.65). In order to check whether $\mathcal{D}^{\mathrm{Q}}_{t,t_0;\rho_{\mathrm{A}}(t_0)}$ behaves unital or not, we consider the initial state

$$\rho(t_0) = \mathbb{1}_{\mathrm{Q}} \otimes \rho_{\mathrm{A}}(t_0) \qquad \rho_{\mathrm{A}}(t_0) = \begin{pmatrix} p^{\mathrm{e}}_{\mathrm{A}} & \gamma_{\mathrm{A}} \\ \gamma^{\star}_{\mathrm{A}} & p^{\mathrm{g}}_{\mathrm{A}} \end{pmatrix}, \tag{5.70}$$

where $p^{\mathrm{g}}_{\mathrm{A}}$ ($p^{\mathrm{e}}_{\mathrm{A}}$) is the ancilla's ground (excited) state population and $\gamma_{\mathrm{A}} \in \mathbb{C}$ its coherences. Using Eq. (5.69), we find for an arbitrary time-evolution operator $\mathsf{U} = \mathsf{U}_{t,t_0} \in \mathrm{SU}(4)$ that

$$\mathcal{D}^{\mathrm{Q}}_{t,t_0;\rho_{\mathrm{A}}(t_0)}\left[\mathbb{1}_{\mathrm{Q}}\right] = \mathrm{tr}_{\mathrm{A}}\left\{\mathsf{U}\left(\mathbb{1}_{\mathrm{Q}} \otimes \rho_{\mathrm{A}}(t_0)\right)\mathsf{U}^{\dagger}\right\} = \mathsf{K}_{\mathrm{Q}}\mathrm{tr}_{\mathrm{A}}\left\{\mathsf{A}\left(\mathbb{1}_{\mathrm{Q}} \otimes \rho'_{\mathrm{A}}\right)\mathsf{A}^{\dagger}\right\}\mathsf{K}^{\dagger}_{\mathrm{Q}}, \tag{5.71}$$

where

$$\rho'_{\mathrm{A}} = \mathsf{K}'_{\mathrm{A}}\rho_{\mathrm{A}}(t_0)\mathsf{K}'^{\dagger}_{\mathrm{A}} = \begin{pmatrix} p^{\mathrm{e}\prime}_{\mathrm{A}} & \gamma'_{\mathrm{A}} \\ \gamma'^{*}_{\mathrm{A}} & p^{\mathrm{g}\prime}_{\mathrm{A}} \end{pmatrix} \tag{5.72}$$

is the locally transformed ancilla state. Unitality of $\mathcal{D}^{\mathrm{Q}}_{t,t_0;\rho_{\mathrm{A}}(t_0)}$ is determined by the partial trace in Eq. (5.71), since $\mathsf{K}_{\mathrm{Q}}\mathbb{1}_{\mathrm{Q}}\mathsf{K}^{\dagger}_{\mathrm{Q}} = \mathbb{1}_{\mathrm{Q}}$ for any $\mathsf{K}_{\mathrm{Q}} \in \mathrm{SU}(2)$. We therefore see that the non-local part A is indeed the only relevant part from U. Evaluating the partial trace yields

$$\begin{aligned}\mathrm{tr}_{\mathrm{A}}\left\{\mathsf{A}\left(\mathbb{1}_{\mathrm{Q}} \otimes \rho'_{\mathrm{A}}\right)\mathsf{A}^{\dagger}\right\} = \mathbb{1}_{\mathrm{Q}} &+ \left[2\mathfrak{Re}\left\{\gamma'_{\mathrm{A}}\right\}\sin(c_2)\sin(c_3)\right]\sigma_{\mathrm{x}} \\ &- \left[2\mathfrak{Im}\left\{\gamma'_{\mathrm{A}}\right\}\sin(c_1)\sin(c_3)\right]\sigma_{\mathrm{y}}\end{aligned}$$

$$- \left[\left(p_{\mathrm{A}}^{\mathrm{g}\prime} - p_{\mathrm{A}}^{\mathrm{e}\prime} \right) \sin(c_1) \sin(c_2) \right] \sigma_{\mathrm{z}}. \tag{5.73}$$

From Eq. (5.73) we can conclude that any $\mathsf{U} \in \mathrm{SU}(4)$, which gives rise to only a single non-vanishing NL coordinate c_k necessarily yields a unital map $\mathcal{D}^{\mathrm{Q}}_{t,t_0;\rho_{\mathrm{A}}(t_0)}$ for the qubit, and qubit purification is not possible at all. This follows from the fact that with only one non-vanishing NL coordinates, i.e. two vanishing ones, each term in the right hand side of Eq. (5.73) contains at least one vanishing sine factor, which causes all terms except $\mathbb{1}_{\mathrm{Q}}$ to vanish. The occurrence of two non-vanishing NL coordinates is thus necessary but not yet sufficient to guarantee non-unitality of $\mathcal{D}^{\mathrm{Q}}_{t,t_0;\rho_{\mathrm{A}}(t_0)}$. With two non-vanishing NL coordinates at least one term besides $\mathbb{1}_{\mathrm{Q}}$ has two non-vanishing sine factors. However, this term can still vanish due to its dependence on ρ'_{A}, i.e., on the initial ancilla state $\rho_{\mathrm{A}}(t_0)$ and local operation K'_{A}. A guarantee of non-unitality for $\mathcal{D}^{\mathrm{Q}}_{t,t_0;\rho_{\mathrm{A}}(t_0)}$, independent of the ancilla's initial state ρ'_{A}, is only given by three non-vanishing NL coordinates. Note that we always assume $\rho_{\mathrm{A}}(t_0) \neq \mathbb{1}_{\mathrm{A}}/2$, since this would otherwise imply $p_{\mathrm{A}}^{\mathrm{g}\prime} = p_{\mathrm{A}}^{\mathrm{e}\prime} = 1/2$ and $\gamma'_{\mathrm{A}} = 0$ and $\mathcal{D}^{\mathrm{Q}}_{t,t_0;\rho_{\mathrm{A}}(t_0)}$ would always be unital. This observation is in accordance with physical and thermodynamical intuition. If the ancilla is initially in a completely mixed state, i.e., $\rho_{\mathrm{A}}(t_0) = \mathbb{1}_{\mathrm{A}}/2$, it contains the largest possible amount of entropy and can therefore not absorb any further entropy from the qubit. Non-unitality is therefore the most fundamental requirement for qubit reset.

We now compare the requirements for $\mathsf{U} \in \mathrm{SU}(4)$ to give rise to a non-unital qubit map $\mathcal{D}^{\mathrm{Q}}_{t,t_0;\rho_{\mathrm{A}}(t_0)}$ with the requirements for $\mathsf{U} \in \mathrm{SU}(4)$ to give rise to an entangling operation between qubit and ancilla. The latter can also be conveniently analyzed via U's non-local part A and the Weyl chamber [245]. While the two points marked by O and L1 in the Weyl chamber, cf. Fig. 5.13, correspond to the case $\mathsf{A} = \mathbb{1}$, all remaining points give rise to an entangling operation A between qubit and ancilla. The shaded polyhedron in the Weyl chamber's center describes the set of perfectly entangling operations, i.e., those operations for which at least one factorized state exists on input that becomes maximally entangled on output. See Ref. [246] for a definition and measure of a quantum gate's entangling capability. From Fig. 5.13 it is immediately clear that the c_1-axis represents all operations A with at most one non-vanishing NL coordinate. Due to Eq. (5.73), we know that it gives rise to only unital dynamical maps $\mathcal{D}^{\mathrm{Q}}_{t,t_0;\rho_{\mathrm{A}}(t_0)}$. Surprisingly, the c_1-axis even contains one point of the polyhedron of perfect entanglers — the point L, which corresponds to the cNOT gate [2] and all gates that are locally equivalent to it, which for instance includes the cPHASE gate. However, albeit being perfect entanglers, cNOT and cPHASE yield unital maps $\mathcal{D}^{\mathrm{Q}}_{t,t_0;\rho_{\mathrm{A}}(t_0)}$ for the qubit, irrespective of $\rho_{\mathrm{A}}(t_0)$. We can therefore conclude that the capability of $\mathsf{U} \in \mathrm{SU}(4)$ to create entanglement between qubit

and ancilla is a necessary but not a sufficient condition for purification of the qubit. This implies the rather surprising and non-intuitive conclusion that qubit purification is an even more challenging task for the dynamics than to create entanglement.

5.3.3 Time-Optimal Qubit Reset

In the last subsection, we have identified the fundamental requirements for the time-evolution operator $\mathsf{U}_{t,t_0} \in \mathrm{SU}(4)$ to yield a non-unital dynamical map $\mathcal{D}^{\mathrm{Q}}_{t,t_0;\rho_{\mathrm{A}}(t_0)}$ for the reduced system of the qubit from a mathematical perspective. These requirements hold independent on how the actual Hamiltonian that generates U_{t,t_0} looks like in practice. Now, in order to have a physically well motivated model, we explicitly consider Hamiltonian (5.63) as the generator of the dynamics. Thus, as a next step, we need to examine whether it fulfills the requirements, i.e., gives rise to at least two non-vanishing NL coordinates. To this end, we first take the static Hamiltonian of qubit and ancilla to be given by $\mathsf{H}_{\mathrm{Q}} = \omega_{\mathrm{Q}}\sigma_{\mathrm{z}}^{\mathrm{Q}}/2$ and $\mathsf{H}_{\mathrm{A}} = \omega_{\mathrm{A}}\sigma_{\mathrm{z}}^{\mathrm{A}}/2$, respectively, where ω_{Q} and ω_{A} are their static energy level splittings. However, the total qubit-ancilla Hamiltonian (5.63) is still not fully specified due to the freedom to choose $\mathsf{O}_{\mathrm{ctrl}}, \mathsf{O}_{\mathrm{Q}}, \mathsf{O}_{\mathrm{A}} \in \mathfrak{su}(2)$, i.e., to choose the type of local qubit control and qubit-ancilla interaction. We will first restrict them to be one of the three Pauli operators, i.e., $\mathsf{O}_{\mathrm{ctrl}}, \mathsf{O}_{\mathrm{Q}}, \mathsf{O}_{\mathrm{A}} \in \{\sigma_{\mathrm{x}}, \sigma_{\mathrm{y}}, \sigma_{\mathrm{z}}\}$, although we will lift this restriction later.

In order to connect the Hamiltonian (5.63) to the purification condition, stated in terms of the number N_{nl} of non-vanishing NL coordinates of the joint qubit-ancilla time-evolution operator U_{t,t_0}, we first consider the Hamiltonian's dynamical Lie algebra $\mathfrak{g}$ that each combination of $\mathsf{O}_{\mathrm{ctrl}}, \mathsf{O}_{\mathrm{Q}}, \mathsf{O}_{\mathrm{A}} \in \{\sigma_{\mathrm{x}}, \sigma_{\mathrm{y}}, \sigma_{\mathrm{z}}\}$ gives rise to. As explained in more detail in Subsec. 2.3.1, the dynamical Lie algebra describes the set $\mathfrak{g} \subset \mathfrak{su}(4)$ of elements from the full algebra $\mathfrak{su}(4)$ that can be realized by Hamiltonian (5.63). It therefore determines the set of time-evolution operators $\mathcal{U} = \exp\{\mathfrak{g}\} \subset \mathrm{SU}(4)$ that can be realized by at least on feasible choice of the control field $\mathcal{E}(t)$. We know that the Cartan decomposition of $\mathcal{U}$ will immediately tell us whether we can expect $N_{\mathrm{nl}} \leq 2$, i.e., at least two non-vanishing NL coordinates in the non-local part of the time-evolution operator $\mathsf{U}_{t,t_0} \in \mathcal{U}$. However, for Hamiltonian (5.63), it is also possible to see this from the dynamical Lie algebra $\mathfrak{g}$ and its Cartan decomposition $\mathfrak{g} = \mathfrak{k} \oplus \mathfrak{p}$. To this end, note that while the dynamical Lie algebra $\mathfrak{g}$ depends on the specific choice of $\mathsf{O}_{\mathrm{ctrl}}, \mathsf{O}_{\mathrm{Q}}$ and O_{A}, this dependence gets also transferred to the Cartan decomposition $\mathfrak{g} = \mathfrak{k} \oplus \mathfrak{p}$ for each of these choices. For each Cartan decomposition $\mathfrak{g} = \mathfrak{k} \oplus \mathfrak{p}$, we then need to identify a Cartan subalgebra $\mathfrak{a} \subset \mathfrak{p}$ for which we know that, on the level of the corresponding Lie group $\mathcal{U} = \exp\{\mathfrak{g}\}$, it determines the non-local part $\mathsf{A} \in \exp\{\mathfrak{a}\}$ within $\mathsf{U} = \mathsf{K}'\mathsf{A}\mathsf{K}'$ where $\mathsf{K}, \mathsf{K}' \in \exp\{\mathfrak{k}\}$, cf. Eq. (5.69). The

$\mathsf{O}_\mathrm{Q}\otimes\mathsf{O}_\mathrm{A}$	O_ctrl	$\mathfrak{k}$	$\mathfrak{p}$	$\mathfrak{a}$
$\sigma_\mathrm{x}\sigma_\mathrm{x}$	$\sigma_\mathrm{x}^\mathrm{Q}$	$\sigma_\mathrm{z}^\mathrm{A},\sigma_\mathrm{x}^\mathrm{Q},\sigma_\mathrm{y}^\mathrm{Q},\sigma_\mathrm{z}^\mathrm{Q}$	$\sigma_\mathrm{x}\sigma_\mathrm{x},\sigma_\mathrm{x}\sigma_\mathrm{y},\sigma_\mathrm{y}\sigma_\mathrm{x},\sigma_\mathrm{y}\sigma_\mathrm{y},\sigma_\mathrm{z}\sigma_\mathrm{x},\sigma_\mathrm{z}\sigma_\mathrm{y}$	$\sigma_\mathrm{x}\sigma_\mathrm{x},\sigma_\mathrm{y}\sigma_\mathrm{y}$
$\sigma_\mathrm{x}\sigma_\mathrm{x}$	$\sigma_\mathrm{y}^\mathrm{Q}$	$\sigma_\mathrm{z}^\mathrm{A},\sigma_\mathrm{x}^\mathrm{Q},\sigma_\mathrm{y}^\mathrm{Q},\sigma_\mathrm{z}^\mathrm{Q}$	$\sigma_\mathrm{x}\sigma_\mathrm{x},\sigma_\mathrm{x}\sigma_\mathrm{y},\sigma_\mathrm{y}\sigma_\mathrm{x},\sigma_\mathrm{y}\sigma_\mathrm{y},\sigma_\mathrm{z}\sigma_\mathrm{x},\sigma_\mathrm{z}\sigma_\mathrm{y}$	$\sigma_\mathrm{x}\sigma_\mathrm{x},\sigma_\mathrm{y}\sigma_\mathrm{y}$
$\sigma_\mathrm{x}\sigma_\mathrm{x}$	$\sigma_\mathrm{z}^\mathrm{Q}$	$\sigma_\mathrm{z}^\mathrm{A},\sigma_\mathrm{z}^\mathrm{Q}$	$\sigma_\mathrm{x}\sigma_\mathrm{x},\sigma_\mathrm{x}\sigma_\mathrm{y},\sigma_\mathrm{y}\sigma_\mathrm{x},\sigma_\mathrm{y}\sigma_\mathrm{y}$	$\sigma_\mathrm{x}\sigma_\mathrm{x},\sigma_\mathrm{y}\sigma_\mathrm{y}$
$\sigma_\mathrm{x}\sigma_\mathrm{y}$	$\sigma_\mathrm{x}^\mathrm{Q}$	$\sigma_\mathrm{z}^\mathrm{A},\sigma_\mathrm{x}^\mathrm{Q},\sigma_\mathrm{y}^\mathrm{Q},\sigma_\mathrm{z}^\mathrm{Q}$	$\sigma_\mathrm{x}\sigma_\mathrm{x},\sigma_\mathrm{x}\sigma_\mathrm{y},\sigma_\mathrm{y}\sigma_\mathrm{x},\sigma_\mathrm{y}\sigma_\mathrm{y},\sigma_\mathrm{z}\sigma_\mathrm{x},\sigma_\mathrm{z}\sigma_\mathrm{y}$	$\sigma_\mathrm{x}\sigma_\mathrm{x},\sigma_\mathrm{y}\sigma_\mathrm{y}$
$\sigma_\mathrm{x}\sigma_\mathrm{y}$	$\sigma_\mathrm{y}^\mathrm{Q}$	$\sigma_\mathrm{z}^\mathrm{A},\sigma_\mathrm{x}^\mathrm{Q},\sigma_\mathrm{y}^\mathrm{Q},\sigma_\mathrm{z}^\mathrm{Q}$	$\sigma_\mathrm{x}\sigma_\mathrm{x},\sigma_\mathrm{x}\sigma_\mathrm{y},\sigma_\mathrm{y}\sigma_\mathrm{x},\sigma_\mathrm{y}\sigma_\mathrm{y},\sigma_\mathrm{z}\sigma_\mathrm{x},\sigma_\mathrm{z}\sigma_\mathrm{y}$	$\sigma_\mathrm{x}\sigma_\mathrm{x},\sigma_\mathrm{y}\sigma_\mathrm{y}$
$\sigma_\mathrm{x}\sigma_\mathrm{y}$	$\sigma_\mathrm{z}^\mathrm{Q}$	$\sigma_\mathrm{z}^\mathrm{A},\sigma_\mathrm{z}^\mathrm{Q}$	$\sigma_\mathrm{x}\sigma_\mathrm{x},\sigma_\mathrm{x}\sigma_\mathrm{y},\sigma_\mathrm{y}\sigma_\mathrm{x},\sigma_\mathrm{y}\sigma_\mathrm{y}$	$\sigma_\mathrm{x}\sigma_\mathrm{x},\sigma_\mathrm{y}\sigma_\mathrm{y}$
$\sigma_\mathrm{x}\sigma_\mathrm{z}$	$\sigma_\mathrm{x}^\mathrm{Q}$	$\sigma_\mathrm{z}^\mathrm{A},\sigma_\mathrm{x}^\mathrm{Q},\sigma_\mathrm{y}^\mathrm{Q},\sigma_\mathrm{z}^\mathrm{Q}$	$\sigma_\mathrm{x}\sigma_\mathrm{z},\sigma_\mathrm{y}\sigma_\mathrm{z},\sigma_\mathrm{z}\sigma_\mathrm{z}$	$\sigma_\mathrm{z}\sigma_\mathrm{z}$
$\sigma_\mathrm{x}\sigma_\mathrm{z}$	$\sigma_\mathrm{y}^\mathrm{Q}$	$\sigma_\mathrm{z}^\mathrm{A},\sigma_\mathrm{x}^\mathrm{Q},\sigma_\mathrm{y}^\mathrm{Q},\sigma_\mathrm{z}^\mathrm{Q}$	$\sigma_\mathrm{x}\sigma_\mathrm{z},\sigma_\mathrm{y}\sigma_\mathrm{z},\sigma_\mathrm{z}\sigma_\mathrm{z}$	$\sigma_\mathrm{z}\sigma_\mathrm{z}$
$\sigma_\mathrm{x}\sigma_\mathrm{z}$	$\sigma_\mathrm{z}^\mathrm{Q}$	$\sigma_\mathrm{z}^\mathrm{A},\sigma_\mathrm{z}^\mathrm{Q}$	$\sigma_\mathrm{x}\sigma_\mathrm{z},\sigma_\mathrm{y}\sigma_\mathrm{z}$	$\sigma_\mathrm{x}\sigma_\mathrm{z}$
$\sigma_\mathrm{y}\sigma_\mathrm{x}$	$\sigma_\mathrm{x}^\mathrm{Q}$	$\sigma_\mathrm{z}^\mathrm{A},\sigma_\mathrm{x}^\mathrm{Q},\sigma_\mathrm{y}^\mathrm{Q},\sigma_\mathrm{z}^\mathrm{Q}$	$\sigma_\mathrm{x}\sigma_\mathrm{x},\sigma_\mathrm{x}\sigma_\mathrm{y},\sigma_\mathrm{y}\sigma_\mathrm{x},\sigma_\mathrm{y}\sigma_\mathrm{y},\sigma_\mathrm{z}\sigma_\mathrm{x},\sigma_\mathrm{z}\sigma_\mathrm{y}$	$\sigma_\mathrm{x}\sigma_\mathrm{x},\sigma_\mathrm{y}\sigma_\mathrm{y}$
$\sigma_\mathrm{y}\sigma_\mathrm{x}$	$\sigma_\mathrm{y}^\mathrm{Q}$	$\sigma_\mathrm{z}^\mathrm{A},\sigma_\mathrm{x}^\mathrm{Q},\sigma_\mathrm{y}^\mathrm{Q},\sigma_\mathrm{z}^\mathrm{Q}$	$\sigma_\mathrm{x}\sigma_\mathrm{x},\sigma_\mathrm{x}\sigma_\mathrm{y},\sigma_\mathrm{y}\sigma_\mathrm{x},\sigma_\mathrm{y}\sigma_\mathrm{y},\sigma_\mathrm{z}\sigma_\mathrm{x},\sigma_\mathrm{z}\sigma_\mathrm{y}$	$\sigma_\mathrm{x}\sigma_\mathrm{x},\sigma_\mathrm{y}\sigma_\mathrm{y}$
$\sigma_\mathrm{y}\sigma_\mathrm{x}$	$\sigma_\mathrm{z}^\mathrm{Q}$	$\sigma_\mathrm{z}^\mathrm{A},\sigma_\mathrm{z}^\mathrm{Q}$	$\sigma_\mathrm{x}\sigma_\mathrm{x},\sigma_\mathrm{x}\sigma_\mathrm{y},\sigma_\mathrm{y}\sigma_\mathrm{x},\sigma_\mathrm{y}\sigma_\mathrm{y}$	$\sigma_\mathrm{x}\sigma_\mathrm{x},\sigma_\mathrm{y}\sigma_\mathrm{y}$
$\sigma_\mathrm{y}\sigma_\mathrm{y}$	$\sigma_\mathrm{x}^\mathrm{Q}$	$\sigma_\mathrm{z}^\mathrm{A},\sigma_\mathrm{x}^\mathrm{Q},\sigma_\mathrm{y}^\mathrm{Q},\sigma_\mathrm{z}^\mathrm{Q}$	$\sigma_\mathrm{x}\sigma_\mathrm{x},\sigma_\mathrm{x}\sigma_\mathrm{y},\sigma_\mathrm{y}\sigma_\mathrm{x},\sigma_\mathrm{y}\sigma_\mathrm{y},\sigma_\mathrm{z}\sigma_\mathrm{x},\sigma_\mathrm{z}\sigma_\mathrm{y}$	$\sigma_\mathrm{x}\sigma_\mathrm{x},\sigma_\mathrm{y}\sigma_\mathrm{y}$
$\sigma_\mathrm{y}\sigma_\mathrm{y}$	$\sigma_\mathrm{y}^\mathrm{Q}$	$\sigma_\mathrm{z}^\mathrm{A},\sigma_\mathrm{x}^\mathrm{Q},\sigma_\mathrm{y}^\mathrm{Q},\sigma_\mathrm{z}^\mathrm{Q}$	$\sigma_\mathrm{x}\sigma_\mathrm{x},\sigma_\mathrm{x}\sigma_\mathrm{y},\sigma_\mathrm{y}\sigma_\mathrm{x},\sigma_\mathrm{y}\sigma_\mathrm{y},\sigma_\mathrm{z}\sigma_\mathrm{x},\sigma_\mathrm{z}\sigma_\mathrm{y}$	$\sigma_\mathrm{x}\sigma_\mathrm{x},\sigma_\mathrm{y}\sigma_\mathrm{y}$
$\sigma_\mathrm{y}\sigma_\mathrm{y}$	$\sigma_\mathrm{z}^\mathrm{Q}$	$\sigma_\mathrm{z}^\mathrm{A},\sigma_\mathrm{z}^\mathrm{Q}$	$\sigma_\mathrm{x}\sigma_\mathrm{x},\sigma_\mathrm{x}\sigma_\mathrm{y},\sigma_\mathrm{y}\sigma_\mathrm{x},\sigma_\mathrm{y}\sigma_\mathrm{y}$	$\sigma_\mathrm{x}\sigma_\mathrm{x},\sigma_\mathrm{y}\sigma_\mathrm{y}$
$\sigma_\mathrm{y}\sigma_\mathrm{z}$	$\sigma_\mathrm{x}^\mathrm{Q}$	$\sigma_\mathrm{z}^\mathrm{A},\sigma_\mathrm{x}^\mathrm{Q},\sigma_\mathrm{y}^\mathrm{Q},\sigma_\mathrm{z}^\mathrm{Q}$	$\sigma_\mathrm{x}\sigma_\mathrm{z},\sigma_\mathrm{y}\sigma_\mathrm{z},\sigma_\mathrm{z}\sigma_\mathrm{z}$	$\sigma_\mathrm{z}\sigma_\mathrm{z}$
$\sigma_\mathrm{y}\sigma_\mathrm{z}$	$\sigma_\mathrm{y}^\mathrm{Q}$	$\sigma_\mathrm{z}^\mathrm{A},\sigma_\mathrm{x}^\mathrm{Q},\sigma_\mathrm{y}^\mathrm{Q},\sigma_\mathrm{z}^\mathrm{Q}$	$\sigma_\mathrm{x}\sigma_\mathrm{z},\sigma_\mathrm{y}\sigma_\mathrm{z},\sigma_\mathrm{z}\sigma_\mathrm{z}$	$\sigma_\mathrm{z}\sigma_\mathrm{z}$
$\sigma_\mathrm{y}\sigma_\mathrm{z}$	$\sigma_\mathrm{z}^\mathrm{Q}$	$\sigma_\mathrm{z}^\mathrm{A},\sigma_\mathrm{z}^\mathrm{Q}$	$\sigma_\mathrm{x}\sigma_\mathrm{z},\sigma_\mathrm{y}\sigma_\mathrm{z}$	$\sigma_\mathrm{x}\sigma_\mathrm{z}$
$\sigma_\mathrm{z}\sigma_\mathrm{x}$	$\sigma_\mathrm{x}^\mathrm{Q}$	$\sigma_\mathrm{z}^\mathrm{A},\sigma_\mathrm{x}^\mathrm{Q},\sigma_\mathrm{y}^\mathrm{Q},\sigma_\mathrm{z}^\mathrm{Q}$	$\sigma_\mathrm{x}\sigma_\mathrm{x},\sigma_\mathrm{x}\sigma_\mathrm{y},\sigma_\mathrm{y}\sigma_\mathrm{x},\sigma_\mathrm{y}\sigma_\mathrm{y},\sigma_\mathrm{z}\sigma_\mathrm{x},\sigma_\mathrm{z}\sigma_\mathrm{y}$	$\sigma_\mathrm{x}\sigma_\mathrm{x},\sigma_\mathrm{y}\sigma_\mathrm{y}$
$\sigma_\mathrm{z}\sigma_\mathrm{x}$	$\sigma_\mathrm{y}^\mathrm{Q}$	$\sigma_\mathrm{z}^\mathrm{A},\sigma_\mathrm{x}^\mathrm{Q},\sigma_\mathrm{y}^\mathrm{Q},\sigma_\mathrm{z}^\mathrm{Q}$	$\sigma_\mathrm{x}\sigma_\mathrm{x},\sigma_\mathrm{x}\sigma_\mathrm{y},\sigma_\mathrm{y}\sigma_\mathrm{x},\sigma_\mathrm{y}\sigma_\mathrm{y},\sigma_\mathrm{z}\sigma_\mathrm{x},\sigma_\mathrm{z}\sigma_\mathrm{y}$	$\sigma_\mathrm{x}\sigma_\mathrm{x},\sigma_\mathrm{y}\sigma_\mathrm{y}$
$\sigma_\mathrm{z}\sigma_\mathrm{x}$	$\sigma_\mathrm{z}^\mathrm{Q}$	$\sigma_\mathrm{z}^\mathrm{A},\sigma_\mathrm{z}^\mathrm{Q}$	$\sigma_\mathrm{z}\sigma_\mathrm{x},\sigma_\mathrm{z}\sigma_\mathrm{y}$	$\sigma_\mathrm{z}\sigma_\mathrm{x}$
$\sigma_\mathrm{z}\sigma_\mathrm{y}$	$\sigma_\mathrm{x}^\mathrm{Q}$	$\sigma_\mathrm{z}^\mathrm{A},\sigma_\mathrm{x}^\mathrm{Q},\sigma_\mathrm{y}^\mathrm{Q},\sigma_\mathrm{z}^\mathrm{Q}$	$\sigma_\mathrm{x}\sigma_\mathrm{x},\sigma_\mathrm{x}\sigma_\mathrm{y},\sigma_\mathrm{y}\sigma_\mathrm{x},\sigma_\mathrm{y}\sigma_\mathrm{y},\sigma_\mathrm{z}\sigma_\mathrm{x},\sigma_\mathrm{z}\sigma_\mathrm{y}$	$\sigma_\mathrm{x}\sigma_\mathrm{x},\sigma_\mathrm{y}\sigma_\mathrm{y}$
$\sigma_\mathrm{z}\sigma_\mathrm{y}$	$\sigma_\mathrm{y}^\mathrm{Q}$	$\sigma_\mathrm{z}^\mathrm{A},\sigma_\mathrm{x}^\mathrm{Q},\sigma_\mathrm{y}^\mathrm{Q},\sigma_\mathrm{z}^\mathrm{Q}$	$\sigma_\mathrm{x}\sigma_\mathrm{x},\sigma_\mathrm{x}\sigma_\mathrm{y},\sigma_\mathrm{y}\sigma_\mathrm{x},\sigma_\mathrm{y}\sigma_\mathrm{y},\sigma_\mathrm{z}\sigma_\mathrm{x},\sigma_\mathrm{z}\sigma_\mathrm{y}$	$\sigma_\mathrm{x}\sigma_\mathrm{x},\sigma_\mathrm{y}\sigma_\mathrm{y}$
$\sigma_\mathrm{z}\sigma_\mathrm{y}$	$\sigma_\mathrm{z}^\mathrm{Q}$	$\sigma_\mathrm{z}^\mathrm{A},\sigma_\mathrm{z}^\mathrm{Q}$	$\sigma_\mathrm{z}\sigma_\mathrm{x},\sigma_\mathrm{z}\sigma_\mathrm{y}$	$\sigma_\mathrm{z}\sigma_\mathrm{x}$
$\sigma_\mathrm{z}\sigma_\mathrm{z}$	$\sigma_\mathrm{x}^\mathrm{Q}$	$\sigma_\mathrm{z}^\mathrm{A},\sigma_\mathrm{x}^\mathrm{Q},\sigma_\mathrm{y}^\mathrm{Q},\sigma_\mathrm{z}^\mathrm{Q}$	$\sigma_\mathrm{x}\sigma_\mathrm{z},\sigma_\mathrm{y}\sigma_\mathrm{z},\sigma_\mathrm{z}\sigma_\mathrm{z}$	$\sigma_\mathrm{z}\sigma_\mathrm{z}$
$\sigma_\mathrm{z}\sigma_\mathrm{z}$	$\sigma_\mathrm{y}^\mathrm{Q}$	$\sigma_\mathrm{z}^\mathrm{A},\sigma_\mathrm{x}^\mathrm{Q},\sigma_\mathrm{y}^\mathrm{Q},\sigma_\mathrm{z}^\mathrm{Q}$	$\sigma_\mathrm{x}\sigma_\mathrm{z},\sigma_\mathrm{y}\sigma_\mathrm{z},\sigma_\mathrm{z}\sigma_\mathrm{z}$	$\sigma_\mathrm{z}\sigma_\mathrm{z}$
$\sigma_\mathrm{z}\sigma_\mathrm{z}$	$\sigma_\mathrm{z}^\mathrm{Q}$	$\sigma_\mathrm{z}^\mathrm{A},\sigma_\mathrm{z}^\mathrm{Q}$	$\sigma_\mathrm{z}\sigma_\mathrm{z}$	$\sigma_\mathrm{z}\sigma_\mathrm{z}$

Table 5.2: Dynamical Lie algebras $\mathfrak{g}$, their respective Cartan decompositions $\mathfrak{g}=\mathfrak{k}\oplus\mathfrak{p}$ and a possible choice for the Cartan subalgebra $\mathfrak{a}\subset\mathfrak{p}$ for all possible combinations of Hamiltonian (5.63) with $\mathsf{O}_\mathrm{ctrl},\mathsf{O}_\mathrm{Q},\mathsf{O}_\mathrm{A}\in\{\sigma_\mathrm{x},\sigma_\mathrm{y},\sigma_\mathrm{z}\}$. The interaction part and the qubit control are given by $\mathsf{H}_\mathrm{I}=J(\mathsf{O}_\mathrm{Q}\otimes\mathsf{O}_\mathrm{A})$ and $\mathsf{H}_\mathrm{ctrl}(t)=\mathcal{E}(t)\mathsf{O}_\mathrm{ctrl}$, respectively. Note that for brevity, we use the short notation $\sigma_\mathrm{x}^\mathrm{Q}\otimes\mathbb{1}_\mathrm{A}\to\sigma_\mathrm{x}^\mathrm{Q}$ and $\sigma_\mathrm{y}^\mathrm{Q}\otimes\sigma_\mathrm{z}^\mathrm{A}\to\sigma_\mathrm{y}\sigma_\mathrm{z}$.

rationale behind this is that the dynamical Lie algebra $\mathfrak{g}$ in general — and the Cartan subalgebra $\mathfrak{a}$ in particular — already determines on the level of the algebra whether we can expect a qubit-ancilla dynamics that gives rise to $N_{\mathrm{nl}} \geq 2$ for the specific combination $\mathsf{O}_{\mathrm{ctrl}}, \mathsf{O}_{\mathrm{Q}}, \mathsf{O}_{\mathrm{A}} \in \{\sigma_{\mathrm{x}}, \sigma_{\mathrm{y}}, \sigma_{\mathrm{z}}\}$. For Hamiltonian (5.63) we find the equivalence $N_{\mathrm{nl}} = \dim\{\mathfrak{a}\}$. Since $\mathfrak{a}$ can be entirely determined from the Hamiltonian and no further knowledge of the actual dynamics is required, this provides an easy recipe to determine N_{nl}. It thus allows to determine those combinations of $\mathsf{O}_{\mathrm{ctrl}}, \mathsf{O}_{\mathrm{Q}}, \mathsf{O}_{\mathrm{A}} \in \{\sigma_{\mathrm{x}}, \sigma_{\mathrm{y}}, \sigma_{\mathrm{z}}\}$, which allow for $N_{\mathrm{nl}} \geq 2$ and are therefore fundamentally capable for qubit purification. Table 5.2 summarizes the dynamical Lie algebras $\mathfrak{g}$ for all combinations $\mathsf{O}_{\mathrm{ctrl}}, \mathsf{O}_{\mathrm{Q}}, \mathsf{O}_{\mathrm{A}} \in \{\sigma_{\mathrm{x}}, \sigma_{\mathrm{y}}, \sigma_{\mathrm{z}}\}$ and presents possible choices for $\mathfrak{a}$. Out of the $3 \times 3 \times 3 = 27$ possible combinations of $\mathsf{O}_{\mathrm{ctrl}}, \mathsf{O}_{\mathrm{Q}}, \mathsf{O}_{\mathrm{A}} \in \{\sigma_{\mathrm{x}}, \sigma_{\mathrm{y}}, \sigma_{\mathrm{z}}\}$, we find that only 16 have a Cartan subalgebra $\mathfrak{a}$ of dimension 2, while the remaining 11 combinations have $\dim\{\mathfrak{a}\} = 1$ and are therefore incapable of resetting the qubit. However, it should be noted that the equivalence of $N_{\mathrm{nl}} = \dim\{\mathfrak{a}\}$ does not hold in general but is a rather convenient coincidence for the current scenario.

While the analysis of the dynamical Lie algebra $\mathfrak{g}$ readily reveals those combinations of $\mathsf{O}_{\mathrm{ctrl}}, \mathsf{O}_{\mathrm{Q}}, \mathsf{O}_{\mathrm{A}} \in \{\sigma_{\mathrm{x}}, \sigma_{\mathrm{y}}, \sigma_{\mathrm{z}}\}$ that are fundamentally capable of qubit reset in the first place, it does not provide any information on how the control field $\mathcal{E}(t)$ needs to be chosen in practice in order to reset the qubit. By now, we merely know that it is generally possible by a suitable choice of $\mathcal{E}(t)$. Thus, in the remainder of this subsection we will derive the time-optimal solution for all 16 combinations that allow for qubit reset. We will discuss the solution explicitly and exemplarily for $\mathsf{O}_{\mathrm{Q}} = \mathsf{O}_{\mathrm{A}} = \sigma_{\mathrm{x}}$ and two choices of the control Hamiltonian, (i) $\mathsf{O}_{\mathrm{ctrl}} = \sigma_{\mathrm{x}}$ and (ii) $\mathsf{O}_{\mathrm{ctrl}} = \sigma_{\mathrm{z}}$. The reason behind this is that the solutions for other combinations follow the same scheme and yield identical results. We therefore restrict our discussion to these two cases. We assume a factorized initial state $\rho(t_0) = \rho_{\mathrm{Q}}(t_0) \otimes \rho_{\mathrm{A}}(t_0)$ with the ancilla in thermal equilibrium, i.e., without ancilla coherences,

$$\rho(t_0) = \rho_{\mathrm{Q}}(t_0) \otimes \rho_{\mathrm{A}}(t_0) = \begin{pmatrix} p_{\mathrm{Q}}^{\mathrm{e}} & \gamma_{\mathrm{Q}} \\ \gamma_{\mathrm{Q}}^{\star} & p_{\mathrm{Q}}^{\mathrm{g}} \end{pmatrix} \otimes \begin{pmatrix} p_{\mathrm{A}}^{\mathrm{e}} & 0 \\ 0 & p_{\mathrm{A}}^{\mathrm{g}} \end{pmatrix}. \tag{5.74}$$

$p_{\mathrm{Q}}^{\mathrm{g}}$ ($p_{\mathrm{Q}}^{\mathrm{e}}$) and $p_{\mathrm{A}}^{\mathrm{g}}$ ($p_{\mathrm{A}}^{\mathrm{e}}$) are the ground (excited) state population of qubit and ancilla, respectively, and γ_{Q} is the qubit's coherences.

It should be mentioned that case (ii) is very similar — albeit not identical — to the model and scenario discussed in Sec. 5.2. Here, we seek to maximize the qubit's purity instead of its ground state population $p_{\mathrm{Q}}^{\mathrm{g}}(T)$ at final time T, cf. Eq. (5.66). From a physical perspective, this means that we do not optimize towards a specific target state but rather towards any pure state that can be reached. The optimization

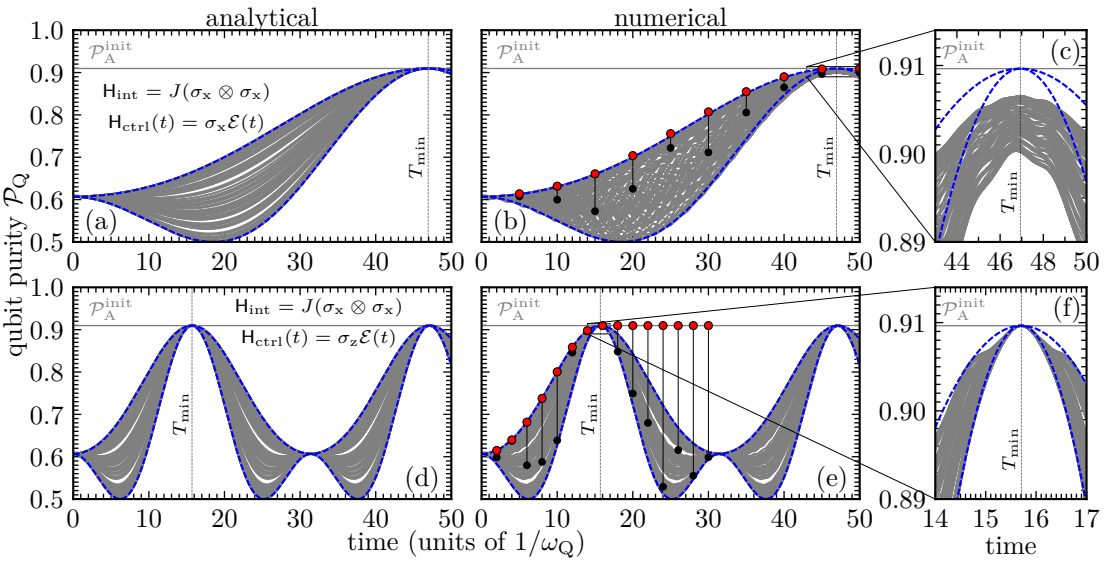

Figure 5.14: Qubit purity $\mathcal{P}_Q(t)$ as function of time. The gray area corresponds to the superimposed evolutions of different initial states $\rho(t_0) = \rho_Q(t_0) \otimes \rho_A(t_0)$ with $\rho_A(t_0)$ the thermal equilibrium state and $\rho_Q(t_0)$ sampled randomly under the condition of identical purity. The red (black) dots indicate the values for $\mathcal{P}_Q(\tau)$ obtained with optimized (constant resonant) $\mathcal{E}(t)$ evaluate at final time τ. Panels (a), (d) show $\mathcal{P}_Q(t)$ determined analytically by Eq. (5.84), (b) and (e) show the corresponding numerical results without any approximation, and (c) and (f) present a zoomed-in view around T_{min}. The dashed blue lines indicate the upper and lower bound of $\mathcal{P}_Q(t)$ as predicted by Eq. (5.84). The parameters are $\omega_Q = 1$, $\omega_A = 3$, $J = 0.1$, and inverse temperature $\beta = 1$.

target is therefore less restrictive and should in principle allow for more solutions. We can nevertheless use the physical insights from Sec. 5.2 as a starting point to solve this more general control problem. For the case (ii), we know from Sec. 5.2 that a time-optimal qubit reset is achieved by a constant field $\mathcal{E}(t) = \mathcal{E}$ that puts qubit and ancilla into resonance, i.e., $\mathcal{E}$ is chosen such that $\lambda_1 - \lambda_0 = \omega_A$ where $\lambda_0 < \lambda_1$ are the eigenvalues of the driven qubit Hamiltonian $\mathsf{H}_Q + \mathcal{E}\mathsf{O}_{ctrl}$. Therefore, a constant resonant field seems to be a suitable guess field for numerical optimization of the qubit purity, i.e., minimization of Eq. (5.66). To this end, Fig. 5.14 shows the time-evolution of the qubit purity $\mathcal{P}_Q(t)$ under a resonant field for one hundred randomly chosen initial qubit states $\rho_Q(t_0)$. Figure 5.14 compares an analytical approximation, panels (a) and (d), which we will discuss in a bit, and a full numerical solution, panels (b) and (e), for cases (i) and (ii). Interestingly, for all initial states $\rho_Q(t_0)$, maximal purity $\mathcal{P}_Q^{max} = \mathcal{P}_A^{init}$ occurs at roughly the same time T_{min} for the same constant resonant field, cf. Fig. 5.14(c,f). $\mathcal{P}_A^{init}$ denotes the ancilla's initial purity. Surprisingly, T_{min} differs for cases (i) and (ii). While in case (ii) it coincides with the minimal $T_{min} = \pi/(2J)$, which has already been

identified in Sec. 5.2 as the quantum speed limit for factorizing initial states, in case (i) it is much longer. Thus, a quite natural question to ask is whether this prolongation of the reset time compared to case (ii) is a consequence of the resonant guess field that, potentially, constitutes a bad choice here. Again, this question can be naturally answered by optimal control. To this end, we use Krotov's method to optimize the field $\mathcal{E}(t)$, $t \in [0, \tau]$, such that it maximizes $\mathcal{P}_\mathrm{Q}(\tau)$, i.e., minimizes Eq. (5.66), for final times $\tau \neq T_\mathrm{min}$. For a few choices of τ, the red and black dots in Fig. 5.14(b,e) compare the qubit purity $\mathcal{P}_\mathrm{Q}(\tau)$ obtained with constant resonant and optimized fields, respectively. In general, the optimized fields improve $\mathcal{P}_\mathrm{Q}(t)$ compared to the constant resonant field. However, for $\tau < T_\mathrm{min}$, the optimization results reveal that an upper bound for $\mathcal{P}_\mathrm{Q}(\tau)$ exists. A closer inspection reveals that this upper bound can be attained exactly when employing a constant resonant field and when $\rho_\mathrm{Q}(t_0)$ is initially coherence-free, i.e., $\gamma_\mathrm{Q} = 0$, and fulfills $p_\mathrm{Q}^\mathrm{g} > p_\mathrm{Q}^\mathrm{e}$. For all other initial qubit states $\rho_\mathrm{Q}(t_0)$, i.e., in the presence of initial qubit coherences or when $p_\mathrm{Q}^\mathrm{g} < p_\mathrm{Q}^\mathrm{e}$, the control field $\mathcal{E}(t)$ needs to rotate the coherences into population or invert the population distribution. Only after that, the control fields again establish resonance, which causes the maximal flow of entropy from the qubit to the ancilla within the given time $\tau < T_\mathrm{min}$. This explains why, in case (i), the optimized fields $\mathcal{E}(t)$, which couple via $\mathsf{O}_\mathrm{ctrl} = \sigma_\mathrm{x}^\mathrm{Q}$, all exhibit a strong off-resonant peak in the beginning, followed by the resonant protocol. While the idea is in general very similar to that discussion for Fig. 5.12, here the off-resonant peak only controls the coherences γ_Q of the qubit and not the correlations between qubit and ancilla. To this end, for the case (ii) with $\mathsf{O}_\mathrm{ctrl} = \sigma_\mathrm{z}$, a second control field $\mathcal{E}'(t)$ that couples via $\mathsf{O}'_\mathrm{ctrl} = \sigma_\mathrm{x}$ has been added and utilized during the optimization. This has been necessary, since the original control field $\mathcal{E}(t)$ couples only via $\mathsf{O}_\mathrm{ctrl} = \sigma_\mathrm{z}$ and is therefore not sufficient to control γ_Q. However, in both cases (i) and (ii), only for times $\tau \geq T_\mathrm{min}$ it is possible to reach $\mathcal{P}_\mathrm{Q}^\mathrm{max}$, which corresponds to a swap of purities between qubit and ancilla. Moreover, we observe in Fig. 5.14 that the constant resonant field, that has been used as a guess field for the optimization, readily gives rise to this swap of purities in minimal time T_min. When allowing for times $\tau > T_\mathrm{min}$, a purity swap between qubit and ancilla remains the optimal purification result with the corresponding optimal fields being more complex than the constant resonant solution for $\tau = T_\mathrm{min}$. This is in agreement with the findings of Sec. 5.2 but extends these results to new types of couplings between qubit and ancilla and new types of local control on the qubit.

Based on these numerical results, we conjecture that time-optimal purification always requires us to choose a constant resonant field, i.e., $\mathcal{E}(t) = \mathcal{E}$ such that $\lambda_1 - \lambda_0 = \omega_\mathrm{A}$, independent of $\mathsf{O}_\mathrm{ctrl}, \mathsf{O}_\mathrm{Q}$ and O_A. Hence, in order to get some more insight about what

causes the differences in $T_{\min}$ between cases (i) and (ii), we will analytically solve the dynamics of the joint qubit-ancilla system under a resonant field in the following. It will provide us with an analytical formula for the qubit purity $\mathcal{P}_{\mathrm{Q}}(t)$ and an analytical expression for $T_{\min}$. This is desirable, since $T_{\min}$ depends strongly on the combination $\mathsf{O}_{\mathrm{ctrl}}, \mathsf{O}_{\mathrm{Q}}, \mathsf{O}_{\mathrm{A}} \in \{\sigma_{\mathrm{x}}, \sigma_{\mathrm{y}}, \sigma_{\mathrm{z}}\}$ — not only for cases (i) and (ii) but also for all remaining combinations that have not been explicitly discussed for far. It will therefore allow us to understand the difference in $T_{\min}$ observed for case (i) and (ii) and, moreover, it will also enable us to predict $T_{\min}$ for every combination. To this end, we exemplarily demonstrate the procedure to obtain $T_{\min}$ analytically for case (i). However, it should be again emphasized that this procedure works similarly for any other combination of $\mathsf{O}_{\mathrm{ctrl}}, \mathsf{O}_{\mathrm{Q}}, \mathsf{O}_{\mathrm{A}} \in \{\sigma_{\mathrm{x}}, \sigma_{\mathrm{y}}, \sigma_{\mathrm{z}}\}$.

In case (i), the resonant field is given by $\mathcal{E}(t) = \mathcal{E} = \sqrt{\omega_{\mathrm{A}}^2 - \omega_{\mathrm{Q}}^2}/2$ and we will fix it at this value for the remainder of the section. We start by applying a transformation $\mathsf{T} = \mathsf{T}_{\mathrm{Q}} \otimes \mathbb{1}_{\mathrm{A}}$, where T_{Q} is chosen such that it diagonalizes the driven qubit Hamiltonian $\mathsf{H}_{\mathrm{Q}} + \mathcal{E}\mathsf{O}_{\mathrm{ctrl}}$. The transformed version H' of the joint qubit-ancilla Hamiltonian H becomes

$$\mathsf{H}' = \mathsf{T}^\dagger \mathsf{H} \mathsf{T} = \begin{pmatrix} \omega_{\mathrm{A}} & B & 0 & A \\ B^* & 0 & A & 0 \\ 0 & A & 0 & -B \\ A & 0 & -B^* & -\omega_{\mathrm{A}} \end{pmatrix} \tag{5.75}$$

with $A = J\omega_{\mathrm{Q}}/\omega_{\mathrm{A}}$ and $B = J\sqrt{\omega_{\mathrm{A}}^2 - \omega_{\mathrm{Q}}^2}/\omega_{\mathrm{A}}$. Note that the resonance condition implies $J^2 = |A|^2 + |B|^2$. The time-evolution operator U_{t,t_0} can be calculated analytically for Hamiltonian (5.75) and reads (dropping time-dependencies in the following)

$$\mathsf{U}_{t,t_0} = e^{-\mathrm{i}\mathsf{H}'(t-t_0)} = \begin{pmatrix} u_{11} & u_{12} & u_{13} & u_{14} \\ u_{12} & u_{22} & u_{23} & u_{13} \\ u_{13} & u_{23} & u_{22}^* & u_{12}^* \\ u_{14} & u_{13} & u_{12}^* & u_{11}^* \end{pmatrix} \tag{5.76}$$

with

$$\begin{aligned} u_{11} = \frac{1}{2}\Bigg[& \delta_+ \cos(\Phi_+) + \delta_- \cos(\Phi_-) - \mathrm{i}\frac{1}{\eta_+}\left(\delta_+\omega_{\mathrm{A}} + \frac{2|B|^2}{\Omega}\right)\sin(\Phi_+) \\ & - \mathrm{i}\frac{1}{\eta_-}\left(\delta_-\omega_{\mathrm{A}} - \frac{2|B|^2}{\Omega}\right)\sin(\Phi_-)\Bigg], \end{aligned} \tag{5.77a}$$

$$u_{12} = \frac{B}{\Omega}\big(\cos(\Phi_+) - \cos(\Phi_-)\big) - \mathrm{i}\frac{B}{2}\left(\frac{\delta_+}{\eta_+}\sin(\Phi_+) + \frac{\delta_-}{\eta_-}\sin(\Phi_-)\right), \tag{5.77b}$$

$$u_{13} = -\mathrm{i}\frac{AB}{\Omega}\left(\frac{1}{\eta_+}\sin(\Phi_+) - \frac{1}{\eta_-}\sin(\Phi_-)\right), \tag{5.77c}$$

$$u_{14} = -\mathrm{i}\frac{A}{2}\left(\frac{\delta_+}{\eta_+}\sin(\Phi_+) + \frac{\delta_-}{\eta_-}\sin(\Phi_-)\right), \tag{5.77d}$$

$$u_{22} = \frac{1}{2}\left[\delta_+\cos(\Phi_-) + \delta_-\cos(\Phi_+) - \mathrm{i}\frac{2|B|^2}{\eta_+\Omega}\sin(\Phi_+) + \mathrm{i}\frac{2|B|^2}{\eta_-\Omega}\sin(\Phi_-)\right], \tag{5.77e}$$

$$u_{23} = -\mathrm{i}\frac{A}{2}\left(\frac{\delta_+}{\eta_-}\sin(\Phi_-) + \frac{\delta_-}{\eta_+}\sin(\Phi_+)\right), \tag{5.77f}$$

where $\delta_\pm = 1 \pm \omega_\mathrm{A}/\Omega$, $\Omega^2 = \omega_\mathrm{A}^2 + 4|B|^2$,

$$\eta_\pm^2 = J^2 + \frac{\omega_\mathrm{A}}{2}\left(\omega_\mathrm{A} \pm \Omega\right) \tag{5.78}$$

and $\Phi_\pm = \Phi_\pm(t) = \eta_\pm t$ is the only time-dependent quantity in Eq. (5.77).

While Eqs. (5.76) and (5.77) are exact, we can find substantially simpler expressions by employing some approximations. This is necessary in order to find sufficiently simple analytical expressions for $\mathcal{P}_\mathrm{Q}(t)$ and T_min. To this end, we first notice that each element of the time-evolution operator U_{t,t_0} is given by a sum of trigonometric functions. We then compare their amplitudes in order to identify the dominant terms. As an illustration, we will demonstrate the approximations explicitly for the amplitude of the final term of u_{11} in Eq. (5.77a), even though the procedure is equivalent for all other contributions. Using the relation $J^2 = |A|^2 + |B|^2$, we express all variables in terms of A, B, and ω_A. For the final term in Eq. (5.77a), this results in

$$\delta_- = 1 - \frac{\omega_\mathrm{A}}{2\sqrt{\omega_\mathrm{A}^2 + |B|^2}}, \qquad \eta_-^2 = |A|^2 + |B|^2 + \frac{\omega_\mathrm{A}^2}{2} - \frac{\omega_\mathrm{A}}{2}\sqrt{\omega_\mathrm{A}^2 + 4|B|^2}. \tag{5.79}$$

Since $J \ll \omega_\mathrm{A}$ and $|B| \leq J$, this suggests an expansion of all variables in B,

$$\delta_- \approx \frac{2|B|^2}{\omega_\mathrm{A}^2} + \mathcal{O}\left(|B|^4\right), \tag{5.80a}$$

$$\eta_- \approx |A| + \mathcal{O}\left(|B|^4\right), \tag{5.80b}$$

$$\Omega \approx \omega_\mathrm{A} + \frac{2|B|^2}{\omega_\mathrm{A}^2} + \mathcal{O}\left(|B|^4\right). \tag{5.80c}$$

With these approximated variables, we find

$$\frac{\mathrm{i}}{\eta_-}\left(\delta_-\omega_\mathrm{A} - \frac{2|B|^2}{\Omega}\right) \sim \mathcal{O}\left(|B|^4\right), \tag{5.81}$$

and can conclude that we can neglect the final term in Eq. (5.77a). Carrying out similar approximations for the other terms in Eq. (5.77) leads to

$$u_{11} \approx \cos(\Phi_+) - \mathrm{i}\sin(\Phi_+), \tag{5.82a}$$
$$u_{12} \approx 0, \tag{5.82b}$$
$$u_{13} \approx 0, \tag{5.82c}$$
$$u_{14} \approx 0, \tag{5.82d}$$
$$u_{22} \approx \cos(\Phi_-), \tag{5.82e}$$
$$u_{23} \approx \mathrm{i}\sin(\Phi_-). \tag{5.82f}$$

The corresponding approximated time-evolution operator U_{t,t_0} allows us to obtain a simplified expression for the time-evolution of the qubit purity $\mathcal{P}_\mathrm{Q}(t)$. In order to derive it, we assume the initial state of qubit and ancilla to be of the form (5.74). In that case, the qubit purity is given by

$$\begin{aligned}\mathcal{P}_\mathrm{Q}(t) &= \mathrm{tr}\left\{\mathrm{tr}_\mathrm{A}^2\left\{\mathsf{U}_{t,t_0}\big(\rho_\mathrm{Q}(t_0)\otimes\rho_\mathrm{A}(t_0)\big)\mathsf{U}_{t,t_0}^\dagger\right\}\right\}\\ &= \left[p_\mathrm{Q}^\mathrm{e}p_\mathrm{A}^\mathrm{e}|u_{11}|^2 + p_\mathrm{Q}^\mathrm{e}p_\mathrm{A}^\mathrm{g}|u_{22}|^2 + p_\mathrm{Q}^\mathrm{g}p_\mathrm{A}^\mathrm{e}|u_{23}|^2\right]^2\\ &\quad + \left[p_\mathrm{Q}^\mathrm{g}p_\mathrm{A}^\mathrm{g}|u_{11}|^2 + p_\mathrm{Q}^\mathrm{g}p_\mathrm{A}^\mathrm{e}|u_{22}|^2 + p_\mathrm{Q}^\mathrm{e}p_\mathrm{A}^\mathrm{g}|u_{23}|^2\right]^2 + 2|\gamma_\mathrm{Q}|^2|u_{11}|^2|u_{22}|^2.\end{aligned} \tag{5.83}$$

Inserting the approximated expression from Eq. (5.82), the qubit purity becomes

$$\begin{aligned}\mathcal{P}_\mathrm{Q}(t) &\approx \left[p_\mathrm{Q}^\mathrm{g}p_\mathrm{A}^\mathrm{g} + p_\mathrm{Q}^\mathrm{g}p_\mathrm{A}^\mathrm{e}\cos^2(\eta t) + p_\mathrm{Q}^\mathrm{e}p_\mathrm{A}^\mathrm{g}\sin^2(\eta t)\right]^2\\ &\quad + \left[p_\mathrm{Q}^\mathrm{e}p_\mathrm{A}^\mathrm{e} + p_\mathrm{Q}^\mathrm{g}p_\mathrm{A}^\mathrm{e}\sin^2(\eta t) + p_\mathrm{Q}^\mathrm{e}p_\mathrm{A}^\mathrm{g}\cos^2(\eta t)\right]^2 + 2|\gamma_\mathrm{Q}|^2\cos^2(\eta t),\end{aligned} \tag{5.84}$$

where

$$\eta^2 = J^2 + \frac{\omega_\mathrm{A}}{2}\left(\omega_\mathrm{A} - \sqrt{\omega_\mathrm{A}^2 + 4|B|^2}\right), \qquad B = J\frac{\sqrt{\omega_\mathrm{A}^2 - \omega_\mathrm{Q}^2}}{\omega_\mathrm{A}}. \tag{5.85}$$

In order to determine the minimum time for purification T_min, we demand a local maximum in $\mathcal{P}_\mathrm{Q}(t)$. Mathematically, this implies that we ask for a time t, where the

maximum criteria $\dot{\mathcal{P}}_{\mathrm{Q}}(t) = 0$ and $\ddot{\mathcal{P}}_{\mathrm{Q}}(t) < 0$ are fulfilled. Plugging in the u_{ij}'s from Eq. (5.82), we find the solution

$$T_{\min} = \frac{\pi}{2\eta} \approx \frac{\pi}{2|A|}, \tag{5.86}$$

for which we analytically obtain $\mathcal{P}_{\mathrm{Q}}(T_{\min}) = \mathcal{P}_{\mathrm{Q}}^{\max} = \mathcal{P}_{\mathrm{A}}^{\mathrm{init}}$, i.e., $T_{\min}$ corresponds to the minimal time that yields a swap of purities between qubit and ancilla. Note that we have used the approximation $\eta \approx |A|$ from Eq. (5.80b) in the second step of Eq. (5.86). We will discuss this approximation later.

We now have an analytical expression for the qubit's purity $\mathcal{P}_{\mathrm{Q}}(t)$ as well as the minimal reset time $T_{\min}$, derived for case (i). However, before proceeding to discuss what actually determines $T_{\min}$ for different combinations $\mathsf{O}_{\mathrm{ctrl}}, \mathsf{O}_{\mathrm{Q}}, \mathsf{O}_{\mathrm{A}} \in \{\sigma_{\mathrm{x}}, \sigma_{\mathrm{y}}, \sigma_{\mathrm{z}}\}$, it should first be mentioned how the derivation of $\mathcal{P}_{\mathrm{Q}}(t)$ and $T_{\min}$ differs for other combinations. To this end, we need to recall that 16 out of the 27 possible combinations $\mathsf{O}_{\mathrm{ctrl}}, \mathsf{O}_{\mathrm{Q}}, \mathsf{O}_{\mathrm{A}} \in \{\sigma_{\mathrm{x}}, \sigma_{\mathrm{y}}, \sigma_{\mathrm{z}}\}$ give rise to $N_{\mathrm{nl}} = \dim\{\mathfrak{a}\} = 2$, cf. Table 5.2. Moreover, it is important to notice that the derivation for case (i), which has been presented so far, is valid for all Hamiltonians of the form (5.75) — independent on how the two parameters A and B look in practice but provided that the approximations in Eq. (5.82) hold. We therefore know that the presented derivation holds for all combinations $\mathsf{O}_{\mathrm{ctrl}}, \mathsf{O}_{\mathrm{Q}}, \mathsf{O}_{\mathrm{A}} \in \{\sigma_{\mathrm{x}}, \sigma_{\mathrm{y}}, \sigma_{\mathrm{z}}\}$ that, upon transforming from H to H' via T, cf. Eq. (5.75), give rise to the same form of H' and thus the same solution — irrespective of their difference in H. We will label this form as $\mathsf{H}' = \mathsf{H}'_1$ in the following. Next, it can be shown that all 16 combinations from Table 5.2, which allow for qubit reset in the first place, are described either by H'_1 or one of the following three forms

$$\mathsf{H}'_2 = \begin{pmatrix} \omega_{\mathrm{A}} & B & 0 & A^* \\ B^* & 0 & A & 0 \\ 0 & A^* & 0 & -B \\ A & 0 & -B^* & -\omega_{\mathrm{A}} \end{pmatrix}, \tag{5.87a}$$

$$\mathsf{H}'_3 = \begin{pmatrix} \omega_{\mathrm{A}} & B & 0 & A^* \\ B^* & 0 & A^* & 0 \\ 0 & A & 0 & -B \\ A & 0 & -B^* & -\omega_{\mathrm{A}} \end{pmatrix}, \tag{5.87b}$$

$\mathsf{O}_\mathrm{Q} \otimes \mathsf{O}_\mathrm{A}$	O_ctrl	form	A	B	T_min (model)	T_min (set 1)	T_min (set 2)	T_min (set 3)
$\sigma_\mathrm{x}\sigma_\mathrm{x}$	$\sigma_\mathrm{x}^\mathrm{Q}$	(1)	$J\frac{\omega_\mathrm{Q}}{\omega_\mathrm{A}}$	$2J\frac{\mathcal{E}}{\omega_\mathrm{A}}$	46.9	191 ns	81 ns	402 ns
$\sigma_\mathrm{x}\sigma_\mathrm{x}$	$\sigma_\mathrm{y}^\mathrm{Q}$	(3)	$-\mathrm{i}J$	0	15.7	152 ns	49 ns	395 ns
$\sigma_\mathrm{x}\sigma_\mathrm{x}$	$\sigma_\mathrm{z}^\mathrm{Q}$	(1)	J	0	15.7	152 ns	49 ns	395 ns
$\sigma_\mathrm{x}\sigma_\mathrm{y}$	$\sigma_\mathrm{x}^\mathrm{Q}$	(2)	$\mathrm{i}J\frac{\omega_\mathrm{Q}}{\omega_\mathrm{A}}$	$-2\mathrm{i}J\frac{\mathcal{E}}{\omega_\mathrm{A}}$	46.9	191 ns	81 ns	402 ns
$\sigma_\mathrm{x}\sigma_\mathrm{y}$	$\sigma_\mathrm{y}^\mathrm{Q}$	(4)	J	0	15.7	152 ns	49 ns	395 ns
$\sigma_\mathrm{x}\sigma_\mathrm{y}$	$\sigma_\mathrm{z}^\mathrm{Q}$	(2)	$\mathrm{i}J$	0	15.7	152 ns	49 ns	395 ns
$\sigma_\mathrm{x}\sigma_\mathrm{z}$	$\sigma_\mathrm{x}^\mathrm{Q}$	-	-	-	-	-	-	-
$\sigma_\mathrm{x}\sigma_\mathrm{z}$	$\sigma_\mathrm{y}^\mathrm{Q}$	-	-	-	-	-	-	-
$\sigma_\mathrm{x}\sigma_\mathrm{z}$	$\sigma_\mathrm{z}^\mathrm{Q}$	-	-	-	-	-	-	-
$\sigma_\mathrm{y}\sigma_\mathrm{x}$	$\sigma_\mathrm{x}^\mathrm{Q}$	(3)	$\mathrm{i}J$	0	15.7	152 ns	49 ns	395 ns
$\sigma_\mathrm{y}\sigma_\mathrm{x}$	$\sigma_\mathrm{y}^\mathrm{Q}$	(1)	$J\frac{\omega_\mathrm{Q}}{\omega_\mathrm{A}}$	$2J\frac{\mathcal{E}}{\omega_\mathrm{A}}$	46.9	191 ns	81 ns	402 ns
$\sigma_\mathrm{y}\sigma_\mathrm{x}$	$\sigma_\mathrm{z}^\mathrm{Q}$	(3)	$\mathrm{i}J$	0	15.7	152 ns	49 ns	395 ns
$\sigma_\mathrm{y}\sigma_\mathrm{y}$	$\sigma_\mathrm{x}^\mathrm{Q}$	(4)	$-J$	0	15.7	152 ns	49 ns	395 ns
$\sigma_\mathrm{y}\sigma_\mathrm{y}$	$\sigma_\mathrm{y}^\mathrm{Q}$	(2)	$\mathrm{i}J\frac{\omega_\mathrm{Q}}{\omega_\mathrm{A}}$	$-2\mathrm{i}J\frac{\mathcal{E}}{\omega_\mathrm{A}}$	46.9	191 ns	81 ns	402 ns
$\sigma_\mathrm{y}\sigma_\mathrm{y}$	$\sigma_\mathrm{z}^\mathrm{Q}$	(4)	$-J$	0	15.7	152 ns	49 ns	395 ns
$\sigma_\mathrm{y}\sigma_\mathrm{z}$	$\sigma_\mathrm{x}^\mathrm{Q}$	-	-	-	-	-	-	-
$\sigma_\mathrm{y}\sigma_\mathrm{z}$	$\sigma_\mathrm{y}^\mathrm{Q}$	-	-	-	-	-	-	-
$\sigma_\mathrm{y}\sigma_\mathrm{z}$	$\sigma_\mathrm{z}^\mathrm{Q}$	-	-	-	-	-	-	-
$\sigma_\mathrm{z}\sigma_\mathrm{x}$	$\sigma_\mathrm{x}^\mathrm{Q}$	(1)	$-2J\frac{\mathcal{E}}{\omega_\mathrm{A}}$	$J\frac{\omega_\mathrm{Q}}{\omega_\mathrm{A}}$	16.7	250 ns	62 ns	2055 ns
$\sigma_\mathrm{z}\sigma_\mathrm{x}$	$\sigma_\mathrm{y}^\mathrm{Q}$	(1)	$-2J\frac{\mathcal{E}}{\omega_\mathrm{A}}$	$J\frac{\omega_\mathrm{Q}}{\omega_\mathrm{A}}$	16.7	250 ns	62 ns	2055 ns
$\sigma_\mathrm{z}\sigma_\mathrm{x}$	$\sigma_\mathrm{z}^\mathrm{Q}$	-	-	-	-	-	-	-
$\sigma_\mathrm{z}\sigma_\mathrm{y}$	$\sigma_\mathrm{x}^\mathrm{Q}$	(2)	$-2\mathrm{i}J\frac{\mathcal{E}}{\omega_\mathrm{A}}$	$-\mathrm{i}J\frac{\omega_\mathrm{Q}}{\omega_\mathrm{A}}$	16.7	250 ns	62 ns	2055 ns
$\sigma_\mathrm{z}\sigma_\mathrm{y}$	$\sigma_\mathrm{y}^\mathrm{Q}$	(2)	$-2\mathrm{i}J\frac{\mathcal{E}}{\omega_\mathrm{A}}$	$-\mathrm{i}J\frac{\omega_\mathrm{Q}}{\omega_\mathrm{A}}$	16.7	250 ns	62 ns	2055 ns
$\sigma_\mathrm{z}\sigma_\mathrm{y}$	$\sigma_\mathrm{z}^\mathrm{Q}$	-	-	-	-	-	-	-
$\sigma_\mathrm{z}\sigma_\mathrm{z}$	$\sigma_\mathrm{x}^\mathrm{Q}$	-	-	-	-	-	-	-
$\sigma_\mathrm{z}\sigma_\mathrm{z}$	$\sigma_\mathrm{y}^\mathrm{Q}$	-	-	-	-	-	-	-
$\sigma_\mathrm{z}\sigma_\mathrm{z}$	$\sigma_\mathrm{z}^\mathrm{Q}$	-	-	-	-	-	-	-

Table 5.3: Summary of the parameters A and B for all interactions $\mathsf{H}_\mathrm{I} = J\,(\mathsf{O}_\mathrm{Q} \otimes \mathsf{O}_\mathrm{A})$ and local qubit controls $\mathsf{H}_\mathrm{ctrl}(t) = \mathcal{E}(t)\mathsf{O}_\mathrm{ctrl}$ with $\mathcal{E}(t) = \mathcal{E} = \sqrt{\omega_\mathrm{A}^2 - \omega_\mathrm{Q}^2}/2$ and $\mathsf{O}_\mathrm{ctrl}, \mathsf{O}_\mathrm{Q}, \mathsf{O}_\mathrm{A} \in \{\sigma_\mathrm{x}, \sigma_\mathrm{y}, \sigma_\mathrm{z}\}$. The third column indicates the form (i) of the Hamiltonian H_i', cf. Eq. (5.87). The last four columns provide the minimal time T_min, predicted by Eq. (5.86), for purification of the qubit, evaluated with the same parameters as in Fig. 5.14 (column labeled "model") and for the physical setting of two coupled superconducting qubits [247] with three sets of experimental parameters (set 1: $\omega_\mathrm{Q}/2\pi = 12.8\,\mathrm{GHz}$, $\omega_\mathrm{A}/2\pi = 16.1\,\mathrm{GHz}$, $J/2\pi = 65\,\mathrm{MHz}$; set 2: $\omega_\mathrm{Q}/2\pi = 9.8\,\mathrm{GHz}$, $\omega_\mathrm{A}/2\pi = 16.1\,\mathrm{GHz}$, $J/2\pi = 200\,\mathrm{MHz}$; set 3: $\omega_\mathrm{Q}/2\pi = 15.8\,\mathrm{GHz}$, $\omega_\mathrm{A}/2\pi = 16.1\,\mathrm{GHz}$, $J/2\pi = 25\,\mathrm{MHz}$ [248]). For brevity, we use the short notation $\sigma_\mathrm{x}^\mathrm{Q} \otimes \mathbb{1}_\mathrm{A} \to \sigma_\mathrm{x}^\mathrm{Q}$ and $\sigma_\mathrm{y}^\mathrm{Q} \otimes \sigma_\mathrm{z}^\mathrm{A} \to \sigma_\mathrm{y}\sigma_\mathrm{z}$.

$$\mathsf{H}_4' = \begin{pmatrix} \omega_\mathrm{A} & B & 0 & A \\ B^* & 0 & -A & 0 \\ 0 & -A & 0 & -B \\ A & 0 & -B^* & -\omega_\mathrm{A} \end{pmatrix}. \tag{5.87c}$$

Table 5.3 provides an overview about which combinations of $\mathsf{O}_\mathrm{ctrl}, \mathsf{O}_\mathrm{Q}, \mathsf{O}_\mathrm{A} \in \{\sigma_\mathrm{x}, \sigma_\mathrm{y}, \sigma_\mathrm{z}\}$ give rise to which Hamiltonian $\mathsf{H}_1', \ldots, \mathsf{H}_4'$ and summarizes the individual expressions for A and B. It should be furthermore noted that all Hamiltonians $\mathsf{H}_1', \ldots, \mathsf{H}_4'$ can be obtained with the same procedure, which is to choose a transformation operator $\mathsf{T} = \mathsf{T}_\mathrm{Q} \otimes \mathbb{1}_\mathrm{A}$ such that T_Q diagonalizes the driven qubit Hamiltonian $\mathsf{H}_\mathrm{Q} + \mathcal{E}\mathsf{O}_\mathrm{ctrl}$, where $\mathcal{E}$ is always chosen resonantly. Although the expressions for A and B differ for each Hamiltonian and depend on the considered combination $\mathsf{O}_\mathrm{ctrl}, \mathsf{O}_\mathrm{Q}, \mathsf{O}_\mathrm{A} \in \{\sigma_\mathrm{x}, \sigma_\mathrm{y}, \sigma_\mathrm{z}\}$, cf. Table 5.3, all of them give rise to an analytical solution for the time-evolution operator. For Hamiltonian H_1' we have $\mathsf{U}_{t,t_0}^{(1)} = \mathsf{U}_{t,t_0}$ as in Eq. (5.76) and for the remaining forms $\mathsf{H}_2', \mathsf{H}_3', \mathsf{H}_4'$ we find

$$\mathsf{U}_{t,t_0}^{(2)} = \begin{pmatrix} u_{11} & u_{12} & u_{13} & -u_{14} \\ -u_{12} & u_{22} & u_{23} & u_{13} \\ u_{13} & -u_{23} & u_{22}^* & -u_{12}^* \\ u_{14} & u_{13} & u_{12}^* & u_{11}^* \end{pmatrix}, \tag{5.88a}$$

$$\mathsf{U}_{t,t_0}^{(3)} = \begin{pmatrix} u_{11} & u_{12} & u_{13} & -u_{14} \\ -u_{12} & u_{22} & -u_{23} & u_{13} \\ u_{13} & u_{23} & u_{22}^* & -u_{12}^* \\ u_{14} & u_{13} & u_{12}^* & u_{11}^* \end{pmatrix}, \tag{5.88b}$$

$$\mathsf{U}_{t,t_0}^{(4)} = \begin{pmatrix} u_{11} & u_{12} & u_{13} & u_{14} \\ -u_{12} & u_{22} & -u_{23} & u_{13} \\ u_{13} & -u_{23} & u_{22}^* & u_{12}^* \\ u_{14} & u_{13} & u_{12}^* & u_{11}^* \end{pmatrix}. \tag{5.88c}$$

The matrix elements for $\mathsf{U}_{t,t_0}^{(2)}, \ldots, \mathsf{U}_{t,t_0}^{(4)}$ are identical to those used for $\mathsf{U}_{t,t_0}^{(1)}$, i.e., identical to Eq. (5.77). Due to the similarity of the time-evolution operators $\mathsf{U}_{t,t_0}^{(1)}, \ldots, \mathsf{U}_{t,t_0}^{(4)}$, we find that the qubit purity $\mathcal{P}_\mathrm{Q}(t)$ is given by Eq. (5.84) in all cases. Hence, the formula for the minimal time T_min, cf. Eq. (5.86), is also identical.

Equations (5.84) and (5.86) provide a unified framework to describe the qubit reset for all combinations of $\mathsf{O}_\mathrm{ctrl}, \mathsf{O}_\mathrm{Q}, \mathsf{O}_\mathrm{A} \in \{\sigma_\mathrm{x}, \sigma_\mathrm{y}, \sigma_\mathrm{z}\}$ — given that qubit purification is possible in the first place. Both equations are the basis for the analytical approximations for the qubit's purity dynamics and minimal reset time shown in Fig. 5.14(a,d). In order to

evaluate the incisiveness of the approximations, it needs to be compared to their non-approximated, numerical solution in Fig. 5.14(b,e), for which we observe that Eq. (5.84) describes the numerical results for $\mathcal{P}_{\mathrm{Q}}(t)$ very accurately. Especially the minimum time T_{min} is predicted very accurately and matches the numerical observation for cases (i) and (ii) in Fig. 5.14, as well as all other combinations $\mathsf{O}_{\mathrm{ctrl}}, \mathsf{O}_{\mathrm{Q}}, \mathsf{O}_{\mathrm{A}} \in \{\sigma_{\mathrm{x}}, \sigma_{\mathrm{y}}, \sigma_{\mathrm{z}}\}$ that have not been explicitly discussed here. Moreover, as we can confirm based on the results from the numerical optimizations presented in Fig. 5.14(b,e), T_{min} indeed represents the quantum speed limit for qubit reset for all combinations $\mathsf{O}_{\mathrm{ctrl}}, \mathsf{O}_{\mathrm{Q}}, \mathsf{O}_{\mathrm{A}} \in \{\sigma_{\mathrm{x}}, \sigma_{\mathrm{y}}, \sigma_{\mathrm{z}}\}$. Note that this has also been confirmed beyond the cases (i) and (ii) presented and discussed so far. In addition, with a constant resonant control field $\mathcal{E}$, the qubit's purity $\mathcal{P}_{\mathrm{Q}}(t)$ always achieves its maximum at T_{min}, independent on the qubit's initial state $\rho_{\mathrm{Q}}(t_0)$. This is reflected by Eq. (5.84) as well as by the non-approximated, numerical dynamics evaluated for one hundred random initial states for $\rho_{\mathrm{Q}}(t_0)$ in Fig. 5.14(b,e).

The presented findings are strong numerical evidence that we have actually identified a time-optimal solution for qubit reset for all combinations of $\mathsf{O}_{\mathrm{ctrl}}, \mathsf{O}_{\mathrm{Q}}, \mathsf{O}_{\mathrm{A}} \in \{\sigma_{\mathrm{x}}, \sigma_{\mathrm{y}}, \sigma_{\mathrm{z}}\}$. The time-evolution operator $\mathsf{U}_{t,t_0} \in \mathrm{SU}(4)$ corresponding to the resonant purification protocol can also be analyzed in the Weyl chamber. The path it takes as time t moves from t_0 to T_{min} is shown as green axis in Fig. 5.13. It is identical for all 16 combinations from Table 5.2 with $N_{\mathrm{nl}} = 2$. Although the numerical optimization results are strictly speaking not a mathematical proof of time-optimality, we can nevertheless prove time-optimality for the resonant reset protocol in eight of 16 cases by employing the time-optimal tori theorem from Ref. [249]. In brevity, the latter defines a lower bound for the minimal time T_{qsl} to implement any two qubit operation $\mathsf{U} \in \mathrm{SU}(4)$. This lower bound is entirely determined by the NL coordinates c_1, c_2, c_3 that describe the non-local part of U within the Weyl chamber, cf. Eq. (5.69). For Hamiltonian (5.63), this lower bound is given by $T_{\mathrm{qsl}} = \sum_{k=1}^{3} |c_k|/(2J)$. Since we know from our numerical solutions that the path of the time-optimal qubit reset corresponds to the green axis, we have $(c_1, c_2, c_3) = (\pi/2, \pi/2, 0)$ as our target operation within the Weyl chamber and thus $T_{\mathrm{qsl}} = \pi/(2J)$. This lower bound coincides with the minimal reset time T_{min} that we have derived for eight out of the 16 combinations of Table 5.3, where qubit reset is feasible. Hence, for these cases it proves that the resonant reset protocol is time-optimal. Although this theorem can, unfortunately, not be applied to the remaining eight cases, it nevertheless still strongly supports our numerical evidence of time-optimality for the resonant protocol. Our conjecture of time-optimality is also in line with other use cases, where numerical optimal control has allowed to determine the quantum speed limit of various quantum operations [250–252].

In the remainder of this subsection, we will examine what determines the strong differences in reset times $T_{\min}$ for different combinations of $\mathsf{O}_{\mathrm{ctrl}}, \mathsf{O}_{\mathrm{Q}}, \mathsf{O}_{\mathrm{A}} \in \{\sigma_{\mathrm{x}}, \sigma_{\mathrm{y}}, \sigma_{\mathrm{z}}\}$. To this end, we first note that $T_{\min}$ is only determined by η, cf. Eq. (5.85), and thus essentially by $|A|$, cf. Eq. (5.86). The latter should therefore be as large as possible in order for $T_{\min}$ to be minimal. Unfortunately, A can not be chosen at will but is determined by the choice of $\mathsf{O}_{\mathrm{ctrl}}, \mathsf{O}_{\mathrm{Q}}, \mathsf{O}_{\mathrm{A}} \in \{\sigma_{\mathrm{x}}, \sigma_{\mathrm{y}}, \sigma_{\mathrm{z}}\}$ and by the resonance condition $\lambda_1 - \lambda_0 = \omega_{\mathrm{A}}$. From Table 5.3 we see that $|A|$ exists in three different magnitudes that give rise to three different reset times, namely

$$T_{\min}^{(1)} = \frac{\pi}{2J}, \qquad T_{\min}^{(2)} = \frac{\pi}{2J} \cdot \frac{\omega_{\mathrm{A}}}{\omega_{\mathrm{Q}}}, \qquad T_{\min}^{(3)} = \frac{\pi}{2J} \cdot \frac{\omega_{\mathrm{A}}}{\sqrt{\omega_{\mathrm{A}}^2 - \omega_{\mathrm{Q}}^2}}. \tag{5.89}$$

Among these times, $T_{\min}^{(1)}$ always represents the global minimum amid all Hamiltonians discussed in Table 5.3. While all these times correspond to a time-optimal solution for qubit reset, it still shows that depending on the characteristics of the Hamiltonian (5.63) not all combinations $\mathsf{O}_{\mathrm{ctrl}}, \mathsf{O}_{\mathrm{Q}}, \mathsf{O}_{\mathrm{A}} \in \{\sigma_{\mathrm{x}}, \sigma_{\mathrm{y}}, \sigma_{\mathrm{z}}\}$ allow for the fastest reset and care is required when designing the respective physical devises. To emphasize this, Table 5.3 lists $T_{\min}$ for the model parameters used in Fig. 5.14 as well as exemplarily for a potential experimental realization with two superconducting qubits [247, 248]. On the one hand, it demonstrates that qubit reset is in general feasible on a time scale of the order of 100 ns — or even shorter, depending on the device parameters. On the other hand, however, it shows that the type of qubit-ancilla coupling and local qubit control give rises to very distinct minimal reset times — some of them even differing by an order of magnitude.

From a physical perspective, knowledge about which combinations $\mathsf{O}_{\mathrm{ctrl}}, \mathsf{O}_{\mathrm{Q}}, \mathsf{O}_{\mathrm{A}} \in \{\sigma_{\mathrm{x}}, \sigma_{\mathrm{y}}, \sigma_{\mathrm{z}}\}$ give rise to which reset time is already very helpful. However, we still do not have an explanation why the reset times differ that much — even in cases where two combinations of $\mathsf{O}_{\mathrm{ctrl}}, \mathsf{O}_{\mathrm{Q}}, \mathsf{O}_{\mathrm{A}} \in \{\sigma_{\mathrm{x}}, \sigma_{\mathrm{y}}, \sigma_{\mathrm{z}}\}$ differ only slightly, for instance in only one of the three operators. Unfortunately, this problem can not be answered on the level of the dynamical Lie algebra $\mathfrak{g}$ as can be easily demonstrated by the following example. Let the qubit-ancilla interaction be given by $\mathsf{O}_{\mathrm{Q}} = \mathsf{O}_{\mathrm{A}} = \sigma_{\mathrm{x}}$ and let us consider the two combinations where $\mathsf{O}_{\mathrm{ctrl}} = \sigma_{\mathrm{x}}$ and $\mathsf{O}_{\mathrm{ctrl}} = \sigma_{\mathrm{y}}$. Both sets of operators $\{\mathsf{O}_{\mathrm{ctrl}}, \mathsf{O}_{\mathrm{Q}}, \mathsf{O}_{\mathrm{A}}\}$ differ only by $\mathsf{O}_{\mathrm{ctrl}}$. Interestingly, although both sets still give rise to the same dynamical Lie algebra $\mathfrak{g}$, cf. Table 5.2, they yield different reset times, i.e., $T_{\min}$ belongs to different cases of Eq. (5.89), cf. Table 5.3. A possible explanation thus needs to be sought in the different Hamiltonians, i.e., in the difference of $\mathsf{O}_{\mathrm{ctrl}} = \sigma_{\mathrm{x}}$ and $\mathsf{O}_{\mathrm{ctrl}} = \sigma_{\mathrm{y}}$. By inspecting Table 5.3, we observe that the globally minimal reset time $T_{\min} = T_{\min}^{(1)} = \pi/(2J)$ applies for all combinations, where the commutator $[\mathsf{O}_{\mathrm{Q}}, \mathsf{O}_{\mathrm{ctrl}}]$ has maximal norm, i.e., where

$\mathcal{N} = \|[\mathsf{O}_\mathrm{Q}, \mathsf{O}_\mathrm{ctrl}]\|_\mathrm{HS}$ is maximal with $\|\cdot\|_\mathrm{HS} = \langle\!\langle \cdot|\cdot \rangle\!\rangle$ the Hilbert-Schmidt norm. It can be shown that $\mathcal{N}$ is related to the energy exchange, i.e., entropy exchange, between qubit and ancilla [244]. On the on hand and quite intuitively, maximization of $\mathcal{N}$ should therefore maximize the qubit's purification rate. On the other hand, in view of Eq. (5.86), we also know that maximizing $|A|$ will minimize T_min, which should therefore maximize the purification rate as well. The latter always implies maximization of the magnitude of the anti-diagonal of $\mathsf{H}'_1, \ldots, \mathsf{H}'_4$.

Reference [244] explore the maximization of $\mathcal{N}$ and $|A|$ and their connection in more detail. To this end, it also lifts the restriction $\mathsf{O}_\mathrm{ctrl}, \mathsf{O}_\mathrm{Q}, \mathsf{O}_\mathrm{A} \in \{\sigma_\mathrm{x}, \sigma_\mathrm{y}, \sigma_\mathrm{z}\}$ and allows for $\mathsf{O}_\mathrm{ctrl}, \mathsf{O}_\mathrm{Q}, \mathsf{O}_\mathrm{A} \in \mathfrak{su}(2)$, i.e., it considers the most general case for the qubit-ancilla interaction and the local qubit control. Although no analytical expression for the time-evolution operator exists in this general case, we are still able to obtain analytical formulas for $\mathcal{N}$ and $|A|$ [244] and can therefore compare the two strategy to maximize them. Reference [244] reveals broad agreement with only minor differences between both quantities. Although the exact origin of the remaining small differences still needs to be explored, this observation suggests that the reset task might be solved time-optimally by only inspecting the joint qubit-ancilla Hamiltonian. This is also in agreement with the Lie algebraic analysis of Subsec. 5.3.2.

Finally, it is possible to generalize the control problem once more and exchange the two-level ancilla with a d-level ancilla. From a physical perspective, this is a realistic scenario, since ancillas or "qubits" such as superconducting qubits often intrinsically possess more than two levels. In experiments, their dynamics is typically just restricted artificially to two levels — usually their ground and first excited state. Reference [244] takes such energetically higher levels into account and explores whether they are detrimental or beneficial for the reset task. In terms of the reset time, Ref. [244] shows numerically that the lower bound of $T_\mathrm{min} = \pi/(2J)$, previously identified for two-level ancillas, seems to remain the lower bound even for higher dimensional ancillas. In contrast to that, higher dimensional ancillas indeed allow for better qubit reset in terms of fidelity. For a d_Q dimensional qudit that couples to a d_A dimensional ancilla, Ref. [244] proves the following proposition that links maximally achievable qudit purity and ancilla dimension.

Proposition 5.1. *Let $\mathcal{H}_\mathrm{Q}$ and $\mathcal{H}_\mathrm{A}$ be two Hilbert spaces with dimension d_Q and d_A, respectively, and $\mathfrak{L}_{\mathcal{H}_\mathrm{Q}}$ and $\mathfrak{L}_{\mathcal{H}_\mathrm{A}}$ their corresponding Liouville spaces. Let $\rho_\mathrm{A} \in \mathfrak{L}_{\mathcal{H}_\mathrm{A}}$ be a density matrix with $\lceil d_\mathrm{A}(d_\mathrm{Q}-1)/d_\mathrm{Q} \rceil$ eigenvalues below $\epsilon/(2d_\mathrm{A}(d_\mathrm{Q}-1))$, where $\epsilon > 0$ is small. Then, for all density matrices $\rho_\mathrm{Q} \in \mathfrak{L}_{\mathcal{H}_\mathrm{Q}}$, there exists a $\mathsf{U} \in \mathrm{SU}(d_\mathrm{Q} d_\mathrm{A})$ such that*

$$1 - \mathcal{P}'_\mathrm{Q} = 1 - \mathrm{tr}\left\{\rho'^2_\mathrm{Q}\right\} \leq \epsilon, \qquad \rho'_\mathrm{Q} = \mathrm{tr}_\mathrm{A}\left\{\mathsf{U}\big(\rho_\mathrm{Q} \otimes \rho_\mathrm{A}\big)\mathsf{U}^\dagger\right\}, \tag{5.90}$$

i.e., the purity $\mathcal{P}'_{\mathrm{Q}}$ *of* ρ'_{Q} *gets* ϵ *close to unity.*

Proof. See Ref. [244]. □

As an example, it is insightful to apply this proposition to the cases discussed before. For $d_{\mathrm{Q}} = d_{\mathrm{A}} = 2$, i.e., a qubit coupling to a two-level ancilla, we find that we need $\lceil d_{\mathrm{A}}(d_{\mathrm{Q}}-1)/d_{\mathrm{Q}} \rceil = \lceil 2(2-1)/2 \rceil = 1$ initially vanishing eigenvalues of ρ_{A} in order for ρ'_{Q} to be pure, i.e., $\mathcal{P}'_{\mathrm{Q}} = 1$. If we assume an ancilla with $d_{\mathrm{A}} = 3$, we find $\lceil 3(2-1)/2 \rceil = 2$, which means that we still require a pure state ρ_{A} in order to obtain $\mathcal{P}'_{\mathrm{Q}} = 1$. Interestingly, for $d_{\mathrm{A}} = 4$, two small eigenvalues of ρ_{A} suffice, which means that neither ρ_{Q} nor ρ_{A} have to be initially pure in order to obtain $\mathcal{P}'_{\mathrm{Q}} = 1$ [244].

To conclude this last section, we have generalized the model for ancilla-based qubit reset introduced in the previous section and have examined how the type of qubit-ancilla interaction and local qubit control influences the reset protocol. We have shown that a constant protocol that puts both qubit and ancilla into resonance is time-optimal for factorizing initial conditions where the ancilla is initially thermalized. We have identified those combinations of qubit-ancilla interaction and local qubit control that do not allow for qubit purification in the first place and have revealed that the reset time differs quite substantially in the remaining cases.

6

Optimal Control of Quantum Discrimination and Estimation

Quantum metrology constitutes an important pillar of quantum technologies. Its fundamental idea is to utilize quantum effects in order to improve sensing and measurement tasks beyond what is possible with classical devices. Like all quantum technologies, it strongly relies on the feasibility to accurately control quantum systems, since its technological advantage can otherwise not be realized in practice. It is therefore a quite natural platform where concepts from quantum optimal control find application. However, while the defining figure of merit for e.g. qubit reset is the fidelity with which a pure state can be prepared, quantum metrology poses a somewhat different challenge for quantum control. Its most general figure of merit is the quantum Fisher information [253], which generalizes the classical Fisher information to the quantum realm. It states how precise a statistical parameter θ can be estimated. Although the direct maximization of the quantum Fisher information is a feasible task for optimal control [254], it is nevertheless rather challenging, as it compresses various aspects that are important for the metrological task into a single quantity and does therefore not admit an analytical formula. From a physical perspective, a slightly more accessible quantity that quantum metrology — and in particular quantum discrimination and estimation as two prominent subfields — rely on, is given by the distinguishability of different quantum states [253]. To this end, it should be noted that the physical quantity θ, which needs to be discriminated or estimated, is

typically encoded in the system's dynamics and a measurement of the system's final state is then connected to a specific outcome of θ. For instance, in case of a discrimination problem, such an outcome decides whether the dynamics was governed by θ or $\theta + \mathrm{d}\theta$ with $\mathrm{d}\theta$ small compared to θ. Thus, from the perspective of optimal control, an indirect but suitable control target is to simply increase the distinguishability of a set of quantum states or dynamical maps at final time [255–269]. This also emphasizes that quantum discrimination and estimation does not have a well-defined target state or dynamical map [270–284]. Nevertheless, a physically well motivated control target — other than a target state or dynamical map — is to increase the distinguishability of the final states. This follows the simple intuition that better distinguishability readily improves the discrimination and estimation task while it avoids more complicated optimization targets like the quantum Fisher information. In contrast to the optimization of the estimation's precision, which has been widely addressed in the literature [254, 285–293], quantum discrimination has been scarcely tackled by quantum control [294, 295].

In this chapter, we will consider a quantum discrimination problem in the presence of dissipation and investigate how suitable control fields, shaped by optimal control, can help to improve the system's metrological performance. Our aim will be twofold. On the one hand, we will check in general whether a deviation from the Ramsey scheme, which is a standard scheme for such tasks, allows to improve the discrimination protocol. On the other hand and in line with the thesis' fundamental question, we will investigate how optimized control fields can help to mitigate the detrimental effect of the environment. In Sec. 6.1, we will introduce the model, which will consist of a qubit evolving under Markovian dynamics, and the control problem, which will be to increase the distinguishability of the qubit's final states with each state evolving under a slightly different Hamiltonian. In Sec. 6.2, we will then compare the state distinguishability that can be achieved by the Ramsey scheme with the one that is obtained with optimized control fields.

The results in this chapter are taken from Ref. [296].

6.1 Model and Control Problem

Throughout this chapter, we consider an open system dynamics described by the Lindblad master equation (2.21),

$$\begin{aligned}\frac{\mathrm{d}}{\mathrm{d}t}\rho_m(t) &= -\mathrm{i}\left[\mathsf{H}_m(t), \rho_m(t)\right] + \sum_k \gamma_k \left(\mathsf{L}_k \rho_m(t) \mathsf{L}_k^\dagger - \frac{1}{2}\left\{\mathsf{L}_k^\dagger \mathsf{L}_k, \rho_m(t)\right\}\right) \\ &= \boldsymbol{\mathcal{L}}_m(t)\left[\rho_m(t)\right], \end{aligned} \tag{6.1}$$

where the Hamiltonian is given by

$$\mathsf{H}_m(t) = \mathsf{H}_{\mathrm{d},m} + \mathsf{H}_{\mathrm{ctrl}}(t), \tag{6.2}$$

within which $\mathsf{H}_{\mathrm{d},m}$ describes the drift part and $\mathsf{H}_{\mathrm{ctrl}}(t)$ describes the coupling to a set of external control fields. The Lindblad operators L_k and their associated decay rates γ_k model the environment's impact. We will specify the exact form of all operators in a bit.

In a typical quantum estimation protocol we want to estimate the continuous physical quantity θ. However, here we consider a quantum discrimination problem in which case we want to distinguish between several possible Hamiltonians $\mathsf{H}_{\mathrm{d},m} = \mathsf{H}(\theta_m)$, where m labels the elements from a discrete set of values $\{\theta_1, \theta_2, \dots\}$ of the physical quantity θ. For the discrimination problem, it is therefore irrelevant whether θ is continuous or discrete in reality. In the following, we consider the case where we want to distinguish between two possible Hamiltonians, $\mathsf{H}_{\mathrm{d},1}$ and $\mathsf{H}_{\mathrm{d},2}$, corresponding to the physical quantities θ_1 and θ_2. Since $\mathsf{H}_{\mathrm{d},m}$ can not be measured directly, the discrimination, respectively estimation, is usually achieved by the measurement of the time-evolved state $\rho_m(T)$ starting from the same initial state $\rho_{\mathrm{in}} = |\Psi_{\mathrm{in}}\rangle\langle\Psi_{\mathrm{in}}|$. For the discrimination of two Hamiltonians, the two states $\rho_1(T)$ and $\rho_2(T)$ should therefore be made as distinguishable as possible in order to make the measurement results as significant as possible, i.e., in order to infer with confidence from the measurement result whether the underlying Hamiltonian has been $\mathsf{H}_{\mathrm{d},1}$ or $\mathsf{H}_{\mathrm{d},2}$. This is slightly different for the estimation task, where only the estimation's precision matters, which is essentially determined by the quantum Fisher information as we will see in a bit. Although the latter can be connected to the distinguishability of two states that are evolved under two neighboring Hamiltonians with $\mathsf{H}_{\mathrm{d},1} = \mathsf{H}(\theta - \delta\theta/2)$ and $\mathsf{H}_{\mathrm{d},2} = \mathsf{H}(\theta - \delta\theta/2)$, it technically requires $\delta\theta$ to be an infinitesimally small shift of the actual physical quantity θ [253]. In a standard discrimination task, $\delta\theta$ is not necessarily constrained. Even though this emphasizes that the figure of merit for quantum discrimination and estimation is not fundamentally different, it still highlights that we strive for slightly different dynamics, as the magnitude of $\delta\theta$ has a huge impact on the reachable state distinguishability — especially in the presence of an environment. The figure of merit for the discrimination is typically given by the success probability P_{succ} to distinguish the two final states $\rho_1(T)$ and $\rho_2(T)$. For P_{succ}, we find [297]

$$P_{\mathrm{succ}} = \frac{1}{2}\left(1 + d_{\mathrm{tr}}\left(\rho_1(T), \rho_2(T)\right)\right) \in \left[\frac{1}{2}, 1\right], \tag{6.3}$$

where d_{tr} is the trace distance, cf. Eq. (6.2). Conversely, the figure of merit for the

estimation process is its precision, which is determined by the quantum Cramer-Rao bound [253] via $S[(\hat{\theta}-\theta)^2] \geq 1/(R\mathcal{F}_\mathrm{Q})$, where $S[(\hat{\theta}-\theta)^2]$ is the variance of an unbiased estimator $\hat{\theta}$, R is the number of repetition of the experiment and $\mathcal{F}_\mathrm{Q}$ is the quantum Fisher information. Under the two Hamiltonians $\mathsf{H}_{\mathrm{d},1} = \mathsf{H}(\theta - \delta\theta/2)$ and $\mathsf{H}_{\mathrm{d},2} = \mathsf{H}(\theta + \delta\theta/2)$, the quantum Fisher information $\mathcal{F}_\mathrm{Q}$ can be related to the Bures distance d_bures, cf. Eq. (3.11), between $\rho_1(T)$ and $\rho_2(T)$ as [253]

$$\mathcal{F}_\mathrm{Q} = \frac{4d^2_\mathrm{bures}(\rho_1, \rho_2)}{(\delta\theta)^2}, \tag{6.4}$$

where $\delta\theta$ needs to be small in order for this formula to be accurate.

The two Hamiltonians that we want to discriminate within this chapter are given by $\mathsf{H}_{\mathrm{d},1} = \mathsf{H}(B_1) = B_1\sigma_\mathrm{z}/2$ and $\mathsf{H}_{\mathrm{d},2} = \mathsf{H}(B_2) = B_2\sigma_\mathrm{z}/2$, where B_1 and B_2 are the two physical quantities that should be distinguished. In the following, they replace the rather abstract variable θ that has been used to far. Physically, this discrimination task can be related to the estimation whether a magnetic field B, which interacts with a qubit via σ_z, has a field strength $B_1 = B - \delta B/2$ or $B_2 = B + \delta B/2$ with δB small compared to B. This model thus implies that we roughly know the field's magnitude B but not its exact value — the latter is accounted for by the unknown value δB. Note that B occurs here in units of energy and should therefore be seen as an *effective* magnetic field. It should be emphasized that this model, as well as the results within this chapter, also represent the more abstract discrimination task between the two Hamiltonians $\mathsf{H}_{\mathrm{d},1} = \omega_1\sigma_\mathrm{z}/2$ and $\mathsf{H}_{\mathrm{d},2} = \omega_2\sigma_\mathrm{z}/2$ with ω_1 and ω_2 two energy level splittings of arbitrary physical origin.

A standard procedure to solve such a discrimination problem is given by the Ramsey scheme. It will therefore serve as reference to which we will compare our optimized protocol in Sec. 6.2. While both the Ramsey as well as the optimized protocol start by preparing the qubit in the initial state $\rho_\mathrm{in} = |\Psi_\mathrm{in}\rangle\langle\Psi_\mathrm{in}|$, the Ramsey scheme subsequently lets the state evolve under the constant Hamiltonian $\mathsf{H}_{\mathrm{d},m}$, i.e., it assumes $\mathsf{H}_\mathrm{ctrl}(t) = 0$ in terms of Eq. (6.2). Due to the difference in B_1 and B_2 the state $\rho_m(t)$ will evolve differently for $m = 1$ or $m = 2$ and the measurement at final time T then reveals whether the field has been B_1 or B_2. In contrast to the Ramsey scheme, the optimized protocol will allow for time-dependent control fields, i.e., $\mathsf{H}_\mathrm{ctrl}(t) \neq 0$. We will optimize these control fields to make the two states $\rho_1(T)$ and $\rho_2(T)$ as distinguishable as possible at final time T. In other words, optimal control needs to maximize a distance measure $d(\rho_1(T), \rho_2(T))$ between both states. Since both states can be mixed it is important to employ a reliable distance measure, cf. Chap. 3. For the discrimination, the distance is the trace distance d_tr, since it is linearly related to the successful probability of the

discrimination, cf. Eq. (6.3). If d_{tr} is expressed in terms of the Bloch vectors $\boldsymbol{r}_1$ and $\boldsymbol{r}_2$ for states ρ_1 and ρ_2, cf. Eq. (3.8), it reads $d_{\mathrm{tr}}(\rho_1, \rho_2) = |\boldsymbol{r}_1 - \boldsymbol{r}_2|/\sqrt{2}$ [2]. Thus, the trace distance d_{tr} coincides with the geometric distance between the Bloch vectors $\boldsymbol{r}_1$ and $\boldsymbol{r}_2$ and maximal distinguishability is achieved iff $\boldsymbol{r}_1$ and $\boldsymbol{r}_2$ are on opposite points on the Bloch sphere. Hence, the maximization of d_{tr} will be our physical goal for the discrimination task.

Although the drive Hamiltonian $\mathsf{H}_{\mathrm{ctrl}}(t)$ is usually neglected in the Ramsey protocol, there is no physical reason to not utilize it as its presence allows to influence the evolution of d_{tr} quite non-trivially. For the driven Hamiltonian $\mathsf{H}_m(t)$, cf. Eq. (6.2), we make the general assumption

$$\mathsf{H}_{\mathrm{ctrl}}(t) = \frac{1}{2}\Big[\mathcal{E}_{\mathrm{x}}(t)\sigma_{\mathrm{x}} + \mathcal{E}_{\mathrm{y}}(t)\sigma_{\mathrm{y}} + \mathcal{E}_{\mathrm{z}}(t)\sigma_{\mathrm{z}}\Big], \tag{6.5}$$

where $\mathcal{E}_{\mathrm{x}}(t), \mathcal{E}_{\mathrm{y}}(t), \mathcal{E}_{\mathrm{z}}(t) \in \mathbb{R}$ are control fields that couple via σ_{x}, σ_{y} and σ_{z} to the qubit, respectively. In order to understand, why the drive's influence is non-trivially it should be noted that while $\mathsf{H}_{\mathrm{ctrl}}(t)$ is identical for both Hamiltonians, $\mathsf{H}_1(t)$ and $\mathsf{H}_2(t)$, it still influences the dynamics in the two cases differently due to the difference in the drift Hamiltonians, $\mathsf{H}_{\mathrm{d},1}$ and $\mathsf{H}_{\mathrm{d},2}$. This is because the different drift Hamiltonians commute differently with $\mathsf{H}_{\mathrm{ctrl}}(t)$, which leads to different dynamics in each case. It can thus be exploited to maximize d_{tr}. The presence of $\mathsf{H}_{\mathrm{ctrl}}(t)$ thus turns the discrimination problem into a control problem, which seeks to answer the question how to choose the three fields $\mathcal{E}_{\mathrm{x}}(t)$, $\mathcal{E}_{\mathrm{y}}(t)$ and $\mathcal{E}_{\mathrm{z}}(t)$ such that d_{tr} is maximized at final time T when the state $\rho_m(T)$ is measured.

In the following, we again derive suitable control fields via optimal control and Krotov's method. To this end and the specific task of maximizing d_{tr} at final time T, we choose the final time functional as

$$\mathcal{J}_T\left[\{\rho_1, \rho_2\}, T\right] = 1 - d_{\mathrm{tr}}^2\left(\rho_1(T), \rho_2(T)\right) = 1 - d_{\mathrm{HS}}\left(\rho_1(T), \rho_2(T)\right) \tag{6.6}$$

with d_{HS} the Hilbert-Schmidt distance, cf. Eq. (3.14). Note that the relation $d_{\mathrm{tr}}^2 = d_{\mathrm{HS}}$ only holds for qubits in which case maximization of d_{tr} and maximization of d_{HS} are mathematically equivalent. Since both distances are reliable measures of state distinguishability, cf. Chap. 3, we choose d_{HS} for maximization in optimal control as it is more suitable for that purpose and admits analytical gradients with respect to the states ρ_1 and ρ_2.

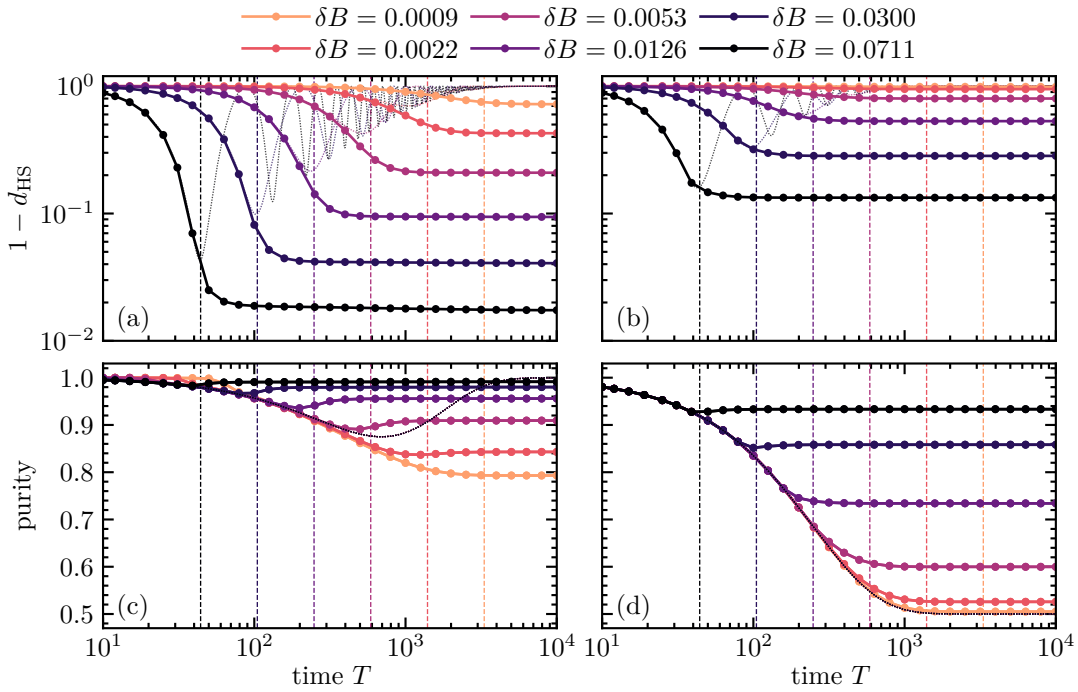

Figure 6.1: Improvement of the state distinguishability under the optimized control fields. The upper graphs show the indistinguishability $1 - d_{\mathrm{HS}}$ as a function of protocol duration in case of (a) relaxation with $T_1 = 1000$ and (b) pure dephasing with $T_2 = 1000$. The dotted lines correspond to the Ramsey protocol whereas the markers indicates the reachable value of $1 - d_{\mathrm{HS}}$ under the optimized control fields at the respective final time T. The vertical lines indicate the quantum speed limit T_{qsl} given by Eq. (6.7). Panels (c) and (d) show the purity of the two states corresponding to the dynamics of (a) and (b), respectively. Note that both states have almost identical purity, hence there is just one visible line.

6.2 Improving the Standard Ramsey Protocol

Before we start to compare the performance of the discrimination task under the Ramsey and the optimized protocol, we need to emphasize that two different time scales will play an important role. On the one hand, we have the quantum speed limit for the discrimination task. While the general concept of quantum speed limits has been discussed in Subsec. 2.3.2, the situation is slightly different for the current discrimination task. In contrast to a standard situation, where a quantum speed limit typically indicates the minimal time to transfer an initial state into a target state or to implement a target operation, here we are interested in the relative distance d_{HS} between the two time-evolved states $\rho_1(t)$ and $\rho_2(t)$ and not into their individual distance with respect to the initial state ρ_{in}. Hence, the time scale on which d_{HS} increases is defined by their relative speed of evolution, which, in turn, is entirely determined by δB. The latter becomes immediately

clear by considering the extreme case of $\delta B = 0$, which implies $\mathsf{H}_{\mathrm{d},1} = \mathsf{H}_{\mathrm{d},2}$ and thus $\rho_1(t) = \rho_2(t)$ for all t. In this case, no matter how the control Hamiltonian $\mathsf{H}_{\mathrm{ctrl}}(t)$ is chosen, a discrimination is not possible as nothing can be discriminated. The quantum speed limit can thus be regarded as being infinite. Since we can expect it to behave continuously and smoothly, it is thus intuitively clear that a small δB will imply a large quantum speed limit and vice versa. For the discrimination task, the quantum speed limit is determined by δB via the coherent part of the dynamics and can be estimated by

$$T_{\mathrm{qsl}} = \frac{\pi}{\delta B}. \tag{6.7}$$

It should be noted that this is the minimal time required for perfect state distinguishability with $d_{\mathrm{HS}} = 1$ in case of the Ramsey protocol. Equation (6.7) also assumes a closed quantum system, i.e., no dissipation. On the other hand, dissipation will unfortunately play a role in practice as it will continuously decrease d_{HS} and thus cause both states, $\rho_1(t)$ and $\rho_2(t)$, evolving under $\mathsf{H}_1(t)$ and $\mathsf{H}_2(t)$, to evolve towards the same steady state ρ_{ss}. The time scale set by the dissipation is completely independent of δB — in contrast to T_{qsl}. In the following, since the impact of relaxation and pure dephasing, characterized by T_1 and T_2, respectively, cf. Eq. (2.19), is quite different, we consider them individually in order to evaluate their respective impact individually. This assumption is reasonable, since in most physical settings the environmental noise is either T_1 or T_2 dominated. In the following, we take ρ_{in} with $|\Psi_{\mathrm{in}}\rangle = |+\rangle = (|0\rangle + |1\rangle)/\sqrt{2}$ as initial state for the discrimination task. For our dynamical description this means that we do not account for the process preparing ρ_{in}. This is justified as such a preparation process does not pose an experimental challenge and can also be done very accurately.

We start our examination in Fig. 6.1 by comparing the achievable distinguishability d_{HS} as a function of the protocol length T for the Ramsey and optimized protocol. In detail, the dotted lines in Fig. 6.1(a) show the dynamics of $1 - d_{\mathrm{HS}}$ for the Ramsey protocol, i.e., $\mathsf{H}_{\mathrm{ctrl}}(t) = 0$, for several δB. The environmental noise is given by relaxation, i.e., the Lindblad master equation (6.1) contains only a single Lindblad operator $\mathsf{L} = |0\rangle\langle 1|$ with decay rate $\gamma = 1/T_1$. The dashed vertical lines indicate the quantum speed limit T_{qsl} according to Eq. (6.7). Starting initially at $d_{\mathrm{HS}} = 0$, the distinguishability d_{HS} increases until it reaches the maximum of $d_{\mathrm{HS}}^{\mathrm{max}}$, i.e., minimum of $1 - d_{\mathrm{HS}}^{\mathrm{max}}$, at approximately $T \approx T_{\mathrm{qsl}}$. Note that due to the presence of the dissipation the latter does not perfectly coincide with T_{qsl}. For times $T > T_{\mathrm{qsl}}$, the distinguishability d_{HS} decreases exponentially as the relaxation causes $\rho_1(t)$ and $\rho_2(t)$ to evolve towards the same ground/steady state $\rho_{\mathrm{ss}} = |0\rangle\langle 0|$. This is in contrast to the ideal, i.e., noiseless, unitary dynamics, where d_{HS}

would show perfect oscillations between $d_{\mathrm{HS}} = 0$ and $d_{\mathrm{HS}} = 1$ with its oscillation frequency determined by δB. While the oscillations are clearly visible, the fact that we can not reach the maximal distinguishability $d_{\mathrm{HS}} = 1$ is solely due to dissipation.

Interestingly, we observe that the decay of the state distinguishability d_{HS} after its first maximum, respectively first minimum of $1 - d_{\mathrm{HS}}$, caused by the relaxation, can be completely suppressed by using tailored, i.e., optimized, control fields. The markers in Fig. 6.1(a) show the reachable distinguishability d_{HS} at the respective final time T used in the optimization. There are two interesting effects to observe from these optimization results. On the one hand, the reachable maximal distinguishability $d_{\mathrm{HS}}^{\max}$ increases compared to what is reachable with the Ramsey scheme. We can therefore conclude that in the presence of relaxation, optimized control fields allow in general for better distinguishability. This can even be observed despite the rather counter-intuitive fact that the optimized scheme prefers slightly longer protocol durations (factor $\lesssim 2$) in order to reach $d_{\mathrm{HS}}^{\max}$. On the other hand and independent of the value $d_{\mathrm{HS}}^{\max}$, the state distinguishability can not only be improved but also be stabilized at that maximally reachable distance $d_{\mathrm{HS}}^{\max}$ against decay for protocol durations T much longer than the T_1 time. Figure 6.1(a) demonstrates this stabilization for times T up to $10 \times T_1$ but suggests that it should, in principle, be feasible for arbitrary long times.

Besides the distinguishability d_{HS} itself, an interesting quantity to investigate is the purity of the two states $\rho_1(t)$ and $\rho_2(t)$ in dependence of d_{HS}. For maximal distinguishability $d_{\mathrm{HS}} = 1$, the two states need to be on opposite points of the Bloch sphere, i.e., they must lie on its surface and are therefore necessarily pure. In contrast, for $d_{\mathrm{HS}} < 1$ it is very likely that at least one or both states become mixed. Figure 6.1(c) shows the purity of states $\rho_1(t)$ and $\rho_2(t)$ corresponding to the data in Fig. 6.1(a), both for the Ramsey protocol (dotted lines) and at final time T after an evolution under the optimized control fields (markers). The dotted lines show an intermediate purity loss in the Ramsey protocol due to the relaxation. The final gain in purity for $t \to \infty$ is here an indicator for the incoherent process of both states approaching the same (pure) ground/steady state $\rho_{\mathrm{ss}} = |0\rangle\langle 0|$. In contrast, the behavior of the purity in case of the improved and stabilized d_{HS} depends strongly on δB. While for larger δB the loss of purity is avoided at all T by the respective optimized control fields, the improvement in case of small δB comes along with a loss in purity. It can therefore be argued that the improvement in distinguishability comes at the expense of purity. However, this is not a severe problem in practice, since the purity itself does not play a role in the discrimination process as only the state distinguishability matters — and the latter is still larger in the optimized protocol despite the loss in purity. Figure 6.1(c) shows that the loss of purity under

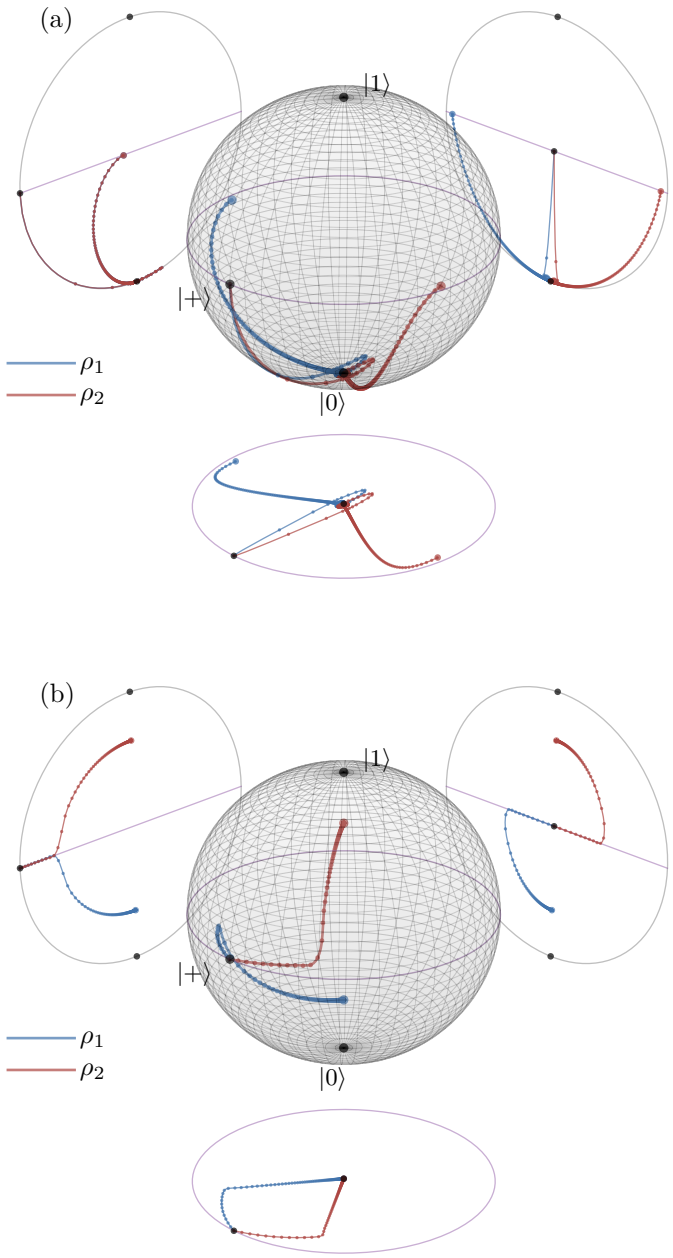

Figure 6.2: Exemplary dynamics of the two states $\rho_1(t)$ and $\rho_2(t)$ under the optimized fields within the Bloch sphere for (a) relaxation and (b) pure dephasing. The parameters are $\delta B = 0.011$ with (a) $T_1 = 1000$ and (b) $T_2 = 1000$. The total time is $T = 2511$ and the corresponding optimized fields are shown in Fig. 6.3(a) and (b). The density of dots on each line indicates the speed of the evolution with a low density corresponding to high speed and vice versa.

the optimized protocol is distributed equally between both states. In Fig. 6.1(c), this is evidenced by the fact that the markers indicate the purity for both states, $\rho_1(t)$ and $\rho_2(t)$, simultaneously as their value is almost identical.

The improvement and stabilization of d_{HS}, observed in Fig. 6.1(a), is achieved via a simple control strategy which can be most conveniently understood on the Bloch sphere, cf. Fig. 6.2(a). To this end, we choose the control field $\mathcal{E}_{\mathrm{z}}$ such that it cancels the known B, i.e., $\mathcal{E}_{\mathrm{z}}(t) = -B$. This eliminates the fast, coherent oscillations of $\boldsymbol{r}_1(t)$ and $\boldsymbol{r}_2(t)$ around the z-axis, which do not contribute to the distinguishability d_{HS} as the effect of B is identical for both states. Note that the feasibility to cancel B via $\mathcal{E}_{\mathrm{z}}$ is also the reason why the exact value of B does not have any impact for the discrimination task as only δB matters. In order to protect both states, $\boldsymbol{r}_1(t)$ and $\boldsymbol{r}_2(t)$, as much as possible from the detrimental relaxation, i.e., prevent their vectors from shrinking, we "kick" both states from their initial position $\rho_{\mathrm{in}} = |+\rangle\langle+|$ on the equator close to the ground/steady state $\rho_{\mathrm{ss}} = |0\rangle\langle 0|$. This is achieved by a $\pi/2$ like pulse via $\mathcal{E}_{\mathrm{y}}$ right at the beginning of the protocol. This can be seen in Fig. 6.2(a) by the states' fast initial motion towards the Bloch sphere's south pole. The states stay close to ρ_{ss} for the largest part of the protocol. Their dynamics becomes effectively decoherence-free in the vicinity of ρ_{ss}. For the measurement at final time T both states are transferred back to the equator by a second, inverse $\pi/2$ like pulse. In Fig. 6.2(a), it can be seen that this inverse motion towards the equator happens on a much longer time scale than the initial kick that transfers them away from it. Whether this has a physical origin or is just a feature of the numerical optimization is unfortunately not clear yet.

It is important to stress that this strategy of protecting both states close to the ground/steady state ρ_{ss} for as long as possible has been identified in several steps. In numerical optimal control, it is a quite common procedure to approach the final control solution iteratively — not only in terms of the optimization algorithm itself but also in terms of which control fields among a given selection of conceivable fields are used in practice and how their guess fields are chosen. Conceptually, the optimization was initially allowed to optimize all three control fields $\mathcal{E}_{\mathrm{x}}, \mathcal{E}_{\mathrm{y}}, \mathcal{E}_{\mathrm{z}}$ and the optimization was started without any strategic choice for their respective guess fields. However, the strategy that has been described in the last paragraph was identified (with only slight deviations) even when using this extended initial set of control fields and despite the lack of physical intuition in the guess fields. Nevertheless, its quintessence and reduced version consists of the strategy described before, i.e., it consists of a constant $\mathcal{E}_{\mathrm{z}}$ and no $\mathcal{E}_{\mathrm{x}}$ at all such that $\mathcal{E}_{\mathrm{y}}$ is the only time-dependent field that needs to be optimized in practice.

In order to explore the solution in more detail, Fig. 6.3(a) shows the guess and optimized

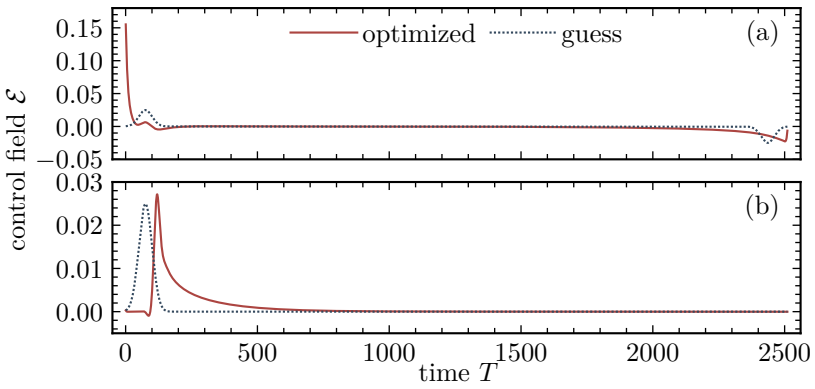

Figure 6.3: Guess (dotted) and unconstrained optimized (solid) field for the case of (a) relaxation with the control field $\mathcal{E}_y(t)$ and (b) pure dephasing where the control is $\mathcal{E}_x(t)$. The corresponding Bloch sphere dynamics is depicted in Fig. 6.2(a) and (b), respectively.

form of $\mathcal{E}_y(t)$ in an exemplary case when guiding the optimization with a guess field that already incorporates the initial $\pi/2$ like kick in the beginning and its inverse counterpart at the end. Compared to the guess field, the optimization increases the intensity of the first kick such that the rotation from the initial equatorial state $\rho_{\text{in}} = |+\rangle\langle+|$ towards $\rho_{\text{ss}} = |0\rangle\langle 0|$ is carried out as fast as possible. The corresponding Bloch sphere dynamics is shown in Fig. 6.2(a). After the first kick, the two states $\rho_1(t)$ and $\rho_2(t)$ remain close to the ground/steady state ρ_{ss} most of the time, which effectively protects them from dissipation. The second, inverse kick happens much slower and transfers the states symmetrically to the equatorial plane such that d_{HS} becomes maximal at T, i.e., the final time of measurement. Note that the optimized field in Fig. 6.3(a) and its corresponding dynamics on the Bloch sphere, cf. Fig. 6.2(a), have been selected as a representative of an entire class of solutions for the problem of maximizing distinguishability in the presence of relaxation. The exact details of the optimized control field and corresponding dynamics differ depending on δB and T, but the general control strategy remains similar.

We now turn to the case of pure dephasing, which means that we again consider Eq. (6.1) with a single Lindblad operator $\mathsf{L} = \sigma_z$ and decay rate $\gamma = 1/T_2$. Figure 6.1(b) shows the dynamics for the Ramsey protocol as dotted lines. In comparison to the case of T_1 decay, cf. Fig. 6.1(a), pure dephasing seems to have a more severe influence on d_{HS} even if the decay rates are identical, i.e., $\gamma = 1/T_2 = 1/T_1$. Nevertheless, also in this case, the optimization is capable of improving d_{HS} with respect to the Ramsey protocol — again at the expense of longer protocol durations (factor $\lesssim 2$). The effect of stabilizing d_{HS} at the maximal reachable distance $d_{\text{HS}}^{\max}$ for times much longer than the decay time can be observed as well. However, the dynamics, both in the Ramsey protocol

as well as under the optimized control fields, look quite different compared to the case of relaxation shown in Fig. 6.1(a) and discussed earlier. With pure dephasing, no unique, single steady state exists but rather a set of states, namely the coherence-free states given by $\{\rho_{\mathrm{ss}} = p\,|0\rangle\langle 0| + (1-p)\,|1\rangle\langle 1|\,|p \in [0,1]\}$. Geometrically, these correspond to the states on the z-axis of the Bloch sphere. Since neither the drift $\mathsf{H}_{\mathrm{d},m}$ nor the dephasing causes a change of any state's z-component, the two states $\boldsymbol{r}_1(t)$ and $\boldsymbol{r}_2(t)$, that start initially in the equatorial plane, precess around the z-axis while loosing purity, i.e., shrink within the equatorial plane. Hence, they evolve towards the Bloch sphere's center, i.e., the completely mixed state. This is evidenced by the dotted lines in Fig. 6.1(d), which show the purity evolving towards 1/2 for $t \to \infty$ under the Ramsey protocol. For the optimized protocol, we observe a similar behavior as for the case of relaxation. While a larger δB in general allows for larger purity of the final states under the optimized protocol and vice versa, it should be noted that all states from the stabilized plateau have higher purity compared to the Ramsey scheme, cf. the markers and dotted lines in Fig. 6.1(d).

An optimization of all three available control fields $\mathcal{E}_{\mathrm{x}}$, $\mathcal{E}_{\mathrm{y}}$, $\mathcal{E}_{\mathrm{z}}$ again yields a simple control strategy. Like in the case of relaxation, it can in practice be realized by only a single time-dependent control field. The procedure that leads to this reduced control scheme is identical to that discussed for the case of relaxation. However, for simplicity, we will only discuss its final, reduced version in the following. This time, in case of pure dephasing, the only time-dependent control field is $\mathcal{E}_{\mathrm{x}}(t)$, while $\mathcal{E}_{\mathrm{z}}(t) = -B$ again cancels the known field strength B and $\mathcal{E}_{\mathrm{y}}$ is not needed at all. Figure 6.3(b) shows the guess field for $\mathcal{E}_{\mathrm{x}}(t)$, which, in contrast to the guess field of Fig. 6.3(a), exhibits only a single peak at the beginning. This peak is modified by the optimization in a clever way such that it splits the two states $\boldsymbol{r}_1(t)$ and $\boldsymbol{r}_2(t)$ entirely within the equatorial plane in a first step and then rotates them onto the z-axis in a second step. The two steps are clearly visible in the corresponding Bloch sphere dynamics shown in Fig. 6.2(b). Once the states reach the z-axis, $\mathcal{E}_{\mathrm{x}}(t) \approx 0$ is essentially turned off and the states become invariants of the dynamics, which implies that their distinguishability d_{HS} can essentially be preserved forever. This readily yields an explanation of the stabilization observed in Fig. 6.1(b). Note that the respective dynamics and optimized field in Fig. 6.2(b) and (b) again represent an example for the entire class of solutions for the problem of maximizing distinguishability in the case of pure dephasing. The exact details depend again on δB and T.

Next, we relate the improved distinguishability d_{HS} observed in Fig. 6.1 to the quantum Fisher information $\mathcal{F}_{\mathrm{Q}}$, which, as we have discussed earlier, constitutes the most fundamental figure of merit for any quantum metrological application and goes beyond the

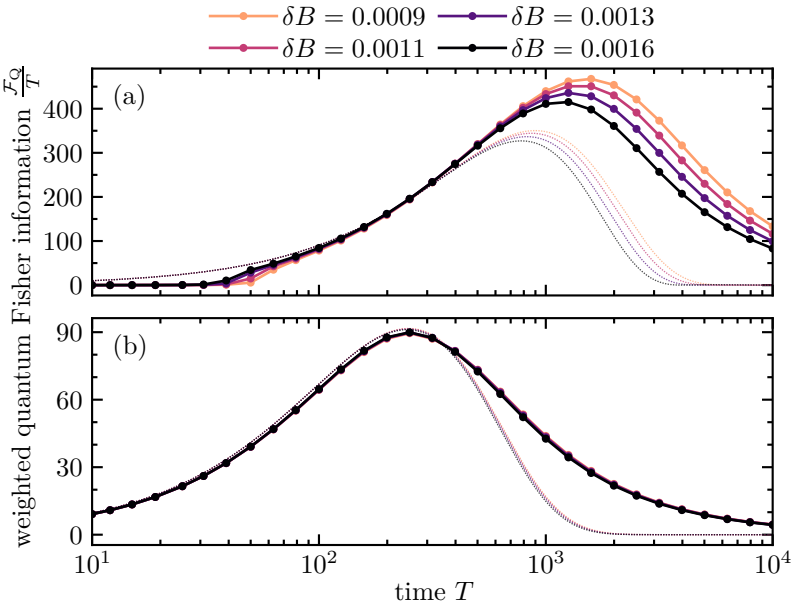

Figure 6.4: Quantum Fisher information $\mathcal{F}_Q$ (weighted by the protocol duration T) for small values of δB. Panel (a) corresponds to the case of relaxation presented in Fig. 6.1(a) while panel (b) corresponds to the case of pure dephasing in Fig. 6.1(b). The dotted lines indicate the values for the Ramsey protocol whereas the markers show the optimized results.

simple concept of state distinguishability. Nevertheless, we can obtain a good estimate for $\mathcal{F}_Q$ via the state distinguishability by evaluating Eq. (6.4) for small $\delta\theta$, i.e., small δB in our case. It depends on the Bures distance d_{bures}, which is a distance metric on the set of density matrices, just as the trace distance d_{tr} or the Hilbert-Schmidt distance d_{HS}, cf. Eqs. -(3.14). Unfortunately, unlike the trace distance d_{tr} discussed above, d_{bures} cannot be related analytically to d_{HS} — not even in the simple case of qubits. Nevertheless, as we have seen in Sec. 3.4 and especially Fig. 3.8, we can reliably expect that the increase of d_{HS} increases d_{bures} as well. For the maximization of d_{HS}, shown in Fig. 6.1, this is in fact true and d_{bures} is readily improved alongside d_{HS}.

While Eq. (6.4) is technically only an approximation for $\mathcal{F}_Q$ for small δB, it furthermore needs to be weighted by the protocol duration T in order to quantify the amount of information that can be obtained per unit time for any given protocol. To this end, Fig. 6.4 shows the quantum Fisher information $\mathcal{F}_Q$ weighted by the protocol duration T for small values of δB. In the case of pure dephasing and in agreement with Fig. 6.1(b), we observe a small improvement in d_{HS}, respectively d_{bures}, for the optimized protocol compared to the Ramsey protocol. However, this improvement, if taken into account for calculating the quantum Fisher information $\mathcal{F}_Q$ and weighted by the protocol duration T,

is shown in Fig. 6.4(b) and reveals that the effects of larger $\mathcal{F}_\mathrm{Q}$ and larger T roughly cancel each other and the maximally reachable value of $\mathcal{F}_\mathrm{Q}/T$ is almost identical for the Ramsey and optimized protocols. Conversely, for the case of relaxation shown in Fig. 6.4(a), the significant improvement of d_HS, respectively d_bures, realized by the optimized protocol gives rise to an improvement of $\mathcal{F}_\mathrm{Q}/T$ despite the slightly longer protocol duration T. In this case, we can thus expect a metrological gain of the optimized protocol compared to the Ramsey protocol.

So far, we have only considered decay rates determined by $T_1 = 1000$ and $T_2 = 1000$, i.e., by a single time scale for dissipation. However, as we have pointed out at the beginning of this section, the dissipation sets a time scale for the control task that is independent form the quantum speed limit T_qsl set by δB via Eq. (6.7). Hence, it is only natural to ask whether the control strategy that has been identified above depends on the actual value of the decay rates. To this end, we examine how the improvement of d_HS, respectively $d_\mathrm{tr} = \sqrt{d_\mathrm{HS}}$, observed in Fig. 6.1, behaves for different relaxation and dephasing times. In detail, we are interested in the behavior of

$$M_\gamma(\delta B) \equiv \min_t \left\{1 - d_\mathrm{tr}\left(\rho_1(t), \rho_2(t)\right)\right\}, \tag{6.8}$$

as a function of δB for various decay rates $1/T_1$ and $1/T_2$. It should be emphasized that the function M_γ measures, for a given δB, the maximally reachable distinguishability $d_\mathrm{tr}^\mathrm{max}$, independent of the time it takes to reach it. In other words, it can be written as $M_\gamma(\delta B) = 1 - d_\mathrm{tr}^\mathrm{max}$. It is therefore the relevant figure of merit if, for a given physical or metrological task, the protocol duration is not crucial and only the maximally achievable state distinguishability is of importance. For the Ramsey protocol with its time-independent Hamiltonian $\mathsf{H}_m(t) = \mathsf{H}_{\mathrm{d},m}$ with $\mathsf{H}_\mathrm{ctrl}(t) = 0$, Eq. (6.8) can be solved analytically. To this end, we first need to find an expression for $\rho_m(t)$, which can be obtained analytically by solving the Lindblad master equation (6.1) with $\mathsf{H}_m(t) = \mathsf{H}_{\mathrm{d},m}$. With this, we can readily obtain an analytical expression for $d_\mathrm{HS}(t) = d_\mathrm{HS}(\rho_1(t), \rho_2(t))$. For relaxation as well as pure dephasing, we find the same solution

$$d_\mathrm{HS}(t) = e^{-\gamma t} \sin^2\left(\frac{\delta B}{2} t\right), \tag{6.9}$$

although we have to note the difference by a factor of four as the solution for relaxation implies $\gamma = \gamma_1 = 1/T_1$ while the one for pure dephasing implies $\gamma = \gamma_2 = 4/T_2$. As a next step, we then need to find the time at which $d_\mathrm{HS}(t)$ reaches its global maximum as well as its corresponding globally maximal value $d_\mathrm{HS}^\mathrm{max}$. This can be done analytically as well. Since we have $d_\mathrm{tr} = \sqrt{d_\mathrm{HS}}$, we can deduce $d_\mathrm{tr}^\mathrm{max} = \sqrt{d_\mathrm{HS}^\mathrm{max}}$. The latter readily solves

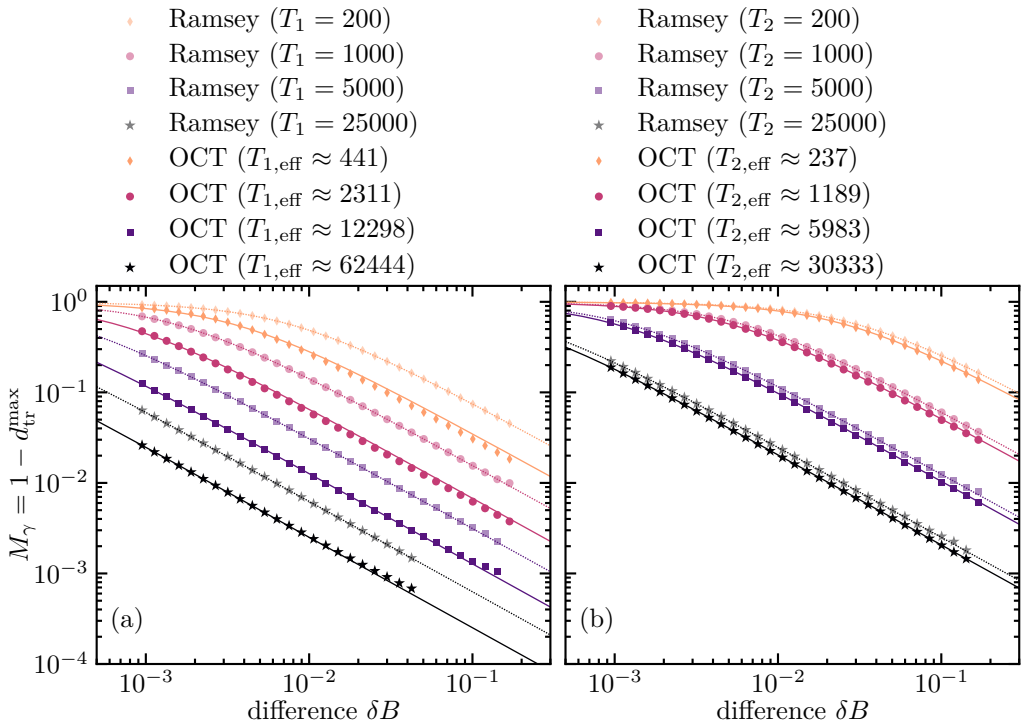

Figure 6.5: Improvement of the state distinguishability in terms of effective decay rates. The plot shows the maximal trace distance $d_{\text{tr}}^{\max}$, i.e., minimal M_γ, as a function of δB for several (a) relaxation and (b) dephasing times. The values for the Ramsey scheme (opaque markers) follow the analytical prediction of Eq. (6.10), shown as dotted lines. The non-opaque markers correspond to the optimized values of $D_{\text{tr}}^{\max}$, i.e., numerical evaluation of Eq. (6.8). The solid lines are fits of the optimized values to Eq. (6.10) with fitting parameter (a) $\gamma = 1/T_{1,\text{eff}}$ and (b) $\gamma = 4/T_{2,\text{eff}}$.

Eq. (6.8) and yields

$$M_\gamma(\delta B) = 1 - \sqrt{\frac{(\delta B)^2}{(\delta B)^2 + \gamma^2} \times \exp\left\{-\frac{\gamma}{\delta B} \arccos\left(\frac{\gamma^2 - (\delta B)^2}{\gamma^2 + (\delta B)^2}\right)\right\}}. \tag{6.10}$$

As for Eq. (6.9), the solution for relaxation is given by $\gamma = \gamma_1 = 1/T_1$ and for pure dephasing by $\gamma = \gamma_2 = 4/T_2$. The dotted lines in Fig. 6.5(a) and (b) show M_γ for the Ramsey protocol for relaxation and pure dephasing, respectively. The dotted lines perfectly fit the numerical values given by the opaque markers, as we expect for the analytical solution (6.10). In contrast, for the dynamics under the optimized control fields it is not possible to find an analytical solution like Eq. (6.10). This is because of the Hamiltonian $\mathsf{H}_m(t)$ being time-dependent due to $\mathsf{H}_{\text{ctrl}}(t) \neq 0$. However, in this case it is still possible to evaluate Eq. (6.8) numerically. This yields the non-opaque markers in

Fig. 6.5. Remarkably, these show an almost identical functional dependence compared to the dotted lines of the time-independent Ramsey scheme. We therefore fit the data points obtained with the optimized protocol and by numerically evaluate Eq. (6.8) to Eq. (6.10) using effective relaxation and dephasing times, $T_{1,\mathrm{eff}}$ and $T_{2,\mathrm{eff}}$, as fitting parameters. This yields the solid lines in Fig. 6.5, which demonstrate that M_γ accurately describe the dependence also for the optimized data points with effective decay times $T_{1,\mathrm{eff}}$ or $T_{2,\mathrm{eff}}$ — see Fig. 6.5 for their exact value. From a physical perspective, this is not obvious as the coherent dynamics of the Ramsey and optimized protocol differ drastically, which makes the resemblance in their functional behavior of M_γ remarkable. For relaxation, the obtained effective decay times satisfy $T_{1,\mathrm{eff}}/T_1 \approx 2.4$, whereas for pure dephasing, the ratio is $T_{2,\mathrm{eff}}/T_2 \approx 1.2$. Thus, the maximally reachable distinguishability $d_{\mathrm{tr}}^{\max}$ of the optimized protocol behaves as though it would have been measured by a Ramsey scheme with 2.4 times longer T_1, respectively 1.2 times longer T_2 time, which greatly improves the distinguishability.

In summary, we have shown in this chapter that optimized control fields allow to improve the distinguishability of two states in the presence of either relaxation or pure dephasing. By utilizing optimize control fields, we are also able to stabilize the distinguishability at its maximum for times that are at least one order of magnitude longer than the decay times for dissipation. We have identified the underlying control strategy to take advantage of existing decoherence-free subspaces within the system.

7

Optimization of an Entangling Operation between Bosonic Modes

In this last chapter, we will explore how optimal control can mitigate the dissipation's detrimental influence on a fundamental task of quantum computing — namely an entangling gate between qubits. While the feasibility to entangle qubits is what gives rise to a quantum computer's computational power in the first place, it is still one of the most error-prone operations. Especially the dissipation causes the achievable gate fidelity to drop below the error correction threshold, which thus prevents to build fully fault-tolerant quantum computers [218]. While many physical qubit platforms like NV centers [298], trapped ions [299], quantum dots [300] or even photons [301] have emerged over time, superconducting qubits [142, 218] have become one of the leading platforms. Among the several requirements that any qubit platform needs to fulfill [187], superconducting qubits already satisfy many of them. For instance, it has already been demonstrated that they allow for accurate state initialization [191] and measurement [302], coupling of different qubits [303] and the implementation of entangling gates [304, 305]. Hence, they are promising candidates for building fault-tolerant quantum computers.

While it is still an active field of research whether quantum error correction schemes can be realized with superconducting qubits in a large-scale quantum computer and in view of various experimental challenges [218, 306], continuous variable quantum computing [307, 308] is yet another promising approach to tackle these challenges. Especially

in combination with quantum error correction schemes like binomial coding [309], its is a promising approach to achieve fault-tolerant quantum computing. While continuous variable quantum computing harness the infinite dimensional Hilbert space of bosonic modes to store and process information, binomial coding provides a scheme how to reliably encode qubits into bosonic modes such that typical errors can be reliably detected and corrected.

A convenient physical platform to realize continuous variable quantum computing is given by superconducting photon cavities [310]. They are an excellent choice for such bosonic modes, since their coherence times exceed those of conventional superconducting qubits like transmons [311] by orders of magnitude and are thus much less prone to errors. Interestingly, transmons are traditionally used to represent qubits while cavities are used to control them [306]. Thus, in the continuous variable scenario, those traditional roles are reversed as the cavities are used to encode qubits while the transmons constitute a convenient choice to control the cavities [312]. However, with the experimentally demonstrated feasibility of binomial encoding [313] and of an entangling gate between such bosonic modes [314], this setup constitutes a promising new approach to tackle the challenges towards universal, fault-tolerant and error corrected quantum computing. Unfortunately, even though this new setup enables efficient quantum error correction on its qubits, i.e., the cavities, the error-prone transmons, required to mediate the interaction between the cavities, still pose a remaining source of incorrectable errors that needs to be taken care of.

In the following, we will examine how optimal control allows to mitigate the environmentally induced errors for a system of two superconducting photon cavities coupled via an intermediate transmon. The control task will be to realize a high-fidelity beamsplitter interaction between both cavities by virtue of only driving the transmon [315]. As for the discrimination task considered in Chap. 6, we can assume the dissipation to be purely detrimental. Therefore, it should be avoided at all costs. The most promising approach is thus to find a control strategy that simply accomplishes the task in less time — at best even at the quantum speed limit — such that the environment has less time to compromise the operation.

Section 7.1 introduces the physical model, i.e, two superconducting photon cavities coupled via a joint transmon. It will also summarize details regarding a recent method to realize a beamsplitter interaction between the two cavities [315]. We will also specify the control task and how optimal control can be used to solve it. In the subsequent Sec. 7.2, we will then present the optimization results, i.e., a new control scheme that readily increases the beamsplitter interaction between both cavities and which gives to

faster entangling gates. We will support this new scheme by establishing an analytical Hamiltonian to describe the reduced dynamics of only the two cavities.

7.1 Model and Control Problem

We consider a tripartite system consisting of two harmonic oscillators, labeled A and B, respectively, and a driven, intermediate anharmonic oscillator, labeled C. Physically, the two harmonic oscillators, A and B, are represented by superconducting cavities [310], while the anharmonic oscillator is given by a transmon [311], which serves as coupling element between the cavities. The Hamiltonian for this tripartite system reads [316]

$$\begin{aligned}\mathsf{H}(t) = \omega_{\mathrm{a}}\mathsf{a}^\dagger\mathsf{a} + \omega_{\mathrm{b}}\mathsf{b}^\dagger\mathsf{b} + \omega_{\mathrm{c}}\mathsf{c}^\dagger\mathsf{c} - \frac{\alpha_{\mathrm{c}}}{2}\mathsf{c}^\dagger\mathsf{c}^\dagger\mathsf{c}\mathsf{c} + g_{\mathrm{a}}\left(\mathsf{a}\mathsf{c}^\dagger + \mathsf{a}^\dagger\mathsf{c}\right) + g_{\mathrm{b}}\left(\mathsf{b}\mathsf{c}^\dagger + \mathsf{b}^\dagger\mathsf{c}\right) \\ + \sum_k \left(\Omega_k e^{-\mathrm{i}\omega_k t}\mathsf{c}^\dagger + \Omega_k^* e^{\mathrm{i}\omega_k t}\mathsf{c}\right),\end{aligned} \tag{7.1}$$

where a, b and c are the annihilation operators for cavities A and B and transmon C, respectively. ω_{a} and ω_{b} are the frequencies of the two cavities and ω_{c} corresponds to the frequency difference of the ground and first excited state of the transmon C. $\alpha_{\mathrm{c}} \ll \omega_{\mathrm{c}}$ describes the transmon's anharmonicity for higher level splittings. g_{a} and g_{b} describe the static coupling between cavities A and B and transmon C, respectively. Note that double exciting terms like $\mathsf{a}^\dagger\mathsf{c}^\dagger$ and $\mathsf{b}^\dagger\mathsf{c}^\dagger$ as well as double de-exciting terms like $\mathsf{a}\mathsf{c}$ and $\mathsf{b}\mathsf{c}$ have been neglected in $\mathsf{H}(t)$, i.e., a rotating wave approximation is taken into account. The last row in Eq. (7.1) describes the interaction of a set of continuous-wave (cw) control fields with transmon C, where Ω_k and ω_k describe the amplitude and frequency of field k, respectively. In addition, we take into account that each subsystem in the tripartite systems interacts with the environment — the latter gives rise to T_1 and T_2 decay processes, cf. Eq. (2.19), on each individual subsystem. The Lindblad operators and decay rates are respectively given by

$$\begin{aligned}
&\mathsf{L}_1^{\mathrm{a}} = \mathsf{a}, && \mathsf{L}_2^{\mathrm{a}} = \mathsf{a}^\dagger\mathsf{a}, && \Gamma_1^{\mathrm{a}} = \frac{1}{T_1^{\mathrm{a}}}, && \Gamma_2^{\mathrm{a}} = \frac{1}{T_2^{\mathrm{a}}}, \\
&\mathsf{L}_1^{\mathrm{b}} = \mathsf{b}, && \mathsf{L}_2^{\mathrm{b}} = \mathsf{b}^\dagger\mathsf{b}, && \Gamma_1^{\mathrm{b}} = \frac{1}{T_1^{\mathrm{b}}}, && \Gamma_2^{\mathrm{b}} = \frac{1}{T_2^{\mathrm{b}}}, \\
&\mathsf{L}_1^{\mathrm{c}} = \mathsf{c}, && \mathsf{L}_2^{\mathrm{c}} = \mathsf{c}^\dagger\mathsf{c}, && \Gamma_1^{\mathrm{c}} = \frac{1}{T_1^{\mathrm{c}}}, && \Gamma_2^{\mathrm{c}} = \frac{1}{T_2^{\mathrm{c}}},
\end{aligned} \tag{7.2}$$

The dynamics of this open quantum system is described by the standard Lindblad master equation (2.21). A sketch of this open tripartite system is given in Fig. 7.1.

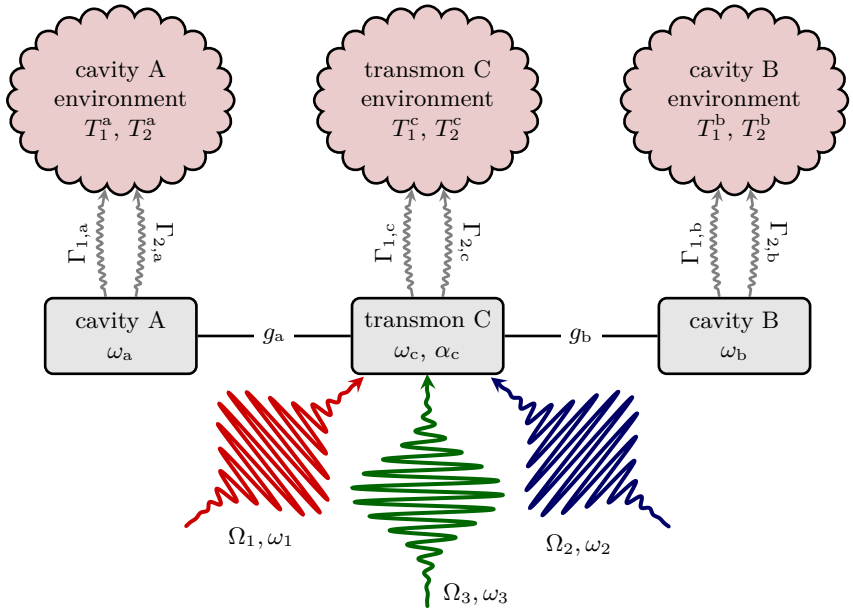

Figure 7.1: Sketch of the tripartite system consisting of two cavities, called A and B with frequencies ω_a and ω_b, respectively, and an intermediate transmon, called C with frequency ω_c and anharmonicity α_c. Cavities A and B are both coupled to transmon C with coupling strength g_a and g_b, respectively. The transmon is driven by a set of continuous-wave (cw) control fields, each with constant amplitude Ω_k and constant frequency ω_k. Each individual subsystem couples to its respective environment which causes it to suffer T_1 and T_2 decay, cf. Eq. (2.19)

Since we need to simulate the dynamics of the tripartite system described by Hamiltonian (7.1), it is advisable to avoid high frequencies like ω_a, ω_b and ω_c in the Hamiltonian. Thus, for the sake of numerical efficiency, it is favorable to change into the rotating frame via

$$\mathsf{H}'(t) = \mathsf{O}^\dagger(t)\mathsf{H}(t)\mathsf{O}(t) - \mathrm{i}\mathsf{O}(t)\frac{\mathrm{d}\mathsf{O}^\dagger}{\mathrm{d}t}, \tag{7.3}$$

where we choose the transformation operator to read

$$\mathsf{O}(t) = \exp\left\{-\mathrm{i}\left(\omega_a \mathsf{a}^\dagger\mathsf{a} + \omega_b \mathsf{b}^\dagger\mathsf{b} + \omega_c \mathsf{c}^\dagger\mathsf{c}\right)t\right\}. \tag{7.4}$$

In the rotating frame, the Hamiltonian becomes

$$\begin{aligned}\mathsf{H}'(t) = &-\frac{\alpha_c}{2}\mathsf{c}^\dagger\mathsf{c}^\dagger\mathsf{c}\mathsf{c} + g_a\left(e^{-\mathrm{i}(\omega_a-\omega_c)t}\mathsf{a}\mathsf{c}^\dagger + e^{\mathrm{i}(\omega_a-\omega_c)t}\mathsf{a}^\dagger\mathsf{c}\right) + g_b\left(e^{-\mathrm{i}(\omega_b-\omega_c)t}\mathsf{b}\mathsf{c}^\dagger + e^{\mathrm{i}(\omega_b-\omega_c)t}\mathsf{b}^\dagger\mathsf{c}\right)\\ &+ \sum_k\left(\Omega_k e^{-\mathrm{i}(\omega_k-\omega_c)t}\mathsf{c}^\dagger + \Omega_k^* e^{\mathrm{i}(\omega_k-\omega_c)t}\mathsf{c}\right).\end{aligned} \tag{7.5}$$

Note that although more terms are time-dependent in Eq. (7.5) than in Eq. (7.1), it should be stressed that only frequency differences like $\omega_a - \omega_b$ and similar differences appear in the rotating frame. The transformation from Hamiltonian (7.1) to Hamiltonian (7.5) does not involve any further approximation and is therefore a mere change of frame. Moreover, note that the dissipator in the Lindblad master equation (2.21) remains invariant under this transformation. The Lindblad operators (7.2) are therefore valid in both frames.

In view of encoding information in the two cavities and use them to build a quantum computer, an entangling operation needs to be realized between them. While this typically implies the choice of a specific entangling gate between two qubits, i.e., between two two-level systems, cf. Refs. [317, 318], here we are interested in an entangling operation between the two infinite dimensional cavities A and B. The advantage of such a slightly more general entangling operation in combination with the infinite dimensional Hilbert spaces of A and B is that it does not require any particular choice of how to encode qubits into these infinite dimensions. It therefore works with any encoding and thus with a large variety of error correction schemes that all require different choices of encoding. In order to realize an entangling operation between A and B, an interaction between A and B is required but needs to be mediated by the transmon C as the cavities do not couple directly to each other. In order to overcome this problem, Ref. [315] has shown that an effective beamsplitter interaction of the form

$$\mathsf{H}_{\mathrm{BS}}^{\mathsf{ab}}(t) = g_{\mathrm{BS}}(t)\mathsf{a}\mathsf{b}^\dagger + g_{\mathrm{BS}}^*(t)\mathsf{a}^\dagger\mathsf{b} \tag{7.6}$$

can be engineered between cavities A and B, i.e., on the reduced system of the two cavities. $g_{\mathrm{BS}}(t)$ corresponds to their effective interaction strength. Such an interaction can be realized by appropriately choosing two driving fields that interact exclusively with transmon C [315]. To this end, both fields need to be operated as cw fields, i.e., have constant amplitudes Ω_1 and Ω_2 as well as constant frequencies ω_1 and ω_2. In detail, the two frequencies of the cw fields need to fulfill [315]

$$\omega_b - \omega_a = \omega_2 - \omega_1. \tag{7.7}$$

Physically, this condition ensures conservation of energy when a photon is transferred between cavities A and B in the interaction process described by Eq. (7.6), since the energy difference of ω_a and ω_b is compensated by transferring photons between the two driving fields. It should be noted that — albeit neglected in the following — also other energy conserving photon transfers between cavities and driving fields are possible. These give rise to other types of interactions which are not of relevance for the following

discussion [316]. Unfortunately, satisfying Eq. (7.7) is not as straightforward in practice, since both cavities are Stark shifted individually due to the presence of the driving fields on transmon C. The strength of the individual Stark shift depends non-trivially on the cw fields' amplitudes Ω_1 and Ω_2 and on their frequencies ω_1 and ω_2 and causes an effective shift of ω_a and ω_b that needs to be corrected for by adapting ω_1 and ω_2 accordingly [316].

The control task that we will consider in the following is to accelerate the beamsplitter operation, i.e, how to increase the effective beamsplitter interaction $|g_\mathrm{BS}(t)|$ in Eq. (7.6). To this end, it should be noted that, although Ref. [315] technically already provides a solution, dissipation is still a problem in practice. Hence, achieving the same task faster minimizes the time in which the environment can compromise it. In order to explore whether we can accelerate the beamsplitter operation between the cavities, we take the two-drive protocol reported in Ref. [315] as a starting point for optimal control. However, in contrast to other control problems discussed in this thesis, this time we will not replace the analytical shapes of the two cw fields by optimized and thus time-dependent ones obtained with a gradient-based optimization technique like Krotov's method, cf. Subsec. 2.3.5. Instead, we will employ a gradient-free optimization technique and simply examine how the addition of a third cw field — with constant amplitude Ω_3 and frequency ω_3 — allows to increase the effective beamsplitter interaction $|g_\mathrm{BS}(t)|$. Hence, our primary control parameters are just Ω_3 and ω_3.

Unfortunately, there is no easy way to formulate an optimization functional that quantifies how well the dynamics within the reduced subsystem of cavities A and B behaves compared to the desired dynamics described by the beamsplitter Hamiltonian (7.6). Such a functional would in any case require information from all times $t_0 \leq t \leq T$ and can not be expressed via a specific figure of merit at final time T. However, note that a beamsplitter interaction of the form (7.6) will, at some point T, give rise to a swap of the cavity states, i.e., it will give rise to a dynamics like

$$\mathcal{D}^{\mathrm{ab}}_{T,t_0}\left[\rho_\mathrm{a}(t_0) \otimes \rho_\mathrm{b}(t_0)\right] = \rho_\mathrm{b}(t_0) \otimes \rho_\mathrm{a}(t_0) \tag{7.8}$$

within the reduced system of the two cavities, where $\rho_\mathrm{a}(T) = \rho_\mathrm{b}(t_0)$ and $\rho_\mathrm{b}(T) = \rho_\mathrm{a}(t_0)$ for any initial states $\rho_\mathrm{a}(t_0)$ and $\rho_\mathrm{b}(t_0)$ of cavities A and B. Although we can not easily optimize towards the effective beamsplitter Hamiltonian (7.6) that gives rise to this dynamics, we can optimize towards the swap operation (7.8) that such an effective interaction gives rise to. We ensure such an operation within the tripartite system either

by choosing the final-time functional to read

$$\mathcal{J}_T^{\mathrm{abc}}\left[\{\rho_l\},T\right] = 1 - \frac{1}{N_\mathrm{a}N_\mathrm{b}}\sum_{i_\mathrm{a}}\sum_{i_\mathrm{b}}\left\langle\!\!\left\langle |i_\mathrm{b},i_\mathrm{a}\rangle\langle i_\mathrm{b},i_\mathrm{a}|\otimes\rho(t_0)\middle|\mathcal{D}_{T,t_0}\left[|i_\mathrm{a},i_\mathrm{b}\rangle\langle i_\mathrm{a},i_\mathrm{b}|\otimes\rho_\mathrm{c}(t_0)\right]\right\rangle\!\!\right\rangle \tag{7.9a}$$

or

$$\mathcal{J}_T^{\mathrm{ab}}\left[\{\rho_l\},T\right] = 1 - \frac{1}{N_\mathrm{a}N_\mathrm{b}}\sum_{i_\mathrm{a}}\sum_{i_\mathrm{b}}\left\langle\!\!\left\langle |i_\mathrm{b},i_\mathrm{a}\rangle\langle i_\mathrm{b},i_\mathrm{a}|\middle|\mathrm{tr}_\mathrm{c}\left\{\mathcal{D}_{T,t_0}\left[|i_\mathrm{a},i_\mathrm{b}\rangle\langle i_\mathrm{a},i_\mathrm{b}|\otimes\rho_\mathrm{c}(t_0)\right]\right\}\right\rangle\!\!\right\rangle, \tag{7.9b}$$

where $\{|i_\mathrm{a}\rangle\}$ and $\{|i_\mathrm{b}\rangle\}$ are bases for Hilbert spaces $\mathcal{H}_\mathrm{a}$ and $\mathcal{H}_\mathrm{b}$ of cavity A and B, respectively. Note that we have used the short notation $|i_\mathrm{a},i_\mathrm{b}\rangle = |i_\mathrm{a}\rangle\otimes|i_\mathrm{b}\rangle$ to denote a state in $\mathcal{H}_\mathrm{a}\otimes\mathcal{H}_\mathrm{b}$. Note that N_a and N_b are the dimensions of the subspaces $\mathcal{H}_\mathrm{a}'\subset\mathcal{H}_\mathrm{a}$ and $\mathcal{H}_\mathrm{b}'\subset\mathcal{H}_\mathrm{b}$ within which functionals (7.9) measure the effect of the beamsplitter interaction. In fact, both functionals in Eq. (7.9) simply ensure that the swap, illustrated by Eq. (7.8), is realized at final time T for an entire basis of $\mathcal{H}_\mathrm{a}'\otimes\mathcal{H}_\mathrm{b}'$. However, while $\mathcal{J}_T^{\mathrm{abc}}$ ensures that, besides performing the swap, the initial state $\rho_\mathrm{c}(t_0)$ of the transmon is preserved at final time, $\mathcal{J}_T^{\mathrm{ab}}$ does not impose any condition on the transmon's final state except of it being uncorrelated with both cavities. At last, it should again be emphasized that both functionals, $\mathcal{J}_T^{\mathrm{abc}}$ and $\mathcal{J}_T^{\mathrm{ab}}$, optimize towards a specific target operation at final time T. From a mathematical perspective, this does not explicitly demand for a beamsplitter interaction like in Eq. (7.6) to emerge on the reduced system of the two cavities. However, it does so in practice, as we will see in Sec. 7.2.

We take physical parameters for the setting sketched in Fig. 7.1 from the experiment reported in Ref. [315]. The parameters are summarized in Table 7.1. As a remark regarding how some of these parameters have been obtained, it should be noted that for instance the direct coupling strengths g_a and g_b can not be directly measured in an experiment. However, they can be deduced from the experimentally accessible nonlinear couplings $\chi_\mathrm{ac} = \delta\omega_{\mathrm{a},1} - \delta\omega_{\mathrm{a},0}$ and $\chi_\mathrm{bc} = \delta\omega_{\mathrm{b},1} - \delta\omega_{\mathrm{b},0}$ between cavities A and B and transmon C, respectively. These are given via the transmon-induced frequency shifts [316]

$$\delta\omega_{\mathrm{k},m} = |g_\mathrm{k}|^2\frac{\delta_\mathrm{k}-\alpha_\mathrm{c}}{(\delta_\mathrm{k}-m\alpha_\mathrm{c})\left(\delta_\mathrm{k}-(m-1)\alpha_\mathrm{c}\right)}, \qquad \mathrm{k}=\mathrm{a},\mathrm{b}. \tag{7.10}$$

If these are known, the static couplings can be calculated by

$$g_\mathrm{a} = \delta_\mathrm{a}\sqrt{\frac{\chi_\mathrm{ac}}{2\alpha_\mathrm{c}}\frac{\delta_\mathrm{a}+\alpha_\mathrm{c}}{\delta_\mathrm{a}}}, \qquad g_\mathrm{b} = \delta_\mathrm{b}\sqrt{\frac{\chi_\mathrm{bc}}{2\alpha_\mathrm{c}}\frac{\delta_\mathrm{b}+\alpha_\mathrm{c}}{\delta_\mathrm{b}}}. \tag{7.11}$$

frequency cavity A	$\omega_\mathrm{a}/2\pi$	5.554 GHz
frequency cavity B	$\omega_\mathrm{b}/2\pi$	6.543 GHz
base frequency transmon C	$\omega_\mathrm{c}/2\pi$	5.901 GHz
anharmonicity transmon C	$\alpha_\mathrm{c}/2\pi$	74 MHz
coupling between cavity A and transmon C	$g_\mathrm{a}/2\pi$	−19.921 MHz
coupling between cavity B and transmon C	$g_\mathrm{b}/2\pi$	28.417 MHz
intensity driving field 1	$\Omega_1/2\pi$	94.200 MHz
intensity driving field 2	$\Omega_2/2\pi$	229.725 MHz
intensity driving field 3	$\Omega_3/2\pi$	271.093 MHz
frequency driving field 1	$\omega_1/2\pi$	6.058 MHz
frequency driving field 2	$\omega_2/2\pi$	7.049 624 MHz
frequency driving field 3	$\omega_3/2\pi$	6.749 MHz
relaxation of cavity A	T_1^a	500 µs
relaxation of cavity B	T_1^b	500 µs
relaxation of transmon C	T_1^c	50 µs
dephasing of cavity A	T_2^a	500 µs
dephasing of cavity B	T_2^b	500 µs
dephasing of transmon C	T_2^c	15 µs

Table 7.1: Parameters for the tripartite system of cavity A and B and transmon C as reported in Ref. [315]. Note that the coupling strength g_a and g_b and intensities Ω_1 and Ω_2 have been calculated from other experimentally measurable quantities. The third control field and its parameters Ω_3 and ω_3 are not contained in Ref. [315]. They reflect the optimization results from this chapter and are added for completeness.

The intensities of the cw fields are given by $\Omega_k = \delta_k \xi_k$ with ξ_k denoting the effective driving strength of field k. In both definitions, we have used $\delta_x = \omega_x - \omega_\mathrm{c}$ with $x \in \{\mathrm{a}, \mathrm{b}, 1, 2\}$ to indicate the corresponding detuning with respect to ω_c. In Ref. [315], the effective nonlinear couplings are given by $\chi_\mathrm{ac}/2\pi = 0.62\,\mathrm{MHz}$ and $\chi_\mathrm{bc}/2\pi = 0.26\,\mathrm{MHz}$. The effective driving strengths are chosen as $\xi_1 = 0.6$ and $\xi_2 = 0.2$ in accordance with typical values reported in Ref. [315]. These values give rise to the parameters in Table 7.1.

7.2 Increasing the Beamsplitter Interaction

We start the discussion by first inspecting the two-drive protocol proposed in Ref. [315]. To this end, it is important to note that the required resonance condition (7.7) needs to be fulfilled very accurately, since already small deviations therein can cause significant deviations from the intended effective beamsplitter interaction (7.6). Nevertheless, with the parameters from Table 7.1, which already account for the Stark shifts of cavity frequencies ω_a and ω_b, an effective beamsplitter interaction is generated between cavities

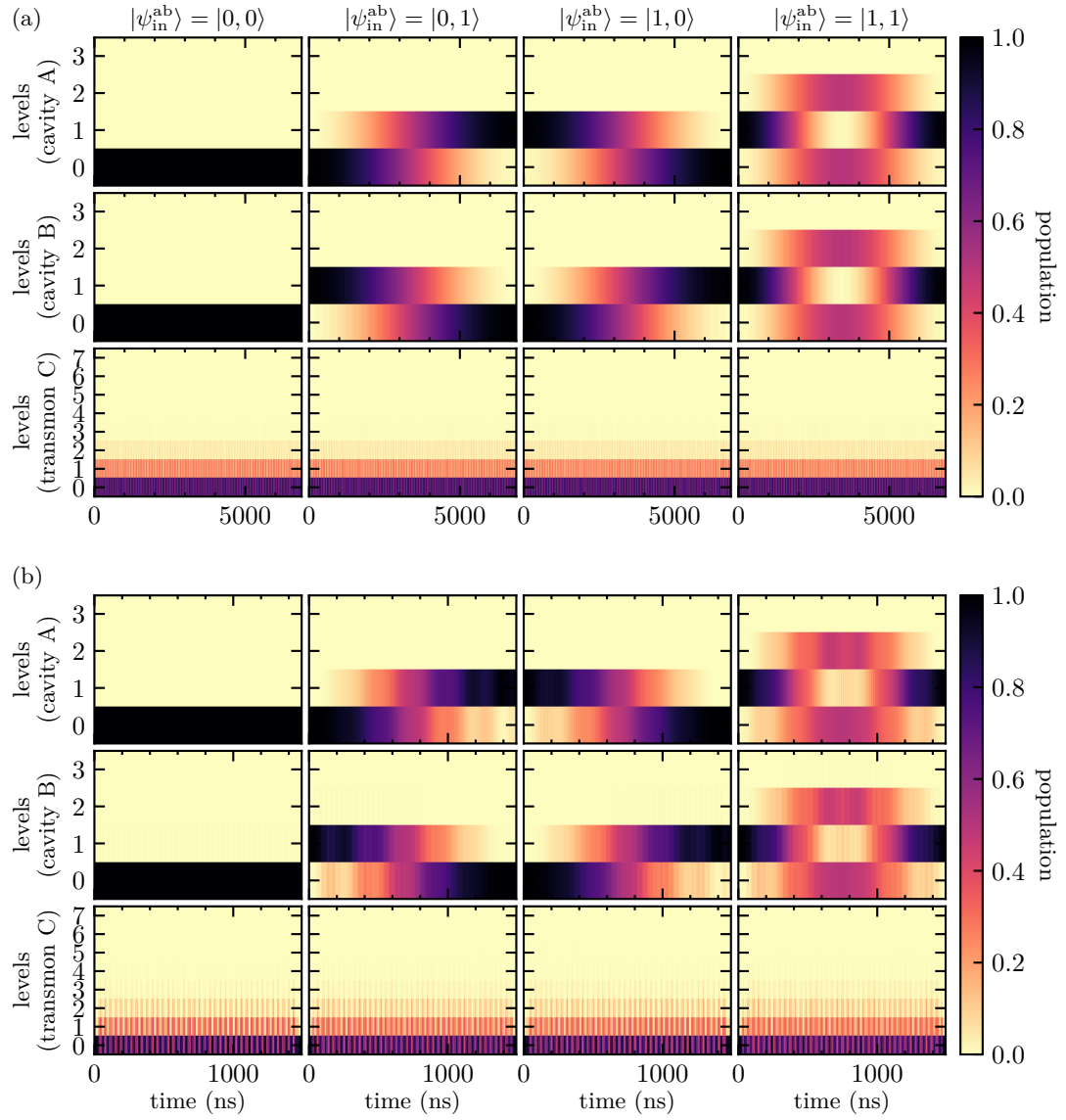

Figure 7.2: Population dynamics of the tripartite system of cavities A and B and transmon C. The initial state is $|\psi_{\text{in}}\rangle(t_0) = |\psi_{\text{in}}^{\text{ab}}\rangle \otimes |0\rangle$, where $|\psi_{\text{in}}^{\text{ab}}\rangle$ is given as indicated at the top of each column. Panel (a) shows the population dynamics for the original two-drive protocol as proposed in Ref. [315] based on two cw fields and the parameters as presented in Table 7.1 and a protocol duration of $T = 6780\,\text{ns}$. Panel (b) shows the optimized protocol extended by a third cw field characterized by $\Omega_3/2\pi = 271.093\,\text{MHz}$ and $\omega_3/2\pi = 6.749\,\text{GHz}$ and a protocol duration of $T \approx 1492\,\text{ns}$.

A and B. This can be confirmed by inspecting the population dynamics of Fig. 7.2(a). It shows the population dynamics in the full tripartite system when starting in different states from the subspace $\{|0,0\rangle, |0,1\rangle, |1,0\rangle, |1,1\rangle\}$ of the two cavities and with the transmon

in $|0\rangle$, i.e., the initial state of the tripartite system is given by $|\psi_{\text{in}}(t_0)\rangle = |\psi_{\text{in}}^{\text{ab}}\rangle \otimes |0\rangle$. As can be seen, the engineered interaction between both cavities yields an effective swap of populations at time $T = 6780\,\text{ns}$, i.e., it maps the initial state of the two cavities from $|\psi_{\text{in}}^{\text{ab}}\rangle = |i,j\rangle$ to $|j,i\rangle$ and therefore follows the desired dynamics (7.8). However, at intermediate times, the population dynamics is more complex and it partially drives the population out of the initial subspace $\{|0,0\rangle, |0,1\rangle, |1,0\rangle, |1,1\rangle\}$. This effect becomes even pronounced when considering cavity states with higher initial excitations. Nevertheless, such a beamsplitter interaction gives rise to a swap gate at final time T but realizes an entangling gate intermediately at $T/2$.

There are two important things to notice regarding the two-drive protocol of Ref. [315]. On the one hand, it requires the two cw fields to be switched on and off smoothly in the beginning and end of the protocol. In the current scenario, this is more than just an experimental requirement, as it ensures a smooth transition from the transmon's initial ground state $\rho_{\text{c}}(t_0) = |0\rangle\langle 0|$ to a low-energy Floquet state in which the transmon remains during the protocol and a smooth transition back at final time T. The protocol's success depends on the transmon being in the Floquet state at intermediate times [316]. On the other hand, this also ensures that the transmon is only virtually populated during the protocol and always remains close to its absolute ground state, cf. the lower row in Fig. 7.2(a). This is favorable, since it naturally minimizes the dissipation's impact, which affects the transmon the most, cf. Table 7.1, and ensures that the transmon stays uncorrelated with either of the two cavities at all times. From a physical perspective, this also tells us that $\mathcal{J}_T^{\text{abc}}$ is favorable over $\mathcal{J}_T^{\text{ab}}$, as the latter would not necessarily ensure that the transmon is brought back to its ground state at final time T. We will therefore use $\mathcal{J}_T^{\text{abc}}$ in the following.

If we take the subspace $\{|0,0\rangle, |0,1\rangle, |1,0\rangle, |1,1\rangle\}$ of cavities A and B as our logical two qubit subspace in which we want to perform computations, we can evaluate $\mathcal{J}_T^{\text{abc}}$ for the dynamics shown in Fig. 7.2(a) to yield an error of

$$\mathcal{J}_{T,\text{diss}}^{2,\text{abc}} = 2.27\%, \qquad \mathcal{J}_{T,\text{nodiss}}^{2,\text{abc}} = 0.85\% \tag{7.12}$$

in the case with and without dissipation, respectively. The superscript 2 indicates values for the two-drive protocol. Furthermore note that the dynamics presented in Fig. 7.2(a) is without dissipation. The dynamics including dissipation is visually identical and is therefore not present here. Taking into account the physical errors from Eq. (7.12), the challenge for optimal control is to find a three-drive protocol, which is significantly faster than $T = 6780\,\text{ns}$ and still yields an error below $\mathcal{J}_{T,\text{diss}}^{2,\text{abc}}$.

In the following, we use the gradient-free Nelder-Mead optimization method [67] and take the amplitude and frequency, Ω_3 and ω_3, of a third cw field together with the final time T as optimization parameters. Note that, albeit possible, we do not optimize the parameters of the first two drives. For the sake of numerical efficiency, the optimization has been conducted in Hilbert space, i.e., without explicitly accounting for dissipation. This is justified, since we already know that the dissipation acts purely detrimental and we just need to be sufficiently fast to minimize its influence. Hence, in a first step, the optimization needs to find a coherent error $\mathcal{J}_{T,\text{nodiss}}^{3,\text{abc}}$ for the three-drive protocol that is smaller than the dissipative error $\mathcal{J}_{T,\text{diss}}^{2,\text{abc}}$ of the two-drive protocol. Employing optimal control, we find that including the third drive allows to reach a coherent error $\mathcal{J}_{T,\text{nodiss}}^{3,\text{abc}}$ that — albeit not lower — is at least comparable to $\mathcal{J}_{T,\text{diss}}^{2,\text{abc}}$ but reaches it in significant less time. The corresponding parameters are given by $\Omega_3/2\pi = 271.093\,\text{MHz}$ and $\omega_3/2\pi = 6.749\,\text{GHz}$, while the final time becomes $T \approx 1492\,\text{ns}$. We find the errors of the three-drive protocol to read

$$\mathcal{J}_{T,\text{diss}}^{3,\text{abc}} = 2.67\%, \qquad \mathcal{J}_{T,\text{nodiss}}^{3,\text{abc}} = 2.27\%. \tag{7.13}$$

Note that although we have not explicitly accounted for dissipation, we have still accounted for it implicitly by suppressing population of highly excited transmon levels, for which we know that they are prone to dissipation. This has been achieved by deliberately adding imaginary energies to these higher levels such that any state looses norm proportional to the amount of population in theses levels. Since any loss of norm in any propagated state is equivalent to an increase of the final-time functional $\mathcal{J}_T$, this effectively penalizes highly excited transmon states and causes the optimization to search preferably for solution where only lower levels are populated.

In the following, we compare the errors under the three-drive protocol, cf. Eq. (7.13), to the ones from the two-drive protocol, cf. Eq. (7.12). On the one hand, the experimentally relevant errors $\mathcal{J}_{T,\text{diss}}^{2,\text{abc}}$ and $\mathcal{J}_{T,\text{diss}}^{3,\text{abc}}$ show that both protocols yield very similar errors overall. However, the three-drive protocol still achieves the same target 4.54 times faster than the two-drive protocol. On the other hand, the results also show that the environment's detrimental impact can be significantly minimized by decreasing the protocol duration. This is evidenced by a rather small increase from $\mathcal{J}_{T,\text{nodiss}}^{3,\text{abc}}$ to $\mathcal{J}_{T,\text{diss}}^{3,\text{abc}}$ in case of the three-drive protocol, which needs to be compared to the corresponding errors under the two-drive protocol that reveal a more severe increase. The population dynamics for the tripartite system in case of the optimized and faster three-drive protocol is shown in Fig. 7.2(b). Most importantly, it shows that the dynamics under the optimized

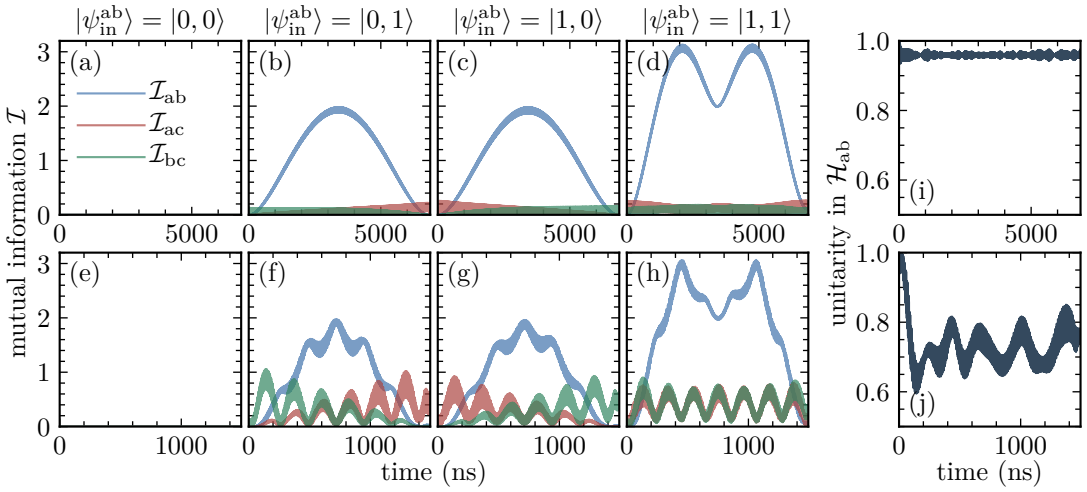

Figure 7.3: The mutual information $\mathcal{I}_{\text{ab}}$, $\mathcal{I}_{\text{ac}}$ and $\mathcal{I}_{\text{bc}}$, i.e., the correlation between the corresponding subsystems, under the two-drive protocol (panels (a-d)) and under the optimized three-drive protocol (panels (e-h)). Each column corresponds to a different initial state $|\psi_{\text{in}}^{\text{ab}}\rangle$ of the two cavities. Panels (i) and (j) show a measure of unitarity for the subspace of the two cavities for the two-drive and three-drive protocol, respectively.

three-drive protocol strongly resembles the dynamics of the original two-drive protocol in structure. Nevertheless, it also shows that the observed speedup comes at the expense of this structure being a slightly more "messy" version of the one from original two-drive protocol presented in Fig. 7.2(a).

There are several factors that are relevant to explain these differences. The last row of Fig. 7.2(b) shows that the three-drive protocol gives rise to slightly more population in higher transmon levels compared to the two-drive protocol. In order to quantify this, a convenient indicator that compresses various information into a single quantity is the mutual information, cf. Eq (5.29), between transmon C and both cavities, respectively. The rationale with respect to the transmon's ground state population is that if the transmon would remain perfectly in its ground state, it would at no time correlate with the cavities and the mutual information would always vanish. In general, finite mutual information between transmon and cavities indicates a deviation from an ideal operation, since the transmon should at best only mediate the coupling between cavities A and B and at no time correlate with any of them. Let $\mathcal{I}_{\text{ab}}, \mathcal{I}_{\text{ac}}$ and $\mathcal{I}_{\text{bc}}$ denote the mutual information between the respective subsystems. Figure 7.3(a-d) and (e-h) show the dynamics of the mutual information for the two- and three-drive protocol, respectively. Similar to the population dynamics, it can be observed that the correlations between cavities A and B follow roughly the same shape in both protocols — albeit the three-drive protocol

can again be interpreted as a slightly less structured version of the two-drive protocol. However, the important difference between the two protocols lies in their correlations between the transmon and both cavities, i.e., $\mathcal{I}_{\mathrm{ac}}$ and $\mathcal{I}_{\mathrm{bc}}$. While only cavities A and B become directly correlated in the two-drive protocol and both are at no time correlated with transmon C, the latter changes in the three-drive protocol, where both cavities show significant correlations with the transmon at intermediate times. The correlations between transmon and cavities A and B furthermore imply that the subsystem of the latter does not evolve unitarily anymore. Figure 7.3(i) and (j) confirm this by showing a measure of unitarity in the subspace $\mathcal{H}_{\mathrm{ab}} = \mathcal{H}_{\mathrm{a}} \otimes \mathcal{H}_{\mathrm{b}}$ of the two cavities within the joint total Hilbert space $\mathcal{H} = \mathcal{H}_{\mathrm{a}} \otimes \mathcal{H}_{\mathrm{b}} \otimes \mathcal{H}_{\mathrm{c}}$. Such a measure is given by Eq. (4.6), which has originally been defined to enable the search for decoherence-free subspaces. While for the two-drive protocol this measure, shown in panel (i), confirms an almost unitary dynamics within $\mathcal{H}_{\mathrm{ab}}$, panel (j) proves the strong non-unitary nature within $\mathcal{H}_{\mathrm{ab}}$ under the three-drive protocol.

Interestingly, the strong differences between the almost unitary evolution within $\mathcal{H}_{\mathrm{ab}}$ in case of the original two-drive protocol and its apparently strongly non-unitary counterpart under the optimized three-drive protocol, evidenced by Fig. 7.3(i) and (j), are not as strongly pronounced in their corresponding population dynamics shown in Fig. 7.2. In the following, we will therefore inspect the dynamics within the relevant subspace $\mathcal{H}_{\mathrm{ab}}$ in detail. To this end, we represent the reduced state $\rho_{\mathrm{ab}}(t) = \mathrm{tr}_{\mathrm{c}}\{\mathcal{D}_{t,t_0}[\rho(t_0)]\}$ of the two cavities by its generalized Bloch vector $\boldsymbol{r}(t) = (r_1(t), \ldots, r_{M^2-1}(t))^{\top}$, cf. Eq. (3.8). We take the generalized Gell-Mann matrices $\{\mathsf{A}_i\}$, $i = 1, \ldots, M^2 - 1$, to expand $\rho_{\mathrm{ab}}(t)$ such that each component of the generalized Bloch vector is given by $r_i(t) = \langle\!\langle \rho_{\mathrm{ab}}(t) | \mathsf{A}_i \rangle\!\rangle$ [109]. M is thereby the dimension of $\mathcal{H}_{\mathrm{ab}}$, which, for the numerical simulations presented so far, is given by $M = 16$. Hence, the generalized Bloch vector $\boldsymbol{r}(t)$ has $16^2 - 1 = 255$ components. Despite this large number of components $r_1(t), \ldots, r_{255}(t)$, we observe that, for the dynamics shown in Fig. 7.2, many of these components are constant or almost constant and only a small fraction shows a significant time-dependence. Thus, in order to ease the discussion, we will only focus on these relevant components and ignore all remaining ones. Note that the actual Gell-Mann matrix A_i, to which each of theses relevant component $r_i(t)$ corresponds to, will also not be discussed as it is not of importance.

The solid lines in Fig. 7.4(a-c) show the dynamics of the relevant components under the original two-drive protocol for the initial states $|\psi_{\mathrm{in}}^{\mathrm{ab}}\rangle \in \{|0,1\rangle, |1,0\rangle, |1,1\rangle\}$, respectively. The initial state $|\psi_{\mathrm{in}}^{\mathrm{ab}}\rangle = |0,0\rangle$ is omitted, since it does not show any significant dynamics. Figure 7.4(d-f) show the same components but for the optimized three-drive protocol. As

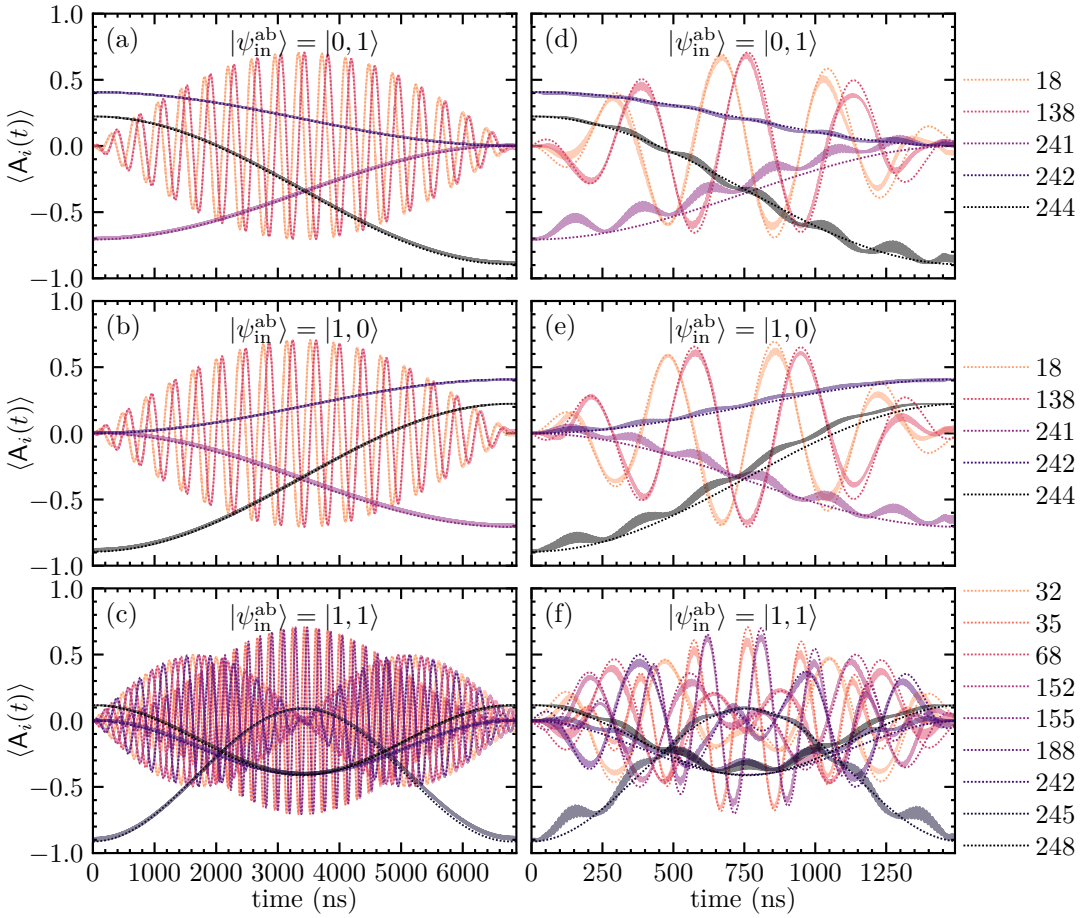

Figure 7.4: Bloch vector trajectories for the reduced state $\rho_{\text{ab}}(t) = \text{tr}_{\text{c}}\{\mathcal{D}_{t,t_0}[\rho(t_0)]\}$ of cavities A and B. Note that only those components $r_i(t) = \langle \mathsf{A}_i(t) \rangle \langle\langle \rho_{\text{ab}}(t) | \mathsf{A}_i \rangle\rangle$ are depicted that show a significant change over time and where it can thus be expected that their origin is intimately connected to the engineered beamsplitter interaction. The labels i for each row specify which are relevant components $r_i(t)$ for that particular initial state $|\psi_{\text{in}}^{\text{ab}}\rangle$. The solid lines correspond to the Bloch vector trajectory of $\rho_{\text{ab}}(t)$ obtained from the dynamics in Fig. 7.2. In contrast, the dotted lines describe the Bloch vector trajectories obtained from the dynamics with the effective Hamiltonian $\mathsf{H}_{\text{eff}}^{\text{ab}}(t)$, cf. Eq. (7.14). Panels (a-c) show the trajectories for the original two-drive protocol while panels (d-e) correspond to the optimized three-drive case.

can be seen from a comparison of Fig. 7.4(a-c) and (d-f), all slowly varying components, for instance like $r_{241}(t), r_{242}(t)$ and $r_{244}(t)$ in panels (a) and (d), follow the same temporal structure in case of the two- and three-drive protocol. The three-drive protocol again gives rise to a slightly more messy version compared to the two-drive protocol. In contrast, the rapidly oscillating components, for instance like $r_{18}(t)$ and $r_{138}(t)$ in panels (a) and (d), only show the same outer shape while their rapid oscillations differ. Nevertheless, the general similarity of the Bloch vector's trajectory in case of the two- and three-drive

protocol confirms that the latter protocol is, as intended, just an accelerated version of the original two-drive protocol.

In order to explain the differences and similarities observed in Fig. 7.4, we want to find an effective description of the dynamics within the subspace $\mathcal{H}_{\mathrm{ab}}$. In detail, we want to find an effective Hamiltonian $\mathsf{H}_{\mathrm{eff}}^{\mathrm{ab}}(t)$ that gives rise to the same Bloch sphere dynamics as shown in Fig. 7.4(a-c) and (d-f) for the two- and three-drive protocol, respectively. Unfortunately, there is no simple procedure to derive such an effective Hamiltonian analytically from the full Hamiltonian (7.1). However, we can still obtain it numerically by means of physical intuition in combination with parameter fitting. We find such an effective Hamiltonian for the reduced system of the two cavities to read

$$\mathsf{H}_{\mathrm{eff}}^{\mathrm{ab}}(t) = -g_{\mathrm{BS}}\left(e^{-\mathrm{i}\omega_{\mathrm{s}}t}\mathsf{a}\mathsf{b}^{\dagger} + e^{\mathrm{i}\omega_{\mathrm{s}}t}\mathsf{a}^{\dagger}\mathsf{b}\right) - \frac{\omega_{\mathrm{s}}}{2}\left(\mathsf{a}^{\dagger}\mathsf{a} - \mathsf{b}^{\dagger}\mathsf{b}\right). \tag{7.14}$$

For the original two-drive protocol, we find the two parameters of the effective Hamiltonian to be given by $g_{\mathrm{BS}}/2\pi = 36.9\,\mathrm{kHz}$ and $\omega_{\mathrm{s}}/2\pi = 2.625\,\mathrm{MHz}$, while for the optimized three-drive protocol, the two parameters are $g_{\mathrm{BS}}/2\pi = 165\,\mathrm{kHz}$ and $\omega_{\mathrm{s}}/2\pi = 2.625\,\mathrm{MHz}$. Hamiltonian $\mathsf{H}_{\mathrm{eff}}^{\mathrm{ab}}(t)$ gives rise to the dynamics indicated by the dotted lines in Fig. 7.4 and therefore describes the solid lines, obtained from numerical simulation with the tripartite system, very well. Hence, we indeed find the beamsplitter Hamiltonian (7.6) to be an accurate description of the reduced dynamics of the two cavities — both for the original two-drive protocol as well as for the optimized three-drive protocol. We also observe that the effective beamsplitter interaction g_{BS} is indeed larger for the optimized three-drive protocol. It increases by a factor of 4.47, which roughly matches the decrease in protocol duration (factor of 4.54), cf. Fig. 7.2. It should be furthermore noted that the rapidly oscillating components in Fig. 7.4 can be reproduced by the same frequency $\omega_{\mathrm{s}}/2\pi = 2.625\,\mathrm{MHz}$ in both protocols. Interestingly, this frequency exactly matches the relative Stark shifts of cavities A and B, i.e., of ω_{a} and ω_{b}, in the original two-drive protocol. This relative Stark shift can be calculated from the parameters of Table 7.1 via

$$(\omega_2 - \omega_1) - (\omega_b - \omega_a) = 2.625\,\mathrm{MHz}. \tag{7.15}$$

The fact that ω_{s} is identical for the two- and three-drive protocol is not obvious at all. Since the third cw drive in the latter case should in principle give rise to different individual Stark shifts of ω_{a} and ω_{b}, there is theoretically no need for the optimization to maintain a relative Stark shift of 2.625 MHz between both cavities.

At last, it should be noted that, although the optimized three-drive protocol is not directly able to yield errors that are smaller than the ones from the two-drive protocol, it

still achieves comparable errors on a much faster time scale. Thus, by taking the cw fields from three-drive protocol as guess fields in a subsequent gradient-based optimization, it should be straightforward to achieve errors that are even lower than the ones from the two-drive protocol — both on a much faster time scale and with experimentally feasible control fields.

To summarize, in this chapter we have replaced the two-drive protocol proposed in Ref. [315], designed to realize an effective beamsplitter interaction between two cavities, by an optimized three-drive protocol. The latter protocol is capable of increasing the effective beamsplitter interaction between the cavities, hence accelerating the implementation of an entangling gate, while keeping the gate error at a similar level. We have moreover derived an effective Hamiltonian that accurately describes the dynamics of the two cavities under the two- and three-drive protocol.

8

Conclusions and Outlook

In this thesis, we have presented a new perspective on how to efficiently and reliably control open quantum systems. We have not only focused on cases where the environment's impact is detrimental but also on cases where the environment can assist or is even necessary for the task's feasibility. We have analyzed and improved, in the presence of dissipation, various tasks that are vital in many quantum technologies.

In order to utilize optimal control techniques in combination with open quantum systems, it is crucial to employ reliable measures, i.e., optimization functionals that correctly asses the success of the intended control task. In Chap. 3, we have therefore outlined mathematical conditions that every reliable optimization functional needs to fulfill. We have furthermore illustrated the failure of common optimization functionals based on state overlaps as indicators for the closeness of states. These violate the conditions for reliable optimization functionals once the states become mixed. This poses a severe problem when optimizing towards a mixed target state. However, even when restricting our analysis to mathematically reliable functionals, like Eqs. (6.2)-(3.14), we have found only the Hilbert-Schmidt distance to be compatible with gradient-based optimization techniques. Since it is beneficial for optimal control to have multiple optimization functionals available, we have therefore employed the geometric picture derived from the Bloch sphere to construct an entirely new distance measure between states. This new measure allows for quantifying dissipative and coherent mismatches, i.e., mismatches in the length or angles of two Bloch vectors, individually. Besides being

reliable, it has been designed to be compatible with gradient-based optimal control techniques and thus naturally extends the set of available optimization functionals. We have successfully utilized this new measure in an optimization with the goal to accelerate the preparation of a mixed squeezed state in an optomechanical system. By suitably shaping the control fields, we have achieved a speedup of at least two orders of magnitude for the state preparation while the control fields remain simple and experimentally feasible. A future study should nevertheless relax the hitherto used requirement to optimize for a particular squeezed target state and replace it by an optimization of the squeezing strength itself. This would not only allow to determine the ultimate limit of the achievable squeezing, but also answer if the trade-off between the target state's squeezing strength and its purity is a property of considered optomechanical setup or the specific protocol proposed in Ref. [134]. It would also allow to determine whether large squeezing can also be generated at higher purities.

For the particular example of optimizing the dynamics in an optomechanical system, the introduced measure has not performed better than the Hilbert-Schmidt distance. Nevertheless, it still provides more information due to its separation of dissipative and coherent state mismatches, which therefore allows for quantifying the origin of the mismatch much better — namely whether the optimization has problems to match a Bloch vector's length or angles with a given target state. If we take this one step further, it might even allow to quantify individual quantum speed limits for the dissipative and coherent part of the evolution. This is based on the idea that quantum speed limits are often estimated via a distance measure between an initial and target state in combination with an estimated speed for the evolution between those states [250, 319–322]. If combined with an effective dissipative and coherent speed for the evolution, the newly constructed measure would allow to create individual speed limits and allow to determine which of these sets the overall speed limit.

Besides the construction of this new distance measure, the results presented in Chap. 4 have furthermore extended the tools available for optimal control of open quantum systems. While quantum optimal control largely focuses on methods for deriving time-dependent control fields that steer a quantum system in a desired way, we have explored a conceptually new direction by employing optimal control methods to search for decoherence-free subspaces (DFSs). To this end, we have first formulated a functional that reliably identifies DFSs and which, by construction, allows for calculating analytical derivatives of this functional with respect to the basis states from that subspace. Secondly, we have introduced an efficient way to parametrize arbitrary subspaces via their basis elements such that the latter maintain their norm and orthogonality even when allowing an op-

timization algorithm to change any parameter. In combination, this has enabled us to employ a gradient-based optimization technique to search for DFSs. We have successfully identified DFSs — previously known ones as well as a completely new one — in a network of qubits.

Since we have constructed the parametrization to work for arbitrary subspaces, it can be readily used to search for subspaces other than just DFSs. Such an adaption of the method is straightforward as it simply requires to apply the same optimization procedure but employing optimization functionals specifically constructed for subspaces other than DFSs. In Sec. 4.5, we have outlined how such functionals might look for different scenarios. The successful demonstration employing DFSs can thus be regarded as a proof of principle of what optimal control is capable of in terms of identifying specific subspaces. It should be emphasized that a potential extension of the presented method would consist in combining the search towards specific subspaces with a second optimization loop for the dynamics itself, for instance by adding time-dependent control fields to the Hamiltonian. This would allow to answer two questions at the same time: How does the subspaces look like and how do the corresponding control fields need to be chosen in order to generate the desired dynamics within this subspace.

After having established new concepts to tackle optimal control problems in open quantum systems in Chaps. 3 and 4, we have turned towards applying optimal control in order to improve the reset of qubits in Chap. 5. This is one of the most fundamental tasks in any quantum technology. The challenge for this particular task is to find a strategy that, on the one hand, bears in mind that the qubit's environment is a fundamental necessity that allows purification in the first place. On the other hand, it needs to allow for sufficient control over the environmental interaction such that, at best, it can be switched on and off on-demand when needed. To this end, we have considered two promising approaches to ensure on-demand qubit reset — one utilizing a tunable environment and one where the environment is effectively given by a single, strongly coupled ancilla mode.

In the first scenario, a qubit is tunably coupled to a cold environment via two intermediate harmonic oscillators. The tunable coupling originates from the feasibility to increase the qubit's effective interaction with the cold environment on-demand by orders of magnitude just by appropriately steering the setup via time-dependent control fields. Starting from an analytical control scheme proposed in Ref. [213], we have successfully improved the reset protocol in time and fidelity by exchanging the analytical control fields by optimized ones. The control strategy leading to this improvements exploits a unique feature of this setup — the fact that not only the coherent part of the dynamics is controllable via the control fields but also the dynamics's dissipative part becomes

time-dependent and thus indirectly controllable. A unique reset strategy has been identified to consist (i) in maximizing the decay rate from one of theses channels and (ii) in engineering non-adiabatic transitions that drive the population into this heavily decaying channel. Interestingly, this has remained to be the only strategy identified by optimal control even when switching between various combinations of conceivable control fields. Since the achievable fidelity of the reset protocol as function of the reset duration is similar in all cases, we believe to have identified the quantum speed limit for this physical setup. The observed interplay of coherent and dissipative dynamics suggests that even more advanced reset strategies might be possible when extending the system's Hilbert space and explicitly accounting for highly excited states that would naturally not become populated. Although this might appear counter-intuitive for the intended qubit reset, higher excitations typically imply larger decay rates and thus might allow for a shortcut to reshuffle population into the qubit's ground state.

In the second scenario, we have considered a qubit within a structured environment given by a single, strongly coupled two-level ancilla and a remaining, weakly coupled reservoir. By employing optimal control, we have demonstrated that an effective interaction between qubit and ancilla can be established on-demand by means of a control field that exclusively interacts with the qubit. This on-demand interaction can be exploited for efficient qubit reset. We have demonstrated that it allows to reset the qubit to purities that exceed those of its steady state — which it would otherwise assume due to continuous but slow thermalization with the environment. This setup therefore allows for significantly faster and more efficient qubit reset. The reachable qubit purity is thereby only limited by the ancilla's initial purity. We have derived the corresponding reset strategy, which is always given by a control field that puts qubit and ancilla in resonance. This strategy, besides being time-optimal and very robust with respect to inaccuracies in the control field, is also independent on the qubit's initial state, provided qubit and ancilla are initially factorized. In the presence of initial correlation, i.e., when the qubit is initially correlated with the ancilla and thus with its environment, we have shown that the reset can be improved even further — both in time and fidelity. We have derived a simple geometric model that readily explains the limits in time and purity in case of factorizing initial conditions and why initial correlations allow to overcome both limits. These results suggest to actively exploit system-environment correlations as a resource instead of viewing them as a mere nuisance.

Moreover, we have revealed an interesting dependence of this reset strategy on the actual type of local control on the qubit and its interaction with the ancilla. The Cartan decomposition of SU(4), i.e., of all conceivable unitary evolutions of the joint qubit-ancilla

system, has enabled us to formulate fundamental requirements that the dynamics of the joint qubit-ancilla system needs to fulfill in order to allow qubit purification in the first place. Whether these requirements are fulfilled can already be determined on the level of the qubit-ancilla Hamiltonian and does not require any knowledge about the dynamics. While we have identified those combinations of local qubit control and qubit-ancilla interaction that do not fulfill the requirements and therefore do not allow for qubit reset, we have also derived the time-optimal reset protocol for all combinations that do fulfill the requirements. We have proven that the time-optimal reset strategy remains to establish resonance between qubit and ancilla via the control field. A swap of purities remains the best in terms of fidelity, considering factorizing initial conditions. Interestingly, we have demonstrated that, despite all these similarities in the reset strategy, the time-optimal protocol differs substantially in time between various combinations of local qubit control and qubit-ancilla interaction. We have derived a simple, analytical model that accurately predicts the protocol duration for all combinations. Our results therefore reveal the fundamental limits for qubit reset if a two-level ancilla is employed as entropy dump.

When allowing for higher dimensional ancillas, we have moreover shown that the maximally achievable qubit purity increases beyond a simple swap of purities. It starts to depend, in addition to the ancilla's initial state, on the ancilla's dimension. It would therefore be interesting to examine whether the conditions derived from the Cartan decomposition of SU(4) can be transferred and generalized — to some extent — to this more complex situation. In general, our results emphasize that special care needs to be taken when designing qubit architectures. This is relevant, since many quantum information platforms, like superconducting qubits, allow for engineering of control mechanisms on qubits and interactions between them with great flexibility and, as we have demonstrated, tasks like qubit reset depend strongly on the right choice.

While qubit reset has been one particular example where an environment is vital for the success of the control task, in the remainder of this thesis we have considered two other control tasks where the environment becomes purely detrimental. In Chap. 6, we have examined how optimized control fields can assist in diminishing the environment's impact on quantum discrimination. To this end, we have considered the task to distinguish two states which evolve under slightly different Hamiltonians — a task that is fundamental in quantum metrology. Under ideal conditions, the Ramsey scheme is a time-optimal protocol to reliably distinguish any two states evolving under different Hamiltonians. However, under realistic conditions where the quantum devices are exposed to dissipation, this does no longer hold. Employing optimal control, we have derived optimized control fields that allow for improving the distinguishability between the two states with respect

to what the Ramsey scheme is capable of. The optimized control strategy in the presence of dissipation consists in utilizing the control fields such as to rapidly kick both states close to a DFS, where they remain most of the protocol duration, and only separate them right before the final time of measurement. Besides improving the states' bare distinguishability, it is also possible to stabilize the states' distinguishability at its maximum for times much longer than the dissipation's time scale. We have moreover shown that the optimized protocol yields an improvement in sensitivity evidenced by an increase of the quantum Fisher information. The results from Chap. 6 therefore emphasize the important role of DFSs in the mitigation of the environment's detrimental impact. It also emphasizes the possibilities which arise from knowledge about existence and form of any DFS, since this knowledge might immediately allow us to design new, sophisticated control schemes.

Finally, we have turned towards the task of implementing an entangling gate between qubits, which is pivotal in quantum computing. In Chap. 7, we have analyzed a control scheme that realizes a beamsplitter interaction between two cavities whose interaction is mediated by an intermediate transmon. Starting from an analytical control scheme proposed in Ref. [315], which realizes the desired beamsplitter interaction by means of driving the transmon with two continuous-wave (cw) fields, we have shown that adding a third cw field, whose amplitude and frequency have been determined by optimal control, allows to substantially increase the effective beamsplitter interaction between the two cavities. The addition of the third drive has two effects. On the one hand, it unfortunately adds some undesired terms to the effective Hamiltonian of the two cavities and therefore increases the gate error of the three-drive protocol compared to the original two-drive protocol. On the other hand, the increased beamsplitter interaction and its entailing decrease in the implementation time for the entangling gate substantially reduces the dissipation's impact on the entire operation. In combination, both effects result in comparable gate errors for the two- and three-drive protocol. However, since the three-drive protocol is much faster, it constitutes an improvement in the generation of entanglement. Although a small error remains, the protocol can probably be further improved, i.e., its error minimized, by applying a gradient-based optimization method for the cw fields. This should readily allow us to obtain gate errors lower than the ones from the original two-drive protocol while still being experimentally feasible. Besides, we have so far only considered the optimization towards a specific entangling gate, respectively a specific form of interaction. However, a straightforward generalization would be to directly optimize towards a general perfect entangler [107, 108] between the cavities. This would allow to identify the fastest perfect entangler [323]. However, in order to correctly account for dissipation, it might be advisable to first generalize the corresponding functional to

also work in an open quantum system where the dynamics is not unitary.

In conclusion, in this thesis we have extended the available tools for optimal control by introducing two new concepts to tackle control tasks in open quantum systems. This covers a new functional for mixed state targets and a new optimization method to search for decoherence-free subspaces. We have furthermore derived new control strategies that cope best with the presence of environmental noise and which have improved some fundamental tasks for quantum technologies. The results emphasize that we need to distinguish between cases, where the ubiquitous environment acts harmful, and cases, where the environment can be exploited for the intended control task. Quantum optimal control can be used in both cases to identify the universal limits for such tasks as well as to derive tailored, robust and experimentally feasible control strategies to boost the performance of state-of-the-art quantum technologies.

References

[1] R. P. Feynman, *Simulating physics with computers*, Int. J. Theor. Phys. **21**, 467 (1982)

[2] M. A. Nielsen and I. L. Chuang, *Quantum Computation and Quantum Information*, Cambridge University Press, 10th edition, 2011

[3] A. Acín, I. Bloch, H. Buhrman, T. Calarco, C. Eichler, J. Eisert, D. Esteve, N. Gisin, S. J. Glaser, F. Jelezko, S. Kuhr, M. Lewenstein, M. F. Riedel, P. O. Schmidt, R. Thew, A. Wallraff, I. Walmsley, and F. K. Wilhelm, *The quantum technologies roadmap: a European community view*, New J. Phys. **20**, 080201 (2018)

[4] P. W. Shor, *Polynomial-Time Algorithms for Prime Factorization and Discrete Logarithms on a Quantum Computer*, SIAM J. Comput. **26**, 1484 (1997)

[5] L. K. Grover, *Quantum Mechanics Helps in Searching for a Needle in a Haystack*, Phys. Rev. Lett. **79**, 325 (1997)

[6] J. Preskill, *Quantum Computing in the NISQ era and beyond*, Quantum **2**, 79 (2018)

[7] F. Arute et al., *Quantum supremacy using a programmable superconducting processor*, Nature **574**, 505 (2019)

[8] S. J. Glaser, U. Boscain, T. Calarco, C. P. Koch, W. Köckenberger, R. Kosloff, I. Kuprov, B. Luy, S. Schirmer, T. Schulte-Herbrüggen, D. Sugny, and F. K. Wilhelm, *Training Schrödinger's cat: quantum optimal control*, Eur. Phys. J. D **69**, 279 (2015)

[9] C. P. Koch, *Controlling open quantum systems: tools, achievements, and limitations*, J. Phys.: Condens. Matter **28**, 213001 (2016)

[10] H.-P. Breuer and F. Petruccione, *The theory of open quantum systems*, Oxford University Press, 1. edition, 2002

[11] D. D'Alessandro, *Introduction to Quantum Control and Dynamics*, Chapman and Hall/CRC, 1. edition, 2007

[12] A. A. Clerk, M. H. Devoret, S. M. Girvin, F. Marquardt, and R. J. Schoelkopf, *Introduction to quantum noise, measurement, and amplification*, Rev. Mod. Phys. **82**, 1155 (2010)

[13] G. Lindblad, *On the generators of quantum dynamical semigroups*, Commun. Math. Phys. **48**, 119 (1976)

[14] V. Gorini, A. Kossakowski, and E. C. G. Sudarshan, *Completely positive dynamical semigroups of N-level systems*, J. Math. Phys. **17**, 821 (1976)

[15] A. Rivas and S. F. Huelga, *Open Quantum Systems*, Springer, Berlin, Heidelberg, 1. edition, 2012

[16] C. W. Gardiner and P. Zoller, *Quantum Noise: A Handbook of Markovian and Non-Markovian Quantum Stochastic Methods with Applications to Quantum Optics*, Springer, Berlin, Heidelberg, 2. edition, 2000

[17] K. Lendi, *Extension of quantum dynamical semigroup generators for open systems to time-dependent Hamiltonians*, Phys. Rev. A **33**, 3358 (1986)

[18] M. J. W. Hall, J. D. Cresser, L. Li, and E. Andersson, *Canonical form of master equations and characterization of non-Markovianity*, Phys. Rev. A **89**, 042120 (2014)

[19] Y. Lin, J. P. Gaebler, F. Reiter, T. R. Tan, R. Bowler, A. S. Sørensen, D. Leibfried, and D. J. Wineland, *Dissipative production of a maximally entangled steady state of two quantum bits*, Nature **504**, 415 (2013)

[20] R. Hanson, L. P. Kouwenhoven, J. R. Petta, S. Tarucha, and L. M. K. Vandersypen, *Spins in few-electron quantum dots*, Rev. Mod. Phys. **79**, 1217 (2007)

[21] A. A. Houck, J. A. Schreier, B. R. Johnson, J. M. Chow, J. Koch, J. M. Gambetta, D. I. Schuster, L. Frunzio, M. H. Devoret, S. M. Girvin, and R. J. Schoelkopf, *Controlling the Spontaneous Emission of a Superconducting Transmon Qubit*, Phys. Rev. Lett. **101**, 080502 (2008)

[22] B. L. Green, S. Mottishaw, B. G. Breeze, A. M. Edmonds, U. F. S. D'Haenens-Johansson, M. W. Doherty, S. D. Williams, D. J. Twitchen, and M. E. Newton, *Neutral Silicon-Vacancy Center in Diamond: Spin Polarization and Lifetimes*, Phys. Rev. Lett. **119**, 096402 (2017)

[23] A. Reiserer, N. Kalb, M. S. Blok, K. J. M. van Bemmelen, T. H. Taminiau, R. Hanson, D. J. Twitchen, and M. Markham, *Robust Quantum-Network Memory Using Decoherence-Protected Subspaces of Nuclear Spins*, Phys. Rev. X **6**, 021040 (2016)

[24] B. Naydenov, F. Dolde, L. T. Hall, C. Shin, H. Fedder, L. C. L. Hollenberg, F. Jelezko, and J. Wrachtrup, *Dynamical decoupling of a single-electron spin at room temperature*, Phys. Rev. B **83**, 081201 (2011)

[25] D. Manzano, *A short introduction to the Lindblad master equation*, AIP Advances **10**, 025106 (2020)

[26] H.-P. Breuer, E.-M. Laine, J. Piilo, and B. Vacchini, *Colloquium: Non-Markovian dynamics in open quantum systems*, Rev. Mod. Phys. **88**, 021002 (2016)

[27] Á. Rivas, S. F. Huelga, and M. B. Plenio, *Quantum non-Markovianity: characterization, quantification and detection*, Rep. Prog. Phys. **77**, 094001 (2014)

[28] I. de Vega and D. Alonso, *Dynamics of non-Markovian open quantum systems*, Rev. Mod. Phys. **89**, 015001 (2017)

[29] G. Burkard, *Non-Markovian qubit dynamics in the presence of* $1/f$ *noise*, Phys. Rev. B **79**, 125317 (2009)

[30] E. Paladino, Y. M. Galperin, G. Falci, and B. L. Altshuler, $1/f$ *noise: Implications for solid-state quantum information*, Rev. Mod. Phys. **86**, 361 (2014)

[31] W. A. Coish and D. Loss, *Hyperfine interaction in a quantum dot: Non-Markovian electron spin dynamics*, Phys. Rev. B **70**, 195340 (2004)

[32] A. C. Johnson, J. R. Petta, J. M. Taylor, A. Yacoby, M. D. Lukin, C. M. Marcus, M. P. Hanson, and A. C. Gossard, *Triplet-singlet spin relaxation via nuclei in a double quantum dot*, Nature **435**, 925 (2005)

[33] F. H. L. Koppens, J. A. Folk, J. M. Elzerman, R. Hanson, L. H. W. van Beveren, I. T. Vink, H. P. Tranitz, W. Wegscheider, L. P. Kouwenhoven, and L. M. K.

Vandersypen, *Control and Detection of Singlet-Triplet Mixing in a Random Nuclear Field*, Science **309**, 1346 (2005)

[34] J.-S. Xu, C.-F. Li, M. Gong, X.-B. Zou, C.-H. Shi, G. Chen, and G.-C. Guo, *Experimental Demonstration of Photonic Entanglement Collapse and Revival*, Phys. Rev. Lett. **104**, 100502 (2010)

[35] H. Lee, Y.-C. Cheng, and G. R. Fleming, *Coherence Dynamics in Photosynthesis: Protein Protection of Excitonic Coherence*, Science **316**, 1462 (2007)

[36] M. M. Wolf, J. Eisert, T. S. Cubitt, and J. I. Cirac, *Assessing Non-Markovian Quantum Dynamics*, Phys. Rev. Lett. **101**, 150402 (2008)

[37] A. Rivas, S. F. Huelga, and M. B. Plenio, *Entanglement and Non-Markovianity of Quantum Evolutions*, Phys. Rev. Lett. **105**, 050403 (2010)

[38] D. Chruściński, A. Kossakowski, and A. Rivas, *Measures of non-Markovianity: Divisibility versus backflow of information*, Phys. Rev. A **83**, 052128 (2011)

[39] H.-P. Breuer, E.-M. Laine, and J. Piilo, *Measure for the Degree of Non-Markovian Behavior of Quantum Processes in Open Systems*, Phys. Rev. Lett. **103**, 210401 (2009)

[40] J. Liu, X.-M. Lu, and X. Wang, *Nonunital non-Markovianity of quantum dynamics*, Phys. Rev. A **87**, 042103 (2013)

[41] X.-M. Lu, X. Wang, and C. P. Sun, *Quantum Fisher information flow and non-Markovian processes of open systems*, Phys. Rev. A **82**, 042103 (2010)

[42] S. Luo, S. Fu, and H. Song, *Quantifying non-Markovianity via correlations*, Phys. Rev. A **86**, 044101 (2012)

[43] S. Lorenzo, F. Plastina, and M. Paternostro, *Role of environmental correlations in the non-Markovian dynamics of a spin system*, Phys. Rev. A **84**, 032124 (2011)

[44] S. Alipour, A. Mani, and A. T. Rezakhani, *Quantum discord and non-Markovianity of quantum dynamics*, Phys. Rev. A **85**, 052108 (2012)

[45] S. Lorenzo, F. Plastina, and M. Paternostro, *Geometrical characterization of non-Markovianity*, Phys. Rev. A **88**, 020102 (2013)

[46] P. Strasberg and M. Esposito, *Non-Markovianity and negative entropy production rates*, Phys. Rev. E **99**, 012120 (2019)

[47] Z. He, C. Yao, Q. Wang, and J. Zou, *Measuring non-Markovianity based on local quantum uncertainty*, Phys. Rev. A **90**, 042101 (2014)

[48] Z. He, L.-Q. Zhu, and L. Li, *Non-Markovianity Measure Based on Brukner–Zeilinger Invariant Information for Unital Quantum Dynamical Maps*, Commun. Theor. Phys. **67**, 255 (2017)

[49] P. Rebentrost, I. Serban, T. Schulte-Herbrüggen, and F. K. Wilhelm, *Optimal Control of a Qubit Coupled to a Non-Markovian Environment*, Phys. Rev. Lett. **102**, 090401 (2009)

[50] B.-H. Liu, L. Li, Y.-F. Huang, C.-F. Li, G.-C. Guo, E.-M. Laine, H.-P. Breuer, and J. Piilo, *Experimental control of the transition from Markovian to non-Markovian dynamics of open quantum systems*, Nature Phys. **7**, 931 (2011)

[51] J.-S. Xu, K. Sun, C.-F. Li, X.-Y. Xu, G.-C. Guo, E. Andersson, R. Lo Franco, and G. Compagno, *Experimental recovery of quantum correlations in absence of system-environment back-action*, Nat. Commun. **4**, 2851 (2013)

[52] D. M. Reich, N. Katz, and C. P. Koch, *Exploiting Non-Markovianity for Quantum Control*, Sci. Rep. **5**, 12430 (2015)

[53] A. W. Chin, S. F. Huelga, and M. B. Plenio, *Quantum Metrology in Non-Markovian Environments*, Phys. Rev. Lett. **109**, 233601 (2012)

[54] G. Dirr, U. Helmke, I. Kurniawan, and T. Schulte-Herbrüggen, *Lie-semigroup structures for reachability and control of open quantum systems: kossakowski-lindblad generators form lie wedge to markovian channels*, Rep. Math. Phys. **64**, 93 (2009)

[55] A. Garon, S. J. Glaser, and D. Sugny, *Time-optimal control of SU(2) quantum operations*, Phys. Rev. A **88**, 043422 (2013)

[56] M. Lapert, Y. Zhang, M. Braun, S. J. Glaser, and D. Sugny, *Singular Extremals for the Time-Optimal Control of Dissipative Spin $\frac{1}{2}$ Particles*, Phys. Rev. Lett. **104**, 083001 (2010)

[57] M. Lapert, E. Assémat, S. J. Glaser, and D. Sugny, *Understanding the global structure of two-level quantum systems with relaxation: Vector fields organized through the magic plane and the steady-state ellipsoid*, Phys. Rev. A **88**, 033407 (2013)

[58] D. Sugny and C. Kontz, *Optimal control of a three-level quantum system by laser fields plus von Neumann measurements*, Phys. Rev. A **77**, 063420 (2008)

[59] N. Khaneja, S. J. Glaser, and R. Brockett, *Sub-Riemannian geometry and time optimal control of three spin systems: Quantum gates and coherence transfer*, Phys. Rev. A **65**, 032301 (2002)

[60] H. A. Rabitz, M. M. Hsieh, and C. M. Rosenthal, *Quantum Optimally Controlled Transition Landscapes*, Science **303**, 1998 (2004)

[61] A. N. Pechen and D. J. Tannor, *Are there Traps in Quantum Control Landscapes?*, Phys. Rev. Lett. **106**, 120402 (2011)

[62] H. Rabitz, M. Hsieh, and C. Rosenthal, *Landscape for optimal control of quantum-mechanical unitary transformations*, Phys. Rev. A **72**, 052337 (2005)

[63] R. Wu, A. Pechen, H. Rabitz, M. Hsieh, and B. Tsou, *Control landscapes for observable preparation with open quantum systems*, J. Math. Phys. **49**, 022108 (2008)

[64] K. W. Moore and H. Rabitz, *Exploring constrained quantum control landscapes*, J. Chem. Phys. **137**, 134113 (2012)

[65] M. Wollenhaupt, A. Präkelt, C. Sarpe-Tudoran, D. Liese, and T. Baumert, *Quantum control and quantum control landscapes using intense shaped femtosecond pulses*, J. Mod. Opt. **52**, 2187 (2005)

[66] M. H. Goerz, D. Basilewitsch, F. Gago-Encinas, M. G. Krauss, K. P. Horn, D. M. Reich, and C. P. Koch, *Krotov: A Python implementation of Krotov's method for quantum optimal control*, SciPost Phys. **7**, 80 (2019)

[67] J. A. Nelder and R. Mead, *A Simplex Method for Function Minimization*, Comput. J. **7**, 308 (1965)

[68] P. Doria, T. Calarco, and S. Montangero, *Optimal Control Technique for Many-Body Quantum Dynamics*, Phys. Rev. Lett. **106**, 190501 (2011)

[69] T. Caneva, T. Calarco, and S. Montangero, *Chopped random-basis quantum optimization*, Phys. Rev. A **84**, 022326 (2011)

[70] N. Rach, M. M. Müller, T. Calarco, and S. Montangero, *Dressing the chopped-random-basis optimization: A bandwidth-limited access to the trap-free landscape*, Phys. Rev. A **92**, 062343 (2015)

[71] R. E. Goetz, M. Merkel, A. Karamatskou, R. Santra, and C. P. Koch, *Maximizing hole coherence in ultrafast photoionization of argon with an optimization by sequential parametrization update*, Phys. Rev. A **94**, 023420 (2016)

[72] H. Tal-Ezer and R. Kosloff, *An accurate and efficient scheme for propagating the time dependent Schrödinger equation*, J. Chem. Phys. **81**, 3967 (1984)

[73] G. Ashkenazi, R. Kosloff, S. Ruhman, and H. Tal-Ezer, *Newtonian propagation methods applied to the photodissociation dynamics of I_3^-*, J. Chem. Phys. **103**, 10005 (1995)

[74] N. Khaneja, T. Reiss, C. Kehlet, T. Schulte-Herbrüggen, and S. J. Glaser, *Optimal control of coupled spin dynamics: design of NMR pulse sequences by gradient ascent algorithms*, J. Magn. Reson. **172**, 296 (2005)

[75] P. de Fouquières, S. Schirmer, S. Glaser, and I. Kuprov, *Second order gradient ascent pulse engineering*, J. Magn. Reson. **212**, 412 (2011)

[76] F. F. Floether, P. de Fouquieres, and S. G. Schirmer, *Robust quantum gates for open systems via optimal control: Markovian versus non-Markovian dynamics*, New J. Phys. **14**, 073023 (2012)

[77] C. G. Broyden, *The Convergence of a Class of Double-rank Minimization Algorithms 1. General Considerations*, IMA J. Appl. Math. **6**, 76 (1970)

[78] R. Fletcher, *A new approach to variable metric algorithms*, Comput. J. **13**, 317 (1970)

[79] D. Goldfarb, *A family of variable-metric methods derived by variational means*, Math. Comp. **24**, 23 (1970)

[80] D. F. Shanno, *Conditioning of quasi-Newton methods for function minimization*, Math. Comp. **24**, 647 (1970)

[81] R. H. Byrd, P. Lu, J. Nocedal, and C. Zhu, *A Limited Memory Algorithm for Bound Constrained Optimization*, SIAM J. Sci. Comp. **16**, 1190 (1995)

[82] C. Zhu, R. H. Byrd, P. Lu, and J. Nocedal, *Algorithm 778: L-BFGS-B: Fortran subroutines for large-scale bound-constrained optimization*, ACM Trans. Math. Softw. **23**, 550 (1997)

[83] J. J. W. H. Sørensen, M. O. Aranburu, T. Heinzel, and J. F. Sherson, *Quantum optimal control in a chopped basis: Applications in control of Bose-Einstein condensates*, Phys. Rev. A **98**, 022119 (2018)

[84] S. Machnes, E. Assémat, D. Tannor, and F. K. Wilhelm, *Tunable, Flexible, and Efficient Optimization of Control Pulses for Practical Qubits*, Phys. Rev. Lett. **120**, 150401 (2018)

[85] V. F. Krotov and I. N. Fel'dman, *An iterative method for solving optimal-control problems*, Engrg. Cybernetics **21**, 123 (1983)

[86] V. F. Krotov, *A Technique of Global Bounds in Optimal Control Theory*, Control Cybern. **17**, 115 (1988)

[87] V. Krotov, *Global Methods in Optimal Control Theory*, CRC Press, 1995

[88] A. I. Konnov and V. F. Krotov, *On global Methods of successive Improvement of Controlled Processes*, Autom. Rem. Contr. **60**, 1427 (1999)

[89] S. E. Sklarz and D. J. Tannor, *Loading a Bose-Einstein Condensate onto an Optical Lattice: An Application of Optimal Control Theory to the Nonlinear Schrödinger Equation*, Phys. Rev. A **66**, 053619 (2002)

[90] J. P. Palao and R. Kosloff, *Optimal control theory for unitary transformations*, Phys. Rev. A **68**, 062308 (2003)

[91] J. Somlói, V. A. Kazakov, and D. J. Tannor, *Controlled dissociation of I2 via optical transitions between the X and B electronic states*, Chem. Phys. **172**, 85 (1993)

[92] A. Bartana, R. Kosloff, and D. J. Tannor, *Laser cooling of molecular internal degrees of freedom by a series of shaped pulses*, J. Chem. Phys. **99**, 196 (1993)

[93] A. Bartana, R. Kosloff, and D. J. Tannor, *Laser cooling of internal degrees of freedom. II*, J. Chem. Phys. **106**, 1435 (1997)

[94] D. M. Reich, M. Ndong, and C. P. Koch, *Monotonically convergent optimization in quantum control using Krotov's method*, J. Chem. Phys. **136**, 104103 (2012)

[95] S. Machnes, U. Sander, S. J. Glaser, P. de Fouquières, A. Gruslys, S. Schirmer, and T. Schulte-Herbrüggen, *Comparing, optimizing, and benchmarking quantum-control algorithms in a unifying programming framework*, Phys. Rev. A **84**, 022305 (2011)

[96] G. Jäger, D. M. Reich, M. H. Goerz, C. P. Koch, and U. Hohenester, *Optimal quantum control of Bose-Einstein condensates in magnetic microtraps: Comparison of GRAPE and Krotov optimization schemes*, Phys. Rev. A **90**, 033628 (2014)

[97] M. Ndong, H. Tal-Ezer, R. Kosloff, and C. P. Koch, *A Chebychev propagator with iterative time ordering for explicitly time-dependent Hamiltonians*, J. Chem. Phys. **132**, 064105 (2010)

[98] D. Basilewitsch, L. Marder, and C. P. Koch, *Dissipative quantum dynamics and optimal control using iterative time ordering: an application to superconducting qubits*, Eur. Phys. J. B **91**, 161 (2018)

[99] D. M. Reich, J. P. Palao, and C. P. Koch, *Optimal control under spectral constraints: enforcing multi-photon absorption pathways*, J. Mod. Opt. **61**, 822 (2014)

[100] J. P. Palao, D. M. Reich, and C. P. Koch, *Steering the optimization pathway in the control landscape using constraints*, Phys. Rev. A **88**, 053409 (2013)

[101] J. P. Palao, R. Kosloff, and C. P. Koch, *Protecting coherence in optimal control theory: State-dependent constraint approach*, Phys. Rev. A **77**, 063412 (2008)

[102] M. Ndong, C. Koch, and D. Sugny, *Time optimization and state-dependent constraints in the quantum optimal control of molecular orientation*, J. Mod. Opt. **61**, 857 (2014)

[103] D. Basilewitsch, C. P. Koch, and D. M. Reich, *Quantum Optimal Control for Mixed State Squeezing in Cavity Optomechanics*, Adv. Quantum Technol. **2**, 1800110 (2019)

[104] M. H. Goerz, D. M. Reich, and C. P. Koch, *Optimal control theory for a unitary operation under dissipative evolution*, New J. Phys. **16**, 055012 (2014)

[105] C. P. Koch, M. Lemeshko, and D. Sugny, *Quantum control of molecular rotation*, Rev. Mod. Phys. **91**, 035005 (2019)

[106] M. M. Müller, D. M. Reich, M. Murphy, H. Yuan, J. Vala, K. B. Whaley, T. Calarco, and C. P. Koch, *Optimizing entangling quantum gates for physical systems*, Phys. Rev. A **84**, 042315 (2011)

[107] P. Watts, J. Vala, M. M. Müller, T. Calarco, K. B. Whaley, D. M. Reich, M. H. Goerz, and C. P. Koch, *Optimizing for an arbitrary perfect entangler: I. Functionals*, Phys. Rev. A **91**, 062306 (2015)

[108] M. H. Goerz, G. Gualdi, D. M. Reich, C. P. Koch, F. Motzoi, K. B. Whaley, J. Vala, M. M. Müller, S. Montangero, and T. Calarco, *Optimizing for an arbitrary perfect entangler. II. Application*, Phys. Rev. A **91**, 062307 (2015)

[109] R. A. Bertlmann and P. Krammer, *Bloch vectors for qudits*, J. Phys. A: Math. Theor. **41**, 235303 (2008)

[110] R. Jozsa, *Fidelity for mixed quantum states*, J. Mod. Opt. **41**, 2315 (1994)

[111] A. Uhlmann, *The "transition probability" in the state space of a $*$-algebra*, Rep. Math. Phys. **9**, 273 (1976)

[112] S. Luo and Q. Zhang, *Informational distance on quantum-state space*, Phys. Rev. A **69**, 032106 (2004)

[113] A. P. Majtey, P. W. Lamberti, and D. P. Prato, *Jensen-Shannon divergence as a measure of distinguishability between mixed quantum states*, Phys. Rev. A **72**, 052310 (2005)

[114] C. H. Bennett, H. J. Bernstein, S. Popescu, and B. Schumacher, *Concentrating partial entanglement by local operations*, Phys. Rev. A **53**, 2046 (1996)

[115] V. V. Dodonov, O. V. Man'ko, V. I. Man'ko, and A. Wünsche, *Hilbert-Schmidt distance and non-classicality of states in quantum optics*, J. Mod. Opt. **47**, 633 (2000)

[116] R. Xu, Y. Yan, Y. Ohtsuki, Y. Fujimura, and H. Rabitz, *Optimal control of quantum non-Markovian dissipation: Reduced Liouville-space theory*, J. Chem. Phys. **120**, 6600 (2004)

[117] M. Aspelmeyer, T. J. Kippenberg, and F. Marquardt, *Cavity optomechanics*, Rev. Mod. Phys. **86**, 1391 (2014)

[118] M. Aspelmeyer, T. J. Kippenberg, and F. Marquardt, editors, *Cavity optomechanics: Nano- and Micromechanical Resonators Interacting with Light*, Quantum Science and Technology, Springer, 2014

[119] A. Cooper, W. K. C. Sun, J.-C. Jaskula, and P. Cappellaro, *Environment-assisted Quantum-enhanced Sensing with Electronic Spins in Diamond*, Phys. Rev. Applied **12**, 044047 (2019)

[120] K. C. McCormick, J. Keller, S. C. Burd, D. J. Wineland, A. C. Wilson, and D. Leibfried, *Quantum-enhanced sensing of a single-ion mechanical oscillator*, Nature **572**, 86 (2019)

[121] R. Schnabel, *Squeezed states of light and their applications in laser interferometers*, Phys. Rep. **684**, 1 (2017)

[122] O. Hosten, N. J. Engelsen, R. Krishnakumar, and M. A. Kasevich, *Measurement noise 100 times lower than the quantum-projection limit using entangled atoms*, Nature **529**, 505 (2016)

[123] J. Aasi et al., *Enhanced sensitivity of the LIGO gravitational wave detector by using squeezed states of light*, Nat. Photonics **7**, 613 (2013)

[124] H. Grote, K. Danzmann, K. L. Dooley, R. Schnabel, J. Slutsky, and H. Vahlbruch, *First Long-Term Application of Squeezed States of Light in a Gravitational-Wave Observatory*, Phys. Rev. Lett. **110**, 181101 (2013)

[125] U. L. Andersen, T. Gehring, C. Marquardt, and G. Leuchs, *30 years of squeezed light generation*, Phys. Scr. **91**, 053001 (2016)

[126] J. F. Poyatos, J. I. Cirac, and P. Zoller, *Quantum Reservoir Engineering with Laser Cooled Trapped Ions*, Phys. Rev. Lett. **77**, 4728 (1996)

[127] H. Krauter, C. A. Muschik, K. Jensen, W. Wasilewski, J. M. Petersen, J. I. Cirac, and E. S. Polzik, *Entanglement generated by dissipation and steady state entanglement of two macroscopic objects*, Phys. Rev. Lett. **107**, 080503 (2011)

[128] S. Shankar, M. Hatridge, Z. Leghtas, K. Sliwa, A. Narla, U. Vool, S. M. Girvin, L. Frunzio, M. Mirrahimi, and M. H. Devoret, *Autonomously stabilized entanglement between two superconducting quantum bits*, Nature **504**, 419 (2013)

[129] D. Kienzler, H.-Y. Lo, B. Keitch, L. de Clercq, F. Leupold, F. Lindenfelser, M. Marinelli, V. Negnevitsky, and J. Home, *Quantum harmonic oscillator state synthesis by reservoir engineering*, Science , 1261033 (2014)

[130] M. E. Kimchi-Schwartz, L. Martin, E. Flurin, C. Aron, M. Kulkarni, H. E. Tureci, and I. Siddiqi, *Stabilizing Entanglement via Symmetry-Selective Bath Engineering in Superconducting Qubits*, Phys. Rev. Lett. **116**, 240503 (2016)

[131] N. Syassen, D. M. Bauer, M. Lettner, T. Volz, D. Dietze, J. J. García-Ripoll, J. I. Cirac, G. Rempe, and S. Dürr, *Strong Dissipation Inhibits Losses and Induces Correlations in Cold Molecular Gases*, Science **320**, 1329 (2008)

[132] P. Schindler, M. Müller, D. Nigg, J. T. Barreiro, E. A. Martinez, M. Hennrich, T. Monz, S. Diehl, P. Zoller, and R. Blatt, *Quantum simulation of dynamical maps with trapped ions*, Nat. Phys. **9**, 361 (2013)

[133] K. P. Horn, F. Reiter, Y. Lin, D. Leibfried, and C. P. Koch, *Quantum optimal control of the dissipative production of a maximally entangled state*, New J. Phys. **20**, 123010 (2018)

[134] A. Kronwald, F. Marquardt, and A. A. Clerk, *Arbitrarily large steady-state bosonic squeezing via dissipation*, Phys. Rev. A **88**, 063833 (2013)

[135] E. E. Wollman, C. U. Lei, A. J. Weinstein, J. Suh, A. Kronwald, F. Marquardt, A. A. Clerk, and K. C. Schwab, *Quantum squeezing of motion in a mechanical resonator*, Science **349**, 952 (2015)

[136] M. Yuan, V. Singh, Y. M. Blanter, and G. A. Steele, *Large cooperativity and microkelvin cooling with a three-dimensional optomechanical cavity*, Nat. Commun. **6**, 8491 (2015)

[137] A. Vinante and P. Falferi, *Feedback-Enhanced Parametric Squeezing of Mechanical Motion*, Phys. Rev. Lett. **111**, 207203 (2013)

[138] C. U. Lei, A. J. Weinstein, J. Suh, E. E. Wollman, A. Kronwald, F. Marquardt, A. A. Clerk, and K. C. Schwab, *Quantum Nondemolition Measurement of a Quantum Squeezed State Beyond the 3 dB Limit*, Phys. Rev. Lett. **117**, 100801 (2016)

[139] U. S. Sainadh and M. A. Kumar, *Squeezing of the mechanical motion and beating 3 dB limit using dispersive optomechanical interactions*, J. Mod. Opt. **64**, 1121 (2017)

[140] C. E. Rogers, J. L. Carini, J. A. Pechkis, and P. L. Gould, *Creation of arbitrary time-sequenced line spectra with an electro-optic phase modulator*, Rev. Sci. Instrum. **82**, 073107 (2011)

[141] T. Häberle, D. Schmid-Lorch, K. Karrai, F. Reinhard, and J. Wrachtrup, *High-Dynamic-Range Imaging of Nanoscale Magnetic Fields Using Optimal Control of a Single Qubit*, Phys. Rev. Lett. **111**, 170801 (2013)

[142] M. H. Devoret and R. J. Schoelkopf, *Superconducting Circuits for Quantum Information: An Outlook*, Science **339**, 1169 (2013)

[143] H. Wang, M. Hofheinz, J. Wenner, M. Ansmann, R. C. Bialczak, M. Lenander, E. Lucero, M. Neeley, A. D. O'Connell, D. Sank, M. Weides, A. N. Cleland, and J. M. Martinis, *Improving the coherence time of superconducting coplanar resonators*, Appl. Phys. Lett. **95**, 233508 (2009)

[144] J. Bylander, S. Gustavsson, F. Yan, F. Yoshihara, K. Harrabi, G. Fitch, D. G. Cory, Y. Nakamura, J.-S. Tsai, and W. D. Oliver, *Noise spectroscopy through dynamical decoupling with a superconducting flux qubit*, Nature Physics **7**, 565 (2011)

[145] J. B. Chang, M. R. Vissers, A. D. Córcoles, M. Sandberg, J. Gao, D. W. Abraham, J. M. Chow, J. M. Gambetta, M. B. Rothwell, G. A. Keefe, M. Steffen, and D. P. Pappas, *Improved superconducting qubit coherence using titanium nitride*, Appl. Phys. Lett. **103**, 012602 (2013)

[146] C. Rigetti, J. M. Gambetta, S. Poletto, B. L. T. Plourde, J. M. Chow, A. D. Córcoles, J. A. Smolin, S. T. Merkel, J. R. Rozen, G. A. Keefe, M. B. Rothwell, M. B. Ketchen, and M. Steffen, *Superconducting qubit in a waveguide cavity with a coherence time approaching 0.1 ms*, Phys. Rev. B **86**, 100506 (2012)

[147] G. Balasubramanian, P. Neumann, D. Twitchen, M. Markham, R. Kolesov, N. Mizuochi, J. Isoya, J. Achard, J. Beck, J. Tissler, V. Jacques, P. R. Hemmer, F. Jelezko, and J. Wrachtrup, *Ultralong spin coherence time in isotopically engineered diamond*, Nature Mater. **8**, 383 (2009)

[148] M. Zhong, M. P. Hedges, R. L. Ahlefeldt, J. G. Bartholomew, S. E. Beavan, S. M. Wittig, J. J. Longdell, and M. J. Sellars, *Optically addressable nuclear spins in a solid with a six-hour coherence time*, Nature **517**, 177 (2015)

[149] K. Saeedi, S. Simmons, J. Z. Salvail, P. Dluhy, H. Riemann, N. V. Abrosimov, P. Becker, H.-J. Pohl, J. J. L. Morton, and M. L. W. Thewalt, *Room-Temperature Quantum Bit Storage Exceeding 39 Minutes Using Ionized Donors in Silicon-28*, Science **342**, 830 (2013)

[150] T. Ruster, C. T. Schmiegelow, H. Kaufmann, C. Warschburger, F. Schmidt-Kaler, and U. G. Poschinger, *A long-lived Zeeman trapped-ion qubit*, Appl. Phys. B **122** (2016)

[151] Y. Wang, M. Um, J. Zhang, S. An, M. Lyu, J.-N. Zhang, L.-M. Duan, D. Yum, and K. Kim, *Single-qubit quantum memory exceeding ten-minute coherence time*, Nature Photon. **11**, 646 (2017)

[152] L. Viola and S. Lloyd, *Dynamical suppression of decoherence in two-state quantum systems*, Phys. Rev. A **58**, 2733 (1998)

[153] L. Viola, E. Knill, and S. Lloyd, *Dynamical Decoupling of Open Quantum Systems*, Phys. Rev. Lett. **82**, 2417 (1999)

[154] L. Viola, S. Lloyd, and E. Knill, *Universal Control of Decoupled Quantum Systems*, Phys. Rev. Lett. **83**, 4888 (1999)

[155] P. W. Shor, *Scheme for reducing decoherence in quantum computer memory*, Phys. Rev. A **52**, R2493 (1995)

[156] D. G. Cory, M. D. Price, W. Maas, E. Knill, R. Laflamme, W. H. Zurek, T. F. Havel, and S. S. Somaroo, *Experimental Quantum Error Correction*, Phys. Rev. Lett. **81**, 2152 (1998)

[157] M. D. Reed, L. DiCarlo, S. E. Nigg, L. Sun, L. Frunzio, S. M. Girvin, and R. J. Schoelkopf, *Realization of three-qubit quantum error correction with superconducting circuits*, Nature **482**, 382 (2012)

[158] N. Ofek, A. Petrenko, R. Heeres, P. Reinhold, Z. Leghtas, B. Vlastakis, Y. Liu, L. Frunzio, S. M. Girvin, L. Jiang, M. Mirrahimi, M. H. Devoret, and R. J. Schoelkopf, *Extending the lifetime of a quantum bit with error correction in superconducting circuits*, Nature **536**, 441 (2016)

[159] J. Chiaverini, D. Leibfried, T. Schaetz, M. D. Barrett, R. B. Blakestad, J. Britton, W. M. Itano, J. D. Jost, E. Knill, C. Langer, R. Ozeri, and D. J. Wineland, *Realization of quantum error correction*, Nature **432**, 602 (2004)

[160] P. Schindler, J. T. Barreiro, T. Monz, V. Nebendahl, D. Nigg, M. Chwalla, M. Hennrich, and R. Blatt, *Experimental Repetitive Quantum Error Correction*, Science **332**, 1059 (2011)

[161] G. Waldherr, Y. Wang, S. Zaiser, M. Jamali, T. Schulte-Herbrüggen, H. Abe, T. Ohshima, J. Isoya, J. F. Du, P. Neumann, and J. Wrachtrup, *Quantum error correction in a solid-state hybrid spin register*, Nature **506**, 204 (2014)

[162] T. H. Taminiau, J. Cramer, T. van der Sar, V. V. Dobrovitski, and R. Hanson, *Universal control and error correction in multi-qubit spin registers in diamond*, Nature Nano. **9**, 171 (2014)

[163] E. Knill, *Resilient Quantum Computation*, Science **279**, 342 (1998)

[164] P. Zanardi and M. Rasetti, *Noiseless Quantum Codes*, Phys. Rev. Lett. **79**, 3306 (1997)

[165] D. A. Lidar, I. L. Chuang, and K. B. Whaley, *Decoherence-Free Subspaces for Quantum Computation*, Phys. Rev. Lett. **81**, 2594 (1998)

[166] P. G. Kwiat, *Experimental Verification of Decoherence-Free Subspaces*, Science **290**, 498 (2000)

[167] M. Mohseni, J. S. Lundeen, K. J. Resch, and A. M. Steinberg, *Experimental Application of Decoherence-Free Subspaces in an Optical Quantum-Computing Algorithm*, Phys. Rev. Lett. **91**, 187903 (2003)

[168] J. B. Altepeter, P. G. Hadley, S. M. Wendelken, A. J. Berglund, and P. G. Kwiat, *Experimental Investigation of a Two-Qubit Decoherence-Free Subspace*, Phys. Rev. Lett. **92**, 147901 (2004)

[169] D. Kielpinski, V. Meyer, M. A. Rowe, C. A. Sackett, W. M. Itano, C. Monroe, and D. J. Wineland, *A Decoherence-Free Quantum Memory Using Trapped Ions*, Science **291**, 1013 (2001)

[170] M. Friesen, J. Ghosh, M. A. Eriksson, and S. N. Coppersmith, *A decoherence-free subspace in a charge quadrupole qubit*, Nat. Commun. **8** (2017)

[171] C. Langer, R. Ozeri, J. D. Jost, J. Chiaverini, B. DeMarco, A. Ben-Kish, R. B. Blakestad, J. Britton, D. B. Hume, W. M. Itano, D. Leibfried, R. Reichle, T. Rosenband, T. Schaetz, P. O. Schmidt, and D. J. Wineland, *Long-Lived Qubit Memory Using Atomic Ions*, Phys. Rev. Lett. **95**, 060502 (2005)

[172] J. Kempe, D. Bacon, D. A. Lidar, and K. B. Whaley, *Theory of decoherence-free fault-tolerant universal quantum computation*, Phys. Rev. A **63**, 042307 (2001)

[173] D. Bacon, J. Kempe, D. A. Lidar, and K. B. Whaley, *Universal Fault-Tolerant Quantum Computation on Decoherence-Free Subspaces*, Phys. Rev. Lett. **85**, 1758 (2000)

[174] A. Beige, D. Braun, B. Tregenna, and P. L. Knight, *Quantum Computing Using Dissipation to Remain in a Decoherence-Free Subspace*, Phys. Rev. Lett. **85**, 1762 (2000)

[175] P. Xue and Y.-F. Xiao, *Universal Quantum Computation in Decoherence-Free Subspace with Neutral Atoms*, Phys. Rev. Lett. **97**, 140501 (2006)

[176] X.-L. Feng, C. Wu, H. Sun, and C. H. Oh, *Geometric Entangling Gates in Decoherence-Free Subspaces with Minimal Requirements*, Phys. Rev. Lett. **103**, 200501 (2009)

[177] B. Weigang, *Identification of Decoherence-Free Subspaces in Open Quantum Systems*, Bachelor's thesis, University of Kassel, 2015

[178] D. Reich, *Efficient Characterisation and Optimal Control of Open Quantum Systems - Mathematical Foundations and Physical Applications*, PhD thesis, University of Kassel, 2014

[179] K. Życzkowski and I. Bengtsson, *On Duality between Quantum Maps and Quantum States*, Open Sys. & Inf. Dyn. **11**, 3 (2004)

[180] Y. Zhou, Q. Zhao, X. Yuan, and X. Ma, *Detecting multipartite entanglement structure with minimal resources*, npj Quantum Inf. **5** (2019)

[181] M. Walter, D. Gross, and J. Eisert, *Multi-partite entanglement*, arXiv:1612.02437 (2016)

[182] H. Donker, H. D. Raedt, and M. Katsnelson, *Decoherence and pointer states in small antiferromagnets: A benchmark test*, SciPost Phys. **2** (2017)

[183] M. Schlosshauer, *Decoherence, the measurement problem, and interpretations of quantum mechanics*, Rev. Mod. Phys. **76**, 1267 (2005)

[184] L.-A. Wu and D. A. Lidar, *Creating Decoherence-Free Subspaces Using Strong and Fast Pulses*, Phys. Rev. Lett. **88**, 207902 (2002)

[185] F. Reiter, private communication

[186] D. Gottesmann, *An Introduction to Quantum Error Correction and Fault-Tolerant Quantum Computation*, arXiv:0904.2557 (2009)

[187] D. P. DiVincenzo, *The Physical Implementation of Quantum Computation*, Fortschr. Phys. **48**, 771 (2000)

[188] J. Fernandez, S. Lloyd, T. Mor, and V. Roychowdhury, *Algorithmic cooling of spins: A practicable method for increasing polarization.*, Int. J. Quantum Inform. **2**, 461 (2004)

[189] T. D. Ladd, F. Jelezko, R. Laflamme, Y. Nakamura, C. Monroe, and J. O'Brien, *Quantum computers*, Nature **464**, 45 (2010)

[190] M. D. Reed, B. R. Johnson, A. A. Houck, L. DiCarlo, J. M. Chow, D. I. Schuster, L. Frunzio, and R. J. Schoelkopf, *Fast reset and suppressing spontaneous emission of a superconducting qubit*, Appl. Phys. Lett. **96**, 203110 (2010)

[191] D. Ristè, J. G. van Leeuwen, H.-S. Ku, K. W. Lehnert, and L. DiCarlo, *Initialization by Measurement of a Superconducting Quantum Bit Circuit*, Phys. Rev. Lett. **109**, 050507 (2012)

[192] J. E. Johnson, C. Macklin, D. H. Slichter, R. Vijay, E. B. Weingarten, J. Clarke, and I. Siddiqi, *Heralded State Preparation in a Superconducting Qubit*, Phys. Rev. Lett. **109**, 050506 (2012)

[193] L. C. G. Govia and F. K. Wilhelm, *Unitary-Feedback-Improved Qubit Initialization in the Dispersive Regime*, Phys. Rev. Applied **4**, 054001 (2015)

[194] R. Kosloff and A. Levy, *Quantum Heat Engines and Refrigerators: Continuous Devices.*, Annu. Rev. Phys. Chem. **65**, 365 (2014)

[195] D. Gelbwaser-Klimovsky, W. Niedenzu, and G. Kurizki, *Thermodynamics of Quantum Systems Under Dynamical Control.*, Adv. At. Mol. Opt. Phys. **64**, 329 (2015)

[196] J. Roßnagel, S. T. Dawkins, K. N. Tolazzi, O. Abah, E. Lutz, F. Schmidt-Kaler, and K. Singer, *A single-atom heat engine*, Science **352**, 325 (2016)

[197] B. Karimi and J. P. Pekola, *Otto refrigerator based on a superconducting qubit: Classical and quantum performance*, Phys. Rev. B **94**, 184503 (2016)

[198] G. Watanabe, B. P. Venkatesh, P. Talkner, and A. del Campo, *Quantum Performance of Thermal Machines over Many Cycles*, Phys. Rev. Lett. **118**, 050601 (2017)

[199] A. Rényi, *On Measures of Entropy and Information*, University of California Press, 1961

[200] C. Tsallis, *Possible generalization of Boltzmann-Gibbs statistics*, J. Stat. Phys. **52**, 479 (1988)

[201] M. Pierre, I.-M. Svensson, S. Raman Sathyamoorthy, G. Johansson, and P. Delsing, *Storage and on-demand release of microwaves using superconducting resonators with tunable coupling*, Appl. Phys. Lett. **104**, 232604 (2014)

[202] K. Y. Tan, M. Partanen, R. E. Lake, J. Govenius, S. Masuda, and M. Möttönen, *Quantum-circuit refrigerator*, Nat. Commun. **8**, 15189 (2017)

[203] M. Partanen, K. Y. Tan, S. Masuda, J. Govenius, R. E. Lake, M. Jenei, L. Grönberg, J. Hassel, S. Simbierowicz, V. Vesterinen, J. Tuorila, T. Ala-Nissila, and M. Möttönen, *Flux-tunable heat sink for quantum electric circuits*, Sci. Rep. **8**, 6325 (2018)

[204] M. Silveri, S. Masuda, V. Sevriuk, K. Y. Tan, M. Jenei, E. Hyyppä, F. Hassler, M. Partanen, J. Goetz, R. E. Lake, L. Grönberg, and M. Möttönen, *Broadband Lamb shift in an engineered quantum system*, Nature Phys. **15**, 533 (2019)

[205] C. H. Wong, C. Wilen, R. McDermott, and M. G. Vavilov, *A tunable quantum dissipator for active resonator reset in circuit QED*, Quantum Sci. Technol. **4**, 025001 (2019)

[206] J. M. Horowitz and K. Jacobs, *Quantum effects improve the energy efficiency of feedback control*, Phys. Rev. E **89**, 042134 (2014)

[207] P. Liuzzo-Scorpo, L. A. Luis A. Correa, R. Schmidt, and G. Adesso, *Thermodynamics of quantum feedback cooling*, Entropy **18**, 48 (2016)

[208] P. Magnard, P. Kurpiers, B. Royer, T. Walter, J.-C. Besse, S. Gasparinetti, M. Pechal, J. Heinsoo, S. Storz, A. Blais, and A. Wallraff, *Fast and Unconditional All-Microwave Reset of a Superconducting Qubit*, Phys. Rev. Lett. **121**, 060502 (2018)

[209] J. Combes and K. Jacobs, *Rapid State Reduction of Quantum Systems Using Feedback Control*, Phys. Rev. Lett. **96**, 010504 (2006)

[210] H. M. Wiseman and J. F. Ralph, *Reconsidering rapid qubit purification by feedback*, New J. Phys. **8**, 90 (2006)

[211] H. M. Wiseman and L. Bouten, *Optimality of Feedback Control Strategies for Qubit Purification*, Quant. Inf. Proc. **7**, 71 (2008)

[212] J. Combes, H. M. Wiseman, K. Jacobs, and A. J. O'Connor, *Rapid purification of quantum systems by measuring in a feedback-controlled unbiased basis*, Phys. Rev. A **82**, 022307 (2010)

[213] J. Tuorila, M. Partanen, T. Ala-Nissilä, and M. Möttönen, *Efficient protocol for qubit initialization with a tunable environment*, npj Quantum Inf. **3**, 27 (2017)

[214] D. Basilewitsch, F. Cosco, N. L. Gullo, M. Möttönen, T. Ala-Nissilä, C. P. Koch, and S. Maniscalco, *Reservoir engineering using quantum optimal control for qubit reset*, New J. Phys. **21**, 093054 (2019)

[215] B. Kraus, H. P. Büchler, S. Diehl, A. Kantian, A. Micheli, and P. Zoller, *Preparation of entangled states by quantum Markov processes*, Phys. Rev. A **78**, 042307 (2008)

[216] F. Reiter, L. Tornberg, G. Johansson, and A. S. Sørensen, *Steady-state entanglement of two superconducting qubits engineered by dissipation*, Phys. Rev. A **88**, 032317 (2013)

[217] M. Mirrahimi, Z. Leghtas, V. V. Albert, S. Touzard, R. J. Schoelkopf, L. Jiang, and M. H. Devoret, *Dynamically protected cat-qubits: a new paradigm for universal quantum computation*, New J. Phys. **16**, 045014 (2014)

[218] J. M. Gambetta, J. M. Chow, and M. Steffen, *Building logical qubits in a superconducting quantum computing system*, npj Quantum Inf. **3**, 2 (2017)

[219] T. Yamamoto, K. Inomata, M. Watanabe, K. Matsuba, T. Miyazaki, W. D. Oliver, Y. Nakamura, and J. S. Tsai, *Flux-driven Josephson parametric amplifier*, Appl. Phys. Lett. **93**, 042510 (2008)

[220] S. Pielawa, G. Morigi, D. Vitali, and L. Davidovich, *Generation of Einstein-Podolsky-Rosen-Entangled Radiation through an Atomic Reservoir*, Phys. Rev. Lett. **98**, 240401 (2007)

[221] S. Diehl, A. Micheli, A. Kantian, B. Kraus, H.-P. Büchler, and P. Zoller, *Quantum states and phases in driven open quantum systems with cold atoms*, Nature Phys. **4**, 878 (2008)

[222] M. J. Kastoryano, F. Reiter, and A. S. Sørensen, *Dissipative Preparation of Entanglement in Optical Cavities*, Phys. Rev. Lett. **106**, 090502 (2011)

[223] D. Basilewitsch, R. Schmidt, D. Sugny, S. Maniscalco, and C. P. Koch, *Beating the limits with initial correlations*, New J. Phys. **19**, 113042 (2017)

[224] B. M. Garraway and P. L. Knight, *Cavity modified quantum beats*, Phys. Rev. A **54**, 3592 (1996)

[225] C. Addis, B. Bylicka, D. Chruściński, and S. Maniscalco, *Comparative study of non-Markovianity measures in exactly solvable one- and two-qubit models*, Phys. Rev. A **90**, 052103 (2014)

[226] A. Levy and R. Kosloff, *The local approach to quantum transport may violate the second law of thermodynamics*, EPL (Europhysics Letters) **107**, 20004 (2014)

[227] L. Henderson and V. Vedral, *Classical, quantum and total correlations*, J. Phys. A: Math. Theor. **34**, 6899 (2001)

[228] C. E. Shannon, *A mathematical theory of communication*, Bell Syst. Tech. J. **27**, 379 (1948)

[229] K. Modi, A. Brodutch, H. Cable, T. Paterek, and V. Vedral, *The classical-quantum boundary for correlations: Discord and related measures*, Rev. Mod. Phys. **84**, 1655 (2012)

[230] H. Ollivier and W. Zurek, *Quantum Discord: A Measure of the Quantumness of Correlations.*, Phys. Rev. Lett. **88**, 01790 (2002)

[231] M. Ali, A. R. P. Rau, and G. Alber, *Quantum discord for two-qubit X states*, Phys. Rev. A **81**, 042105 (2010)

[232] W. K. Wootters, *Entanglement of Formation of an Arbitrary State of Two Qubits*, Phys. Rev. Lett. **80**, 2245 (1998)

[233] K. Rojan, D. M. Reich, I. Dotsenko, J.-M. Raimond, C. P. Koch, and G. Morigi, *Arbitrary-quantum-state preparation of a harmonic oscillator via optimal control*, Phys. Rev. A **90**, 023824 (2014)

[234] K. Geerlings, Z. Leghtas, I. M. Pop, S. Shankar, L. Frunzio, R. J. Schoelkopf, M. Mirrahimi, and M. H. Devoret, *Demonstrating a Driven Reset Protocol for a Superconducting Qubit*, Phys. Rev. Lett. **110**, 120501 (2013)

[235] Y. Shalibo, Y. Rofe, D. Shwa, F. Zeides, M. Neeley, J. M. Martinis, and N. Katz, *Lifetime and Coherence of Two-Level Defects in a Josephson Junction*, Phys. Rev. Lett. **105**, 177001 (2010)

[236] P. O. Boykin, T. Mor, V. Roychowdhury, F. Vatan, and R. Vrijen, *Algorithmic cooling and scalable NMR quantum computers*, Proc. Natl. Acad. Sci. U.S.A. **99**, 3388 (2002)

[237] N. A. Rodríguez-Briones, J. Li, X. Peng, T. Mor, Y. Weinstein, and R. Laflamme, *Heat-bath algorithmic cooling with correlated qubit-environment interactions*, New J. Phys. **19**, 113047 (2017)

[238] N. A. Rodríguez-Briones, E. Martín-Martínez, A. Kempf, and R. Laflamme, *Correlation-Enhanced Algorithmic Cooling*, Phys. Rev. Lett. **119**, 050502 (2017)

[239] L. J. Schulman, T. Mor, and Y. Weinstein, *Physical Limits of Heat-Bath Algorithmic Cooling*, Phys. Rev. Lett. **94**, 120501 (2005)

[240] J. Fischer, D. Basilewitsch, C. P. Koch, and D. Sugny, *Time-optimal control of the purification of a qubit in contact with a structured environment*, Phys. Rev. A **99**, 033410 (2019)

[241] V. Jurdjevic, *Geometric Control Theory*, Cambridge University Press, 1st edition, 1997

[242] U. Boscain, G. Charlot, J.-P. Gauthier, S. Guérin, and H.-R. Jauslin, *Optimal control in laser-induced population transfer for two- and three-level quantum systems*, J. Math. Phys. **43**, 2107 (2002)

[243] D. Sugny, C. Kontz, and H. R. Jauslin, *Time-optimal control of a two-level dissipative quantum system*, Phys. Rev. A **76**, 023419 (2007)

[244] D. Basilewitsch, J. Fischer, D. M. Reich, D. Sugny, and C. P. Koch, *Fundamental Bounds on Qubit Reset*, arXiv:2001.09107 (2020)

[245] J. Zhang, J. Vala, S. Sastry, and K. B. Whaley, *Geometric theory of nonlocal two-qubit operations*, Phys. Rev. A **67**, 042313 (2003)

[246] B. Kraus and J. I. Cirac, *Optimal creation of entanglement using a two-qubit gate*, Phys. Rev. A **63**, 062309 (2001)

[247] C. Rigetti, A. Blais, and M. Devoret, *Protocol for Universal Gates in Optimally Biased Superconducting Qubits*, Phys. Rev. Lett. **94**, 240502 (2005)

[248] C. Rigetti and M. Devoret, *Fully microwave-tunable universal gates in superconducting qubits with linear couplings and fixed transition frequencies*, Phys. Rev. B **81**, 134507 (2010)

[249] N. Khaneja, R. Brockett, and S. J. Glaser, *Time optimal control in spin systems*, Phys. Rev. A **63**, 032308 (2001)

[250] T. Caneva, M. Murphy, T. Calarco, R. Fazio, S. Montangero, V. Giovannetti, and G. E. Santoro, *Optimal Control at the Quantum Speed Limit*, Phys. Rev. Lett. **103**, 240501 (2009)

[251] I. Brouzos, A. I. Streltsov, A. Negretti, R. S. Said, T. Caneva, S. Montangero, and T. Calarco, *Quantum speed limit and optimal control of many-boson dynamics*, Phys. Rev. A **92**, 062110 (2015)

[252] S. van Frank, A. Negretti, T. Berrada, R. Bücker, S. Montangero, J.-F. Schaff, T. Schumm, T. Calarco, and J. Schmiedmayer, *Interferometry with non-classical motional states of a Bose–Einstein condensate*, Nat. Commun. **5** (2014)

[253] S. L. Braunstein and C. M. Caves, *Statistical distance and the geometry of quantum states*, Phys. Rev. Lett. **72**, 3439 (1994)

[254] J. Liu and H. Yuan, *Quantum parameter estimation with optimal control*, Phys. Rev. A **96**, 012117 (2017)

[255] T. Ogawa and H. Nagaoka, *Strong converse and Stein's lemma in quantum hypothesis testing*, IEEE Trans. Inf. Theory **46**, 2428 (2000)

[256] T. Ogawa and M. Hayashi, *On error exponents in quantum hypothesis testing*, IEEE Trans. Inf. Theory **50**, 1368 (2004)

[257] M. Hayashi, *Optimal sequence of quantum measurements in the sense of Stein s lemma in quantum hypothesis testing*, J. Phys. A **35**, 10759 (2002)

[258] K. M. R. Audenaert, J. Calsamiglia, R. Muñoz Tapia, E. Bagan, L. Masanes, A. Acin, and F. Verstraete, *Discriminating States: The Quantum Chernoff Bound*, Phys. Rev. Lett. **98**, 160501 (2007)

[259] K. M. R. Audenaert, M. Nussbaum, A. Szkola, and F. Verstraete, *Asymptotic Error Rates in Quantum Hypothesis Testing*, Commun. Math. Phys. **279**, 251 (2008)

[260] F. Hiai and D. Petz, *The proper formula for relative entropy and its asymptotics in quantum probability*, Commun. Math. Phys. **143**, 99 (1991)

[261] M. Hayashi, *Error exponent in asymmetric quantum hypothesis testing and its application to classical-quantum channel coding*, Phys. Rev. A **76**, 062301 (2007)

[262] A. Acin, *Statistical Distinguishability between Unitary Operations*, Phys. Rev. Lett. **87**, 177901 (2001)

[263] G. M. D'Ariano, P. Lo Presti, and M. G. A. Paris, *Using Entanglement Improves the Precision of Quantum Measurements*, Phys. Rev. Lett. **87**, 270404 (2001)

[264] R. Duan, Y. Feng, and M. Ying, *Entanglement is Not Necessary for Perfect Discrimination between Unitary Operations*, Phys. Rev. Lett. **98**, 100503 (2007)

[265] C. Lu, J. Chen, and R. Duan, *Some Bounds on the Minimum Number of Queries Required for Quantum Channel Perfect Discrimination*, Quantum Info. Comput. **12**, 138 (2012)

[266] G. Chiribella, G. M. D'Ariano, and P. Perinotti, *Memory Effects in Quantum Channel Discrimination*, Phys. Rev. Lett. **101**, 180501 (2008)

[267] R. Duan, Y. Feng, and M. Ying, *Perfect Distinguishability of Quantum Operations*, Phys. Rev. Lett. **103**, 210501 (2009)

[268] A. W. Harrow, A. Hassidim, D. W. Leung, and J. Watrous, *Adaptive versus nonadaptive strategies for quantum channel discrimination*, Phys. Rev. A **81**, 032339 (2010)

[269] R. Duan, Y. Feng, and M. Ying, *Local Distinguishability of Multipartite Unitary Operations*, Phys. Rev. Lett. **100**, 020503 (2008)

[270] H. Yuen, R. Kennedy, and M. Lax, *Optimum testing of multiple hypotheses in quantum detection theory*, IEEE Trans. Inf. Theory **21**, 125 (1975)

[271] V. Giovannetti, S. Lloyd, and L. Maccone, *Advances in quantum metrology*, Nat. Photonics **5**, 222 (2011)

[272] V. Giovannetti, S. Lloyd, and L. Maccone, *Quantum metrology*, Phys. Rev. Lett. **96**, 010401 (2006)

[273] S. L. Braunstein, C. M. Caves, and G. J. Milburn, *Generalized uncertainty relations: theory, examples, and Lorentz invariance*, Ann. Phys. **247**, 135 (1996)

[274] A. Fujiwara and H. Imai, *A fibre bundle over manifolds of quantum channels and its application to quantum statistics*, J. Phys. A **41**, 255304 (2008)

[275] B. M. Escher, R. L. de Matos Filho, and L. Davidovich, *General framework for estimating the ultimate precision limit in noisy quantum-enhanced metrology*, Nat. Phys. **7**, 406 (2011)

[276] R. Demkowicz-Dobrzanski and L. Maccone, *Using entanglement against noise in quantum metrology*, Phys. Rev. Lett. **113**, 250801 (2014)

[277] R. Demkowicz-Dobrzanski, J. Kolodynski, and M. Guta, *The elusive Heisenberg limit in quantum-enhanced metrology*, Nat. Commun. **3**, 1063 (2012)

[278] S. F. Huelga, C. Macchiavello, T. Pellizzari, A. K. Ekert, M. B. Plenio, and J. I. Cirac, *Improvement of frequency standards with quantum entanglement*, Phys. Rev. Lett. **79**, 3865 (1997)

[279] A. W. Chin, S. F. Huelga, and M. B. Plenio, *Quantum metrology in non-Markovian environments*, Phys. Rev. Lett. **109**, 233601 (2012)

[280] D. W. Berry, M. Tsang, M. J. W. Hall, and H. M. Wiseman, *Quantum Bell-Ziv-Zakai Bounds and Heisenberg Limits for Waveform Estimation*, Phys. Rev. X **5**, 031018 (2015)

[281] S. Alipour, M. Mehboudi, and A. T. Rezakhani, *Quantum Metrology in Open Systems: Dissipative Cramér-Rao Bound*, Phys. Rev. Lett. **112**, 120405 (2014)

[282] M. Beau and A. del Campo, *Nonlinear Quantum Metrology of Many-Body Open Systems*, Phys. Rev. Lett. **119**, 010403 (2017)

[283] J. Liu, H. Yuan, X.-M. Lu, and X. Wang, *Quantum Fisher information matrix and multiparameter estimation*, J. Phys. A **53**, 023001 (2019)

[284] M. Tsang, R. Nair, and X.-M. Lu, *Quantum theory of superresolution for two incoherent optical point sources*, Phys. Rev. X **6**, 031033 (2016)

[285] H. Yuan and C.-H. F. Fung, *Optimal feedback scheme and universal time scaling for Hamiltonian parameter estimation*, Phys. Rev. Lett. **115**, 110401 (2015)

[286] H. Yuan, *Sequential feedback scheme outperforms the parallel scheme for Hamiltonian parameter estimation*, Phys. Rev. Lett. **117**, 160801 (2016)

[287] H. Xu, J. Li, L. Liu, Y. Wang, H. Yuan, and X. Wang, *Generalizable control for quantum parameter estimation through reinforcement learning*, npj Quantum Inf. **5** (2019)

[288] J. Liu and H. Yuan, *Control-enhanced multiparameter quantum estimation*, Phys. Rev. A **96**, 042114 (2017)

[289] S. Pang and A. N. Jordan, *Optimal adaptive control for quantum metrology with time-dependent Hamiltonians*, Nat. Commun. **8**, 14695 (2017)

[290] Z. Hou, R.-J. Wang, J.-F. Tang, H. Yuan, G.-Y. Xiang, C.-F. Li, and G.-C. Guo, *Control-Enhanced Sequential Scheme for General Quantum Parameter Estimation at the Heisenberg Limit*, Phys. Rev. Lett. **123**, 040501 (2019)

[291] M. Naghiloo, A. Jordan, and K. Murch, *Achieving optimal quantum acceleration of frequency estimation using adaptive coherent control*, Phys. Rev. Lett. **119**, 180801 (2017)

[292] A. Predko, F. Albarelli, and A. Serafini, *Time-local optimal control for parameter estimation in the Gaussian regime*, Phys. Lett. A **384**, 126268 (2020)

[293] N. Mirkin, M. Larocca, and D. Wisniacki, *Quantum metrology in a non-Markovian quantum evolution*, arXiv:1912.04675 (2019)

[294] A. M. Childs, J. Preskill, and J. Renes, *Quantum information and precision measurement*, J. Mod. Opt. **47**, 155 (2000)

[295] Y. Chen and H. Yuan, *Zero-error quantum hypothesis testing in finite time with quantum error correction*, Phys. Rev. A **100**, 022336 (2019)

[296] D. Basilewitsch, H. Yuan, and C. P. Koch, *Optimally controlled quantum discrimination and estimation*, arXiv:2007.09729 (2020)

[297] C. W. Helstrom, *Quantum Detection and Estimation Theory*, Academic Press, 1976

[298] M. W. Doherty, N. B. Manson, P. Delaney, F. Jelezko, J. Wrachtrup, and L. C. Hollenberg, *The nitrogen-vacancy colour centre in diamond*, Phys. Rep. **528**, 1 (2013)

[299] C. D. Bruzewicz, J. Chiaverini, R. McConnell, and J. M. Sage, *Trapped-ion quantum computing: Progress and challenges*, Appl. Phys. Rev. **6**, 021314 (2019)

[300] C. Kloeffel and D. Loss, *Prospects for Spin-Based Quantum Computing in Quantum Dots*, Annu. Rev. Condens. Matter Phys. **4**, 51 (2013)

[301] S. Slussarenko and G. J. Pryde, *Photonic quantum information processing: A concise review*, Appl. Phys. Rev. **6**, 041303 (2019)

[302] E. Jeffrey, D. Sank, J. Y. Mutus, T. C. White, J. Kelly, R. Barends, Y. Chen, Z. Chen, B. Chiaro, A. Dunsworth, A. Megrant, P. J. J. O'Malley, C. Neill, P. Roushan, A. Vainsencher, J. Wenner, A. N. Cleland, and J. M. Martinis, *Fast Accurate State Measurement with Superconducting Qubits*, Phys. Rev. Lett. **112**, 190504 (2014)

[303] J. Majer, J. M. Chow, J. M. Gambetta, J. Koch, B. R. Johnson, J. A. Schreier, L. Frunzio, D. I. Schuster, A. A. Houck, A. Wallraff, A. Blais, M. H. Devoret, S. M. Girvin, and R. J. Schoelkopf, *Coupling superconducting qubits via a cavity bus*, Nature **449**, 443 (2007)

[304] S. Poletto, J. M. Gambetta, S. T. Merkel, J. A. Smolin, J. M. Chow, A. D. Córcoles, G. A. Keefe, M. B. Rothwell, J. R. Rozen, D. W. Abraham, C. Rigetti, and M. Steffen, *Entanglement of Two Superconducting Qubits in a Waveguide Cavity via Monochromatic Two-Photon Excitation*, Phys. Rev. Lett. **109**, 240505 (2012)

[305] J. M. Chow, J. M. Gambetta, A. D. Córcoles, S. T. Merkel, J. A. Smolin, C. Rigetti, S. Poletto, G. A. Keefe, M. B. Rothwell, J. R. Rozen, M. B. Ketchen, and M. Steffen, *Universal Quantum Gate Set Approaching Fault-Tolerant Thresholds with Superconducting Qubits*, Phys. Rev. Lett. **109**, 060501 (2012)

[306] M. Kjaergaard, M. E. Schwartz, J. Braumüller, P. Krantz, J. I.-J. Wang, S. Gustavsson, and W. D. Oliver, *Superconducting Qubits: Current State of Play*, Annu. Rev. Condens. Matter Phys. **11**, 369 (2020)

[307] S. L. Braunstein, *Error Correction for Continuous Quantum Variables*, Phys. Rev. Lett. **80**, 4084 (1998)

[308] S. L. Braunstein and P. van Loock, *Quantum information with continuous variables*, Rev. Mod. Phys. **77**, 513 (2005)

[309] M. H. Michael, M. Silveri, R. T. Brierley, V. V. Albert, J. Salmilehto, L. Jiang, and S. M. Girvin, *New Class of Quantum Error-Correcting Codes for a Bosonic Mode*, Phys. Rev. X **6**, 031006 (2016)

[310] M. Reagor, H. Paik, G. Catelani, L. Sun, C. Axline, E. Holland, I. M. Pop, N. A. Masluk, T. Brecht, L. Frunzio, M. H. Devoret, L. Glazman, and R. J. Schoelkopf,

Reaching 10ms single photon lifetimes for superconducting aluminum cavities, Appl. Phys. Lett. **102**, 192604 (2013)

[311] J. Koch, T. M. Yu, J. Gambetta, A. A. Houck, D. I. Schuster, J. Majer, A. Blais, M. H. Devoret, S. M. Girvin, and R. J. Schoelkopf, *Charge-insensitive qubit design derived from the Cooper pair box*, Phys. Rev. A **76**, 042319 (2007)

[312] M. Hofheinz, E. M. Weig, M. Ansmann, R. C. Bialczak, E. Lucero, M. Neeley, A. D. O'Connell, H. Wang, J. M. Martinis, and A. N. Cleland, *Generation of Fock states in a superconducting quantum circuit*, Nature **454**, 310 (2008)

[313] L. Hu, Y. Ma, W. Cai, X. Mu, Y. Xu, W. Wang, Y. Wu, H. Wang, Y. P. Song, C.-L. Zou, S. M. Girvin, L.-M. Duan, and L. Sun, *Quantum error correction and universal gate set operation on a binomial bosonic logical qubit*, Nature Physics **15**, 503 (2019)

[314] Y. Y. Gao, B. J. Lester, K. S. Chou, L. Frunzio, M. H. Devoret, L. Jiang, S. M. Girvin, and R. J. Schoelkopf, *Entanglement of bosonic modes through an engineered exchange interaction*, Nature **566**, 509 (2019)

[315] Y. Y. Gao, B. J. Lester, Y. Zhang, C. Wang, S. Rosenblum, L. Frunzio, L. Jiang, S. M. Girvin, and R. J. Schoelkopf, *Programmable Interference between Two Microwave Quantum Memories*, Phys. Rev. X **8**, 021073 (2018)

[316] Y. Zhang, B. J. Lester, Y. Y. Gao, L. Jiang, R. J. Schoelkopf, and S. M. Girvin, *Engineering bilinear mode coupling in circuit QED: Theory and experiment*, Phys. Rev. A **99**, 012314 (2019)

[317] A. Barenco, C. H. Bennett, R. Cleve, D. P. DiVincenzo, N. Margolus, P. Shor, T. Sleator, J. A. Smolin, and H. Weinfurter, *Elementary gates for quantum computation*, Phys. Rev. A **52**, 3457 (1995)

[318] J. Zhang, J. Vala, S. Sastry, and K. B. Whaley, *Exact Two-Qubit Universal Quantum Circuit*, Phys. Rev. Lett. **91**, 027903 (2003)

[319] M. M. Taddei, B. M. Escher, L. Davidovich, and R. L. de Matos Filho, *Quantum Speed Limit for Physical Processes*, Phys. Rev. Lett. **110**, 050402 (2013)

[320] S. Deffner and E. Lutz, *Quantum Speed Limit for Non-Markovian Dynamics*, Phys. Rev. Lett. **111**, 010402 (2013)

[321] D. P. Pires, M. Cianciaruso, L. C. Céleri, G. Adesso, and D. O. Soares-Pinto, *Generalized Geometric Quantum Speed Limits*, Phys. Rev. X **6**, 021031 (2016)

[322] F. Campaioli, F. A. Pollock, and K. Modi, *Tight, robust, and feasible quantum speed limits for open dynamics*, Quantum **3**, 168 (2019)

[323] M. H. Goerz, F. Motzoi, K. B. Whaley, and C. P. Koch, *Charting the circuit QED design landscape using optimal control theory*, npj Quantum Inf. **3** (2017)

Hiermit versichere ich, dass ich die vorliegende Dissertation selbständig, ohne unerlaubte Hilfe Dritter angefertigt und andere als die in der Dissertation angegebenen Hilfsmittel nicht benutzt habe. Alle Stellen, die wörtlich oder sinngemäß aus veröffentlichten oder unveröffentlichten Schriften entnommen sind, habe ich als solche kenntlich gemacht. Dritte waren an der inhaltlichen Erstellung der Dissertation nicht beteiligt; insbesondere habe ich nicht die Hilfe eines kommerziellen Promotionsberaters in Anspruch genommen. Kein Teil dieser Arbeit ist in einem anderen Promotions- oder Habilitationsverfahren durch mich verwendet worden.

_____

Daniel Basilewitsch